Universidad Carlos III de Madrid

Micromechanics of magnesium and its alloys studied by nanoindentation

Raúl Sánchez Martín

Supervised by:
Dr. J.M. Molina Aldareguia
Dr. M.T. Pérez Prado

A thesis submitted for the degree of Doctor of Philosophy
Department of Materials Science and Engineering and Chemical Engineering
November 2016

Universidad
Carlos III de Madrid
www.uc3m.es

Tesis Doctoral

Micromechanics of magnesium and its alloys studied by nanoindentation

Autor: Raúl Sánchez Martín

Directores: Dr. J.M. Molina Aldareguia

Dr. M.T. Pérez Prado

Firma del Tribunal Calificador:

Firma:

Presidente:

Vocal:

Secretario:

Calificación:

Leganés, ... de ..... de .....

Dedicated to my family

Acknowledgements

The present Ph.D. thesis has been carried out at the Madrid Institute for Advanced Studies of Materials (IMDEA Materials) and defended at the Carlos III University of Madrid. It is my pleasure to acknowledge all those who shared with me this incredible journey.

First, I would like to express my gratitude to my advisors Dr. J.M. Molina Aldareguia and Dr. M.T. Pérez Prado. It would have been impossible to success in this challenge without your support, guidance and constant encouragement. Besides being world-leading scientists, you are also incredible people who never hesitate to help me further beyond your professional responsibilities. It has been a complete honour working with you.

I would like to extend my sincere appreciation to Prof. Dr. Javier LLorca, director of IMDEA Materials, for giving me the opportunity of joining a top-notch research institution. Your passion and dedication for science is a remarkable example for all of us.

My sincere gratitude to Prof. Dr. Javier Segurado, for your tremendous and friendly support in the simulation section of my research. Despite your limited availability, you always found time to help me.

I sincerely thank Prof. Dr. Ingo Steinbach for giving me the chance to collaborate with him during my visiting stay at the Interdisciplinary Centre for Advanced Materials Simulation (ICAMS, Bochum, Germany). In addition to improve my simulations skills, I had the chance to immerse myself in the German culture. The scientific and personal support provided by Dr. Efim Borukhovick, Dr. Reza Darvishi and Dr. Oleg Shchyglo is also highly acknowledged.

All the members belonging to the Ph.D. program in Materials Science and Engineering of the Carlos III University are kindly acknowledged for the excellent scientific training provided in their master courses.

I gratefully acknowledge the economical support provided by the European Commission (ExoMet Project, 7^{th} Framework Programme, Contract FP7-NMP3-LA-2012-280421) and

by the Spanish Ministry of Economy, Competitiveness and Sports (FPU13/03037).

I would like to remark the pleasant, friendly and supportive working environment I have enjoined during these years. All the members (past and present) of IMDEA Materials are kindly acknowledged for making this possible. Despite the lack of space, I would like to mention some of them: Miguel Monclús, Saeid Lotfian, Rafael Soler and Alberto Palomares, for their help in the development of the nanomechanical testing experiments; Ana Fernández, Paloma Hidalgo, Nathamar Dudamell and Carmen Cepeda, for their help in the metallographic preparation of magnesium; Aitor Cruzado, Daniel Rodriguez, Marcos Rodriguez, Raúl Muñoz, Francisca Martínez, Sergio Sábada and Fernando Naya, for their help in the finite element simulations; and finally, Eva, Fede, Guillermo, Juan Pedro, Laura, Roberto, Rocío, Julían, Víctor, Irene, Luis, Pablo, Arcadio and many more, for the exceptional working atmosphere they provided.

Gracias a mis buenos amigos Oscar Arteaga, Alejandro Espinosa y Sergio Carrera, por vuestro apoyo y compresión durante estos 4 años.

Por último, querría mostrar mi más sincero agradecimiento a mi familia. A mi hermano Javier, gracias por tu apoyo en esos duros momentos de la tesis, que tú conoces más y mucho mejor que yo. Y por su puesto, a mis padres, por mostrarme vuestro apoyo incondicional en todos y cada uno de los aspectos de mi vida.

Thank you very much to all of you - Muchas gracias a todos,

Raúl Sánchez Martín

Contents

Resumen

La fabricación de vehículos ligeros constituye una estrategia prometedora en cuanto a la reducción del consumo de combustibles fósiles y las emisiones de gases de efecto invernadero. El magnesio es un material muy conveniente para tal fin debido a su excelente resistencia específica. Sin embargo, ciertos aspectos, tales como su baja ductilidad y alta anisotropía mecánica a temperatura ambiente, obstaculizan su uso general a nivel industrial. La aleación de magnesio con otros elementos químicos es una estrategia prometedora dado que este material reacciona fácilmente con otros compuestos formando precipitados y/o fases intermetálicas que afectan de una manera severa a la competición entre los diferentes mecanismos de deformación y microestructura, y por lo tanto, a sus propiedades mecánicas.

Las estrategias tradicionales enfocadas al desarrollo de nuevas aleaciones de magnesio con propiedades mecánicas avanzadas se han basado en extensas, largas y costosas campañas experimentales para evaluar las propiedades de las nuevas aleaciones. Esta limitación podría ser resuelta aplicando *Métodos Combinatorios* en este proceso. Dicha metodología, aplicada inicialmente en la industria química y farmacéutica, permite producir y caracterizar un gran número de nuevos materiales en muy poco tiempo. Sin embargo, su implementación efectiva en procesos metalúrgicos requiere el desarrollo de diversas nuevas tecnologías. En concreto, se pueden destacar dos aspectos tecnológicos sin resolver: en primer lugar, un nuevo método que permita la caracterización de los diferentes mecanismos de deformación del magnesio y sus aleaciones de una forma rápida requiriendo poco material; y segundo, nuevos modelos matemáticos que sean capaces de reproducir el comportamiento mecánico real de estos materiales a nivel tanto micro- como macroscópico. En cuanto al primero, nanoindentación es una técnica muy prometedora ya que, además de ser fácil de usar y rápida, requiere cantidades de material muy reducidas. Respecto al segundo aspecto, los modelos de plasticidad cristalina cumplen con los requisitos dado que son capaces de capturar la deformación plástica por deslizamiento cristalográfico y maclado.

La presente tesis doctoral constituye un elemento fundamental en cuanto a la superación de estas dos limitaciones. El principal objetivo de esta tesis doctoral ha sido el estudio

de la competición de los diferentes mecanismos de deformación del magnesio y sus aleaciones bajo diferentes condiciones, combinando técnicas avanzadas de caracterización, como nanoindentación de monocristales, microscopía de fuerza atómica o microscopía de electrones retrodispersados, junto con avanzadas técnicas de simulación basadas en novedosos modelos de plasticidad cristalina. Se ha constatado que la dureza y la deformación residual y la microtextura alrededor de la indentación dependen de una manera notoria de un efecto combinado de la orientación del cristal indentado así como de la temperatura de ensayo. Dichas dependencias han sido explicadas satisfactoriamente desde un punto de vista tanto analítico como numérico debido a la activación de diferentes modos de deslizamiento y maclado en las áreas cercanas a la zona de ensayo. Se ha demostrado que, mientras que los principales mecanismos de deformación a temperatura ambiente son el deslizamiento basal y el maclado de extensión, la deformación plástica a alta temperatura es dominada por deslizamiento basal y prismático. Se mostrado que el incremento de actividad prismática con la temperatura es compensada con una reducción muy importante de la actividad de maclado de extensión. Además, se ha desarrollado un novedoso modelo de plasticidad cristalina que considera la micromecánica real del maclado de extensión. Además, se ha constatado que es fundamental tener en cuenta que la nucleación de una macla es un proceso que requiere estados tensionales mucho más severos que su propagación a la hora de reproducir la evolución de la actividad de dicho mecanismo de deformación con la temperatura.

Además, se ha demostrado que el maclado de extensión es un mecanismo de deformación afectado severamente por efectos tamaño. Nuestros resultados experimentales evidencian que la activación de una macla requiere la concentración de altas tensiones en un determinado volumen. Finalmente, se ha desarrollado una nueva y práctica metodología para estimar la tensión crítica resuelta de aleaciones de magnesio de interés industrial. Esta metodología, que se basa en la variación de la dureza con la orientación cristalográfica del grano indentado, ha sido diseñada teniendo en cuenta estándares industriales de manera que pueda ser utilizada fácilmente por la comunidad industrial. La metodología propuesta, validada inicialmente para magnesio puro, ha sido utilizada para estudiar los mecanismos de deformación de una aleación de magnesio de tierras raras aleada con un 1% de manganeso y 1% de neodimio. Se ha demostrado que la adicción de tierras raras conlleva una importante reducción de la resistencia relativa de los sistemas de deslizamiento basales y no basales, lo que justifica la mayor isotropía mecánica mostrada por este material en comparación con aleaciones de magnesio convencionales.

Abstract

Weight reduction is a cost-effective approach to decrease the fossil fuel consumption and greenhouse gas emissions of the transport industry. Magnesium, the lightest structural metal, constitutes a significant alternative as weight-saving material. However, some issues hinder its widespread use in the industry, like its low ductility and high mechanical anisotropy at room temperature. Due to its high chemical activity, alloying is a promising strategy to overcome these limitations, as magnesium easily reacts with other compounds to form precipitates and/or intermetallic phases which heavily affect the competition between the different deformation modes and microstructure, and therefore, its physical properties.

Traditional approaches to develop novel magnesium alloys with enhanced mechanical properties rely on vast and time-consuming experimental campaigns in order to assess the mechanical properties of the new alloys. This limitation could be solved with the application of *Combinatorial Methods* in this process. This new methodology, initially applied in the chemist and pharmaceutical industries, allows to produce and characterise a great number of new materials in a very sort time. However, the effective implementation of such approach requires the development of several new technologies. Among others, two main unresolved technological issues can be mentioned: first, a new approach to characterise the different deformation modes of magnesium and its alloys in an easy and fast way; and second, new material models that are able to reproduce the real mechanical behaviour of magnesium and its alloys at the macro- and micro-mechanical scale. Regarding the first one, nanoindentation seems to be a perfect candidate as, in addition to being easy and fast, requires small amount of material. Regarding the second one, crystal plasticity models meet perfectly the requirements as they are able to capture plastic deformation by crystallographic glide and mechanical twinning.

The present Ph.D. thesis constitutes a milestone in order to overcome these two last limitations. The main objective of this research has been to study the competition between the different deformation modes in magnesium and its alloys under different testing conditions, combining advanced characterisation techniques, like single crystal nanoindentation,

atomic force microscopy and electron backscatter diffraction, with novel crystal plasticity modelling approaches. It has been shown that the hardness and the residual deformation and microtexture around an indent highly depend on the combined effect of the orientation of the indented plane and testing temperature. Such dependencies have been successfully explained from an analytical and numerical point of view due to the activation of different slip and twin modes in different areas in the surroundings of the indent. It is demonstrated that, while the main deformation modes at room temperature are basal slip and tensile twinning, the plastic deformation at high temperature is dominated by basal and prismatic slip. It is shown that the increase of prismatic activity with temperature is compensated by a dramatic decrease of tensile twin activity as temperature increases. In addition, a novel crystal plasticity model which takes into account the micromechanics of tensile twinning has been developed. In is shown that, in order to properly reproduce the evolution of tensile twin activity with temperature, it is fundamental to take into account the fact that twin activation is a process which requires a much bigger stress than twin propagation.

It has been also demonstrated that mechanical twinning is a process highly affected by size effects. Our results provides experimental evidences that twin activation requires the concentration of high stresses in a certain activation volume. Finally, a novel and practical methodology has been developed in order to estimate the critical resolved shear stresses of industrial magnesium alloys. This methodology, which is based on the variation of the hardness with the crystallographic orientation of the indented grain, is designed taking into account industrial standards so it can be easily applied by the alloy development community. First validated in pure magnesium, the proposed methodology is applied to study the deformation modes of a rare-earth magnesium alloy containing 1% of Manganese and 1% of Neodymium. It is shown that the addition of rare-earth elements lead to an important reduction between the relative strength of the basal and non-basal slip systems, which justifies the much more isotropic mechanical behaviour of this material in comparison with conventional magnesium alloys.

List of Abbreviations

Mg	Magnesium
RT	Room temperature
Fe	Iron
Al	Aluminium
Mn	Manganese
Zn	Zinc
Zr	Zirconium
EBSD	Electron backscatter diffraction
HCP	Hexagonal close-packed
AFM	Atomic force microscopy
CPFE	Crystal plasticity finite element
CRSS	Critical resolved shear stress
$\mathbf{CRSS_{tw}}$	CRSS for twinning
AZ31	3 wt.% Al, 1 wt.% Zinc, Mg balance
D	Diameter of a micropillar
σ	Normal stress
τ	Shear stress

CP	Crystal plasticity
FE	Finite element
FIB	Focused ion beam
FCC	Face centred cubic
FCT	Face centred tetragonal
ISE	Indentation size effect
BCC	Body centred cubic
MN11	1 wt.% Mn, 1 wt.% Nd, Mg balance
SEM	Scanning electron microscopy
SE	Secondary electrons
BSE	Backscattered electrons
DC	Direct current
AC	Alternating current
PID	Proportional integral derivative
UMAT	User-defined material subroutine
IP	Integration point
GND	Geometrically necessary dislocation
C3D10M	Quadratic tetrahedral element
C3D8	Linear hexahedral element
TT	Tensile twin
GB	Grain boundary
Y	Yttrium
Gd	Gadolinium

Nomenclature

$\boldsymbol{\alpha}$	Internal variables of the CP model
$\boldsymbol{\sigma}$	Cauchy stress tensor
$\boldsymbol{F}$	Deformation gradient
$\boldsymbol{F}^e$	Elastic part of the deformation gradient
$\boldsymbol{F}^p$	Plastic part of the deformation gradient
$\boldsymbol{I}$	Second-order identity tensor
$\boldsymbol{K}^{\boldsymbol{el}}$	Stiffness matrix of a finite element model
$\boldsymbol{L}^{\boldsymbol{p}}_{\boldsymbol{re}\ \ \boldsymbol{sl}}$	Re-slip contribution to the velocity gradient
$\boldsymbol{L}^{\boldsymbol{p}}_{\boldsymbol{sl}}$	Slip contribution to the velocity gradient
$\boldsymbol{L}^{\boldsymbol{p}}_{\boldsymbol{tw}}$	Twin contribution to the velocity gradient
$\boldsymbol{L}$	Velocity gradient
$\boldsymbol{L}^p$	Plastic velocity gradient
$\boldsymbol{m}^{\alpha}_{sl}$	Unit vector in the slip direction of the slip system α
$\boldsymbol{m}^{\xi}_{tw}$	Unit vector in the twin direction of the twin system ξ
$\boldsymbol{n}^{\alpha}_{sl}$	Unit vector perpendicular to the slip plane α
$\boldsymbol{n}^{\xi}_{tw}$	Unit vector perpendicular to the twin plane ξ
$\boldsymbol{Q}^{\xi}$	Rotation matrix associated with the twin transformation of the twin system ξ

$\boldsymbol{R^{\alpha}}$ Loads applied in the nodes of a finite element model

$\boldsymbol{R}(\boldsymbol{F}^e)$ Tensorial residual function depending on the elastic deformation gradient

$\boldsymbol{S}$ Second Piola-Kirchoff stress tensor

$\boldsymbol{S}^{\alpha}$ Schmid tensor of the slip system α

$\boldsymbol{S}^{\xi}$ Second Piola-Kirchoff stress tensor corresponding to the twin plane ξ

$\boldsymbol{S}^{e}$ Green-Lagrange strain tensor

$\boldsymbol{S}^{parent}$ Second Piola-Kirchoff stress tensor of the parent phase

$\boldsymbol{x}$ Nodal displacements of a finite element model

δ Declination angle

δ_{ik} Kronecker delta

$\dot{\gamma}_0$ Reference shear strain rate

$\dot{\gamma}^{\alpha}$ Shear rate of the slip system α

$\dot{f}_0$ Initial twin tranformation rate

Γ Accumulated shear

γ_{tw} Characteristic shear of twinning

$\mathbb{C}$ Fourth-order elastic tensor

$\mathbb{C}^{\xi}$ Stiffness tensor reorientated by the twin transformation of the variant ξ

$\mathbb{J}$ Fourth-order tensor corresponding to the Jacobian obtained as $\frac{\partial \boldsymbol{R}(\boldsymbol{F}^e)}{\partial \boldsymbol{F}^e}$

$\mathbb{K}$ Material tangent matrix

σ Cauchy stress

σ_{tw} Stress state related to the formation of a twin

τ^{α} Shear stress acting on the slip plane α

$\tau^{\alpha}_{c,0}$ Initial critical resolved shear stress of the slip plane α

$\tau^{\alpha}_{c,s}$ Saturation critical resolved shear stress of the slip plane α

τ^{α}_{c} Critical resolved shear stress of the slip system α

τ^{ξ} Shear stress acting on the twin plane ξ

$\tau^{\xi}_{c,0}$ Initial critical resolved shear stress of the twin plane ξ

$\tau^{\xi}_{c,s}$ Saturation critical resolved shear stress of the twin plane ξ

τ_c^ξ	Critical resolved shear stress of the twin plane ξ
τ_{nucl}^ξ	Nucleation stress of the twin plane ξ
τ_{pro}^ξ	Propagation stress of the twin plane ξ
ξ	Twin system ξ
A_c	Contact area of an indentation
a_{sl}	Hardening exponent for slip
a_{tw}	Hardening exponent for twinning
$d\epsilon$	Perturbation in the numerical evaluation of the material tangent matrix
E	Young's modulus
E_i	Young's modulus of the indenter
E_r	Reduced modulus
E_{tw}	Energetic barrier related to the formation of a twin
f^ξ	Volume fraction of the twin system ξ
f_{pro}^ξ	Initial twin volume fraction of the propagation process of the twin plane ξ
H	Hardness
h	Transition depth at which the conical part of an sphero-conical tip begins to stablish contact with the sample
h^α	Hardening modulus of the slip system α
h_0^α	Initial hardening modulus of the slip system α
h_c	Contact depth of an indentation
h_f	Final indentation depth after completing the unloading
h_{max}	Total depth at maximum load during an indentation
J	Determinant of the deformation gradient
m_{sl}	Rate-sensitive exponent for slip
m_{tw}	Rate-sensitive exponent for twinning
N_{sl}	Number of slip systems
N_{tw}	Number of twin systems
P_{max}	Maximum load reached during an indentation

$q^{\alpha\beta}$	Latent hardening parameter
q_{sl-sl}	Slip-to-slip hardening parameter
q_{tw-sl}	Twin-to-slip hardening parameter
S	Stiffness of the unloading curve of an indentation
SF	Schmid factor
v	Poisson's ratio
v_i	Poisson's ratio of the indenter
V_{tw}	Activation volume related to the formation of a twin

"We live in a society exquisitely dependent on science and technology, in which hardly anyone knows anything about science and technology"

Carl Sagan

1 Introduction

1.1 Introduction to magnesium

Magnesium (Mg) is an alkaline-earth metal that belongs to Group II of the periodic table. It is solid at room temperature (RT) and its atomic number and atomic weight are 12 and 24.305 amu respectively. Its melting point is 651 ℃ and it transforms into gas at 1107 ℃ [1].

Mg is the 4^{th} more abundant element on Earth, following iron (Fe), oxygen and silicon. Moreover, it is the second most abundant metal in seawater [2]. However, Mg is never found in nature in its pure state, since it readily reacts with other elements to form compounds [1]. The most common compounds of Mg are dolomite ($MgCO_3 \bullet CaCO_3$) and magnesite ($MgCO_3$).

Table 1.1 shows a comparison of the physical properties of Mg, aluminium (Al) and Fe [2]. Mg has a density (1.74 g/cm^3) of about 2/3 that of Al and 1/4 that of Fe, which makes him the lightest structural metal. In addition to its low weight, this material has useful properties such as shielding against electromagnetic waves, good capacity for vibration damping, dent resistance, machinability, good castability, good weldability (in controlled atmosphere), high

recyclability, and low toxicity in humans [2–4].

Metal	*Specific gravity*	*Melting point (℃)*	*Boiling point (℃)*	*Tensile strength (MPa)*	*Elongation (%)*
Mg	1.74	650	1110	98	5
Al	2.74	660	2486	88	45
Fe	7.86	1535	2754	265	45

Table 1.1: Comparison of the physical properties of Mg, Al and Fe.

The low density of Mg alloys makes them excellent candidates for weight-critical applications. In particular, Mg alloys are very promising materials in the transport industry [5], including the automotive and aerospace sectors, where weight reduction is a top priority in order to decrease the fossil fuel consumption, and therefore, the corresponding CO_2 emissions. With regard to automotive applications, the use of Mg alloys is focused on parts without structural responsibility, such as gearbox housings or steering wheels (Fig. 1.1a), although they are also used in interior parts such as seat frames (Fig. 1.1b), driver's airbag housings or steering column housings. Table 1.2 shows the significant weight reductions that could be achieved if different parts of a car are made of Mg instead of Al or steel.

	Component							
	Engine block		Gear box + clutch housing	Oil pan	Four wheels		Engine cradle	
	Cast iron	Al alloy	Al alloy	Al alloy	Steel	Al alloy	Steel	Al alloy
Traditional solution (kg)	32	23.5	21.5+5	3	36	23	25	17.5
Mg alloy solution (kg)	19		15+3	2	18	18	15	15
Weight reduction (kg)	13	4.5	6.5	1	18	15	10	2.5
Weight reduction (%)	40	19	30	33	50	22.5	40	30

Table 1.2: Advantages in weight reduction offered by Mg alloys in the automotive sector.

Weight reduction is also of great importance in the aerospace industry. Some examples of aircraft parts made of Mg alloys are gearboxes (Fig. 1.1c), thrust reversals or helicopter transmissions casings. Mg alloys are also very attractive for the health care industry [5]. The combination of its elastic modulus, compressive strength and density, which are closer to those of natural bone than those of any other material [6], and its fracture toughness, which is much higher than that of hydroxyapatite, makes Mg alloys perfect candidates for bone replacement applications. In addition, Mg has very good biocompatibility and it is biodegradable in human body fluids. This last feature is critical for biomedical applications where it is necessary to remove the implant, as this step will be performed automatically without any kind of surgery. Absorbable metal stents, which currently are made of Mg (Fig. 1.1d), are a good example of this application.

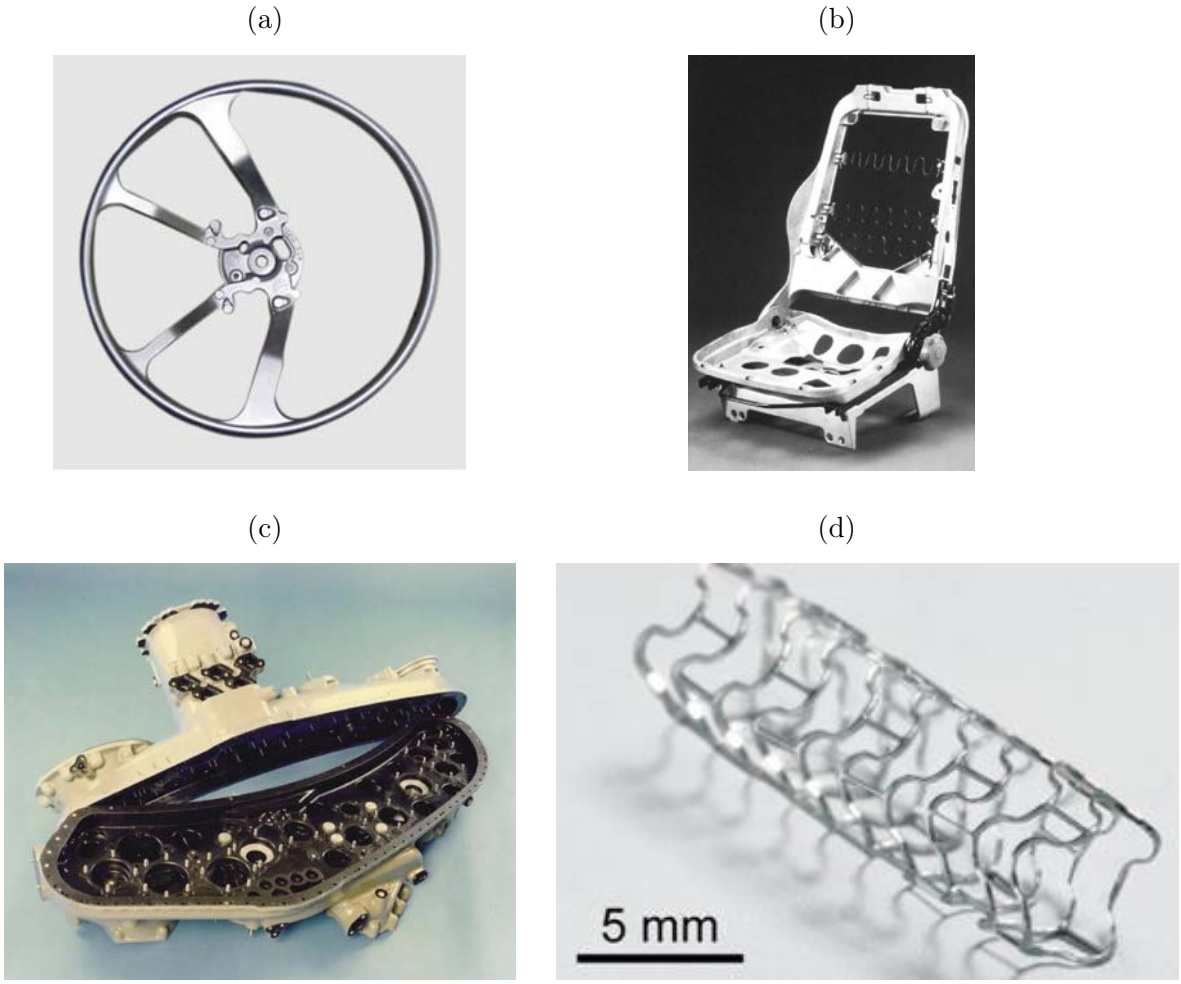

Fig. 1.1: Examples of industrial components made of Mg alloys: (a) Steering wheel; (b) Seat frame; (c) Gear box of a high-bypass turbofan engine; (d) Absorbable metal stent.

However, Mg has also some disadvantages, such as a low strength, low ductility and high mechanical anisotropy at RT, poor mechanical behaviour at high temperature, high percentage of shrinkage cracks during solidification, high chemical reactivity, and low corrosion resistance [3, 4].

1.2 Development of new alloys: classical vs. new approaches

The classical approaches used in order to develop novel alloys are based on changing the composition, application of different thermo-mechanical treatments or a combination of both of them [7–9]. By doing so, it is possible to change different microstructural properties (crystallographic structure, grain size, solute concentration, precipitates distribution, etc.) which lead to dramatic variations of the mechanical, magnetic and electrical properties. In

particular, alloying is an excellent strategy to overcome the main limitations of Mg alloys, as this material is highly chemically active and hence, easily reacts with other alloying elements to form precipitates and intermetallic compounds which modify their deformation mechanics and microstructure. The most common alloying elements in Mg are [5, 10, 11]:

- *Al*, the most common alloying element of Mg alloys, increases their hardness and strength. In addition, it also promotes an improvement in the castability.
- *Zinc (Zn)*, which is usually added together with Al, helps to increase the strength without decreasing the ductility.
- *Manganese (Mn)* improves the resistance of Mg-Al and Mg-Al-Zn alloys against salt-water corrosion. However, its effectiveness is limited by the low solubility of Mn in Mg.
- *Rare earths*, such as Neodymium (Nd), Cerium or Yttrium, increase the strength (specially at high temperature), creep and corrosion resistance. In addition, some rare earth alloying elements have proved to decrease the difference between the strength of basal and non-basal slip systems [12].
- *Zirconium (Zr)* is an excellent grain refiner when incorporated into Mg alloys containing Zn or rare earths.

However, the current alloying-based approaches used to develop enhanced Mg alloys are based on trial-and-error strategies which are expensive and time consuming and, furthermore, demand important amounts of material.

Combinatorial methods for material science is a promising approach to develop new metallic alloys which does not suffer from the limitations of classical methods. This new methodology, initially applied to the chemist and pharmaceutical industries [13], allows scientists to quickly asses a broad range of manufacturing conditions and compositions, as well as the corresponding microstructure and physical properties. This method is based on the manufacturing and characterisation of a great number of materials with different characteristics (chemical composition, grain size, precipitates structure, etc.) in a very short time speeding up the discovery of new metallic alloys. This methodology is based on fabricating large number of sample libraries in one single operation. The technique of diffusion multiple [14], for example, which consists in the creation of composition gradients and intermetallic phases by long-term annealing of junctions of three or more phases/alloys, allows to create microscopic libraries. Other methods, such as high-throughput casting by arc melting, are currently under development to fabricate macroscopic libraries. Characterization techniques such as X-ray diffraction, nanoindentation, electron backscatter diffraction (EBSD) or electron microprobe analyzer, combined with multiscale modelling techniques, such as molecular dynamics, phase field or crystal plasticity (CP), allow to obtain phase diagrams, physico-chemical properties or kinetics of phase transformations corresponding to a high number of compositions using one single sample. However, the application of combinatorial methods to Mg alloys is restricted due to the lack of two main technologies: first, a high-throughput screening technique that allows to map the mechanical properties of hexagonal close-packed

(HCP) metals at the microscale level; and second, novel material models that capture the complex deformation mechanisms of HCP metals that, using the appropriate multiscale modelling framework, are able to reproduce the macroscopic mechanical behaviour of these materials based on their micromechanical properties.

1.3 General objective

The main objective of the present Ph.D. thesis is to develop a novel high-throughput screening technique for the characterisation of the deformation mechanisms of Mg and its alloys at the microscale level together with the development of advanced material models that capture their complex micromechanics. The proposed approach, which combines instrumented nanoindentation, EBSD, atomic force microscopy (AFM) and crystal plasticity finite element (CPFE) simulation, constitutes a milestone in the development of new Mg alloys with enhanced mechanical properties due to its easiness, rapidity and small amount of material required for its application.

"No amount of experimentation can ever prove me right; a single experiment can prove me wrong"

Albert Einstein

2 State of the art

2.1 Magnesium

2.1.1 Crystallographic structure of Mg

The crystallographic structure of pure Mg at RT and atmospheric pressure is HCP [10]. This crystallographic structure has three layers of atoms (Fig. 2.1). In the top and bottom layers, there are six atoms that arrange themselves at the corners of an hexagon and a seventh atom that sits in the middle of the hexagon. The mid layer has three atoms located in the triangular "grooves" of the top and bottom planes. There are six atoms in this HCP unit cell. Each of the 12 atoms at the corners of the hexagon of the top and bottom layers contribute 1/6 atom to the unit cell; the two atoms at the centre of these hexagons contribute 1/2 atom and each of the three atoms in the mid-layer contribute 1 atom. The coordination number is 12. There are six nearest neighbours in the same close-packed layer, three in the layer above and three in the layer below. The packing factor is 0.74.

The distances a and c shown in Fig. 2.1 are the dimensions (lattice parameters) of the unit cell. The values of these parameters for pure Mg at RT are $a = 0.32092$ nm and $c = 0.52105$ nm with axes $a_1 = a_2 = a_3 \neq c$ and angles $\alpha = \beta = 90°, \gamma = 120°$. The c/a ratio

is 1.6236, which is close to the theoretical value (1.633) of a perfect HCP structure [10]. As will be discussed in detail in the following sections, the structure of the HCP crystal lattice confers Mg and its alloys a large degree of anisotropy.

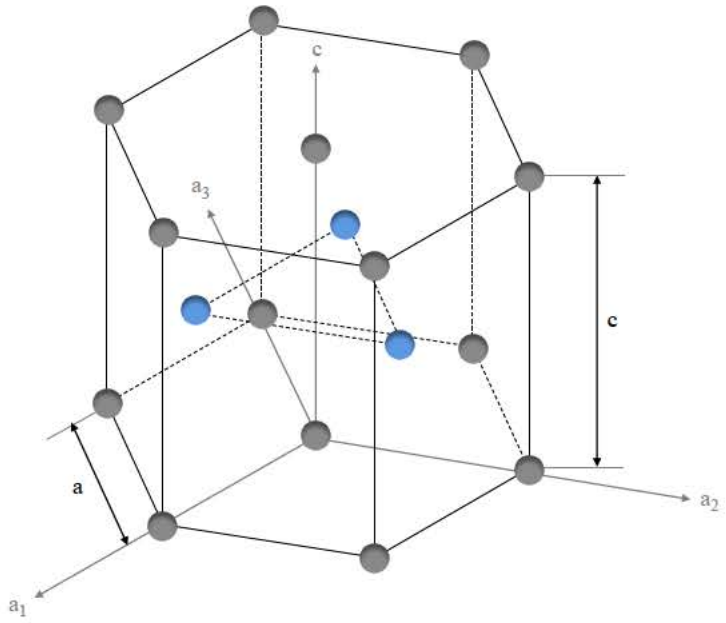

Fig. 2.1: Schematic of the HCP crystallographic structure.

2.1.2 Plastic deformation mechanisms of Mg and its alloys

The mechanisms responsible for the plastic deformation of a crystalline material are mainly crystallographic slip and mechanical twinning. The activation of one mechanism or the other depends on the crystallographic structure of the material, the composition, the grain size, the texture, and the testing conditions, such as the temperature and strain rate.

Crystallographic slip

When a single crystal is subjected to an external stress, plasticity may be accommodated by the movement of dislocations along specific planes and directions, i.e., along certain slip systems. This deformation mechanism is termed *crystallographic slip*. When slip happens, some atomic bonds have to be broken and rebuilt again. The closer the atoms are to each other, the easier this process becomes (Fig. 2.2a). That is the reason why slip usually takes place along the most compact planes.

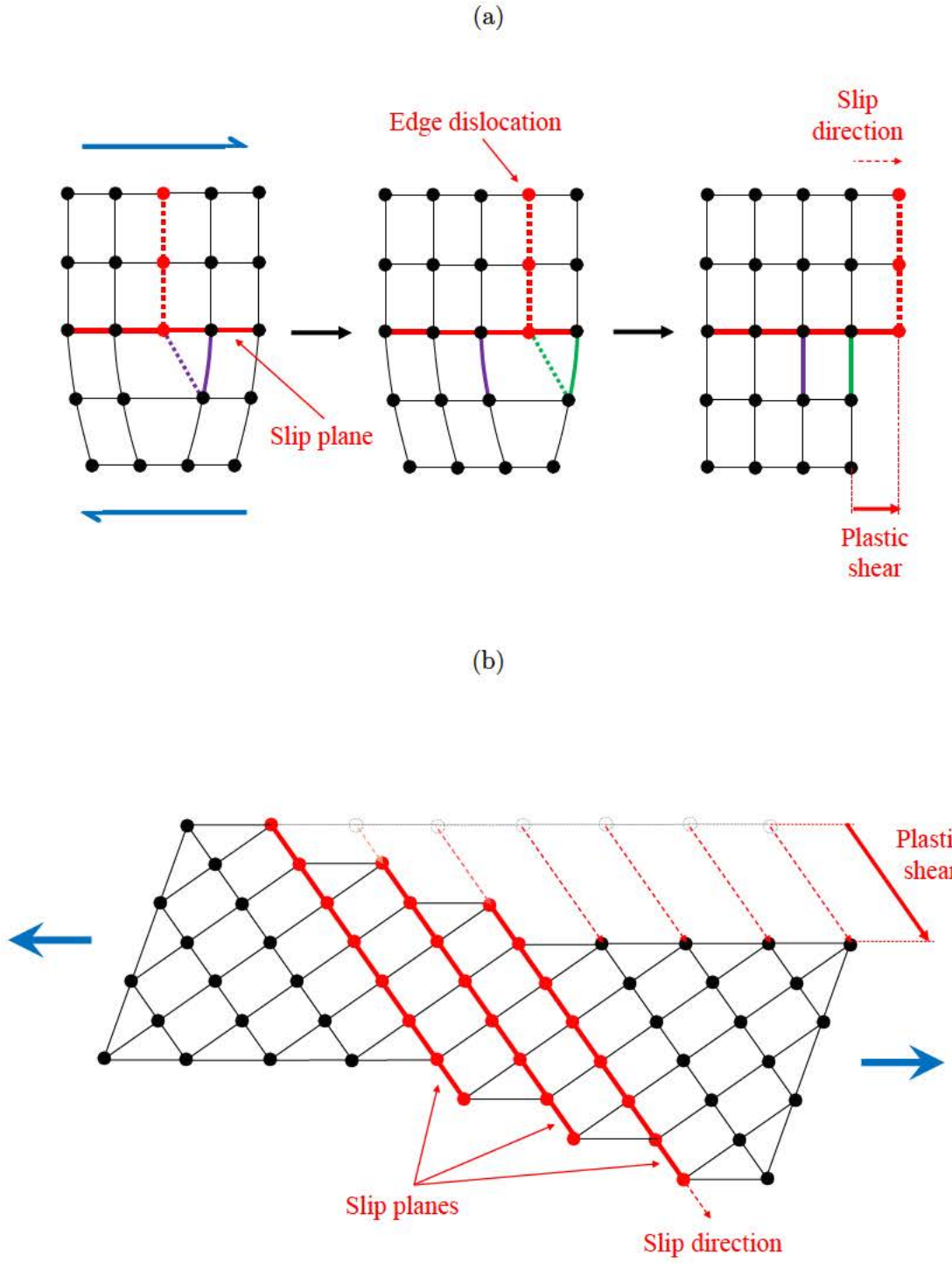

Fig. 2.2: Schematic of the crystallographic glide process: (a) step-by-step process of the movement of an edge dislocation; (b) final configuration of a crystal subjected to a tension stress which has undergone plastic deformation by crystallographic glide.

The slip systems of Mg are plotted schematically in Fig. 2.3. Dislocations can glide on basal, prismatic and pyramidal planes along the $\langle a \rangle$ direction and on first- and second-order pyramidal planes along the $\langle c+a \rangle$ direction.

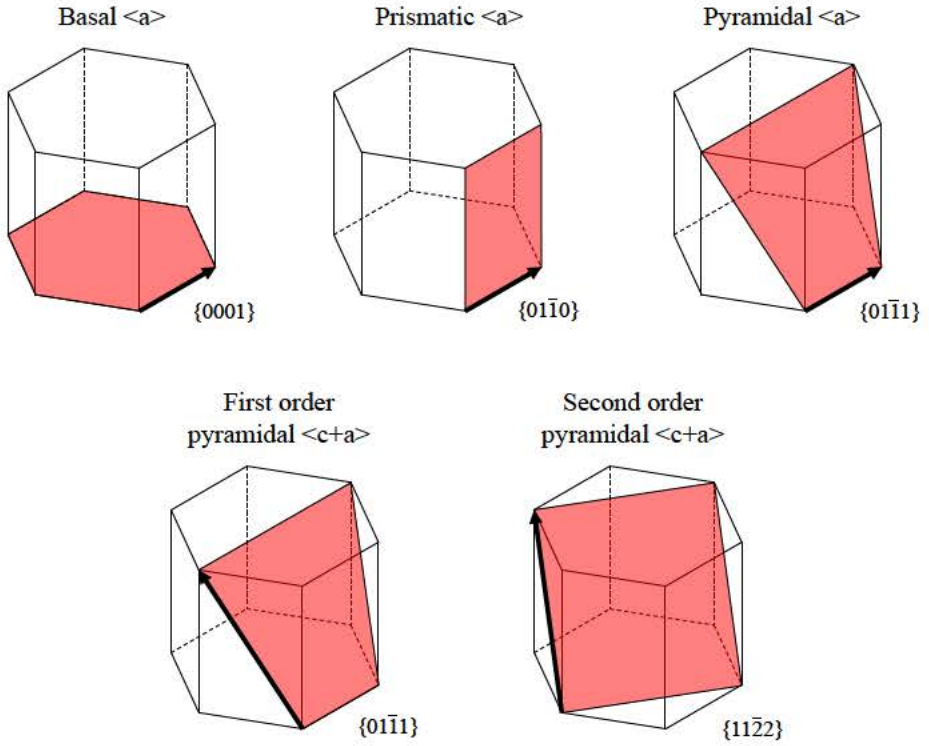

Fig. 2.3: Principal slip systems in Mg.

The onset of crystallographic slip takes place when the projection of the applied stress on the slip plane along the slip direction, the shear stress τ, reaches a critical value, called *critical resolved shear stress* (CRSS). This phenomenon is known as *yield criterium* and, for a single crystal, depends on the relative orientation of the applied force with respect to the crystallographic orientation following the Schmid's law. According to this law, the normal stress σ applied to the sample is related to the shear stress τ acting along a specific slip direction by the following expression:

$$\tau = \sigma cos(\phi) cos(\lambda) \tag{2.1}$$

where ϕ is the angle between the applied stress and the normal to the slip plane, λ is the angle between the applied stress and slip direction and $cos(\phi)cos(\lambda)$ is the so-called Schmid factor (SF, Fig. 2.4 [15]). In most cases, the stress state is much more complex, and thus, the Schmid Tensor $\boldsymbol{S}^{\alpha}$ is used instead of the SF. The Schmid tensor is equal to $\boldsymbol{S}^{\alpha} = \boldsymbol{m}_{sl}^{\alpha} \otimes \boldsymbol{m}_{sl}^{\alpha}$, being α the slip plane, $\boldsymbol{m}_{sl}^{\alpha}$ the unit vector in the slip direction and $\boldsymbol{n}_{sl}^{\alpha}$ the unit vector perpendicular to the slip plane.

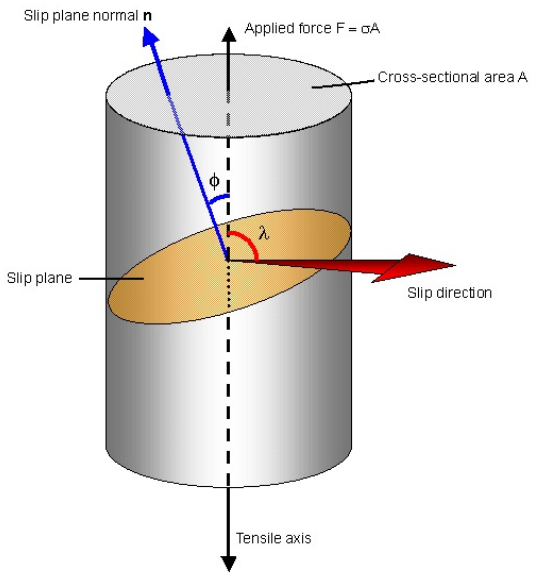

Fig. 2.4: Schematic representation of the relation between the applied normal stress σ and the resolved stress τ. ϕ is the angle between the tensile axis and the vector normal to the slip plane and λ is the angle between the tensile axis and the vector in the slip direction [15].

Mechanical twinning

According to Taylor's criterion [16], the homogeneous deformation of a single crystal requires the activation of five independent slip systems. Nevertheless, some crystallographic structures may present a limited number of active slip systems, which implies that other kind of deformation mechanisms, like *mechanical twinning*, have to be activated in order to accommodate an arbitrary plastic deformation. This is typical in low-symmetry crystallographic structures, like hexagonal crystals with a large c/a ratio [17], such as Mg alloys [12]. Mechanical twinning, which is enhanced by large strain rates and low temperatures [18, 19], strongly affects the mechanical behaviour of Mg alloys, specially their yielding [20], work hardening [21, 22], ductility [23] and dynamic recrystallization [24]. The formation of a twin involves the shearing of a portion of the crystal which is brought into a mirrored orientation relative to the undeformed portion across the twin/habitus plane (Fig. 2.5). As a result, the crystal undergoes a final plastic shear along the twin direction as shown in Fig. 2.5.

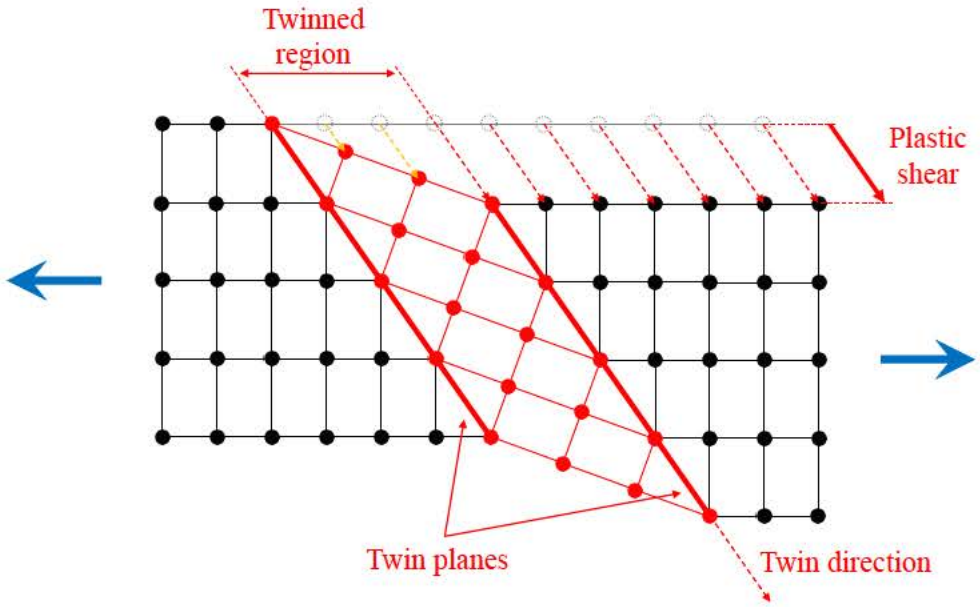

Fig. 2.5: Schematic of mechanical twinning.

Two main kind of twins can be distinguished depending on the direction of the final plastic deformation: *tension twins*, which induces an extension along the c-axis of the crystal; and *compression twins*, which are only activated by stress states that promote a contraction of the crystal along the c-axis [17, 25, 26]. Fig. 2.6 includes the main tension and compression twin modes reported for pure Mg, including in each case the twin plane and twin direction [17, 25, 26]. Tensile twinning along the $\{01\bar{1}2\}$ plane is, by far, the most common twinning mode in pure Mg and its alloys. While compression twins along the $\{01\bar{1}1\}$ and $\{01\bar{1}3\}$ planes have also been reported in the literature, the stress state necessary to activate these compression twin modes is much severe than the one demanded to develop a tension twin at RT, and therefore, the majority of the works performed in Mg alloys have been focused on the latter [17, 27].

It has been generally accepted in the literature that the activation of twinning, as the initiation of crystallographic glide, is controlled by a resolved shear stress acting on the twin/slip plane along the twin/slip direction. Whilst this approximation may be appropriate for many cases, the development of a twin is a much more complex process involving three steps, which take place sequentially: nucleation, propagation and growth [28]. While the stresses required for the propagation and growth of an existing twin are moderately small, the nucleation of a twin embryo is a volume activation process [28, 29] that requires quite severe stress states [30]. Indeed, the high energy required to create a twin boundary in pure Mg justifies the minimum size of the twin embryo to be stable [31]. These features make twinning a deformation mechanism which is highly affected by size effects. For example, Barnett et al. [32] reported the inhibition of twinning in the AZ31 (3 wt.% Al, 1 wt.% Mn, Mg balance) Mg alloy when the grain size drops below one micron. This is related to the decrease in

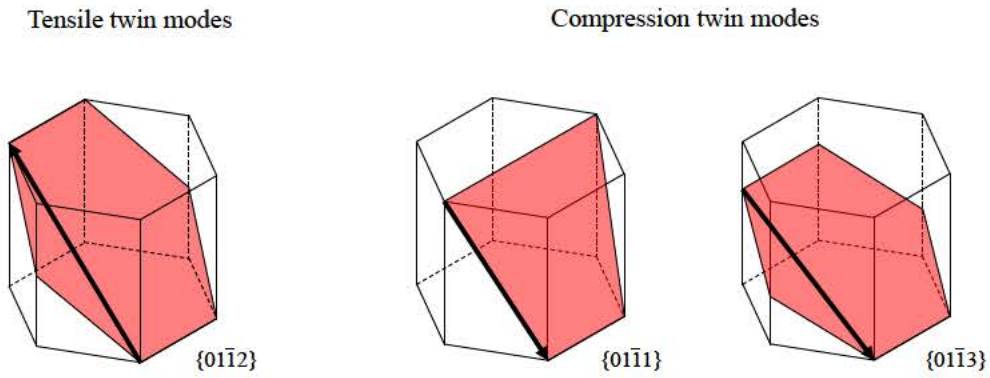

Fig. 2.6: Principal twin systems in Mg.

the number of dislocations forming the pile-ups in the fine-grained microstructures, which leads to a reduction in the local stresses at the boundaries to values below those necessary for twin nucleation [29]. Twinning is also profoundly affected by the size of the deformed specimens. Yu et al. [33] investigated this issue by compressing Titanium-5 at % Al single crystal micropillars of different diameters. Their results show that the stress necessary to nucleate and propagate twinning increases drastically as the diameter of the micropillar (D) decreases. For samples with diameters smaller than a critical value ($D \leqslant 0.7\mu m$), twinning was completely suppressed. Prasad et al. [34] carried out a similar study in pure Mg single crystals with dimensions of different length scales. In particular, the specimens in the micrometer range showed a critical resolved shear stress for twinning ($CRSS_{tw}$) several orders of magnitude larger than that of macroscopic samples. The requirement of high local stresses to nucleate twinning in pure Mg microscale specimens has also been reported by Yu et al. [33].

Anisotropic mechanical behaviour of Mg alloys: effect of temperature

Fig. 2.7 shows the variation of the SF for each slip and twin system in an HCP crystal as a function of the angle between the c-axis and the direction of the applied uniaxial stress. When the c-axis and the uniaxial stress are parallel, the SF of the basal and prismatic planes is zero, which means that no shear stress is acting on those planes. Only the pyramidal slip and the different compression twin modes can be activated. In turn, when the applied stress makes a 45° with the c-axis, basal slip becomes the most favoured deformation mechanism. Finally, when the applied stress makes a 90° angle with the c-axis, prismatic slip and tensile twinning acquire the highest SF.

Fig. 2.8 shows the values reported in the literature for the $CRSS_s$ of the different deformation modes of pure Mg at different temperatures. It can be observed that, at low temperatures, the CRSS of basal slip and tensile twinning, the so-called *soft deformation modes*, are significantly smaller than the CRSS of the *hard deformation modes*, i.e., prismatic

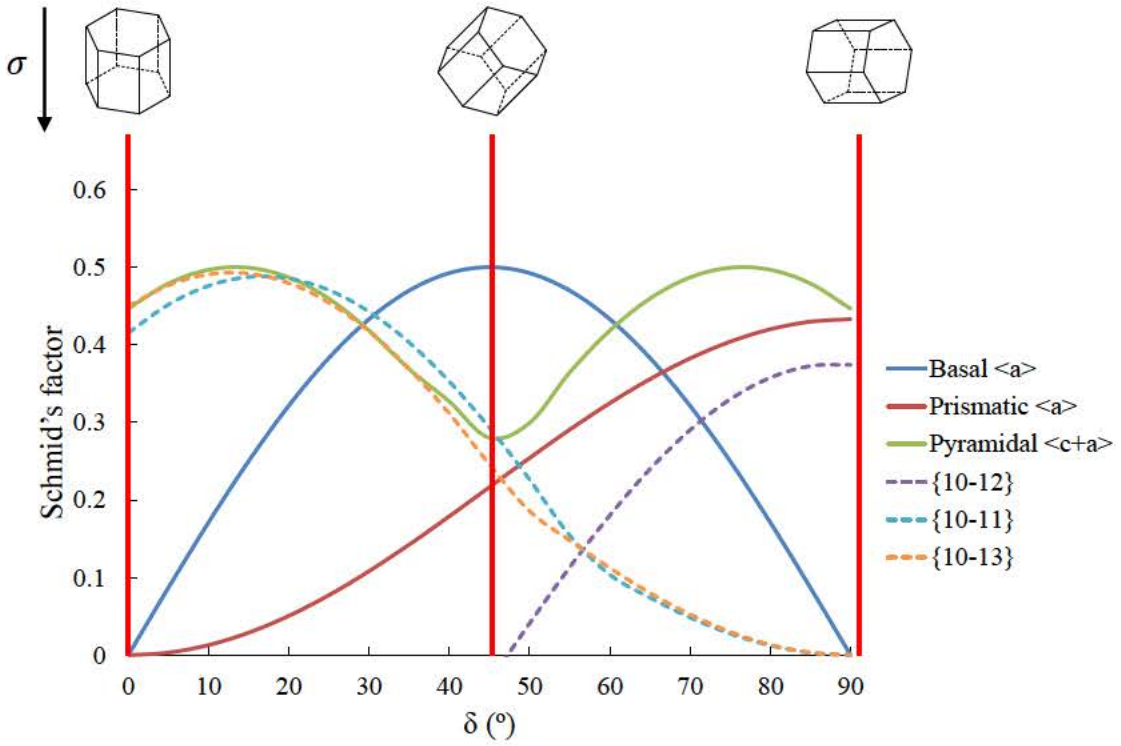

Fig. 2.7: variation of the SF for each slip and twin systems in an hcp crystal as a function of the angle between the c-axis and the direction of the applied uniaxial stress.

and pyramidal slip and the different compression twin modes. A complete different scenario is observed as temperature increases. While basal slip and tensile twinning are almost not affected by temperature, the $CRSS_s$ of the hard deformation modes show a marked down-trend with temperature to such an extent that, at some point, all the deformation modes acquire a similar CRSS. Whilst some authors have reported that basal slip is a thermally activated deformation mechanism [35], RT is close or above to the critical temperature above which this deformation mode is athermal. On the other hand, the higher mobility of $\langle c+a \rangle$ dislocations as temperature increases has been confirmed by molecular dynamics simulations [36]. The negligible dependence of tensile twinning with temperature is related to the large core width of its dislocations, which a the same time explains their great mobility at RT [37]. Finally, the strong temperature dependence of the compression twin modes has been ascribed to the small width of the core of its related dislocations [38].

The strong effect of temperature on the configuration of the $CRSS_s$ (Fig. 2.8) together with the variation of the Schmid's factor of the different deformation modes as a function of the relative direction of the applied stress (Fig. 2.7) justifies the dramatic variations of the mechanical behaviour of Mg alloys with temperature. At low temperatures, the great difference between the $CRSS_s$ of the soft and hard deformation modes will induce a high anisotropy in the mechanical behaviour of a single crystal mechanically tested in tension or in compression or tested uniaxially along different directions (Fig. 2.7). This is one of the main reasons that justifies the highly anisotropic mechanical behaviour of Mg alloys at RT.

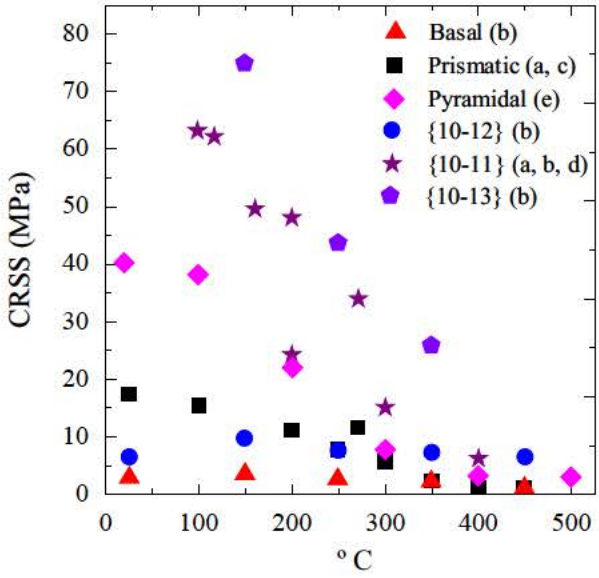

Fig. 2.8: CRSS proposed by several authors for the different slip and twin systems of pure Mg as a function of temperature: (a) Wonziewicz and Backofen [39], (b) Chapuis and Driver [27], (c) Yoshinaga and Horiuchi [40], (d) Yoshinaga and Horiuchi [41] and Obara et al. (e) [42]

However, at high temperatures, all the deformation modes acquire a similar CRSS. This is why, under these conditions, Mg alloys show a much more isotropic mechanical behaviour than at RT.

Despite its importance, no many studies have analysed quantitatively the activation of the different deformation modes of pure Mg as a function of the testing temperature. While this issue has been qualitatively study for some authors [21, 43–45], only Čapek et al. [46] and Cepeda-Jiménez et al. [47] measured the variation of the activities of the different deformation modes as a function of temperature. In addition, the mentioned works were performed in polycrystalline Mg alloys, and therefore, their results are influenced not only by temperature, but also by a combined action of grain boundaries (GB$_s$) and alloying additions. No previous works have quantified the activities of the different deformation modes in pure Mg single crystals as a function of temperature, which may be essential to fully understand the coupled action of these deformation systems, and consequently, the micromechanics of Mg at a wide range of temperatures.

2.2 Methodologies to measure the CRSS$_s$

2.2.1 Classical approaches

Measuring the CRSS$_s$ of a crystalline material is not an easy task. Several approaches combining mechanical testing and modelling have been utilized to tackle this important

question. They are the following:

1. **Single crystal-based methods**:
    - *Macroscopic single crystals*: In this case, large single crystals are grown with different orientations and tested uniaxially to ensure that only one slip/twin mode is activated. Under ideal conditions of alignment and friction-free effects, these experiments can be analysed applying simple analytical models to obtain the $CRSS_s$ [48]. Additionally, single crystal experiments can be reproduced by simulation tools in order to fully characterized the $CRSS_s$. For example, Zhang and Joshi [49] calibrated their CP model to the single crystal experimental data obtained by Kelley and Hosford [48], getting a very accurate set of $CRSS_s$ for pure Mg. However, this methodology has some important drawbacks. First, the fabrication of large single crystals and testing them under restrictive testing conditions is complex and time consuming. Second, this disadvantage is compounded by the fact that one single crystal, and the corresponding mechanical test, is necessary to characterise each deformation mode for each composition.
    - *Micropillars*: The surge of nanotesting methods in the last years has led to the development of a new methodology to measure the $CRSS_s$. This new procedure involves fabricating single crystalline micropillars with specific orientations by Focused Ion Beam (FIB) techniques with a diameter in the nano and micrometer range [50]. The small dimensions of the micropillars open up the possibility of fabricating them from regular polycrystalline samples, thus avoiding the need of producing large single crystals to study the $CRSS_s$. These pillars are compressed using a flat punch in a nanoindenter. The CRSS of the active slip system can then be obtained by analytical or simulation methods. However, two main issues appear when using this technique: *size effects* [51] and *irradiation damage induced by FIB* [52]. In the micro and nanometer range, the yield strength obtained by compressing micropillars increases as the pillar diameter decreases. At this scale, the mechanical properties suffer from size effects, motivated by the limited number of available dislocations sources in the tested small volume [51], which makes the analysis more complicated. On the other hand, FIB micromachining results in the introduction of defects on the surface of the micropillars due to the ion milling, which affects their strength, thus altering the real values of the set of $CRSS_s$ obtained.
2. **Polycrystals-based methods**: In order to avoid the drawbacks related to the fabrication of single crystal specimens, it is possible to measure the $CRSS_s$ by testing conventional polycrystalline specimens. In this case, the use of simulation tools, specially CP models, is totally necessary as the active deformation modes cannot be quantitatively characterised using analytical methods. However, using this methodology, different sets of $CRSS_s$ can lead to the same solution. Although testing textured samples reduces this possibility [20,53], the $CRSS_s$ of non-basal slip systems can be still difficult to determine as their activation is somehow limited due to the specifications of the mechanical test. Moreover, the obtained set of $CRSS_s$ would depend on the grain size due to the Hall-Petch effect. And finally, several specimens will be necessary to assess the $CRSS_s$ corresponding to each chemical composition.

The ideal methodology to measure the $CRSS_s$ should require small amounts of material and be easy to perform. In this context, the use of instrumented nanoindentation fulfils these conditions. In the following section, a detailed review of the use of single crystal indentation for determining the $CRSS_s$ of metallic materials is given, specifying the current limitations of this methodology.

2.2.2 Single crystal indentation of metals: occurrence of twinning

The microdeformation mechanisms of metals may be characterized by indentation of individual grains in such a way that the results are not affected by GB_s. The hardness, residual deformation and microtexture developed around the indent, should be a direct consequence of the activation of different slip/twin systems. By analysing the variation of the indentation response with the crystallographic orientation of the indented planes, and making use of simulation tools, several authors have been able to study the single crystal properties of face centred cubic (FCC) [54–56], face centred tetragonal (FCT) [57] and HCP [58] metals. However, relatively few works have dealt with the occurrence of tensile twinning during indentation, a key deformation mechanisms of Mg alloys. Shin et al. [59] confirmed that, in addition to $\langle c+a \rangle$ dislocations, tensile twinning is necessary to accommodate the plastic deformation developed under an indentation in magnesium single crystals. Moreover, they found that twin formation is influenced by the orientation of the indented plane. Very recently, Zambaldi et al. [60] studied the active deformation mechanisms of Mg at RT using single crystal indentation. They observed different twinning patterns on the surface near the indent depending on the crystal orientation, confirming the orientation dependence found by Shin et al. [59]. By coupling their experimental results with CPFE simulation, Selvarajou et al. [61] were able to relate the deformation patterns induced during the indentation of pure Mg single crystals with the activation and propagation of tensile twins (TT_s), although only for a limited number of crystallographic orientations.

However, despite the works mentioned above, the following issues related to single crystal indentation of pure Mg remain unsolved:

- Understanding the formation of twins and the development of orientation-dependent deformation patterns around the indents for the complete range of crystallographic orientations of the indented plane.
- Due to the small volumes of material affected by small indentations and to the described size effects that affects twin activation (Section 2.1.2), some kind of indentation size effect (ISE) is expected on twin development. To date, no studies have analysed this issue.
- All the single crystal indentation studies on pure Mg were carried out at RT. However, no studies have extended this methodology to high temperature.

2.3 Review of CP models applied to Mg

As it was commented in the Introduction of this Ph.D. theses, the use of simulation tools is a key part in the novel approaches to develop advanced alloys with better mechanical properties. In this section, a detailed description of the main simulation techniques used to reproduce the mechanical behaviour of Mg alloys is given, with particular emphasis on the complexity introduced by mechanical twinning.

CP constitutes one of the most appropriate approaches to reproduce the mechanical behaviour of crystalline materials in the micrometer range. While other simulation techniques, such as dislocation dynamics [62–65] or atomistic simulation [64,66,67], can be used for this purpose, they present drastic length- and time-scale limitations which prevent them to be applied in an effective way. First CP models consider crystallographic glide as the main contributor to plastic deformation [16,68–71]. This deformation mechanism, which is known to introduce a gradual plastic shear as the imposed strain increases, has been successfully implemented for FCC [72–80], body centred cubic (BCC) [72,73,78,81,82], HCP [58,82–84] and FCT metals [57]. In contrast to slip, as discussed in Section 2.1.2, mechanical twinning results in an abrupt rotation of the crystal lattice [25,26] with an associated constant plastic shear. This peculiarity introduces several challenges in the implementation of this deformation mode into conventional CP models. The first author that was able to effectively take into account the reorientation induced by twinning was Van Houtte [85] in a model aimed at modelling the mechanical response and texture evolution of a polycrystalline aggregates. There, the polycrystal is modelled by a set of discrete artificial grains or material points with a particular orientation and a fixed weight. By accurately tracking the evolution of the twinned regions in each individual grain, the model decides at each time step whether to rotate or not the entire grain into the dominant twin system based on the twinned volume fractions in the grain and in the entire polycrystalline aggregate using a Monte Carlo approach. While this model allows to keep the number of grains fixed, and therefore, to overcome the constrains of previous approaches that were limited by the need of increasing the number of material points as more twins are activated, it still presents some limitations. First, the correct application of the mentioned statistical criterion requires an important number of grains in the model in order to be representative of the actual response of the real material. Second, the reorientation of each grain is based on the twinned fraction at each time step, without considering the previous deformation history. In order to overcome the latter limitation, Tomé et al. [86]. modified Van Houtte's model and proposed the so-called *Predominant Twin Reorientation Scheme*, where the reorientation of the whole grain takes place when the cumulative fraction of a twin system reaches a threshold value. However, in this approach, the grain is reoriented only taking into account the dominant twin orientation and therefore, the information of the rest of twin variants activated during the simulation is lost. In order to solve this issue, Tomé et al. [86] suggested a second approach, the *Volume Fraction Transfer Scheme*. In this case, the initial model definition considers a complete set of orientations that represents the whole Euler space, and it assigns the appropriate weights to each orientation. In contrast with the earlier models, these weights are modified during the execution of the simulation in order to take into account all the twin reorientations and their associated volume fractions. However, this model still needs a large number of starting material points as, even if the initial material possesses a strong texture, and therefore, could

be represented by a limited number of initial orientations, the entire Euler space must be covered in order to reproduce the final textures that may be induced during the deformation process which are not known beforehand. This limitation was solved by Kalidindi's model [87], where a different approach was used. In this case, each material point is considered to be a composite material made of two phases: a *parent* or *untwinned* phase, which takes into account the plastic deformation accommodated by crystallograhpic glide on the different slip systems, and a *twinned* phase, which accounts for the plastic deformation and crystallographic reorientation induced by the activation the different twin modes. Each phase is associated to a specific volume fraction that is modified as the deformation is imposed, and therefore, it is possible to track the activity of all the twin systems and its associated volume fraction without the need of defining a minimum number of initial orientations. Kalidindi's approach has been extensively used in the literature in order to capture the effect of twinning on the mechanical response [88–92] and microtexture evolution [89, 91–93] of polycrystalline Mg alloys.

The implementation of Kalidindi's model into the appropiate FE frameworks may open up the possibility of using such approach to reproduce the micromechanics of Mg single crystals. Indeed, Selvarajou et al. [61] were able to qualitatively reproduce the behaviour or pure Mg single crystals subjected to indentation tests using a CPFE model based on Kalidindi's approach. However, Kalidindi's model is based on the underlying idea that each material point represents a grain or at least a large fraction of it. When simulating mechanical tests, like micropillar compression or single crystal indentation, the actual integration volume of each material point is several orders of magnitude smaller than the volume of the crystal. If Kalidindi's model is used directly to simulate this kind of mechanical tests, several issues will arise, such as:

- Under that conditions, only one twin system should be activated per material point. However, Kalidindi's model allows the activation of all the twins systems.
- If only one material point is used to reproduce a grain, the effective local stresses responsible for the twin nucleation and propagation events are not properly captured.

Therefore, in order to properly reproduce the mechanical response of a Mg single crystals, the current models in the literature should be adapted to take into account this issue.

2.4 Objectives and structure of the document

The main purpose of the present Ph.D. dissertation is to overcome all the limitations commented in the previous sections, which will help to speed up significantly the development of new Mg alloys with enhanced mechanical properties. In particular, the project is divided into three main objectives:

1. **Objective 1**: Complete study of the deformation mechanisms of pure Mg single crystals at RT using nanoindentation, EBSD, AFM and CPFE simulation. Special emphasis is placed on the effect of the crystallographic orientation of the indented plane on

the hardness, microtexture and residual deformation around the indents. In addition, a detailed analysis of possible ISE effects on twin development is performed.

2. **Objective 2**: Development of a nanoindentation-based technique to estimate the $CRSS_s$ of Mg alloys under specific testing conditions, i.e, small indentation depths. This technique is validated in pure Mg and used to infer the effect of alloying elements of an MN11 (1 wt.% Mn, 1 wt.% Nd, Mg balance) alloy.

3. **Objective 3**: Extension of the methodologies developed in Objectives 1 and 2 to high temperature. Special attention is paid to the effect of temperature on the competition of the different deformation modes.

In order to fulfil these objectives, the document is structured as follows. The most important materials and experimental techniques used in the present Ph.D. thesis are briefly described in Chapter 3. Chapter 4 includes a detailed description of the simulation tools used in the framework of this project. The results related to Objectives 1, 2 and 3 are included in Chapters 5, 6 and 7 respectively. Finally, the main conclusions drawn from this work and some recommendations for future studies are summarized in Chapter 8.

"If I have seen further than others, it is by standing upon the shoulders of giants"

Isaac Newton

3

Materials and experimental techniques

3.1 Materials

The main material investigated is a rolled and annealed sheet of pure Mg, whose composition is depicted in Table 3.1, with an average grain size of ~ 80 μm and with a strong basal texture. In addition, the rare-earth magnesium MN11, which contains 1 wt.% of Mn and 1 wt.% of Nd, was used in order to analyse the effect of rare-earth elements on the microdeformation mechanisms. The average grain size of this material was ~ 10 μm and it exhibited a weak texture.

Element	Mg	Ca	Fe	Li	Si	Ni	Zn	Al	Mn	Cu	Na	K	Pb	P
(ppm)	balance	12	14	< 1	146	2	33	10	140	5	< 1	2	20	16

Table 3.1: Composition of the pure Mg sheet used during this investigation.

3.2 Sample preparation

Sample preparation was challenging due to the softness of the investigated materials. The procedure followed consisted on three main steps:

- **Cutting & grinding:** First, the sample is cut in such a way that its dimensions are, more or less, 1 cm x 1 cm x 0.3 cm. In general, a wire cutting machine is used to perform such task. After that, the surface of interest is manually ground using abrasive SiC papers with a grit size of 320, 600, 1000 a 2000 (Fig. 3.1). That particular sequence has to be followed ensuring that, in each step, the scratches from the previous abrasive paper are totally removed before applying the next one. In order to avoid any contamination between the different grinding steps, the sample has to be carefully cleaned using ethanol.

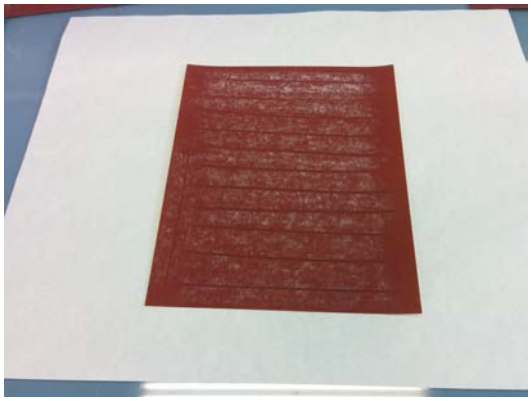

Fig. 3.1: Abrasive SiC paper used for grinding.

- **Mechanical polishing:** The surface is then manually polished using a conventional polishing machine (Fig. 3.2a) following a three-step procedure. First, the sample is polished using a MD-Mol cloth with a 3 μm diamond paste. Then, the sample is further polished making use of a MD-Nap cloth impregnated with 0.25 μm diamond paste. Surface finishing is carried out using a MD-Chem cloth with a OP-S colloidal silica solution. The sample has to be carefully cleaned using ethanol between the different sub-polishing steps. Fig. 3.2b shows the different clothes used.

  The grinding and polishing steps have to be performed manually, without mounting the sample onto any kind of auxiliary material in order to avoid surface damage during unmounting for nanoindentation testing.

- **Surface finishing:** The main objectives of this step are, first, to remove the eventual scratches coming from the previous mechanical polishing processes, achieving a very flat and shiny surface; second, to reveal the microstructural features, mainly GB_s and twins. Two routes were utilized:

  Route A: Electropolishing using a Struers AC2 solution cooled to 5 °C and applying a voltage of 20 V for 45 s.

(a) (b)

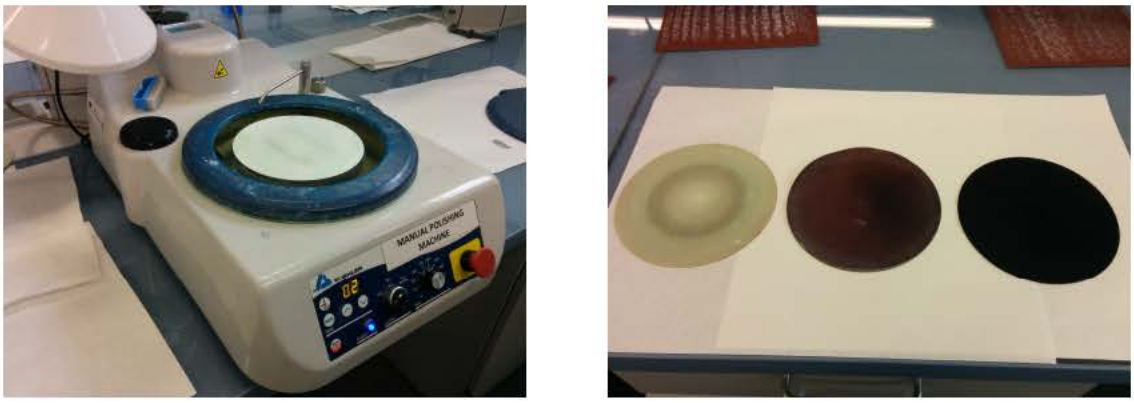

Fig. 3.2: Polishing equipment and accessories: (a) Manual polishing machine; (b) Main polishing clothes: MD-Mol, MD-Nap and MD-Chem (from left to right).

Route B: Chemical polishing using a solution of 75 ml of ethylene glycol, 24 ml of distilled water and 1 ml of nitric acid. Once prepared, the solution is poured into a pre-wet MD-Chem cloth and then, the sample is carefully rubbed against the cloth during $\sim$ 45 s following circular paths. The optimal etching time depends on the average grain size, and thus, this parameter has to be tuned for each specific case.

The sample preparation route utilized in each case will be specified in the corresponding chapter. Fig. 3.3 shows the general aspect (Fig. 3.3a) and the microstructure (Fig. 3.3b) of a sample prepared using *Route B*.

(a) (b)

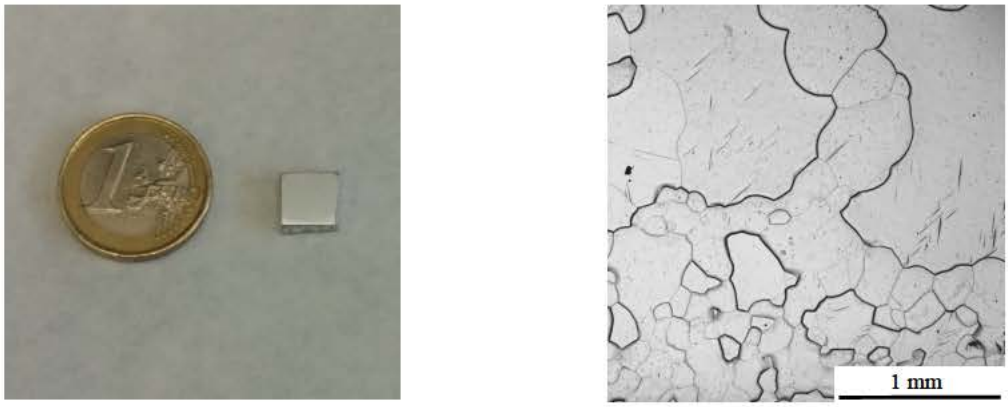

Fig. 3.3: Sample prepared using *Route B* (a) and its microstructure (b).

3.3 Microstructural characterisation techniques

3.3.1 Scanning electron microscopy

Scanning electron microscopy (SEM) uses a beam of accelerated electrons to image the samples' surface. The typical electron beam used in SEM has a wavelength between 1 and 0.50 nm, which, according to the Rayleigh criterion [94], allows for a resolution of a few of nanometers [95].

When an electron beam hits a specimen, it interacts with the atoms of the sample, producing different emissions with different interaction volumes. In particular, three main emissions can be distinguished: secondary electrons (SE), backscattered electrons (BSE) and X-rays. While the interaction volume of the SE is very small and is located at the very top surface, the interaction volume of the X-rays is quite large and goes deep into the sample. The BSE is an intermediate case (Fig. 3.4). Due to its importance in the development of this Ph.D. dissertation, special attention will be placed in SE and BSE. SE are originated from the collision between the electrons of the beam and the loosely-bounded outer electrons form the surface of the sample (Fig. 3.5). As only SE generated close to the surface can escape, SE provides mainly topographic information. Other possibility is that a fraction of the electrons of the incident beam are retarded by the electromagnetic field of the nucleus of the atoms of the sample in such a way that their trajectory is modified (Fig. 3.5). If the scatter angle is large enough, they can escape from the surface, becoming what are called BSE. As they interact with the atomic nucleus of the atoms, BSE provides information related to the atomic structure of the sample.

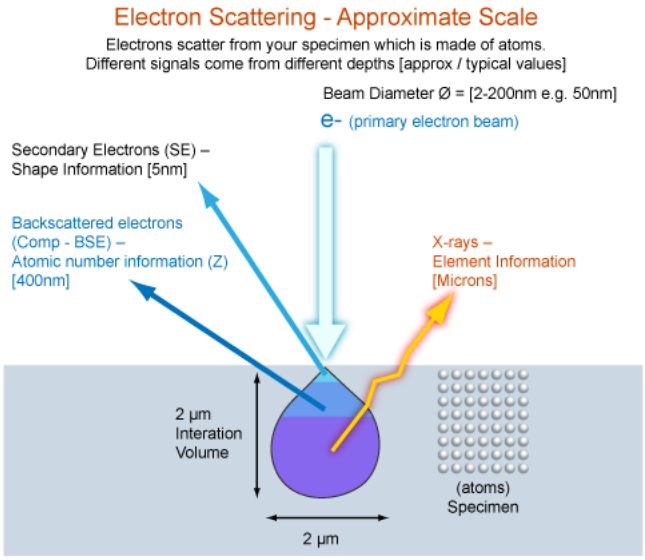

Fig. 3.4: Interaction between an electron beam and the surface of a sample. The different emissions induced and their interaction volumes [96] are illustrated.

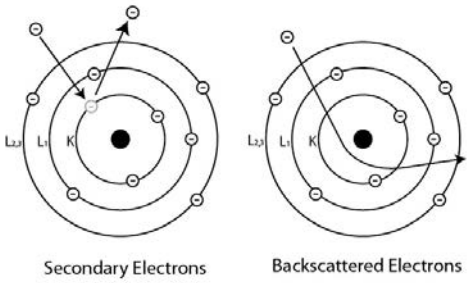

Fig. 3.5: Interaction between an incident electron and an atom producing secondary and backscattered electrons [97].

Fig 3.6 [98] shows the main components of an scanning electron microscope. The electron gun is responsible for the generation of the electron beam which is properly conducted to the sample through the anode, magnetic lens and scanning coils. In order to take an image, the sample, which is mounted onto the proper stage, is scanned by the electron beam following a raster-scan pattern. As the position of the beam is known, using the signal collected by the different detectors in each point, the image can be produced.

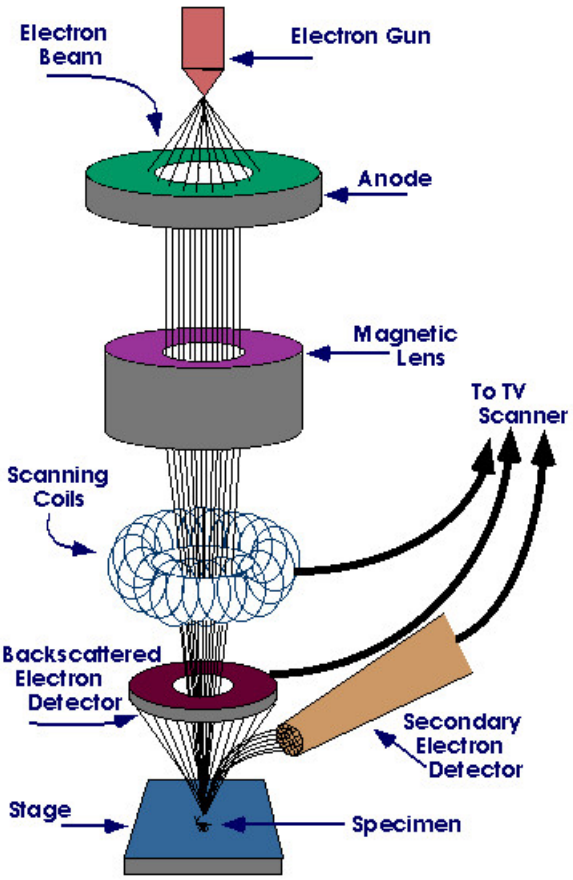

Fig. 3.6: Schematic of the main components of an scanning electron microscope [98].

3.3.2 Electron backscatter diffraction

EBSD is an SEM-based technique which has become a well-known widespread material characterisation method. It allows for microtexture quantification [99], grain and phase boundary characterization [100], phase identification [101] and strain determination [102] in crystalline multiphase materials.

EBSD is based on the acquisition and analysis of Kikuchi diffraction patterns from the surface of a specimen in a SEM. When a stationary beam of electrons hits the specimen surface, BSE are diffracted at the crystal lattice planes within the probe volume, according to Bragg's law and forming a set of paired large angle cones corresponding to each diffraction plane, as shown in Fig. 3.7. The diffracted signal is collected and viewed via a low-light camera interfaced to a phosphor screen, obtaining in this way the Kikuchi diffraction patterns. In order to maximise the number of BSE which are able to escape from the specimen, the sample is placed in a dedicated tilted holder so that it makes a small angle, typically 20°, with the incoming electron beam.

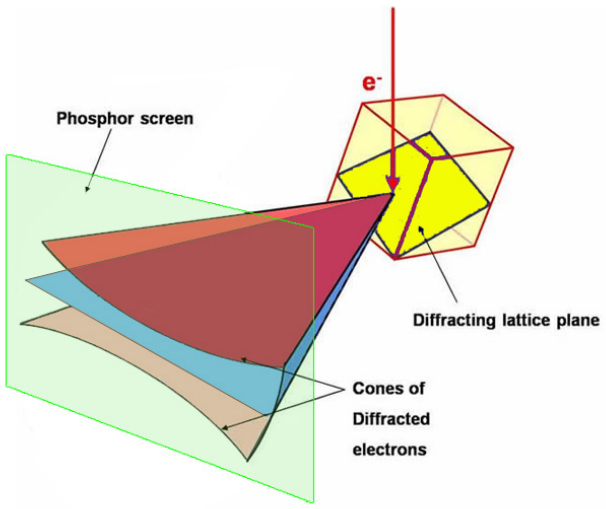

Fig. 3.7: Schematic of the formation of Kikuchi diffraction pattern [103].

The Kikuchi diffraction patterns provide crystallographic information that can be related back to their original position on the specimen. The evaluation and indexing of the diffraction patterns is performed in most cases automatically and the data is output in a variety of both statistical and pictorial formats. One of the most versatile and revealing of these outputs is the *orientation map*, which is a quantitative depiction of an area of microstructure in terms of its crystallographic constituents.

Fig. 3.8 illustrates a standard EBSD setup, including the pre-tilted holder and a sensitive detector which is used to collect the diffraction patterns.

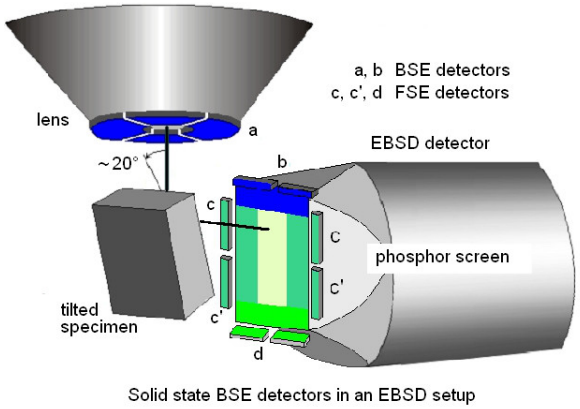

Fig. 3.8: Schematic of the set-up of an EBSD detector inside an scanning electron microscope [104].

In the present Ph.d. thesis, an Helios NanoLab^{TM} DualBeam^{TM} 600i microscope (FEI, [105]) equipped with an Oxford-HKL EBSD detector [106] was used in order to perform EBSD and SEM characterisation. Fig. 3.9 shows the internal set-up of the EBSD detector and the electron beam gun of such microscope.

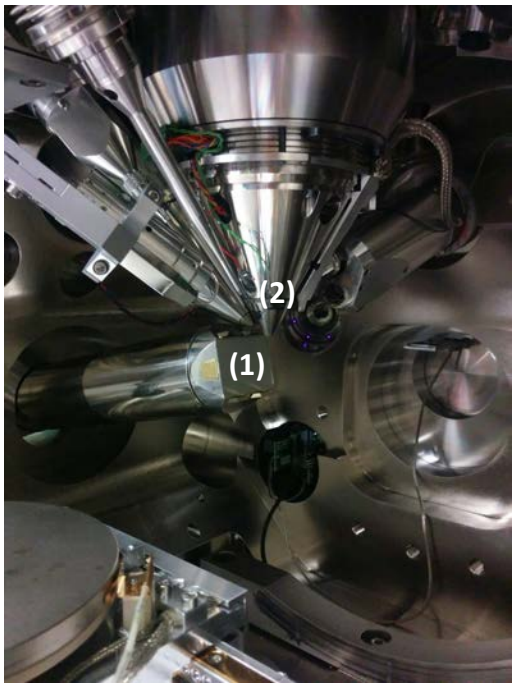

Fig. 3.9: View of the interior of the camber of an Helios NanoLab^{TM} DualBeam^{TM} 600i microscope: (1) Oxford-HKL EBSD detector; (2) Electron beam gun.

3.3.3 Atomic force microscopy

Atomic force microscopy is a scanning probe microscopy technique which is able to measure the topography of a small surface with a very high resolution. With the appropriates modifications, other surface properties such as friction or magnetism can also be characterised. As shown in Fig. 3.10, the main components of an AFM are: (a) a cantilever with an attached tip, (b) a laser source, (c) a photodiode detector and (d) a piezo transducer that moves the sample in X-Y-Z directions. The operation of an AFM can be described as follows. The cantilever holds a very sharp tip which scans the surface of the sample. As the tip interacts with the topographic layout of the surface, the deflection of the cantilever changes. On the other hand, the laser source points at the back of the cantilever, in such a way that the laser is reflected on the photodiode detector, which able the system to easily track the deflection (or height) of the cantilever.

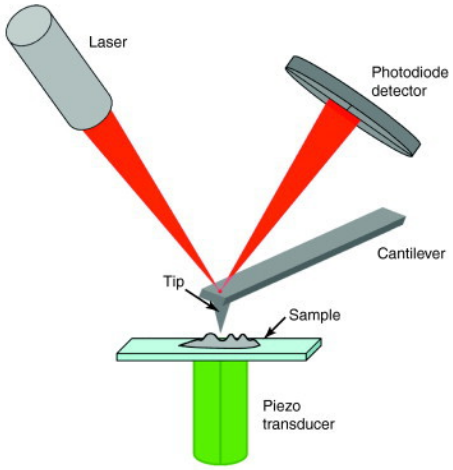

Fig. 3.10: Basic components of an AFM: (a) a cantilever with an attached tip; (b) a laser source; (c) a photodiode detector; (d) a piezo transducer that moves the sample in X-Y-Z directions [107].

A key aspect in the operation of an AFM is the interaction forces between the tip and the sample as a function of the tip-to-sample distance (Fig. 3.11). When the tip is far away form the sample, there is no interaction between them. However, as the distance between the sample and the tip decreases, their atoms begin to attract each other due to the van der Waals forces. This attraction force increases until their electron clouds interact in such a way that they repeal each other. As the tip-to-sample distance is further decreased, this repulsion forces takes over the initial attraction forces.

Depending on the type of interaction between tip and the sample, there are three main working modes of the AFM:

- **Contact mode:** In this mode, the tip is in permanent contact with the surface (Fig. 3.12 (a)), working in the repulsive regime of the tip-sample interaction curve (Fig. 3.11). As the tip scans the samples, the changes in the topography will induce changes

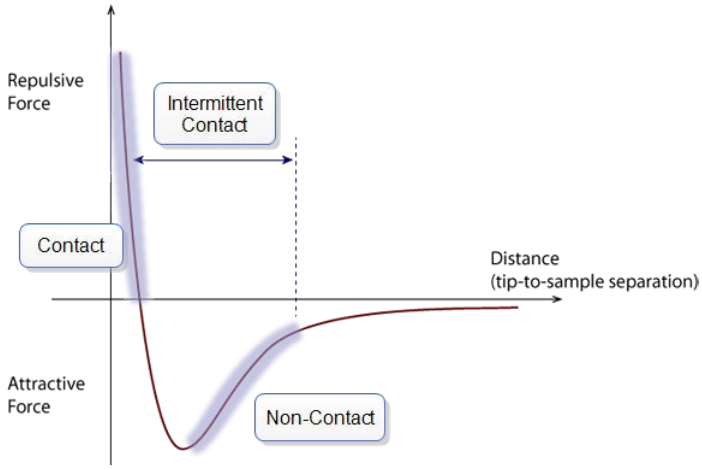

Fig. 3.11: Force interaction between the tip and the sample as a function of the tip-to-sample distance [108].

in the deflection of the cantilever. By using a feedback loop, the AFM system will tend to maintain this deflection constant by changing the height of the cantilever. In this way, the x, y and z coordinates of each point are accurately measured. The main advantages of this mode are the high scan speeds and the high resolution that can be achieved. However, its main disadvantage is that the lateral forces may damage the sample.

- **Non-contact mode:** In this case, the tip is separated from the sample a distance of the order of tens of Angstroms. Therefore, the interatomic force between the cantilever and the sample lies in the attractive regime (Fig. 3.11). In the non-contact mode, the system applies a constant vibration to the cantilever near its resonant frequency, which correspond to an amplitude of a few tens of Angstroms (Fig. 3.12 (b)). At the same time, the actual vibration of the cantilever is measured by the laser-photodiode detector system. As the tip scans the sample, the tip-to-sample distance will vary due to changes in the topography, which will induce variation on the measured oscillation of the cantilever. The AFM system, in an attempt to keep that received oscillation constant, will change the height of the cantilever using the appropriate feedback loop, thus obtaining the x, y and z coordinates of each measured point. The main advantage of this mode is that the lateral forces induced in the sample are very small, and therefore, the damage of the sample surface is less likely than in the contact mode. On the other hand, both the scan speed and the resolution are worse than those achieved in the contact mode.

- **Intermittent contact mode:** Also called TappingMode^{TM} (patented by Bruker [109]), it can be considered a combination of the contact and non-contact modes, as the interaction between the tip and the sample lies between the limits set by the attractive and repulsive regimens (Fig. 3.11). As in the non-contact mode, here a vibration is applied to the cantilever. However, in this case, the amplitude of oscillation is much larger, in such a way that in specific moments the tip is actually in contact with the

surface. The main advantage of this AFM mode is that, while the damaged induced in the surface due to the lateral forces is kept to a minimum, some specifications like the scan speed and the resolution are almost the same than that ones offered by the contact mode.

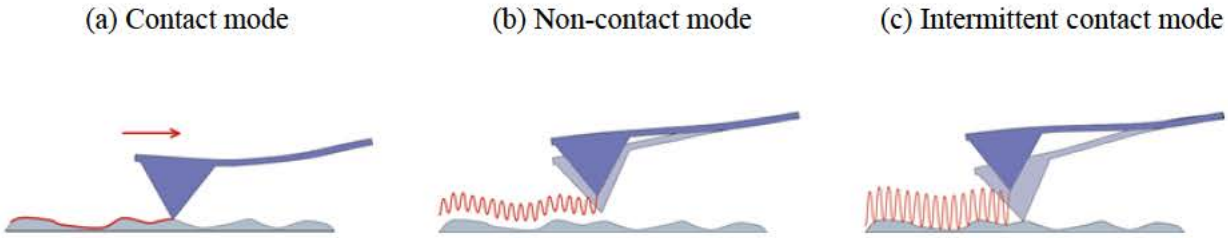

Fig. 3.12: Main modes of operation of an AFM: (a) Contact mode, (b) Non-contact mode and (c) Intermittent contact mode [110].

In this work, the AFM measurements were performed using the Park XE 150 AFM microscope [111] working always in contact mode. Fig. 3.13 shows the main components of this system. In order to isolate the system from acoustic noise, the microscope is placed inside a acoustic isolation cabinet.

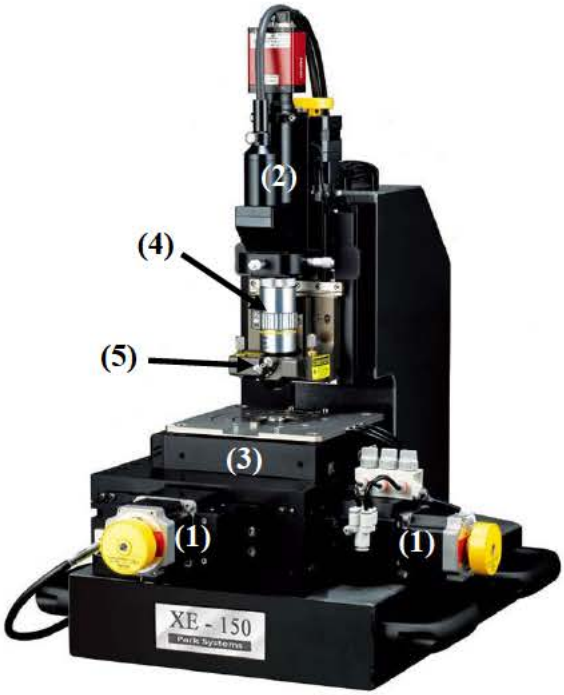

Fig. 3.13: Overview of the Park XE150 AFM microscope: (1) x-y stage, (2) z-stage, (3) sample stage, including the piezo transducer, (4) optic objective and (5) laser manipulators [112].

3.4 Instrumented nanoindentation

3.4.1 Basics of instrumented nanoindentation

Indentation is one of the most common ways of determining the mechanical properties of a wide range of materials due to its ease and speed. It consists on pushing a hard indenter (with spherical, conical or pyramidal shape) onto a flat surface. The hardness (H) value is determined using the following equation [113, 114]:

$$H = \frac{P_{max}}{A_c} \tag{3.1}$$

where P_{max} is the maximum load applied on the indenter and A_c is the contact area of the residual imprint at maximum load. A_c coincides with the area of the residual imprint, as theoretically during the unloading period only elastic recovery takes place and hence, the plastic deformation remains constant.

Traditional indentation testing requires measuring the area of the residual imprint by optical methods. This clearly imposes a lower limit on the length scale of the indentation. The capability developed in the last twenty years of continuously measuring the load and displacement throughout the indentation has allowed to extend the scope of indentation testing down to the nanometer range [115,116]. Fig. 3.14 shows the typical load-displacement curve obtained from an indentation test. By applying the Oliver and Pharr method [115], which is described in the following paragraphs, the contact area A_c can be estimated from the stiffness of the unloading curve S (Fig. 3.14). This peculiarity allows to calculate H without having to measure the area of the residual imprint manually. In addition, the reduced modulus of material, E_r, can be also calculated.

In the Oliver and Pharr method [115], A_c is calculated as a function of the contact depth, h_c (Fig. 3.15), according to:

$$A_c = F(h_c) \tag{3.2}$$

where $F(h_c)$ is called the *area function*, which strongly depends on the shape of the indenter. The most common indenter geometries will be described in depth in the following section. The contact depth, h_c, is related to the total depth at maximum load, h_{max}, and to the displacement of the surface at the perimeter of the contact, h_s (Fig. 3.15), by the following expression:

$$h_c = h_{max} - h_s \tag{3.3}$$

The indentation depth at maximum load, h_{max}, can be calculated from the experimental data. On the other hand, according to Sneddon [117], h_s can be derived as a function of the maximum load reached during the unloading segment, P_{max}, and the contact stiffness, S,

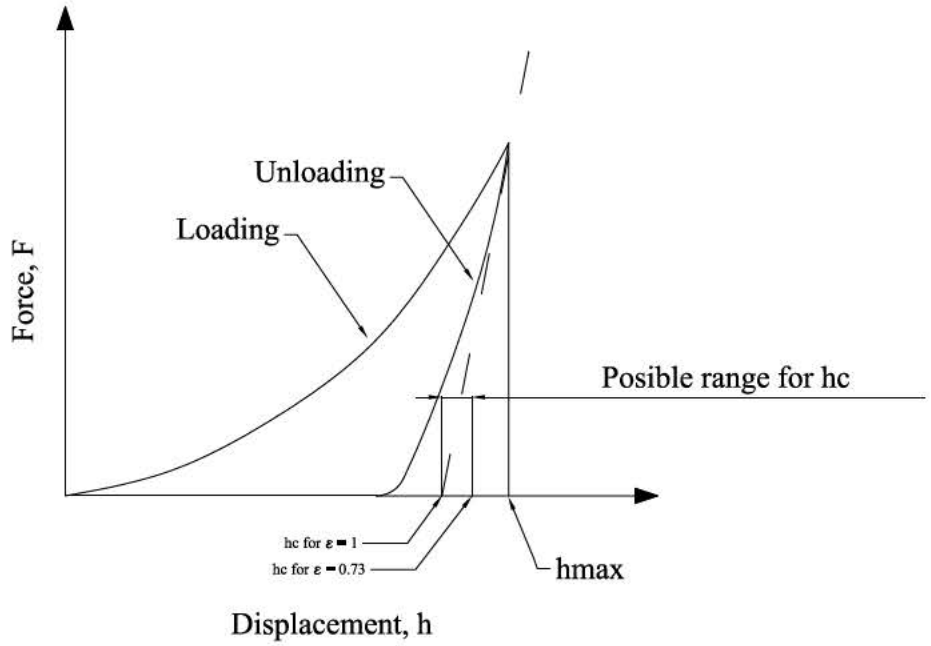

Fig. 3.14: Representative load-displacement curve obtained from an indentation.

according to the following expression:

$$h_s = \epsilon \cdot \left(\frac{P_{max}}{S} \right) \tag{3.4}$$

where ϵ is a geometric constant whose physical interpretation can be observed in Fig. 3.14. On the other hand, S is obtained by fitting the unloading portion of the indentation curve to a power-law relation as below [115]:

$$F = B \cdot (h - h_f)^m \tag{3.5}$$

where B and m are fitting parameters. From this data, S is obtained by analytically differentiating Eq. (3.5) and evaluating the result at the maximum indentation depth:

$$S = \left(\frac{dF}{dh} \right)_{h=h_{max}} = B \cdot m \cdot (h_{max} - h_f)^{m-1} \tag{3.6}$$

Once S is known, h_s can be determined, as P_{max} is obtained from the experimental data (Eq. 3.4). Combining Eqs. 3.3 and 3.4, h_c is easily derived. In addition, A_c is determined using Eq. (3.2). Finally, the hardness can be calculated using Eq. (3.1).

The contact stiffness can be related to the reduced modulus, E_r, and to the contact area, A_c, by the following expression for any indenter that can be described as a body of revolution

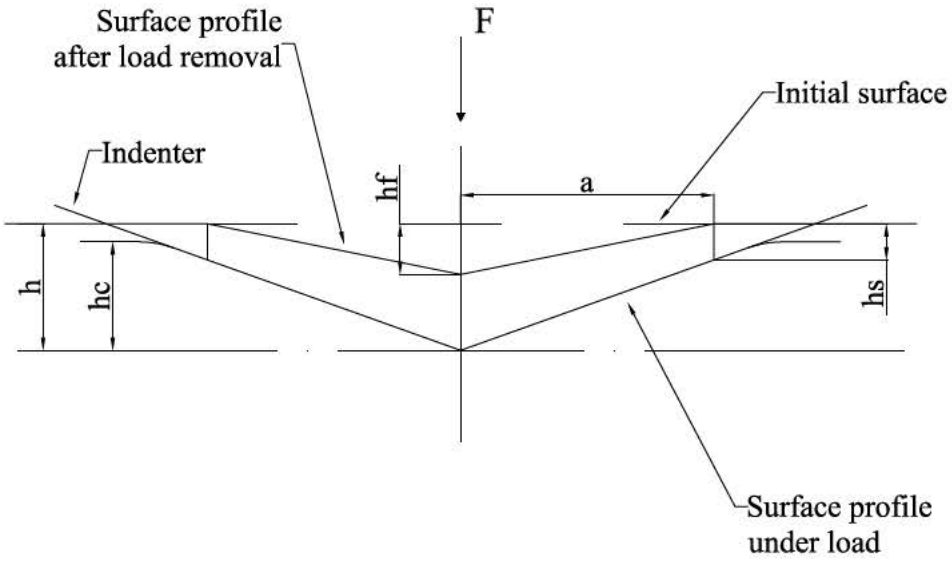

Fig. 3.15: Schematic of the cross section of an indentation. h_{max} is the indentation depth at maximum load, h_c is the contact indentation depth, h_f is the final indentation depth after completing the unloading, and h_s is the displacement of the surface at the perimeter of the contact.

of a smooth function [115]:

$$S = \frac{dP}{dh} = \frac{2}{\sqrt{\pi}} \cdot E_r \cdot \sqrt{A_c} \tag{3.7}$$

Once A_c is calculated, it is straightforward to determinate the reduced modulus, E_r, of the specimen. Finally, the Young's modulus of the material, E, can be determined according to:

$$E = \frac{(1 - v^2)}{\frac{1 - v_i^2}{E_i} - \frac{1}{E_r}} \tag{3.8}$$

where v is the Poisson's ratio of the specimen and E_i and v_i are the Young's modulus and Poisson's ratio of the indenter.

In summary, both the hardness, H, and the Young's Modulus, E, can be derived directly from the load-displacement curve of an indentation experiment applying the Oliver and Pharr method [115].

3.4.2 Indenter geometries

The geometry of the indenter is a key factor during instrumented nanoindentation. The correct application of the Oliver and Pharr method [115] (Section 3.4.1) relies on the accurate knowledge of the real shape of the indenter in order to properly estimate the A_c between the indenter and the sample as a function of the contact depth h_c (Eq. 3.2). In short, the geometry of an indenter can be defined by two factors: (i) the angle between the indentation axis and the surfaces of the indenter that are in contact with the sample (apex angle); and (ii), the degree of symmetry of the indenter with respect to indentation axis. Regarding the first parameter, the apex angle can vary from 0°, theoretical case of an infinitely sharp needle, to 90°, which would correspond to a *flat punch*. Regarding the second factor, the most common probe tips show a four-fold (Vickers), three-fold (Berkovich and Cube Corner) or two-fold (Knoop) symmetry around the indentation axis. Also axisymmetric spherical and conical indenter tips are widely used. Some of these tip probes are schematically shown in Fig. 3.16.

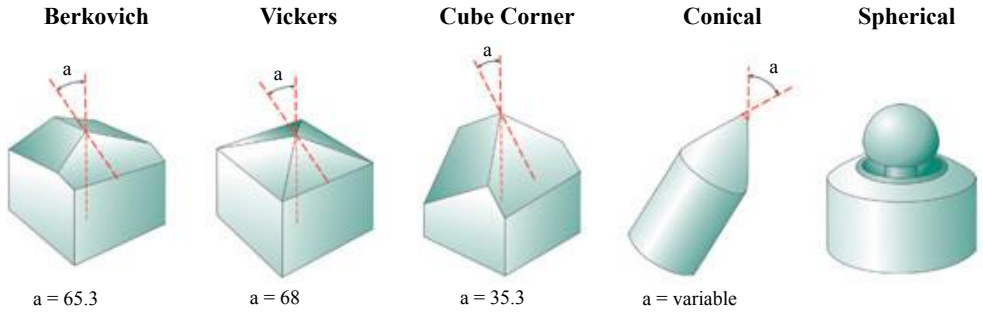

Fig. 3.16: Most common indenter geometries [118].

Regarding conical tips, the fabrication of an infinitely sharp end is almost impossible due to manufacturing constraints. Instead, the most common adopted solution is a spheroconical tip, which is composed by a conical and a spherical part, as shown in Fig. 3.17. One important parameter of this kind of tips is the indentation depth at which the conical part of the indenter begins to establish contact with the sample (refers as h in Fig. 3.17). This *transition depth* can be calculated based on the radius of the spherical part, R, and the apex angle of the conical part, α, according to the following expression:

$$h = R * (1 - sin\,(\alpha)) \tag{3.9}$$

The Berkovich indenter is the most common tip probe used in nanoscale testing owing to two main reasons: (i) three-fold pyramids are easier to grind to a sharp point in comparison with other tip geometries; and (ii), due to their very small tip radius, they display a self-similar geometry even at small indentation depths, which implies that the elastoplastic deformation induced by the indenter is almost independent of the indentation depth. However, as any non-axisymmetric indenter, the residual imprint induced by a Berkovich

indenter is dependent on the relative orientation of the tip with respect to the sample, which makes its physical interpretation more complex. Axisymmetric indenter tips, like sphero-conical probes, do not suffer from this issue. In the present Ph.D. thesis both Berkovich and sphero-conical tips have been used.

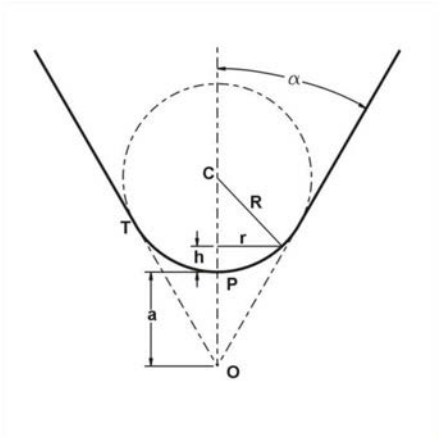

Fig. 3.17: Cross section of an ideal sphero-conical tip. [119].

3.4.3 Pile-up and sink-in deformation patterns

During the indentation of a material, the matter might flow around the indenter in such a way that may differ notably with the theoretical case considered in Fig. 3.15. In particular, two different deformation modes may take place: (i) *Sinking-in*, when the material is pulled down toward the tip of the indent and (ii) *Piling-up*, when the material is pushed away from the centre of the indent (Fig. 3.18). In this context, the determination of the actual contact area becomes difficult and therefore the direct application of the Oliver and Pharr method may lead to significant errors [120]. When the material piles-up around the indent, the actual contact area increases. In addition, for a constant load, the indentation depth will be reduced through better distribution of the load over a larger area. The combined effect of both issues will lead to a important underestimation of the E and H when using the Oliver and Pharr method [115]. Conversely, sinking-in will result in an overestimation of both parameters. Roughly speaking, it can be said that materials which combine a high stiffness with a low yield stress, i.e., in which the $\frac{E}{\tau_y}$ ratio is high, and do not show an important strain hardening, they are prone to pile-up. On the contrary, sink-in deformation patterns are found around materials with a low $\frac{E}{\tau_y}$ ratio. While this criterion may be correct for isotropic materials, it fails when dealing with highly anisotropic materials. It will be shown in this work that the deformation patterns found around an indent performed in a single crystal depends on the complex competition between the different deformation mechanisms, which will depend, among others, on the orientation of the indented plane and temperature.

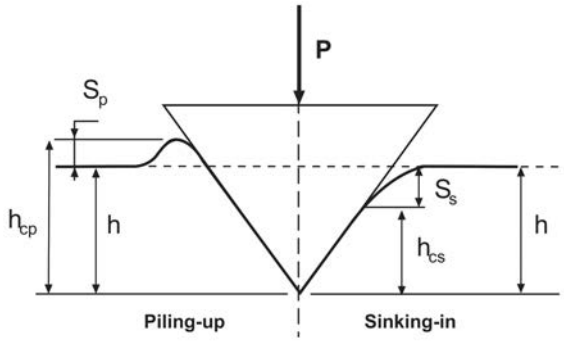

Fig. 3.18: Schematic of pile-up and sink-up deformation patterns formed around an indent [121].

3.4.4 Thermal drift

Thermal drift takes place in a nanoindenter system when any component of the load frame or sample stage expands or contracts during an indentation test due to the presence of changing thermal gradients. This phenomenon will result in the measurement of an apparent displacement that is not a true reflection of the material's force-displacement response. As a result, nanoindentation systems are extremely sensitive to thermal fluctuations, even as small as 1°C. While this may not be a big issue when indenting at RT, thermal drift becomes extremely important when the indentation test is performed at elevated temperature.

The main approaches used in order to correct thermal drift rely on applying a constant load on the sample under the elastic regime. Under these conditions, in absence of thermal drift, the actual displacement of the indenter should be zero. In general, during a regular indentation test, this procedure is performed twice: at the beginning of the indentation, just after establishing contact and applying a very small load, and during the unloading segment, which is supposed to be purely elastic, at a small fraction of the maximum load. By monitoring depth versus time during both states, the pre- and post-indentation drift rates can be obtained and then used to correct the raw load-displacement curves.

An example of a post-indentation drift measurement is shown in Fig. 3.19 [122]. In particular, three different load-displacement curves are shown, which correspond to three indents performed in fused silica at 23, 320 and 500 °C respectively. The drift is measured during the unloading segments holding a load of 1.9 mN for 10 s. The exact moment while this drift measuring is taking place is marked in Fig. 3.19 with black arrows in each curve. It can be observed that the displacement recorded during the drift measurement in the indent performed at 23 °C is almost negligible. However, there is a noticeable displacement of the indenter during this moment in the curves performed at 320 and 500 °C. This drift is considered positive as the indentation depth decreases.

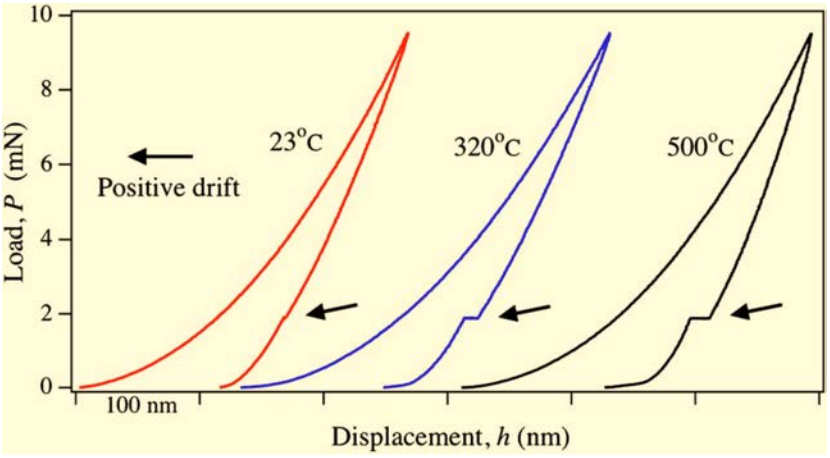

Fig. 3.19: Load-displacement curves recorded on fused silica at 23, 320 and 500 °C. The unload drift is measured by holding a load of 1.9 mN during the unloading segment for 10 s. [122].

It has been found that the most important source of thermal drift is originated by a temperature difference between the tip and the sample, inducing therefore a thermal flow between both of them. If the sample is hotter than the indenter, the heat will flow towards the indenter. In order to keep a constant load, the system will react withdrawing the indenter, producing a very similar behaviour than the one observed in Fig. 3.19 at 320 and 500 °C. On the contrary, i.e., the indenter is hotter than the sample, the heat will flow towards the sample, and the system will be forced to increase the penetration depth in order to maintain a constant load.

3.4.5 Description of experimental apparatus

Two different commercial nanoindenter systems were used in the development of this investigation: a TI 950 Triboindenter® from Hysitron [123] and a NanoTest™ from Micro Materials [124].

The Hysitron 950 Triboindenter® makes use of a vertical-loading system based on a three-plate capacitative transducer. The set-up of such device is schematically shown in Fig. 3.20 [125]. Both the top and bottom plates are fixed, while the centre one is mobile and used as a base for the tip probe. The system is originally load-controlled and works as follows. Firstly, the load is applied by imposing a known direct current (DC) voltage offset between the lower plate of the transducer that electrostatically attracts the centre (floating) plate downwards. In addition, two alternating current (AC) signals 180° out of phase with each other are applied to the top and bottom plates. The centre (floating) plate is utilized to pick up the resulting signal, which is the sum of both AC signals and will correspond to the displacement of the centre plate.

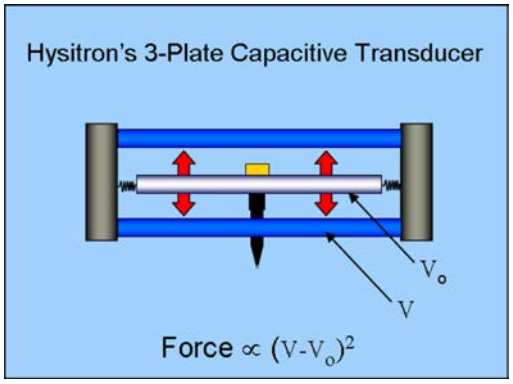

Fig. 3.20: Schematic of the Hysitron's 3-plate capacitative transducer [125].

A granite bridge, which lays on an active vibration isolation system, is used to support the other components of the apparatus. The sample stage is controlled by x-axis and y-axis motors mounted on the bottom of the Triboindenter® base. On the other hand, the transducers and the optic objective are fixed to the z-axis stage that is mounted on the granite bridge. In order to isolate the system from undesired acoustic noise or thermal currents, the entire apparatus is placed inside an acoustic and thermal enclosure (Fig. 3.21).

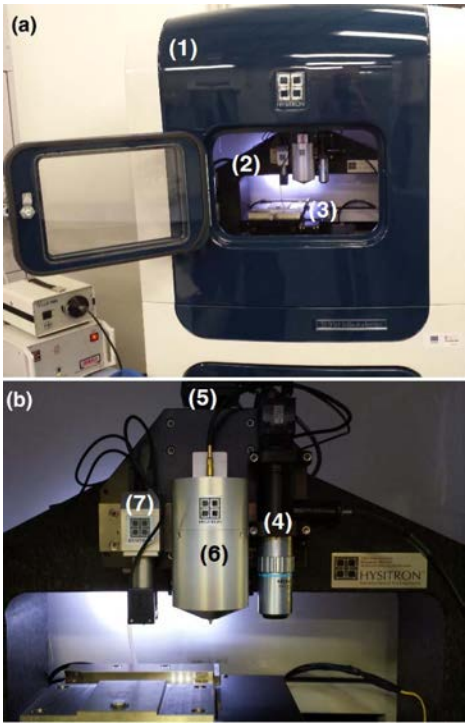

Fig. 3.21: Outside view of the Triboindenter® cabinet: (1) acoustic enclosure, (2) granite bridge, (3) xy-stage; (b) Inside view of the TriboIndenter®: (4) Optic Objective, (5) z-stage, (6) High Load Transducer, (7) Triboscanner that contains the 3-plate capacitative transducer [126].

The NanoTest^{TM} system consists of a horizontal-loading configuration. In particular, the heart of the apparatus is a pendulum that can rotate on a frictionless-pivot, as shown schematically in Fig. 3.22 [126]. By passing a known voltage trough the coil mounted at the top of the pendulum, an attraction force is induced between this coil and the permanent magnet placed just in front of it. This force rotates the pendulum in such a way that the tip is moved towards the sample. The displacement of the tip is measured by means of a set of parallel plate capacitors: one plate is attached to the pendulum and the other one to the main frame of the instrument. When the pendulum moves, the distance between both plates changes, modifying therefore the capacitance of the system.

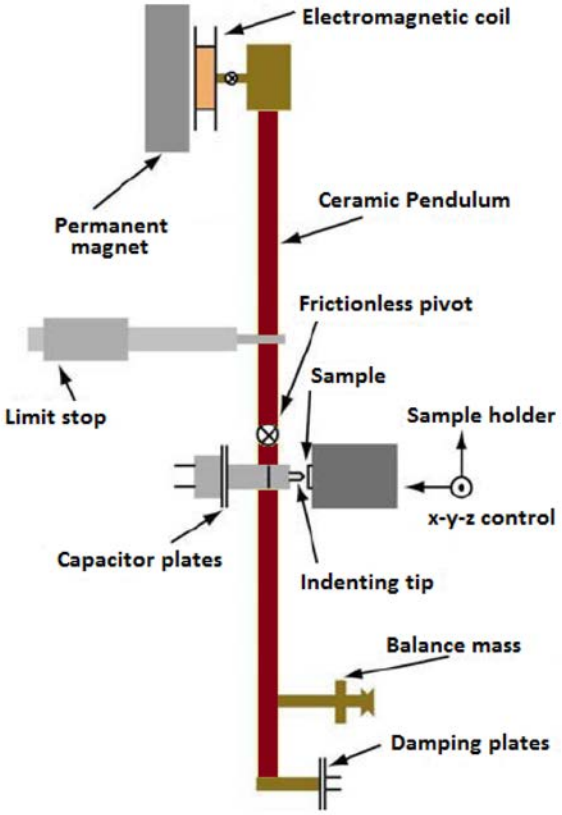

Fig. 3.22: Schematic of the pendulum-based horizontal-loading system of the NanoTest^{TM} indenter [126].

All the components mentioned previously are placed inside an environmental control chamber, which can be purged with inner gas allowing to perform experiments in a controlled atmosphere.

One important capability that is offered by the NanoTest^{TM} system is the separate active heating of both the indenter and the sample. This is achieved by installing independent resistance heaters and control thermocouples in both components, as shown in Fig 3.23 [127]. By applying a suitable proportional integral derivative (PID) control loop on the heating mechanisms, this configuration allows to achieve almost negligible thermal flows

between the tip and sample even at high temperature testing.

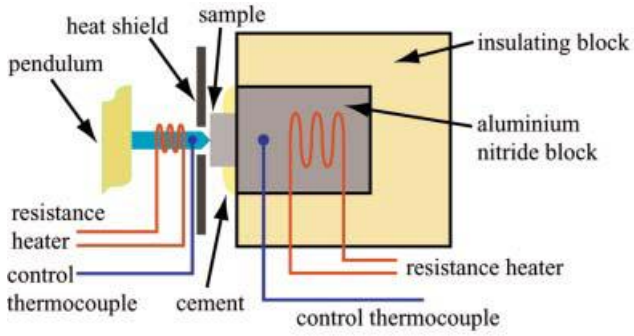

Fig. 3.23: Schematic of the NanoTest^{TM} hot stage showing separated tip and sample heaters [127].

When comparing both indenter systems, the Triboindenter® system is characterized by a much faster PID control loop of the requested load-displacement function than the NanoTest^{TM}. This fact provides the Triboindenter® system with the ability to capture data much more precisely than the NanoTest^{TM}, an aspect that is specially important when fast transient events may occur during the indentation process. In addition, the sample positioning and the automation capabilities offered by the Triboindenter® apparatus are superior than the ones corresponding to the NanoTest^{TM}. However, a complete different scenario comes into play when testing at high temperatures. As commented in Section 3.4.4, the presence of changing thermal gradients inside the indenter may lead to the alteration of the true load-displacement curve of an indentation test due to the thermal expansion of some elements of the loading system. The specific set-up of the NanoTest® system ensures a much less severe thermal drift than the one achieved with the Triboindenter® system due to two main reasons:

- The horizontal-loading system of the NanoTest^{TM} allows the heat to rise in such a way that there is no impact on the depth measurements sensors. Due to the vertical design of the Triboindenter® system, the measurement sensors will be much severe affected.
- The NanoTest^{TM} system allows to heat independently both the tip and the sample (Fig. 3.23). The particular design of the three-plate capacitative transducer (Fig. 3.20) of the Triboindenter® system does not allow to control directly the temperature of the tip, which will result in important thermal flows between the sample and the tip, as shown in Fig. 3.24

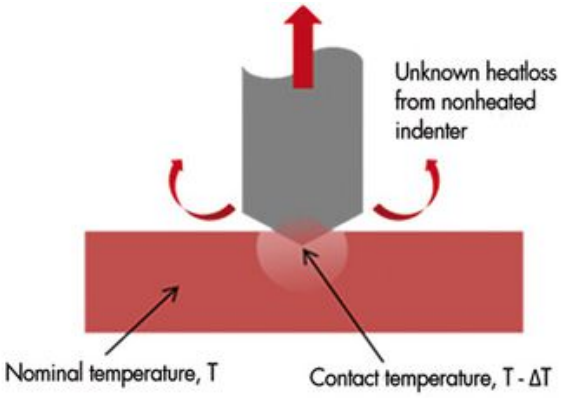

Fig. 3.24: Thermal flow between the sample and the tip without active and separate tip heating [128].

"It is paradoxical, yet true, to say, that the more we know, the more ignorant we become in the absolute sense, for it is only through enlightenment that we become conscious of our limitations. Precisely one of the most gratifying results of intellectual evolution is the continuous opening up of new and greater prospects"

Nikola Tesla

4 Simulation techniques

4.1 Abaqus

The general purpose FE package ABAQUS 6.10 [129] was utilized to simulate the experimental nanoindentations. All the simulations were conduced adopting implicit solution techniques (ABAQUS/Standard). Additionally, in order to capture the complex deformation behaviour of Mg single crystals, several user-defined material subroutines, called UMAT_s, were implemented and integrated in ABAQUS. Fig. 4.1 shows the general working flow adopted by ABAQUS/Standard, underlying the specific steps that are affected by the outcomes provides by UMAT_s. In order to begin an analysis, the first point is to define the initial boundary conditions. After that, the different steps in which the problem has been split into are performed. Each step is solved in a certain number of increments or time steps. Each increment involves a set of non-linear equations, that are solved applying the Newton-Raphson method in a certain number of iterations. In each iteration, first the stiffness matrix of the system, $\boldsymbol{K}^{el}$ is calculated. As shown in Fig. 4.1, is in this step when the outputs from UMAT_s are used. After defining the $\boldsymbol{K}^{el}$, the next step is to calculate the loads $\boldsymbol{R}^{\alpha}$. Finally, the global equation $\boldsymbol{K}^{el}\boldsymbol{x} = \boldsymbol{R}^{\alpha}$ is solved, where $\boldsymbol{x}$ is the displacements of the nodes of the FE model. After that, the residual is calculated. If this residual is greater than the limit imposed at the beginning of the analysis, the iteration has not converged and

another iteration starts. On the contrary, if the iteration has converged, the result is written in the output files. If this iteration means the end of the step, there are two possibilities. Either additional steps are required in the analysis, and therefore, the next step is initiated, or the current step is the last one, and therefore, the analysis reaches its completion.

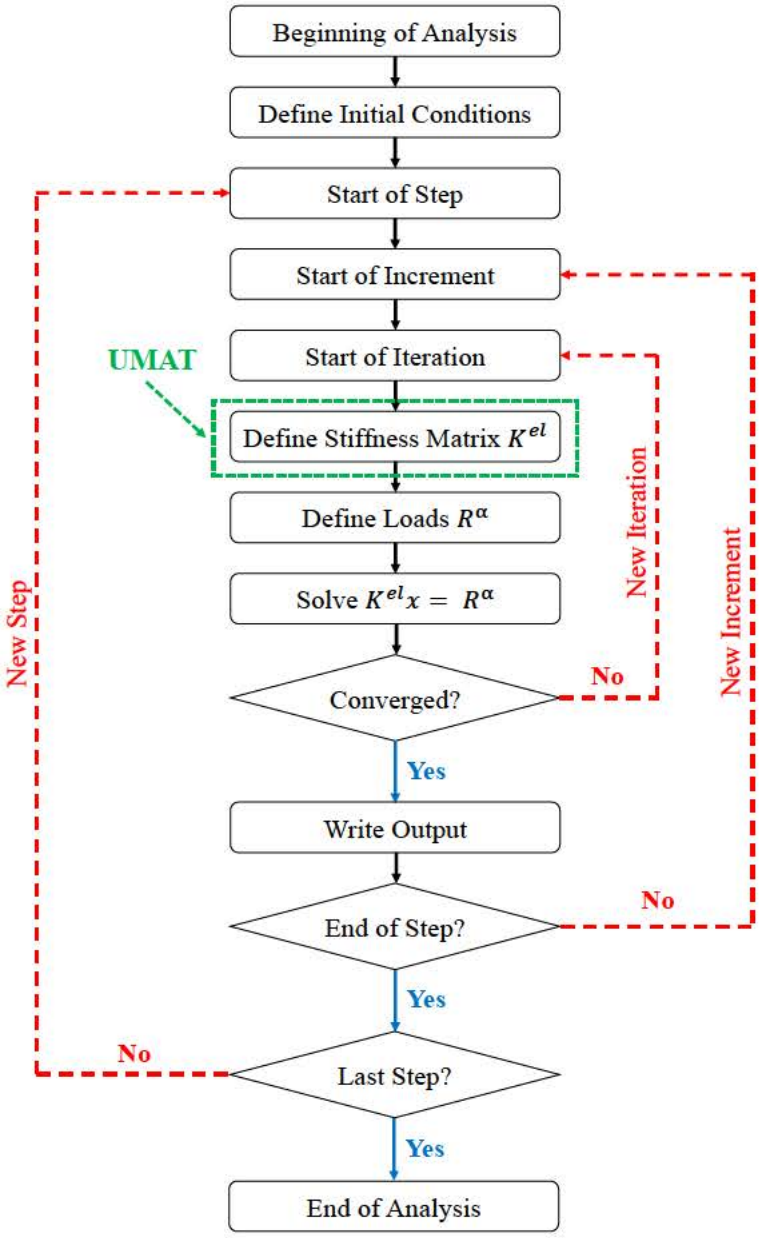

Fig. 4.1: Basic flow of actions from the start to the end of an ABAQUS/Standard analysis.

Fig. 4.2 shows in a more detailed way of how ABAQUS/Standard calculates the element stiffness during an iteration and how this process is affected by UMAT_s. We have to bear in mind that all the field variables (deformation, stresses, etc.) corresponding to

each integration point (IP) are calculated based on nodal values. The first variables to be calculated are the deformations at each IP. After that, the corresponding stresses are calculated. Other important parameter computed in this step is the Jacobian, i.e., how the stresses varies with the deformation ($\frac{\partial \tau}{\partial \varepsilon}$). This Jacobian is quite important as it will be used for ABAQUS/Standard in order to solve the global Newton-Raphson procedure of the next iteration. Finally, the nodal loads are calculated. As shown in Fig. 4.2, the stresses and the Jacobian are calculated by UMAT_s. In the following sections, a complete description of the constitutive equations of the material models used in the framework of this Ph.D. thesis is provided, including a detailed description of its time implementation.

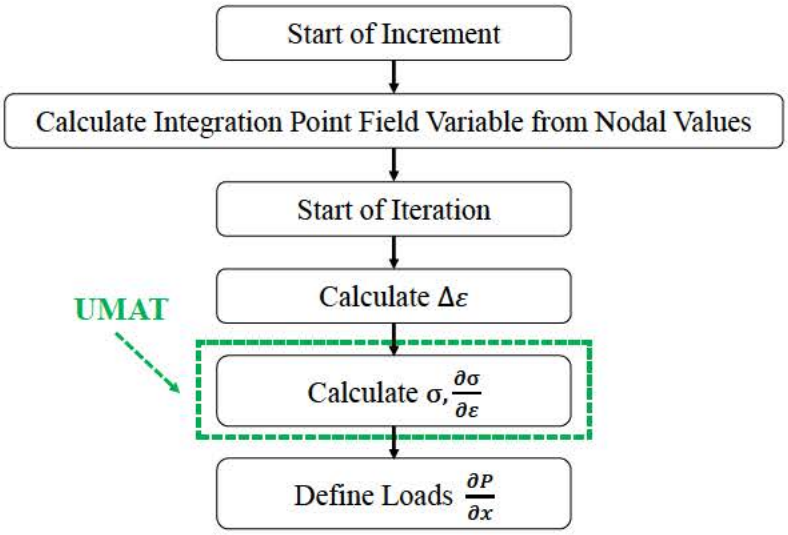

Fig. 4.2: Detailed flow of how ABAQUS/Standard calculates the element stiffness during an iteration.

4.2 Crystal Plasticity Models

The mechanical behaviour of the experimental single crystal indentations were reproduced using several CP models. In the following sections each model will be described in detail, specifying the differences and similarities between them.

4.2.1 CP model 1

The CP model described in this section, which was developed by Segurado and LLorca [130], only takes into account crystallographic glide as contributor to plastic deformation. Therefore, mechanical twinning is not considered and was only used in that cases where the activation of this deformation mechanisms was proved to be negligible.

The present model relies on the multiplicative decomposition of the deformation gradient, $\boldsymbol{F}$, into the elastic, $\boldsymbol{F}^e$, and plastic part, $\boldsymbol{F}^p$, following the next expression [131]:

$$\boldsymbol{F} = \boldsymbol{F}^e \boldsymbol{F}^p \tag{4.1}$$

where $\boldsymbol{F}^p$ is called the relaxed or intermediate configuration (Fig. 4.3)

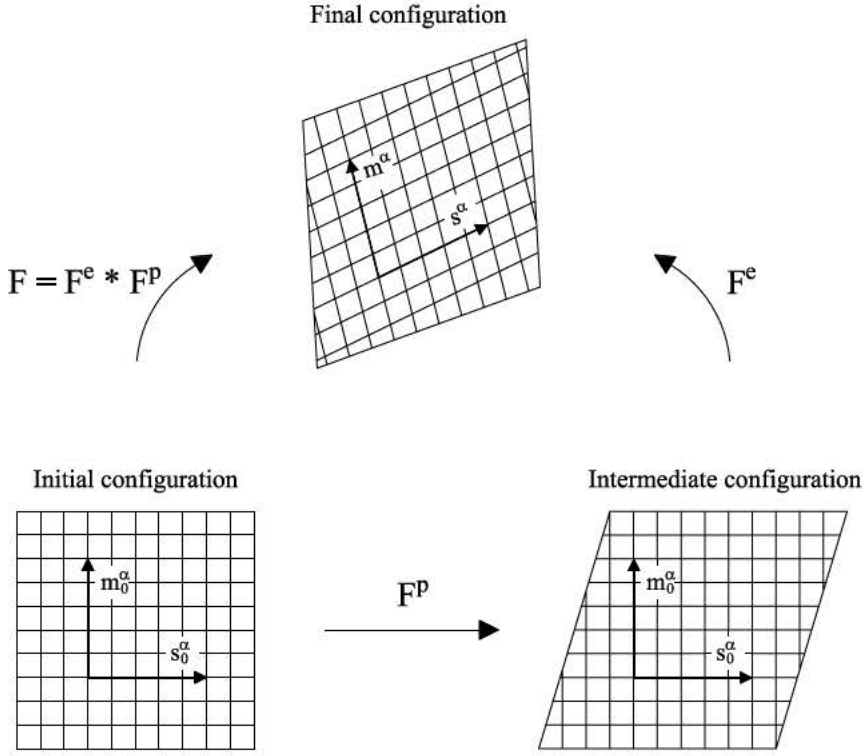

Fig. 4.3: Multiplicative decomposition of the total deformation gradient when plastic deformation is accommodated only by crystallographic glide.

Taking into account the definition of velocity gradient, $\boldsymbol{L}$, Eq. 4.1 leads to:

$$\boldsymbol{L} = \dot{\boldsymbol{F}}\boldsymbol{F}^{-1} = \dot{\boldsymbol{F}}^e \boldsymbol{F}^{e^{-1}} + \boldsymbol{F}^e \dot{\boldsymbol{F}}^p \boldsymbol{F}^{p^{-1}} \boldsymbol{F}^{e^{-1}} \tag{4.2}$$

where $\boldsymbol{L}^p = \dot{\boldsymbol{F}}^p \boldsymbol{F}^{p-1}$ is the plastic velocity gradient corresponding to the intermediate configuration, which is calculated by the sum of the shear rates, $\dot{\gamma}^\alpha$, of each slip system, α, as:

$$\boldsymbol{L}^p = \sum_{\alpha=1}^{N_{sl}} \dot{\gamma}^\alpha \boldsymbol{m}_{sl}^\alpha \otimes \boldsymbol{n}_{sl}^\alpha \tag{4.3}$$

where N_{sl} is the number of slip systems and $\boldsymbol{m}_{sl}^\alpha$ and $\boldsymbol{n}_{sl}^\alpha$ stand for the unit vectors in the slip direction and perpendicular to the slip plane α, respectively.

The plastic behaviour of the crystal, $\dot{\gamma}^{\alpha}$, is modelled following a viscoplastic law as a function of the resolved shear stresses, τ^{α}:

$$\dot{\gamma^{\alpha}} = \dot{\gamma}_0 \left(\frac{|\tau^{\alpha}|}{\tau_c^{\alpha}} \right)^{1/m_{sl}} sing\left(\tau^{\alpha}\right) \tag{4.4}$$

where $\dot{\gamma}_0$ and m_{sl} are the reference shear strain rate and the rate-sensitive exponent for slip [132], respectively.

The evolution of the glide resistance, τ_c^{α}, for a slip system α, is given by the expression proposed by Asaro and Needleman [70]:

$$\dot{\tau_c}^{\alpha} = h^{\alpha}\dot{\gamma}^{\alpha} + \sum_{\beta \neq \alpha} q^{\alpha\beta} h^{\alpha} \dot{\gamma}^{\beta} \tag{4.5}$$

where the first and second terms of the right side of the expression defines the self- and latent-hardening contributions, respectively. The first one refers to the evolution of the CRSS of the slip system α caused only due to the plastic deformation in that specific slip system and is defined by the shear rate on that slip system, $\dot{\gamma}^{\alpha}$, and the hardening modulus, h^{α}, which is defined by the following phenomenological expression:

$$h^{\alpha} = h_0^{\alpha} sech^2 \left| \frac{h_0^{\alpha}\Gamma}{\tau_{c,s}^{\alpha} - \tau_{c,0}^{\alpha}} \right| \tag{4.6}$$

where $\tau_{c,0}^{\alpha}$ represents the value of the τ_c^{α} if the crystal has undergone no plastic deformation (also called as initial CRSS), h_0^{α} is the initial hardening modulus and $\tau_{c,s}^{\alpha}$ the saturation CRSS. Fig. 4.4 shows schematically how the $\tau_{c,0}^{\alpha}$ evolves with the accumulated shear Γ, imposing an initial tangent modulus of h_0^{α}, until it reaches the saturation value $\tau_{c,s}^{\alpha}$ (only if the self-hardening is considered). The accumulated shear Γ can be expressed as:

$$\Gamma = \int \sum_{\alpha} |\dot{\gamma}^{\alpha}| dt \tag{4.7}$$

On the other hand, the latent-hardening contribution is defined by the latent-hardening parameter $q^{\alpha\beta}$ and represents the contribution of the slip on the plane β in the hardening of the slip system α

The second Piola-Kirchoff stress tensor, $\boldsymbol{S}$, is calculated based on the Green-Lagrange strain tensor, $\boldsymbol{E}^e$, both in the reference configuration, according to the following expressions:

$$\boldsymbol{S} = \mathbb{C} : \boldsymbol{E}^e \tag{4.8}$$

$$\boldsymbol{E}^e = \frac{1}{2}\left(\boldsymbol{F}^{e^T} \boldsymbol{F}^e - \boldsymbol{I} \right) \tag{4.9}$$

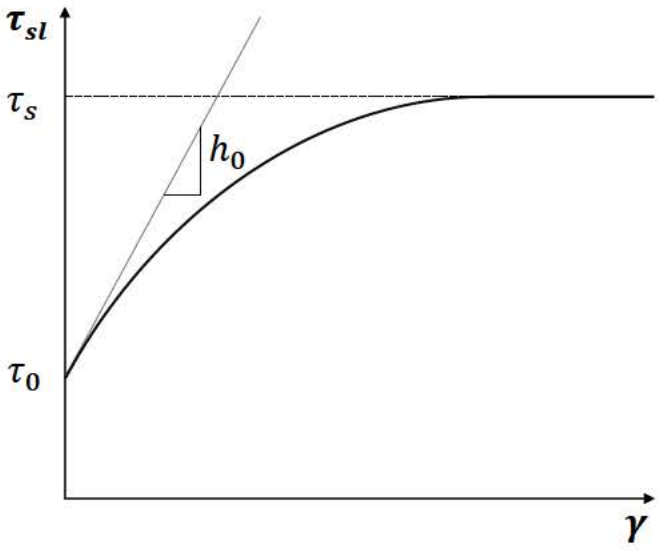

Fig. 4.4: Schematic of the evolution of the τ_c with plastic deformation only due to self-hardening contribution.

where $\mathbb{C}$ is the fourth-order elastic tensor of the crystal and $\boldsymbol{I}$ the second-order identity tensor.

The resolved shear stress, τ^α, is obtained as the projection of the second Piola-Kirchoff stress tensor $\boldsymbol{S}$ on the α slip plane, both defined in the relaxed configuration, according to the expression:

$$\tau^\alpha = \boldsymbol{S} : \boldsymbol{s}^\alpha \otimes \boldsymbol{m}^\alpha \tag{4.10}$$

Finally, the Cauchy stress tensor, $\boldsymbol{\sigma}$, is approximated by

$$\boldsymbol{\sigma} = J^{-1}\boldsymbol{F}^e\boldsymbol{S}\boldsymbol{F}^{eT} \tag{4.11}$$

where $J = det(\boldsymbol{F})$.

4.2.2 CP model 2

The CP model detailed in this section was developed by Herrera-Solaz and coworkers [53] and is based on the model described in the previous section. The latter was modified in order to include mechanical twinning as an additional plastic deformation mechanism.

As in the previous case, this model is based on the multiplicative decomposition of the deformation gradient, $\boldsymbol{F}$, into the elastic, $\boldsymbol{F}^e$, and the plastic part, $\boldsymbol{F}^p$ according to Eq. 4.1. However, in this case and following Kalidindi's approach [87], each material point is divided

into two phases: the parent region, where the conventional plastic glide takes place, and the twinned region, which is formed by a maximum of N_{tw} subregions corresponding each of them to a given twinning system ξ and occupying a volume fraction of f^{ξ} (Fig. 4.5). The hypothesis of iso-strain is assumed, and therefore, $\boldsymbol{F}$ and $\boldsymbol{F}^{e}$ are the same for all the phases belonging to each material point.

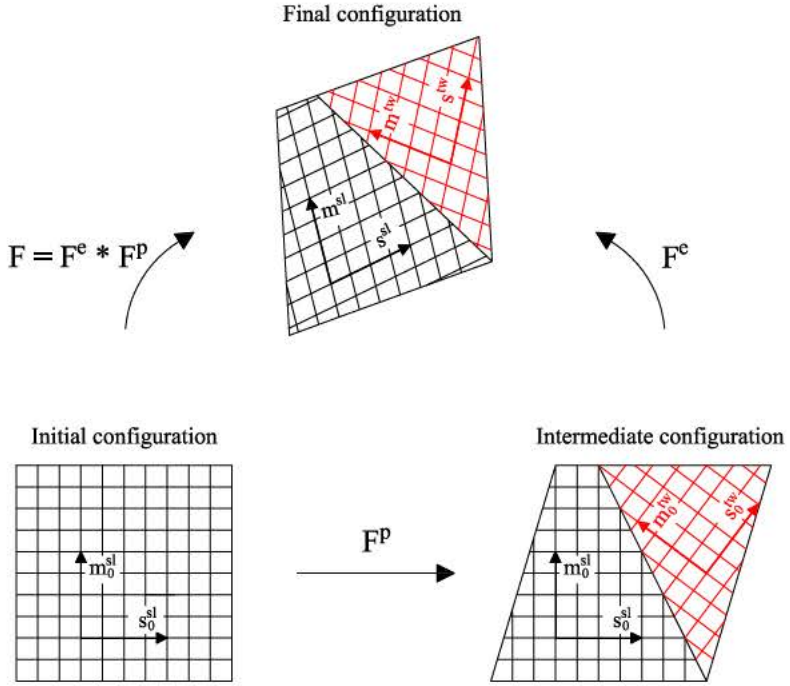

Fig. 4.5: Multiplicative decomposition of the total deformation gradient when plastic deformation is accommodated by crystallographic glide and mechanical twinning.

The plastic deformation is defined by the contribution of three terms: slip in the parent region (slip contribution), twin transformation in the twinned phase (twin contribution) and slip in the transformed regions (re-slip contribution). Therefore, the velocity gradient in the relaxed configuration includes three terms. The first one, $\boldsymbol{L}^{p}_{sl}$, related to the slip contribution, is given by:

$$\boldsymbol{L}^{p}_{sl} = \left(1 - \sum_{\xi=1}^{N_{tw}} f^{\xi}\right) \sum_{\alpha=1}^{N_{sl}} \dot{\gamma}^{\alpha} \boldsymbol{s}^{\alpha}_{sl} \otimes \boldsymbol{m}^{\alpha}_{sl} \tag{4.12}$$

On the other hand, the twin contribution follows the expression:

$$\boldsymbol{L}^{p}_{tw} = \sum_{\xi=1}^{N_{tw}} \dot{f}^{\xi} \gamma_{tw} \boldsymbol{s}^{\xi}_{tw} \otimes \boldsymbol{m}^{\xi}_{tw} \tag{4.13}$$

where $\dot{f}^{\xi}$ is the rate of volume fraction transformation in the twin system ξ, s^{ξ}_{tw} and m^{ξ}_{tw} defines the twinning system ξ and γ_{tw} is the characteristic shear of the twinning mode

considered. In this case, as only tensile twinning is included in the model, $\gamma_{tw} = 0.129$ [49]. Finally, the re-slip contribution, $\boldsymbol{L^p_{re\ \ sl}}$, is expressed as:

$$\boldsymbol{L^p_{re\ \ sl}} = \sum_{\xi=1}^{N_{tw}} \dot{f}^{\xi} \left(\sum_{\alpha^*=1}^{N_{sl-tw}} \dot{\gamma}^{\alpha^*} \boldsymbol{s^{\alpha^*}_{sl}} \otimes \boldsymbol{m^{\alpha^*}_{sl}} \right) \tag{4.14}$$

where $s^{\alpha^*}_{sl}$ and $m^{\alpha^*}_{sl}$ determines the slip system α, which has been reorientated due to the rotation $\boldsymbol{Q^{\xi}}$ associated with the twin transformation of the twin system ξ,

$$\boldsymbol{Q}^{\xi} = 2\boldsymbol{m}^{\xi}_{tw} \otimes \boldsymbol{m}^{\xi}_{tw} - \boldsymbol{I} \tag{4.15}$$

where $\boldsymbol{I}$ is the second order identity tensor.

The plastic slip rates, $\dot{\gamma}^{\alpha}$ and $\dot{\gamma}^{\alpha^*}$, follow the same behaviour than the previous model (Eq. 4.4). In a similar way, the evolution of the twinning transformation rate $\dot{f}^{\xi}$ is also defined by a viscous law:

$$\dot{f}^{\xi} = \dot{f}_0 \left(\frac{\langle \tau^{\xi} \rangle}{\tau^{\xi}_c} \right)^{1/m_{tw}} \tag{4.16}$$

where $\dot{f}_0$ is the initial twin transformation rate, τ^{ξ} the resolved shear stress on the twin plane ξ, τ^{ξ}_c the CRSS of the twin plane ξ and m_{tw} the rate-sensitivity for twinning. The transformation rate, $\dot{f}^{\xi}$, is set equal to zero if $\tau^{\xi} < 0$ or if f^{ξ} reaches the critical value of 0.8.

The second Piola-Kirchhoff tensor in the intermediate configuration, $\boldsymbol{S}$, is defined by the average of the stress tensors in the different phases:

$$\boldsymbol{S} = \left(1 - \sum_{\xi=1}^{N_{tw}} f^{\xi} \right) \boldsymbol{S}^{parent} + \sum_{\xi=1}^{N_{tw}} f^{\xi} \boldsymbol{S}^{\xi} \tag{4.17}$$

The stress on each phase is defined as follows:

$$\boldsymbol{S^{parent}} = \mathbb{C}\boldsymbol{E}^e \tag{4.18}$$

$$\boldsymbol{S}^{\xi} = \mathbb{C}^{\xi}\boldsymbol{E}^e \tag{4.19}$$

where $\mathbb{C}$ is the fourth-order elastic stiffness tensor of the crystal in its original orientation, $\boldsymbol{E}^e$ the Green-Lagrange strain tensor (Eq. 4.9) and $\mathbb{C}^{\xi}$ the stiffness tensor reorientated by the twin transformation of the variant ξ.

The determination of the resolved shear stress on a slip (τ^{α}) or twin plane (τ^{ξ}) in the parent region are calculated as:

$$\tau^{\alpha} = \boldsymbol{S}^{parent} : \boldsymbol{s}_{sl}^{\alpha} \otimes \boldsymbol{m}_{sl}^{\alpha} \tag{4.20}$$

$$\tau^{\xi} = \boldsymbol{S}^{parent} : \boldsymbol{s}_{tw}^{\xi} \otimes \boldsymbol{m}_{tw}^{\xi} \tag{4.21}$$

while the resolved shear stress on a slip plane in the twinned region (τ^{α^*}) is obtained as:

$$\tau^{\alpha^*} = \boldsymbol{S}^{\boldsymbol{\xi}} : \boldsymbol{s}_{\boldsymbol{sl}}^{\boldsymbol{\alpha^*}} \otimes \boldsymbol{m}_{\boldsymbol{sl}}^{\boldsymbol{\alpha^*}}; \tag{4.22}$$

The Cauchy stress tensor, $\boldsymbol{\sigma}$, is calculated using the same expression than in the previous model (Eq. 4.11). The evolution of the CRSS for the slip, twin and re-slip systems, τ_c^{α}, τ_c^{ξ} and $\tau_c^{\alpha^*}$, is based on a classical phenomenological hardening model proposed by Kothari and Anand [133]:

$$\dot{\tau}_c^{\alpha} = q_{sl-sl} \sum_{j=1}^{N_{sl}} h_0^j \left(1 - \frac{\tau^j}{\tau_{sat}^j}\right)^{a_{sl}} \left|\dot{\gamma}^j\right| + q_{tw-sl} \sum_{k=1}^{N_{tw}} h_0^k \left(1 - \frac{\tau^k}{\tau_{sat}^k}\right)^{a_{tw}} \left|\dot{\gamma}^k\right| \tag{4.23}$$

$$\dot{\tau}_c^{\alpha} = q_{tw-tw} \sum_{k=1}^{N_{tw}} h_0^k \left(1 - \frac{\tau^k}{\tau_{sat}^k}\right)^{a_{tw}} \dot{f}^k \gamma_{tw} \tag{4.24}$$

$$\dot{\tau}^{\alpha^*} = q_{sl-sl} \sum_{j^*=1}^{N_{tw}*N_{sl}} h_0^{j^*} \left(1 - \frac{\tau^{j^*}}{\tau_{sat}^{j^*}}\right)^{a_{sl}} \left|\dot{\gamma}^{j^*}\right| \tag{4.25}$$

where the self-hardening behaviour is defined by the saturation stress, τ_{sat}, the initial hardening rate, h_0, and the hardening exponents, a_{tw} and a_{sl}. The physical interpretation of the two first parameters is the same than in the previous model (Fig. 4.4). On the other hand, the cross hardening behaviour is characterized by the slip-to-slip and twin-to-slip hardening parameters, q_{sl-sl} and q_{tw-sl}, assuming that slip does not influence twinning [49, 134].

4.2.3 CP model 3

The model described in the Section 4.2.2 was based on Kalidindi's approach [87] where each material point represents one grain or at least a large fraction of it. As commented in Section 2.3, this assumption has two important implications. First, in order to account for the fact that different twin variants can develop in a same grain, the model described in the previous section allows the activation of several twin variants in each material point. Second, due to the great difference between the volume represented by each material point

in the model and the actual volume where twins are first activated, the model is only able to reflect the effect of twinning on the average response of the grain. However, the volume of the material points of the FE models used here is several orders of magnitude smaller than the actual volume of the grains. Taking into account our experimental observations, in a material point of such characteristics only one twin system should be activated. In addition, the volume represented by the material points is similar to the volumes where the first stages of twin development take place, and therefore, the model should be able to capture the actual micromechanics of mechanical twinning. In order to overcome these limitations, a novel CP model, based on the one one described in Section 4.2.2, was developed in the framework the the present Ph.D. thesis including two main modifications in comparison with Herrera-Solaz's model [53]:

- In the proposed model, only one twin system is allow to be activated in each material point.
- The model accounts for the fact that twin nucleation is a processes that requires much more sever stress states than twin propagation [28].

As in the previous cases, the model relies on the multiplicative decomposition of the deformation gradient, $\boldsymbol{F}$, into the elastic, $\boldsymbol{F}^e$, and the plastic, $\boldsymbol{F}^p$ parts according to Eq. 4.1. Again, each material point is divided into a parent and a twinned phase following the same scheme than the one shown in Fig. 4.5. However, in this case, the twinned fraction, which has a volume of f^{ξ}, is only formed by one twin variant. The model implements such modification as follows. Initially, all the twin systems are allowed to be activated, although their contribution to the overall plastic deformation is neglected. At the same time, the volume fraction of each twin system ξ is saved in a auxiliary variable f^{ξ}_{aux}. Once the f^{ξ}_{aux} of a twin system ξ reaches a critical value f^{ξ}_{nucl}, that specific twin system starts to contribute to the global plastic deformation according to the following expression:

$$\boldsymbol{L}^p_{tw} = \dot{f}^{tw}\gamma_{tw}\boldsymbol{s}_{tw} \otimes \boldsymbol{m}_{tw} \tag{4.26}$$

where $\dot{f}^{tw}$ is the rate of volume fraction transformation of the active twin system, γ_{tw} is the characteristic shear associated with the twin mode ($\gamma_{tw} = 0.129$ in case of conventional tensile twinning [49]), and $\boldsymbol{s}_{tw}$ and $\boldsymbol{m}_{tw}$ are the unit vector in the twin direction and perpendicular to the plane of the active twin. Once a twin system has been activated, the other twin systems are excluded for the rest of the simulations. When f^{tw} reaches a critical value of 0.95, the twinned region are not allowed to grow anymore and undergoes a rotation Q_{tw} induced by the active twin system as shown in Eq. 4.15.

On the other hand, the contribution of the slip in the parent phase, whose volume fraction is $(1 - f^{tw})$, to the overall plastic deformation is given by:

$$\boldsymbol{L}^p_{sl} = \left(1 - f^{tw}\right) \sum_{\alpha=1}^{N_{sl}} \dot{\gamma}^{\alpha} \boldsymbol{s}^{\alpha}_{sl} \otimes \boldsymbol{m}^{\alpha}_{sl} \tag{4.27}$$

In contrast to the model proposed by Herrera-Solaz et al. [53], the re-slip process in the twinned region has not been included in the model, as due to the specifications of the single crystal indentation simulations, no important effects are expected regarding this phenomenon and, in return, an important reduction in the computational cost is achieved.

The same laws than the ones specified in Eqs. 4.4 and 4.16 were used in order to model the slip rate, $\dot{\gamma}^{\alpha}$, and the evolution of the twinned volume fraction, $\dot{f}^{tw}$. As in the previous model, the second Piola-Kirchhoff tensor is calculated as an average of the stress tensors in the different phases

$$\boldsymbol{S} = \left(1 - f^{\xi}\right) \boldsymbol{S}^{parent} + f^{\xi} \boldsymbol{S}^{\xi} \tag{4.28}$$

where $\boldsymbol{S}^{parent}$ and $\boldsymbol{S}^{\xi}$ are defined according to Eqs. 4.18 and 4.19. The resolved shear stress on a slip (τ^{α}) or twin plane (τ^{ξ}) are defined according to Eqs. 4.20 and 4.21. Regarding the Cauchy stress tensor, $\boldsymbol{\sigma}$, the same expression than the one specified in Eq. 4.11 is used.

In order to complete the model, the CRSS of the slip, τ_c^{α}, and twin, τ_c^{ξ}, systems have to be defined. Regarding the first one, the same expression than the one specified in Eq. 4.23 is used. However, in this case, no effect of twin activity is considered in the evolution of τ_c^{α} ($q_{tw-sl} = 0$ in Eq. 4.23). In general, the hardening contribution to slip due to twin activity has been modelled as a fraction of the self-hardening undergone by the twin systems [53]. However, this approximation does not have a proper physical interpretation in the model proposed in this section, where each material point only represents a tiny fraction of the whole crystal. Instead, the ideal model should incorporate the twin-to-slip hardening interaction as a function of the proximity of each material point to the twin interfaces. However, the implementation of such complex model is beyond the scope of this research. In addition this simplification does not severely affect the main qualitative analysis performed in the present Ph.D. thesis.

On the other hand, a different crystal model has been used in order to model the behaviour of mechanical twinning. In particular, the evolution of the CRSS for twinning, τ_c^{ξ}, is considered to evolve with the twinned volume fraction following a simple bi-linear law as shown in Fig. 4.6. In the first part of the law, the initial CRSS for twinning, τ_{nucl}^{ξ}, decreases linearly until a value called τ_{pro}^{ξ}, which has associated a twinned volume fraction of f_{pro}^{ξ}. For larger values of the twinned volume fraction, a fixed value of τ_{pro}^{ξ} is considered for the τ_c^{ξ}. In this way, the model is able to capture the fact that twin nucleation is a processes that requires much more sever stress states than twin propagation, and therefore, the micromechanics of mechanical twinning.

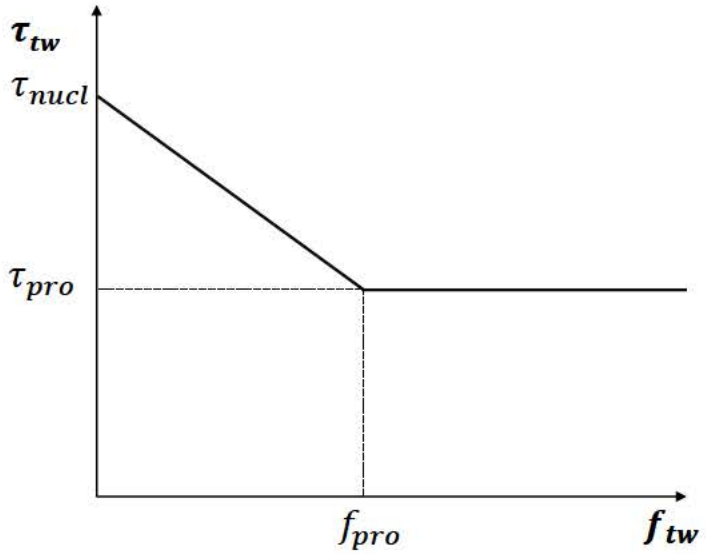

Fig. 4.6: Schematic of the evolution of the CRSS for twinning with twinned volume fraction.

4.2.4 Time discretisation

The FE software Abaqus uses a global Newton-Raphson algorithm in order to solve the general non-linear problem. In this process, which is divided into steps, increments and iterations (Fig. 4.1), the UMAT plays a key role in the calculation of the stiffness matrix in each iteration. In particular, it has to provide the Cauchy stress, $\boldsymbol{\sigma}$, and the Jacobian, $\frac{\partial \Delta \sigma}{\partial \Delta \epsilon}$, that defines the variation of the stresses with deformation (Fig. 4.2) in the final configuration of each iteration. In this section, a detail description of the specific time-dependent algorithm used to solve the equations included in the CP model 1 (Section 4.2.1) is given. This analysis can be easily extended to the other two subroutines (Sections. 4.2.2 and 4.2.3) as they use the same solution procedure.

Let t be the last converged increment. At this time, the total deformation gradient, $\boldsymbol{F}_t$, and their corresponding elastic, $\boldsymbol{F}_t^e$, and plastic, $\boldsymbol{F}_t^p$ parts, together with the Cauchy stress, $\boldsymbol{\sigma}_t$, are known. In addition, the set of internal variables, $\boldsymbol{\alpha}_t$ ($\gamma_{t+\Delta t}$, $\tau_{c,t}^{\alpha}$, ...) are also known. The subroutine, making use of all the equations, laws and expressions detailed in Section 4.2.1, should provide at a time of $t+\Delta t$ the $\boldsymbol{\sigma}_{t+\Delta t}$ and the $\frac{\partial \Delta \sigma_{t+\Delta t}}{\partial \Delta \epsilon_{t+\Delta t}}$. The values of $\boldsymbol{F}_{t+\Delta t}^e$ and $\boldsymbol{\alpha}_{t+\Delta t}$ are also calculated.

The plastic deformation gradient at $t+\Delta t$ can be obtained by integrating this variable in that time step as follows:

$$\sum_{t}^{t+\Delta t} \boldsymbol{L}^p dt = \sum_{t}^{t+\Delta t} \dot{\boldsymbol{F}}^p \boldsymbol{F}^{p^{-1}} \rightarrow \boldsymbol{F}_{t+\Delta t}^p = exp(\Delta t \boldsymbol{L}_{t+\Delta t}^p) \boldsymbol{F}_t^p \tag{4.29}$$

where $exp()$ is the exponential map operator [135]. Combining Eq. 4.2 with the multi-

plicative decomposition of the deformation gradient (4.1), the elastic deformation gradient at $t + \Delta t$, $\boldsymbol{F}^e_{t+\Delta t}$, can be expressed as:

$$\boldsymbol{F}^e_{t+\Delta t} = \boldsymbol{F}^e_0 exp(-\Delta t \boldsymbol{L}^p_{t+\Delta t}(\boldsymbol{F}^e_{t+\Delta t})) \quad with \quad \boldsymbol{F}^e_0 = (\boldsymbol{F}_{t+\Delta t}\boldsymbol{F}_t^{-1})\boldsymbol{F}^e_t \tag{4.30}$$

If the time step increments are small enough, the exponential function $exp(-\Delta t \boldsymbol{L}^p)$ can be approximated by $\boldsymbol{I} - \Delta t \boldsymbol{L}^p$. As a result, Eq. 4.30 can be written as:

$$\boldsymbol{F}^e_{t+\Delta t} = \boldsymbol{F}^e_0(\boldsymbol{I} - \Delta t \boldsymbol{L}^p(\boldsymbol{F}^e_{t+\Delta t})) \tag{4.31}$$

As it can be observed, Eq. 4.31 cannot be solved explicitly as the term $\boldsymbol{F}^e_{t+\Delta t}$ is directly or indirectly included in both sides of the expression. To solve it, an iterative Newton-Raphson scheme is used whose residual function, which depends on the $\boldsymbol{F}^e_{t+\Delta t}$, is expressed as:

$$\boldsymbol{R}(\boldsymbol{F}^e_{\boldsymbol{t+\Delta t}}) = \boldsymbol{F}^e_{t+\Delta t} - \boldsymbol{F}^e_0(\boldsymbol{I} - \Delta t \boldsymbol{L}^p(\boldsymbol{F}^e_{t+\Delta t})) \approx 0 \tag{4.32}$$

In each iteration, the new prediction of the elastic deformation gradient, $\boldsymbol{F}^e_{new}$, is calculated by:

$$\boldsymbol{F}^e_{new} = \boldsymbol{F}^e_{old} - \mathbb{J}^{-1}(\boldsymbol{F}^e_{old}) : \boldsymbol{R}(\boldsymbol{F}^e_{old}) \tag{4.33}$$

where $\mathbb{J}$ is the corresponding Jacobian which is given by:

$$\mathbb{J} = \frac{\partial \boldsymbol{R}(\boldsymbol{F}^e)}{\partial \boldsymbol{F}^e} \tag{4.34}$$

The calculation of the Jacobian $\mathbb{J}$ (Eq. 4.34) is evaluated analytically according to the following expression:

$$\mathbb{J}_{ijkl} = \left[\frac{\partial \boldsymbol{R}(\boldsymbol{F}^e)}{\partial \boldsymbol{F}^e}\right]_{ijkl} = \delta_{ik}\delta_{jl} + \Delta t \boldsymbol{F}^e_{0,im}\mathbb{E}_{mjpq}\left[\sum_{\alpha=1}^{N_{sl}} \dot{\gamma}^\alpha \boldsymbol{s}^\alpha \otimes \boldsymbol{m}^\alpha \otimes \frac{\partial \dot{\gamma}^\alpha}{\partial \boldsymbol{F}^e}\right]_{pqkl} \tag{4.35}$$

In order to perform the calculation, an initial predictor for $\boldsymbol{F}^e_{t+\Delta t}$ is needed. In this case, the following adaptive predictor is used:

$$\boldsymbol{F}^e_{t+\Delta t} = \boldsymbol{F}^e_0(\boldsymbol{I} - \Delta t \boldsymbol{L}^p(t)) \tag{4.36}$$

Once the iterative Newton-Raphson procedure shown in Eq. 4.32 has converged, the values of $\boldsymbol{F}^e_{t+\Delta t}$ and $\boldsymbol{\alpha}_{t+\Delta t}$ are obtained, and therefore, the value of the Cauchy stress in $t + \Delta t$, $\boldsymbol{\sigma}_{t+\Delta t}$ can be calculated using Eq. 4.11.

The second important output that has to be obtained by the UMAT is the material tangent matrix, defined as

$$\mathbb{K} = \frac{\partial \Delta\sigma}{\partial \Delta\epsilon} \tag{4.37}$$

Following the approach proposed by Kalidindi et al. [71], the expression 4.37 is evaluated numerically by carrying out six symmetric perturbations , $\delta \boldsymbol{F}^{i,j}$, of the total deformation gradient at $t + \Delta t$. Each perturbation, which has a fixed size of $d\epsilon$, corresponds to an uniaxial infinitesimal deformation on the final deformed configuration. The final perturbed deformation gradient can be expressed as:

$$\boldsymbol{F}^{per:i,j} = \delta \boldsymbol{F}^{i,j} \boldsymbol{F}_{t+\Delta t} \tag{4.38}$$

For each of the six perturbed deformation gradient, $\boldsymbol{F}^{per:i,j}$, the corresponding perturbed Cauchy stress tensor, $\boldsymbol{\sigma}^{per:i,j}$, is obtained using a very similar Newton-Raphson scheme than the one shown in Eq. 4.32. Finally, the tangent stiffness matrix is obtained as:

$$\left(\frac{\partial \Delta \boldsymbol{\sigma}}{\partial \Delta \boldsymbol{\epsilon}}\right)_{ijkl} \approx \frac{\sigma_{ij}^{per:k,l} - \sigma_{ij}}{d\epsilon} \tag{4.39}$$

"All truths are easy to understand once they are discovered; the point is to discover them"

Galileo Galilei

5

Room temperature micromechanics of pure Mg studied by nanoindentation

5.1 Introduction

In this chapter, a complete study of the main deformation modes of pure Mg at RT is carried out combining nanoindentation, EBSD, AFM and CPFE simulation. In particular, two main aspects are studied: (i) the effect of the crystallographic orientation of the indented plane on the deformation patterns found around the indents and on the maximum load reached during the indentation; and (ii), the effect of the indentation size on the activation of the different deformation modes, specially tensile twinning. Based on analytical models and CPFE simulations, it was confirmed that these dependences (i) were originated due to the activation of certain slip/twin systems in different areas in the vicinity of the indentation region. In addition, it was revealed that twinning is subjected to strong size effects.

5.2 Experimental procedure

The initial material was the rolled and annealed sheet of pure Mg, further annealed at 500 °C, described in Section 3.1. The final grain size is in the mm range, as shown in Fig. 5.1. Eight grains with different orientations were selected for this study. In Grains 1-7, whose declination angles (angle between the c-axis and the indentation axis, δ) are included in Fig. 5.1, several nanoindentations with maximum indentation depths varying from 200 to 7000 nm were carried out using the Hysitron TI 950 Triboindenter® system described in Section 3.4.5. A diamond sphero-conical indenter with a tip radius of 2 μm and an apex angle of 70° (Tip 1) was utilized to carry out indentations up to an h_{max} of 750 nm. A second sphero-conical indenter, with a tip radius of 10 μm and an apex angle of 60° (Tip 2), was used to perform indentations with an h_{max} larger than 750 nm. All the tests were conducted in displacement control mode using a trapezoidal loading curve, with a loading and unloading time of 5 s, and a 2 s holding time at h_{max}. The microstructure and the topography of areas of the free surface in the vicinity of the indents were examined by EBSD, using the Helios NanoLab™ DualBeam™ 600i microscope equipped with an Oxford-HKL EBSD detector described in Section 3.3.2 (operated at a voltage of 15 kV and at an emission current of 2.7 nA), and by AFM, using the Park XE150 AFM microscope described in Section 3.3.3. Grain 8, whose c-axis lies almost perpendicular to the indentation axis ($\delta = 80.1°$), was selected to perform a cross-section EBSD analysis aimed at analysing twinning underneath two indentations: one with an h_{max} of 450 nm, and a significant larger Vickers microindentation, with an h_{max} close to 11 μm. The latter was performed using a SHIMADZU HMV-2 microhardness tester equipped with a Vickers diamond indenter applying a maximum load of 0.05 kg and a dwell time of 15 s. While the cross section of the Vickers microindentation was prepared by conventional manual grinding and polishing, the FIB milling technique was necessary in the case of the 450 nm depth indent. Sample preparation for nanoindentation, EBSD and AFM characterisation was performed using the *Route B* procedure described in Section 3.2.

5.3 Numerical simulations

Two different three dimensional FE models (Model 1 and Model 2) were utilized to simulate the indentation process for each of the tips (Tip 1 and Tip 2, respectively) used in this study. In both models, modified quadratic tetrahedral elements (C3D10M) were chosen. The size of the geometrical model was large enough so that the stresses at the borders could be neglected. The indenter, which was only allowed to move in the z direction, was modelled as an analytical rigid body. Frictionless contact was assumed between the rigid indenter and the material surface in all the simulations. For each model, the mesh size was determined after a convergence study to ensure that the results are mesh-size independent, using a number of elements between 5000 and 6000.

The crystal plasticity model described in Section 4.2.2 was integrated into the FE commercial software ABAQUS [129]. The constitutive parameters of pure Mg were taken form literature [49,136]. The following elastic constants were used in the simulations: C_{11} = 59.4 GPa, C_{12} = 25.6 GPa, C_{13} = 21.4 GPa, C_{33} = 61.6 GPa and C_{44} = 16.4 GPa. A total

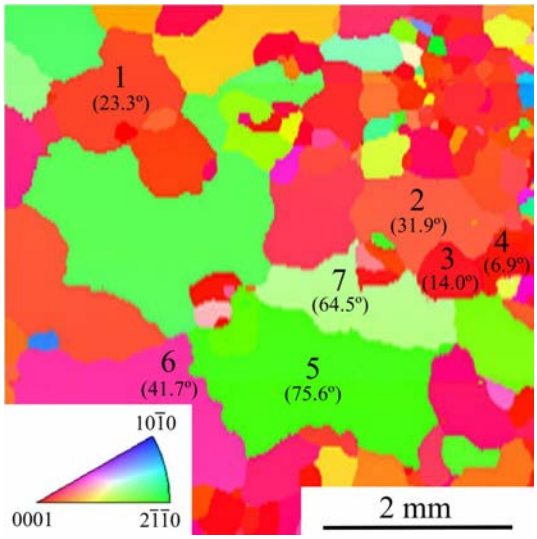

Fig. 5.1: EBSD inverse pole figure map in the normal direction (ND) of the annealed pure Mg sheet illustration 7 out of the 8 grains investigated (the δ of each grain is indicated in brackets).

of 12 slip systems and 6 twin systems were included in the CP model, as listed in Table 6.2. The values of the CP parameters (the yield stress, τ_0, the saturation yield stress, τ_s, and the initial hardening modulus h_0) used in the simulations where taken from Zhang and Joshi [49] and are included in Table 5.1. Regarding the slip-to-slip and twin-to-slip latent hardening parameters, q_{sl-sl} and q_{tw-sl}, the values of 1.0 and 2.0 were chosen respectively. The self-hardening parameters, a_{sl} and a_{tw}, were fixed at 0.6 and 1.0. Finally, the strain rate sensitivity exponents for slip and twinning, m_{sl} and m_{tw} and the reference shear rate, $\dot{\gamma}_0$, were fixed at 0.1 and 1 s^{-1} respectively.

		Slip/twin plane	Slip/twin direction	Number of systems	τ_0 (MPa)	τ_s (MPa)	h_0 (MPa)
Slip system	Basal $\langle a \rangle$	$\{0002\}$	$\langle 11\bar{2}0 \rangle$	3	2	10	20
	Prismatic $\langle a \rangle$	$\{1\bar{1}00\}$	$\langle 11\bar{2}0 \rangle$	3	25	85	1500
	Pyramidal $\langle a \rangle$	$\{10\bar{1}1\}$	$\langle 11\bar{2}0 \rangle$	6	25	85	1500
	Second-order pyramidal $\langle c+a \rangle$	$\{11\bar{2}2\}$	$\langle 11\bar{2}3 \rangle$	6	40	150	3000
Twin systems	Tensile twinning	$\{01\bar{1}2\}$	$\langle 0\bar{1}11 \rangle$	6	3.5	20	100

Table 5.1: Material properties used in the simulations.

5.4 Results

5.4.1 Effect of twinning on the surface topography around an indent

It has been often observed in FCC single crystals that the deformation patterns developed around an indentation are highly dependent on the orientation of the indented plane, due to the activation of different slip systems [54–57,137]. In HCP metals, similar observations have been reported only in Ti, using testing conditions under which twinning was suppressed [57]. To date, there are very few studies relating the influence of twinning on the deformation patterns found around indents in HCP materials. Indeed, only Selvarajou et al. [61] related the deformation patterns induced during the indentation of pure Mg single crystals with the activation and propagation of TT_s in different areas around the indent. However, they only investigated a limited number of crystallographic orientations.

In order to overcome this limitation, a careful analysis of the topographies of the free surfaces around selected indents in three grains of the pure Mg sheet under study, with markedly different orientations, has been carried out. In particular, the following grains were chosen: Grain 1, with a low declination angle ($\delta = 23.3°$), Grain 6, with a medium declination angle ($\delta = 41.7°$) and Grain 5, with a high declination angle ($\delta = 75.6°$), as shown in Fig. 5.1. Indentations were performed at an h_{max} of 4000 nm. Fig 5.2a shows the AFM topography of the free surface close to the indent performed in Grain 1, revealing the presence of a pile-up. This indentation was reproduced using Model 2 (Section 5.3). In particular, two simulations were carried out: in one twinning was suppressed (Fig. 5.2b), while in the second twinning was allowed (Fig. 5.2c). From the comparison of Figs. 5.2b and 5.2c with Fig. 5.2a it can be inferred that twinning is essential in order to obtain a good match between the simulations and experimental observations. Fig 5.2d shows the EBSD inverse pole figure map of the free surface around the indentation in the direction normal to the sample surface. TT_s can clearly be observed around the indent, particularly in the pile-up region.

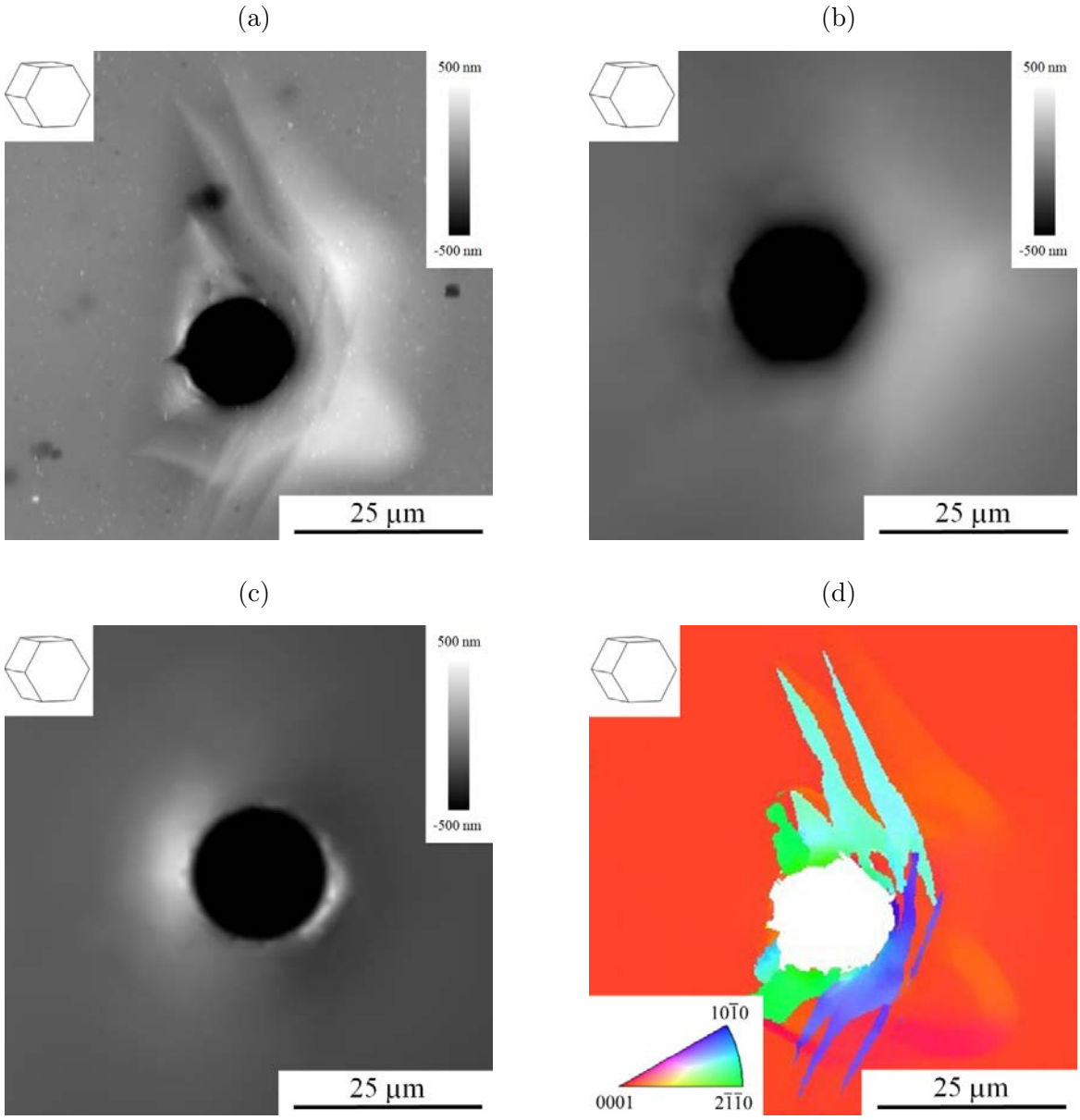

Fig. 5.2: Indentation performed in Grain 1 with a maximum indentation depth of 4000 nm: (a) AFM topography; (b) topography reproduced by CPFE simulation including twinning; (c) topography reproduced by CPFE simulation suppressing twinning; (d) EBSD inverse pole figure map in a direction parallel to the indentation axis.

A similar analysis was carried out in Grain 6 and Grain 5. Figs. 5.3a and 5.4a depict the free surface around the indent in both cases respectively. While a two-fold sink-in profile aligned with the basal planes is observed in Grain 5 (Fig. 5.4a), a similar (but less intense) sink-in pattern, combined with a pile-up aligned with the c-axis, is developed in Grain 6 (Fig. 5.3a). Again, several simulations, suppressing (Figs. 5.3b and 5.4b) and including (Figs. 5.3c and 5.4c) twinning, were performed in order to elucidate the role of this mechanism on the deformation of the free surface around the indent in the studied orientations. Here also only the simulations in which twinning was free to activate (Figs. 5.3c and 5.4c) exhibits the

topography measured experimentally. TT_s are, again, clearly located in the sink-in (Figs. 5.3d and 5.4d and pile-up regions (5.3d).

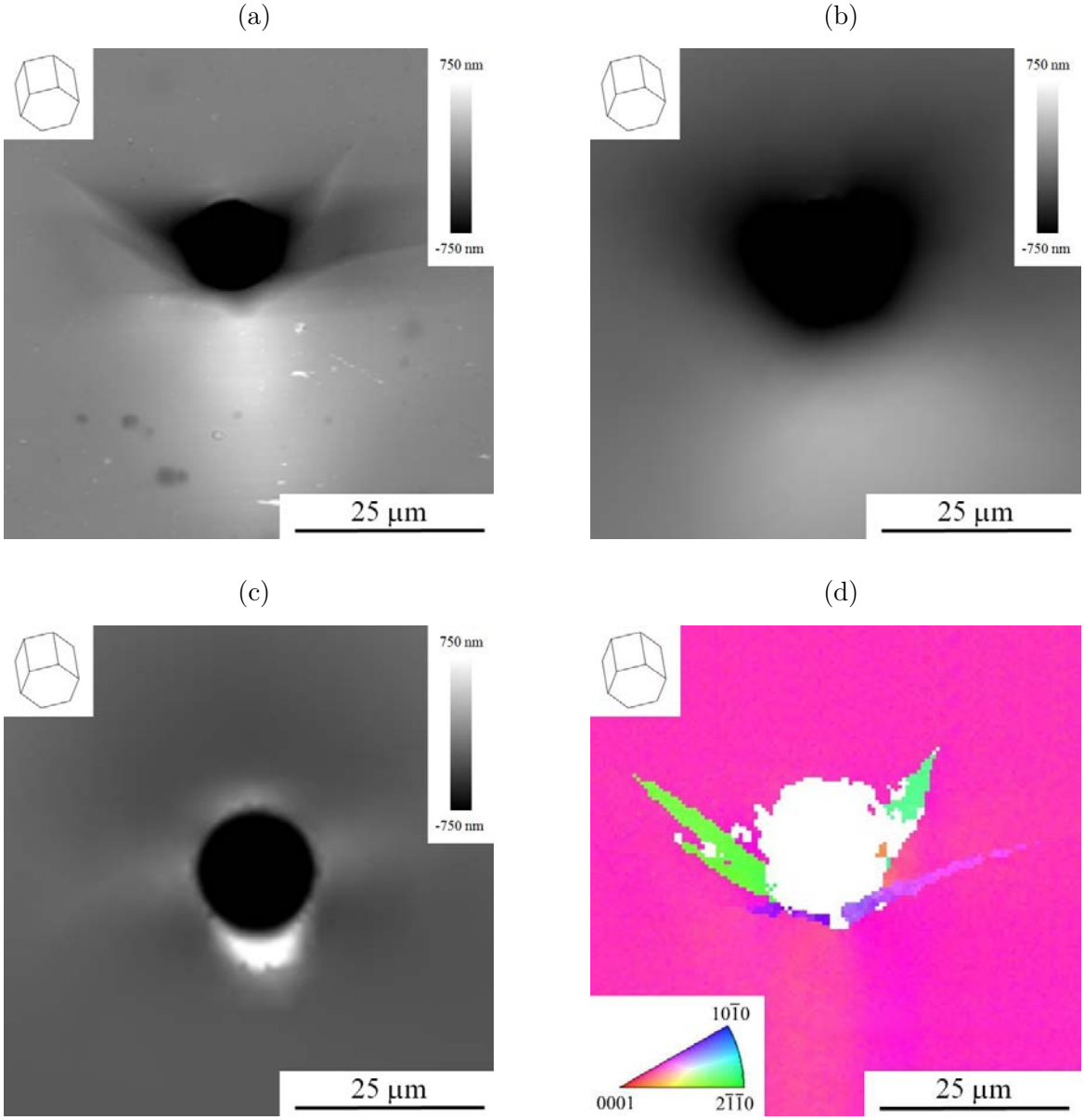

Fig. 5.3: Indentation performed in Grain 6 with a maximum indentation depth of 4000 nm: (a) AFM topography; (b) topography reproduced by CPFE simulation including twinning; (c) topography reproduced by CPFE simulation suppressing twinning; (d) EBSD inverse pole figure map in a direction parallel to the indentation axis.

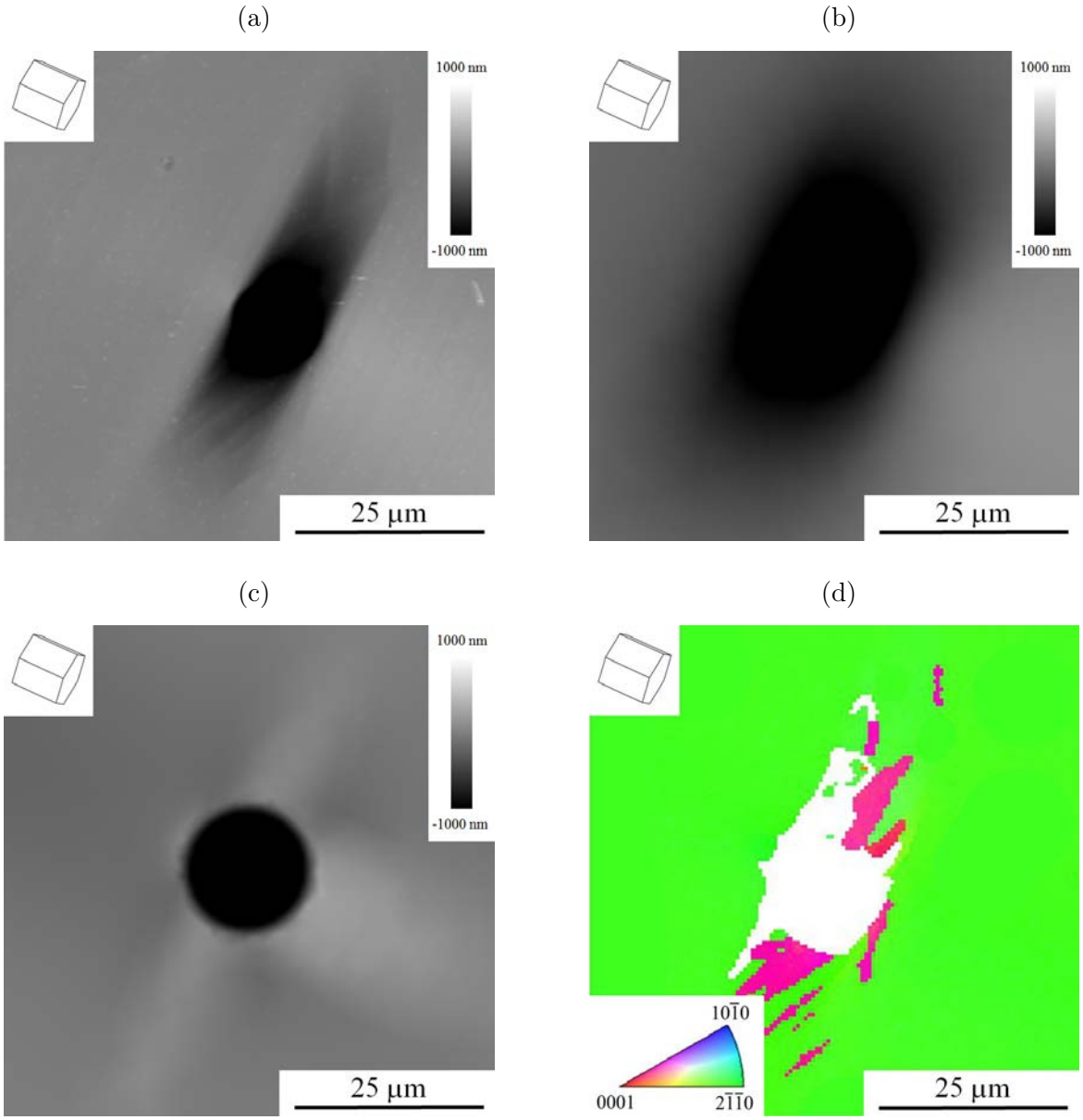

Fig. 5.4: Indentation performed in Grain 5 with a maximum indentation depth of 4000 nm: (a) AFM topography; (b) topography reproduced by CPFE simulation including twinning; (c) topography reproduced by CPFE simulation suppressing twinning; (d) EBSD inverse pole figure map in a direction parallel to the indentation axis.

Fig. 5.5a shows the AFM topographies corresponding to the 4000 nm depth indents performed in Grains (Gr.) 1-7 indicated in Fig. 5.1. All the AFM images are located inside an inverse pole figure according to the crystallographic orientation of the indented plane and are rotated following the convention defined by Zambaldi and Raabe [57]. Fig. 5.5b depicts the deformation patterns predicted by the simulations for each indent shown in Fig. 5.5a. These simulations were performed using Model 2 (Section 5.3) and allowing for twinning in the model. As it can be seen, there is a reasonable qualitative agreement between the experimental results (5.5a) and the simulations (5.5b), illustrating that CPFE models are

able to reproduce the deformation profiles of large indents performed in pure Mg at RT.

(a)

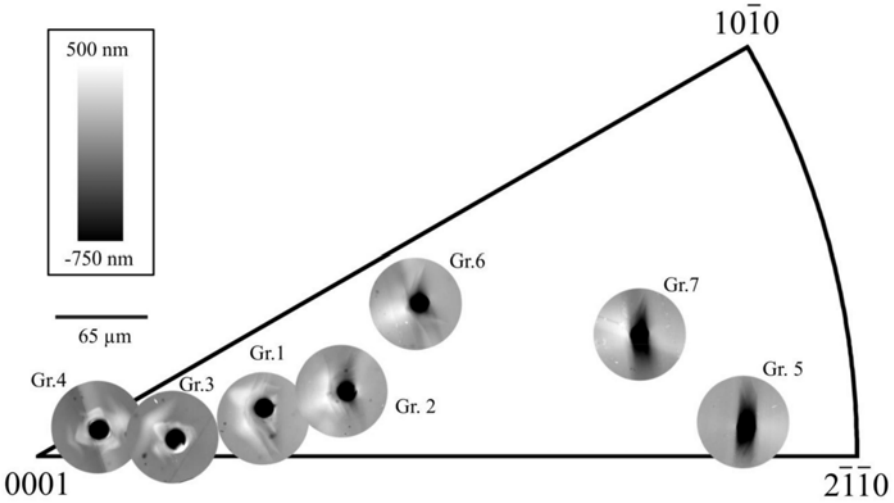

(b)

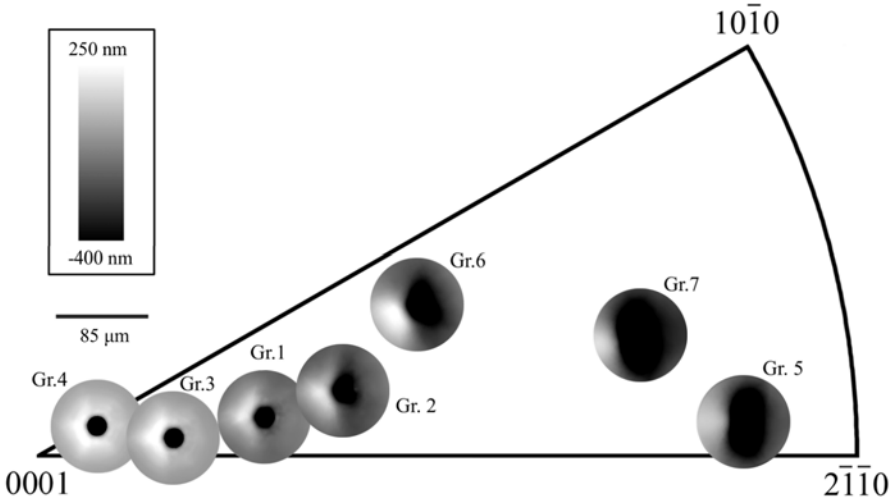

Fig. 5.5: (a) Inverse pole figure of the AFM topographies corresponding to the 4000 nm depth indents performed in Grains (Gr.) 1-7 indicated in Fig. 5.1; (b) deformation patterns predicted by the simulations of every indent shown in (a).

Based on these results, it can be concluded that the pile-up/sink-in patterns around large indents (h_{max} = 4000 nm) performed in pure Mg single crystals are clearly determined by the activation and propagation of TT_s. This can be rationalized taking into account the locations of the zones prone to twinning during and indentation as a function of the crystallographic orientation (Fig. 5.6). In particular, three different ranges of declination angles can be established:

- *Low declination angles* ($\delta < 30$ °): In this case, the twin-favourable zone is located at the sides of the indent. With this configuration, the extension along the c-axis related

with tensile twinning introduces a particular pile-up profile (Fig. 5.6a), which is in agreement with Fig. 5.2a. This behaviour corresponds to Grain 1, Grain 3 and Grain 4 of the present study (Fig. 5.5).

- *High declination angles* ($\delta > 60$ °): In this case, the zone prone to twinning is placed underneath the indent, in such a way that an elongation along the c-axis promotes a two-fold sink-in profile aligned with the basal planes (Fig. 5.6c). This behaviour can be seen in Grain 5 (Fig. 5.4a) and Grain 7 (Fig. 5.5).

- *Medium declination angles* ($30° < \delta < 60°$): On this occasion, only the compression forces that form $\sim 45°$ with the indentation axis, and, at the same time, mean a contraction along the direction perpendicular to the c-axis, are able to induce TT_s. As it can be observed in Fig. 5.6b, the zones that fulfil both conditions, i.e., the twin favourable areas, are not symmetrically distributed under the indent, which differs from the two other cases (Figs. 5.6a and 5.6c). In this instance, the deformation patterns developed in this range of declination angles can be understood as a mixture between the two extreme configurations ($\delta < 30°$ and $\delta > 60°$). On the one hand, the extension nature of twinning ($\delta < 30°$) causes a distinctive pile-up aligned with the ascending direction of the c-axis (Fig. 5.6b). In addition, according to Fig. 5.3b, basal slip also secondary contributes to the formation of this pile-up, as the stress state developed in this region also favours the activation of this deformation mechanism as shown in the CPFE simulations. At the same time, the contraction feature of twinning ($\delta > 60°$, in the direction perpendicular to the c-axis) induces slight sink-in profiles aligned with the basal planes (Fig. 5.6b). These specific deformation patterns can be clearly observed in Grain 6 (Fig. 5.3a), as well as in Grain 2 (Fig. 5.5)

In summary, the above results corroborate that the activation and propagation of TT_s govern the deformation pattern around indentations at relatively high h_{max} in pure Mg single crystals at RT.

(a)

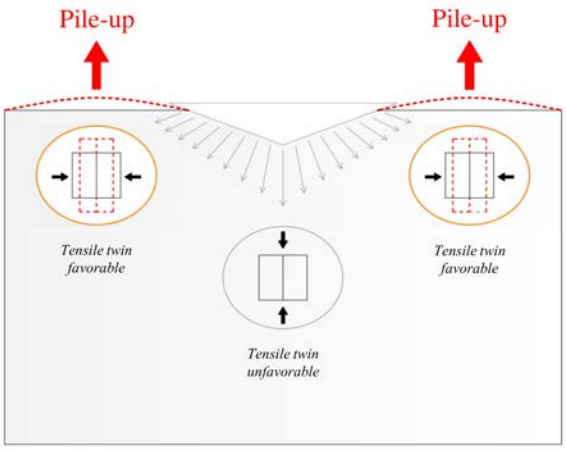

(b)

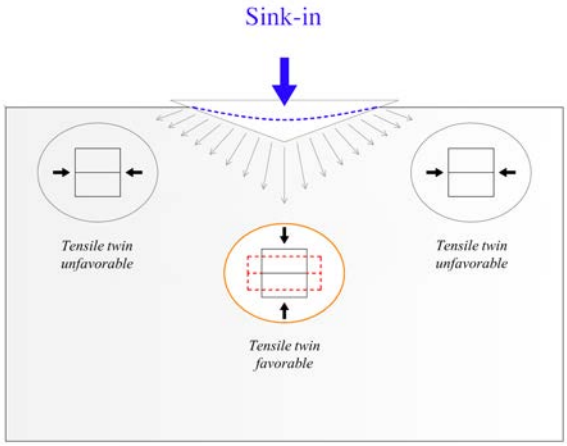

(c)

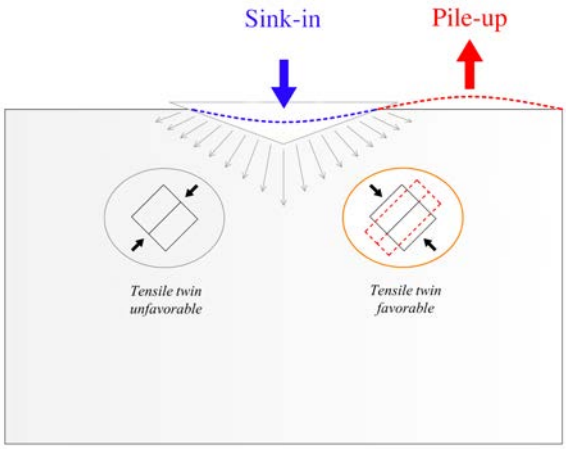

Fig. 5.6: Schematic representation of the zones prone to twinning during an indentation as a function of the crystallographic orientation of the indented plane: (a) low declination angle; (b) high declination angle; (c) medium declination angle. Black arrows indicate schematically the main component of the stress tensor in different areas surrounding the indent.

5.4.2 Evolution of the deformation profiles with decreasing indentation depth

In the absence of any size effect, the deformation pattern around an indent for a self-similar indenter should scale with the indentation depth in such a way that the ratio between the projected pile-up area and the projected residual imprint area (Pile-up/Ap ratio) remains constant. The same reasoning is applicable to the sink-in profile, i.e., the Sink-in/Ap ratio should be the same for all indentation depths. Fig. 5.7a depicts the variation of the Pile-up/Ap ratio for Grain 1 as a function of h_{max}. It can be clearly seen that this ratio increases dramatically with the indentation depth, revealing the presence of a strong ISE. The variation of the Sink-in/Ap ratio with h_{max} in Grain 5 exhibits a very similar trend, as illustrated in Fig. 5.7b and, thus, further confirms the presence of an ISE. This ISE is likely related to variations in the twinning activity with increasing h_{max} since, as shown in Section 5.4.1, the deformation patterns around an indent are clearly determined by this deformation mode. This is confirmed by Fig. 5.8, which reveals that the variation with the h_{max} of the ratio between the projected twinned surface (Tw) and the projected imprint area (Ap) is comparable to that exhibited by the Pile-up/Ap ratio (Fig. 5.7a). This study was not performed in Grain 5 because, since the twinned areas are preferentially located underneath the indentation at high declination angles (Fig. 5.6), the Tw/Ap ratio may not be very representative of the twin activity.

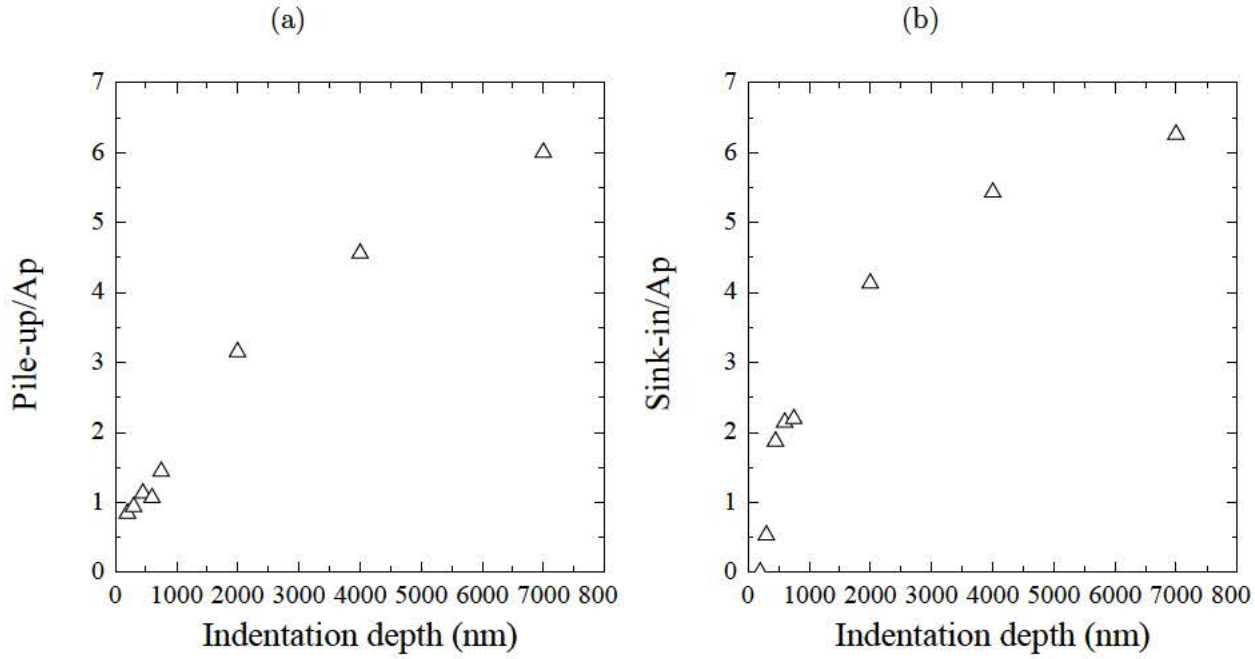

Fig. 5.7: (a) Evolution of the Pile-up/Ap ratio for Grain 1 as a function of the indentation depth. (b) Evolution of the Sink-in/Ap ratio for Grain 5 as a function of the indentation depth.

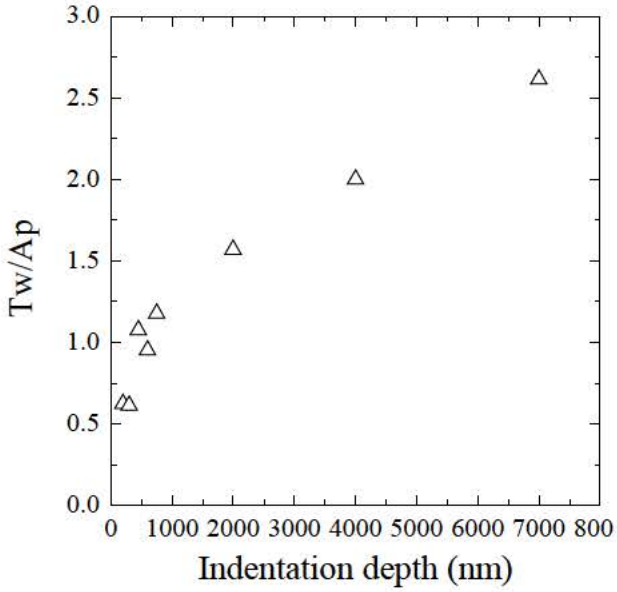

Fig. 5.8: Evolution of the Tw/Ap ratio for Grain 1 as a function of the indentation depth.

5.4.3 Twin evolution at low declination angles as a function of the indentation depth

In order to evaluate the influence of h_{max} on twin activity, the twinned surface patterns were examined by EBSD in Grains 3 ($\delta = 14.0°$) and 4 ($\delta = 6.9°$) for several indents of different sizes. These two grains were chosen because, since both have a very low δ, twinning takes place preferentially at the sides of the indent (Fig. 5.6a) and, thus, it is reasonable to assume that the surface twinned area, measured by 2D EBSD, provides a good approximation to the twin activity.

Fig. 5.9 shows the EBSD inverse pole figure maps in the direction parallel to the indentation axis and the AFM topography maps of several indents performed in Grain 3 at different indentation depths: 450, 600, 2000 and 4000 nm. As expected, the relative twinned area increases as the h_{max} increases. Furthermore, no evidence of twin activity could be found in the 450 nm deep indent (Fig. 5.9a (left)), suggesting that there is a critical size below which twinning is suppressed. Further proof of the absence of twinning at the smallest indentation depth was obtained by analysing the topography of the free area around the four indents under analysis since, as described in Sections 5.4.1 and 5.4.2, twinning activity was strongly linked to the pile-up pattern obtained for this crystallographic orientation. Fig. 5.9 confirms that, while clear pile-up patterns are apparent around the 600 nm (Fig. 5.9b (right)), 2000 nm (Fig. 5.9c (right)) and 4000 nm (Fig. 5.9d (right)) deep indents, the deformation of the free surface around the 450 nm deep indent (Fig. 5.9a (right)) is almost negligible. It should be mentioned that the absence of pile-up in basal grains at very small indentation depths has been already shown by Selvarajou et al. [61]. However, they did not perform an in-depth analysis of this issue. Finally, Fig. 5.9 reveals that the number of TT_s increases with the indentation depth. While only two twins can be distinguished in the vicinity of the

600 and 2000 nm depth indents (Figs. 5.9b (left) and 5.9c (left)), four different twins are apparent around the 4000 nm depth indent (5.9d (left)). The Euler angles and the active twin variant of each twin are listed in Table 5.2. The active twin variants were obtained using the minimum deviation angle approach [138].

The simulation of the 4000 nm deep indent performed in Grain 3 was carried out using Model 2 (Section 5.3) and the appropriate Euler angles. Fig. 5.10 depicts the twins predicted by the simulation, in which the distinct active twin variants are shown in different colours. There is a fair qualitative agreement between the experimental large indent (5.9d (left)) and the simulated (Fig. 5.10) data. Twins 1, 2, 3, 4 of Fig. 5.9d (left) are clearly reproduced in the simulation (Fig. 5.10). Please note the agreement not only in the location of the twins, but also in the active twin variant. On the other hand, Twins Sim* and Sim**, predicted in the simulations (Fig. 5.10), are not observed experimentally. The possible reasons for this will be discussed in Section 5.5.3.

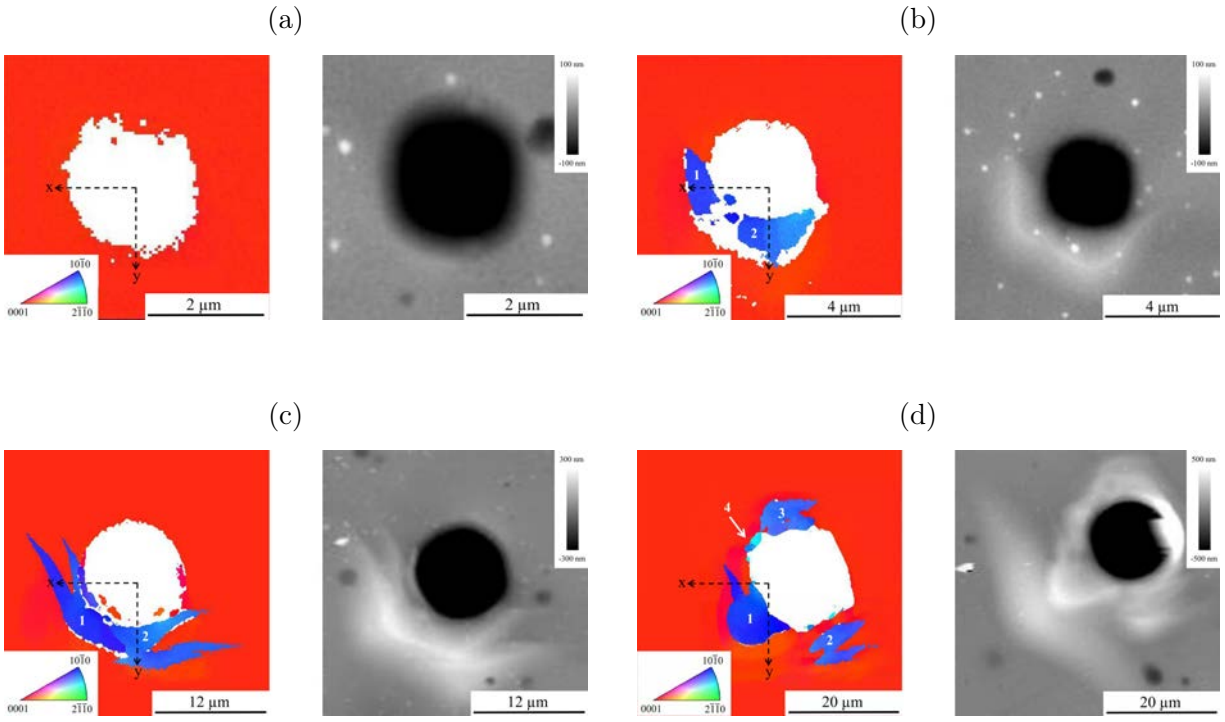

Fig. 5.9: EBSD inverse pole figure maps in the direction parallel to the indentation axis (left) and AFM topography maps illustrating the free surface around several indents (right) performed in Grain 3 ($\delta = 14.0°$) at different maximum indentation depths: (a) 450 nm; (b) 600 nm; (c) 2000 nm; (d) 4000 nm.

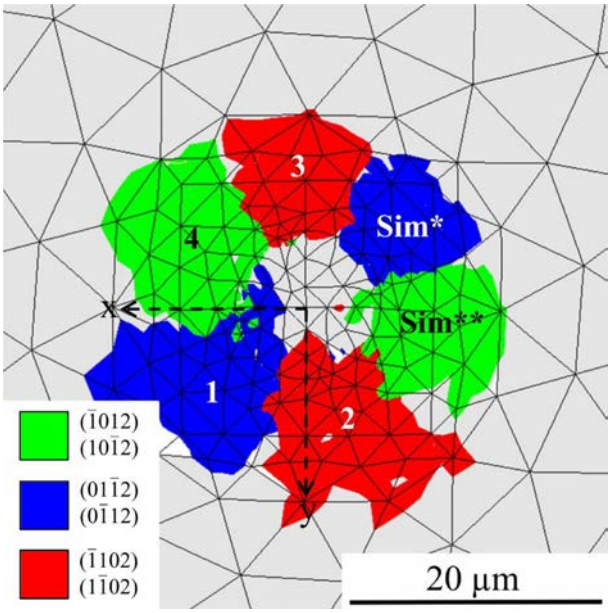

Fig. 5.10: Active twins predicted by simulation of the 4000 nm depth indent performed in Grain 3.

	Grain 3	Twin	Euler angles $(\varphi_1, \Phi, \varphi_2)$	Active twin variant
h_{max}	750 nm	Twin 1	131.6; 97.2; 26.8	$(0\bar{1}12)\ [01\bar{1}1]$
		Twin 2	8.3; 84.2; 23.2	$(1\bar{1}02)\ [\bar{1}101]$
	2000 nm	Twin 1	126.5; 98.3; 22.9	$(0\bar{1}12)\ [01\bar{1}1]$
		Twin 2	13.4; 80.4; 22.6	$(1\bar{1}02)\ [\bar{1}101]$
	4000 nm	Twin 1	129.8; 96.7; 25.2	$(0\bar{1}12)\ [01\bar{1}1]$
		Twin 2	66.7; 92.6; 15.3	$(1\bar{1}02)\ [\bar{1}101]$
		Twin 3	12.4; 80.9; 20.9	$(1\bar{1}02)\ [\bar{1}101]$
		Twin 4	140.5; 81.6; 20.7	$(10\bar{1}2)\ [\bar{1}011]$

Table 5.2: Euler angles and active twin variants corresponding to the TT_s present in the vicinity of indentations of different depths in Grain 3 (Fig. 5.9).

A similar study was carried out in Grain 4. Fig. 5.11 consists of several EBSD inverse pole figure maps in a direction parallel to the indentation axis illustrating the free surface around indents performed in Grain 4 at indentation depths of 750 nm (Fig. 5.11a), 2000 nm (Fig. 5.11b) and 4000 nm (Fig. 5.11c). In this case, twin activity appears to be suppressed at indentation depths as high as 750 nm (Fig. 5.11a). Again, the number of TT_s increases as the indentation depth increases (Figs. 5.11b and 5.11c). In particular, only two TT_s can be distinguished in the vicinity of the 2000 nm indent, while up to seven TT_s are visible around the 4000 nm indent. The Euler angles and the active twin variant of all these twins are summarised in Table 5.3.

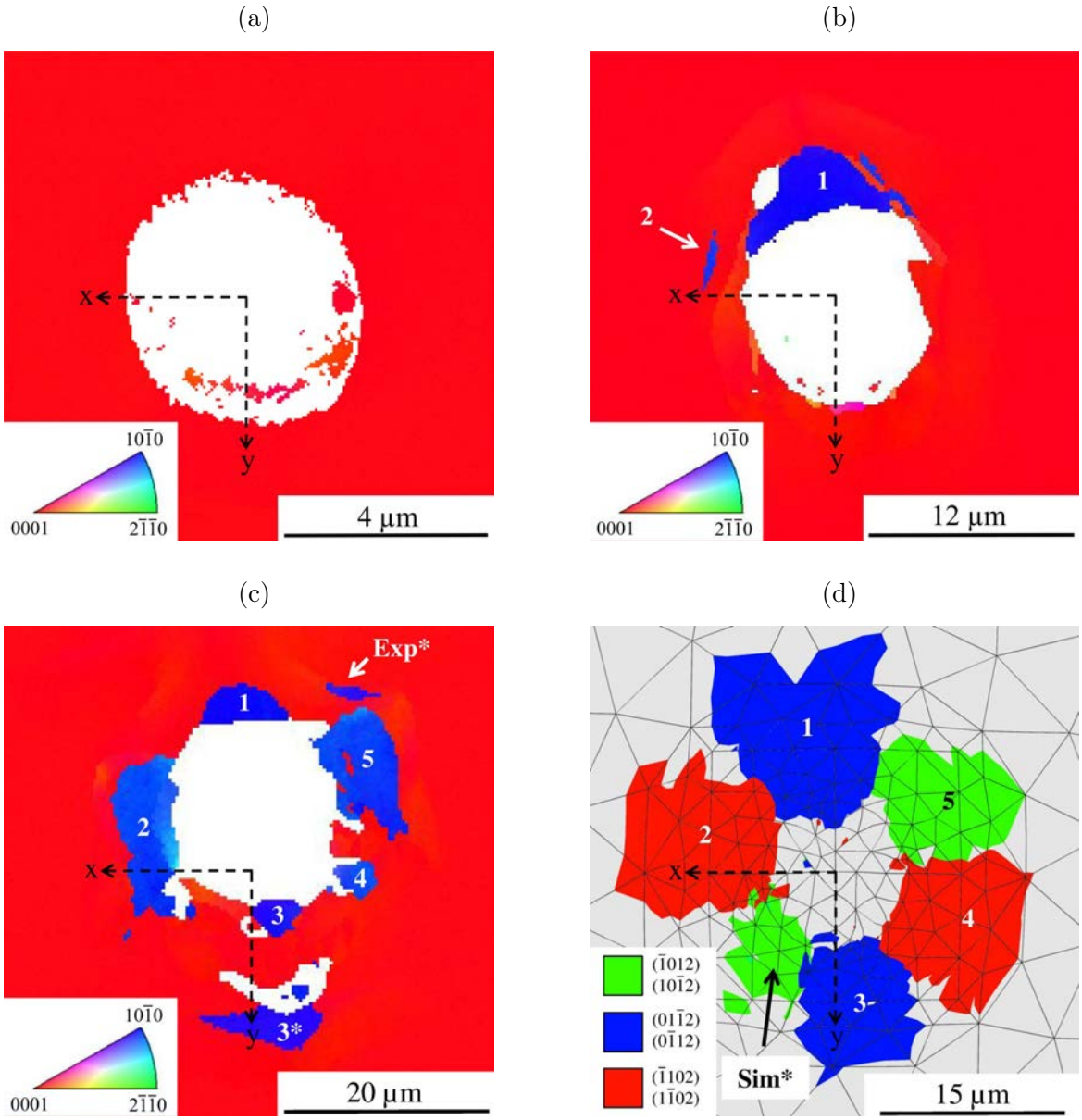

Fig. 5.11: EBSD inverse pole figure maps in a direction parallel to the indentation axis illustrating the free surface around the indents performed in Grain 4 ($\delta = 6.9°$) at different indentation depths: (a) 750 nm; (b) 2000 nm; (c) 4000 nm. (d) Active twins predicted by simulation of the 4000 nm depth indent performed in Grain 4.

5.4.4 Twin evolution at high declination angles as a function of the indentation depth

Fig. 5.12 consists of two EBSD inverse pole figure maps in a direction perpendicular to the indentation axis illustrating the cross section of two indents performed in Grain 8 ($\delta = 80.1°$): a 450 nm depth indent (Fig. 5.12a) and a Vickers microindentation (Fig. 5.12b). Due to the high declination angle of the grain, a sink-in profile was formed around both indents,

	Grain 4	Twin	Euler angles $(\varphi_1, \Phi, \varphi_2)$	Active twin variant
h_{max}	2000 nm	Twin 1	12.1; 95.3; 30.4	$(0\bar{1}12)\ [01\bar{1}1]$
		Twin 2	73.8; 94.5; 34.7	$(\bar{1}102)\ [1\bar{1}01]$
	4000 nm	Twin 1	10.8; 92.2; 31.3	$(0\bar{1}12)\ [01\bar{1}1]$
		Twin 2	74.2; 90.4; 36.5	$(1\bar{1}02)\ [\bar{1}101]$
		Twin 3	10.7; 98.9; 31.6	$(01\bar{1}2)\ [0\bar{1}11]$
		Twin 3*	9.9; 98.0; 31.8	$(01\bar{1}2)\ [0\bar{1}11]$
		Twin 4	74.2; 92.4; 37.2	$(\bar{1}102)\ [1\bar{1}01]$
		Twin 5	128.6; 88.4; 35.9	$(\bar{1}012)\ [10\bar{1}1]$
		Twin Exp*	9.0; 100.2; 31.0	$(01\bar{1}2)\ [0\bar{1}11]$

Table 5.3: Euler angles and active twin variants corresponding to the twins present in the vicinity of indentations of different depths in Grain 4 (Fig. 5.11).

in agreement with Section 5.4.1. In both cases, the cross section plane was parallel to the sink-in direction and passed through the middle of the indentation. It can be clearly seen that only one TT_s is activated bellow the small indent (Fig. 5.12a) while up to 7 different twins are observed underneath the large Vickers microindentation (Fig. 5.12a). The Euler angles and the active twin variants of all the twins analysed are listed in Table 5.4. In agreement with Section 5.4.4, more twin variants are activated as h_{max} increases. In addition to the $(0\bar{1}12)[01\bar{1}1]$ twin variant, which is activated in both Fig. 5.12a (Twin 1) and Fig. 5.12b (Twin 1, Twin 2 and Twin 3), other active twin variants can be observed in the Vickers microindentation (Fig. 5.12b), as shown in Table 5.4. Whereas Twin 4, Twin 5 and Twin 6 belong to the $(10\bar{1}2)[\bar{1}011]$ twin variant, Twin 7 corresponds to the $(\bar{1}102)[1\bar{1}01]$ twin mode (Table 5.4). Moreover, the relative size of the twinned zone is clearly a function of the h_{max}. While in the small indent the width of the twinned area and that of the residual imprint are comparable, the Vickers microindentation induces TT_s that are significantly larger than the residual imprint. Furthermore, this cross section analysis provides further evidence that the sink-in patterns observed around the indents are directly related to the nucleation and propagation of TT_s. In agreement with the results presented in previous sections, it is shown here that the relative activity of twinning underneath the indentations in grains with very high declination angles increases strongly with the indentation size.

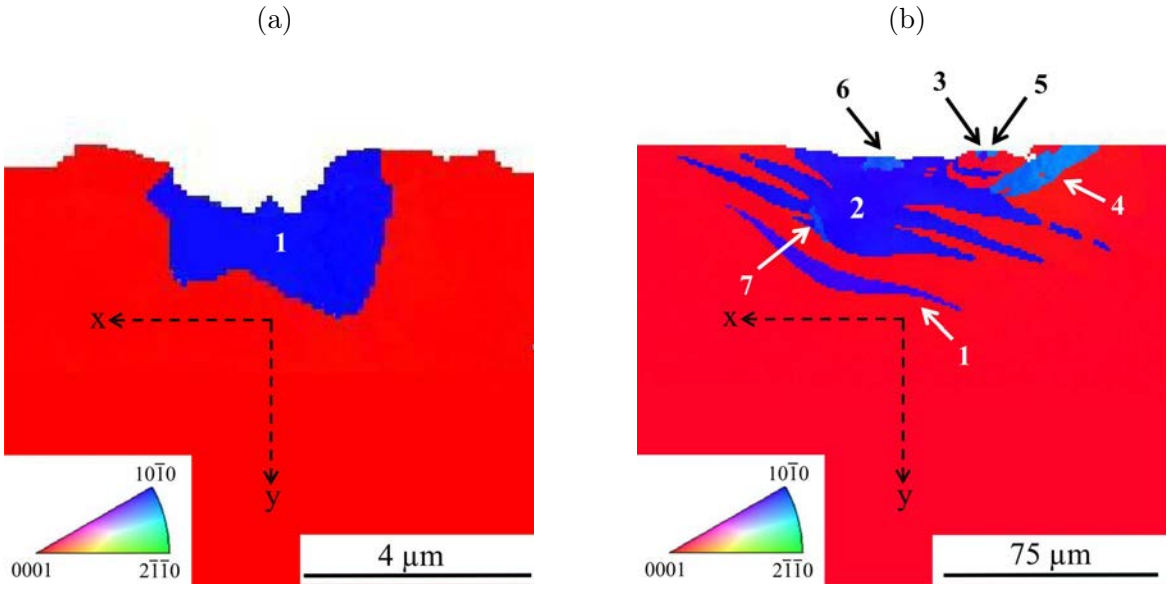

Fig. 5.12: EBSD inverse pole figure maps in a direction parallel to the indentation axis illustrating the cross section of two indentations performed in Grain 8 at different indentation depths: (a) 450 nm; (b) Vickers microindentation.

	Grain 8	Twin	Euler angles $(\varphi_1, \Phi, \varphi_2)$	Active twin variant
h_{max}	450 nm	Twin 1	150.9; 88.6; 29.1	$(0\bar{1}12)\,[01\bar{1}1]$
	$\backsim$ 11 μm	Twin 1	160.4; 76.1; 30.3	$(0\bar{1}12)\,[01\bar{1}1]$
		Twin 2	161.1; 80.7; 30.0	$(0\bar{1}12)\,[01\bar{1}1]$
		Twin 3	161.9; 78.7; 28.6	$(0\bar{1}12)\,[01\bar{1}1]$
		Twin 4	40.7; 90.3; 39.2	$(10\bar{1}2)\,[\bar{1}011]$
		Twin 5	40.8; 94.1; 39.9	$(10\bar{1}2)\,[\bar{1}011]$
		Twin 6	34.7; 93.8; 36.9	$(10\bar{1}2)\,[\bar{1}011]$
		Twin 7	100.1; 87.7; 36.6	$(\bar{1}102)\,[1\bar{1}01]$

Table 5.4: Euler angles and active twin variants corresponding to the twins present in the vicinity of indentations of different depths in Grain 8 (Fig. 5.12).

5.4.5 Effect of indentation depth on the hardness-declination angle curve

In previous sections it has been shown that during single crystal indentation tests performed in pure Mg single crystals, the twin activity dramatically depends on the indentation size. The question that arises, however, is whether the onset of twinning activity when the indentation depth is larger than the corresponding critical value influences the hardness of the Mg grains as a function of their crystallographic orientation. In order to elucidate this effect, we studied the indentation response evolution with grain orientation, measured by

the declination angle δ, as defined in Section 5.4.1, both experimentally and numerically. Experimentally, the impact of twinning activity was assessed by comparing the change of indentation response with grain orientation for very shallow indents, 300 nm deep, with that of very deep indents, 2000 nm deep, for which substantial twinning activity was found. Numerically, the indentation response was simulated using Model 1 (Section 5.3, h_{max} = 300 nm), suppressing and allowing for twinning, respectively. To avoid possible issues related to the application of the Oliver and Pharr method [139] in materials that display high pile-up patterns during and indentation, the maximum load reached during the indentations (P_{max}), instead of the hardness, was compared in each case. To decouple indentation size effects from pure crystallographic orientation effects, the P_{max} was normalised with respect to that in the basal orientation ($\delta = 0°$). Fig. 5.13a compares de experimental P_{max} - δ curves corresponding to the shallow indents (300 nm deep) with the simulations where twinning activity was inhibited. The agreement is remarkable, indicating that the indentation response variation with grain orientation for very shallow indents is determined by the relatively activity of the different slip systems. At larger indentation depths (2000 nm deep), however, Fig. 5.13b shows that the normalized P_{max} decreases more steeply with δ, reaching lower values at high declination angles that can only be predicted when twinning is accounted for in the model. Interestingly, twin activity, although present to accommodate the deformation imposed by the indenter in all cases for large indents, gives rise to a noticeable effect on P_{max} only for δ larger than 30°. This behaviour can be rationalized taking into account that, even though tensile twinning is one of the softest deformation mechanisms in pure Mg, its SF with respect to the indentation direction increases with δ, so that the effect of twinning on indentation response becomes predominant for large declination angles only. On the contrary, for low declination angles, twinning serves as a secondary mechanism to accommodate the displaced volume around the indent, giving rise to large pile ups observed, but less influence on the hardness of the Mg grain.

5.5 Discussion

Our results reveal that twinning is suppressed in grains with low declination angles at indentation depths smaller than a critical value that is a function of orientation. Since for self-similar indenters different indentation depths induce an equivalent stress state, the fact that a minimum indentation depth is necessary to activate twinning indicates the existence of a minimum activation volume for twinning, as suggested by others [28, 29, 33]. Several questions arise: Is the activation of twinning detectable in the indentation curve? Can the process of twin activation be decoupled from the propagation process? And therefore, can these observations provide experimental evidences that support the energetic nature of the twin activation process? In the following sections, we discuss these issues by a careful analysis of the indentation curves and the process of twin formation.

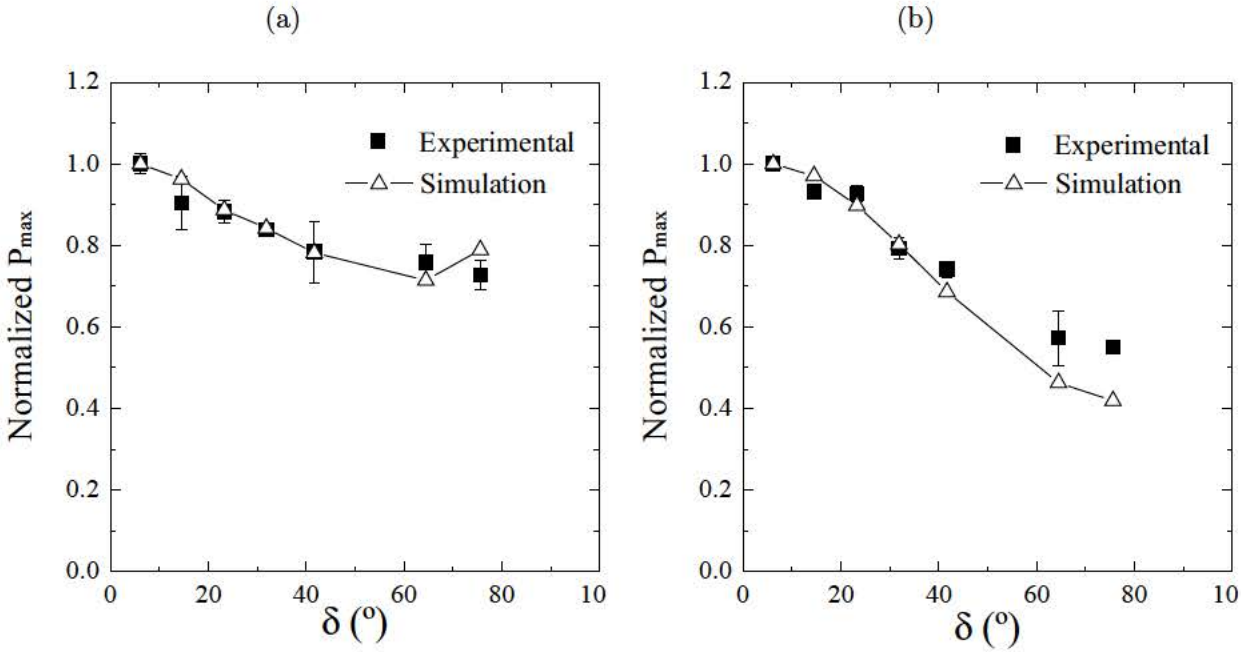

Fig. 5.13: Comparison between the simulated and experimental P_{max} - δ curves at different indentation depths: (a) 300 nm, twinning inhibited in the model; (b) 2000 nm, twinning accounted for in the model.

5.5.1 Is the activation of twinning detectable in the indentation curve?

The study of the indentation response of grains with low declination angles seems to indicate that this is the case. As illustrated in Fig. 5.9, in Grain 3, no twinning activity was detected around the 450 nm deep indent (Fig. 5.9a (left)) while two different twins are clearly apparent in the vicinity of the 600 nm depth indent (Fig. 5.9b (left)). It follows from these observations that the activation of twinning should take place at an indentation depth comprised between 450 and 600 nm. Fig. 5.14 compares the experimental load-displacement curve corresponding to the 600 nm deep indent (Curve 1) with a second curve that would correspond to an indentation of the same depth but in which twinning would be suppressed (Curve 2). Calculation of Curve 2 was carried out by fitting the data points of Curve 1 corresponding to indentation depths smaller than 450 nm to a power law and then, extrapolation of this law to the full range of indentation depths. A note should be made here that Curve 2 is almost identical to the experimental load-displacement curve corresponding to the 600 nm deep indent performed in Grain 4, in which twinning was not activated. This is in agreement with our simulations, which show that, in the absence of twinning, Grain 3 and Grain 4 should display the same mechanical response under indentation. Comparison of Curves 1 and 2 (Fig. 5.14) indicates that they depart at an indentation depth of $\approx$ 479 nm (highlighted in Fig. 5.14 using a blue arrow), suggestion this is the critical depth at which activation of twinning took place in this particular orientation.

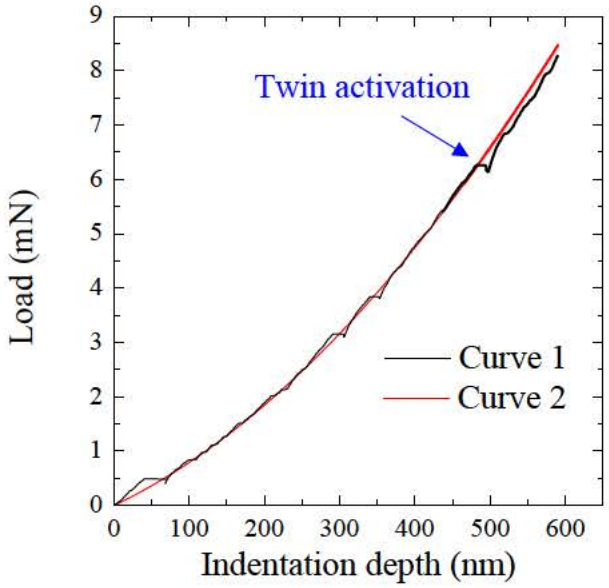

Fig. 5.14: Curve 1: experimental load-displacement curve corresponding to the 600 nm depth indentations performed in Grain 3; Curve 2: simulation of the Curve 1 suppressing twin activation.

5.5.2 Can the process of twin activation be decoupled from the propagation process?

The question that follows is whether the twinned areas in Fig. 5.9b (left) form suddenly during the pop-in event of Fig. 5.14 or whether the initial twin is created and then grows as the indentation depth increases. To address this issue, a careful analysis of the material displaced during the pop-in is made below. First, Twin 2 in Fig. 5.9b (left) correspond to the $(0\bar{1}02)[\bar{1}101]$ variant, whose unit vector in the twin direction projected in the global reference system is [-0.1170, 0.5286, 0.8408]. As the total length of Twin 2 in the y direction is 1.5 μm and tensile twinning has an associated constant shear (γ) of 0.1289 along the twin direction, the total displacement of the material caused by Twin 2 in the y direction, D_y, can be calculated using the following expression:

$$D_y = L_{y,f} - L_{y,0} = L_{y,f}\left(1 - \frac{1}{1+\varepsilon_{y,tw}}\right) \tag{5.1}$$

where $L_{y,f}$ is the final length of Twin 2 in the y direction, $L_{y,0}$ is the initial length of the area that was transformed into Twin 2 and $\varepsilon_{y,tw}$ is the projection of the y axis of the associated shear. In this particular case, D_y is equal to -111 nm, where the negative sign corresponds to a contraction along the y axis. On the other hand, as shown in Fig. 5.15, the vertical offset of the indenter during the pop-in even (dz) would imply a total radial

displacement of the material in contact with the indenter, d_r equal to:

$$d_r = 2 * d_z * tan(\theta) \tag{5.2}$$

where θ is the apex angle of the indenter. Considering the magnitude of the pop-in (dz = 16.3 nm) and the apex angle of the indenter used (70°), a total radial displacement, d_r, of 88.8 nm is obtained, in close agreement with the total displacement of material caused by Twin 2, $|D_y|$ = 111 nm, estimated above. It can be concluded, therefore, that a large fraction of Twin 2 is spontaneously formed at the pop-in observed at the onset of twinning. This is in agreement with the fact that Curve 1 and Curve 2 (Fig. 5.14) are almost parallel after the pop-in, as further twin propagation after this highly inelastic event would result in an increase in the off-set between both curves. It appears, therefore, that the size of the initial detectable twins is the order of micrometers, revealing a strong volume effect of the twin propagation process.

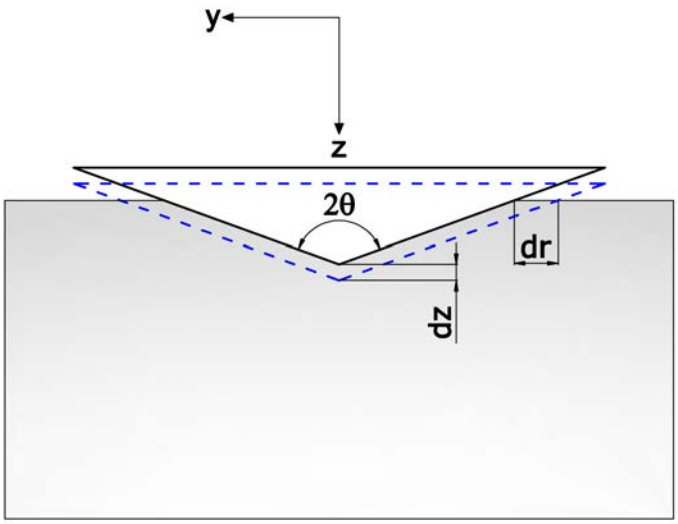

Fig. 5.15: Schematic representation of the material displaced during the pop-in event observed during a 600 nm depth indentation in Grain 3.

5.5.3 Energetic nature of the twin activation process

According to the previous analysis, in Grain 3, twinning is only activated when the indentation depth is larger than 479 nm. Since, neglecting the effect of geometrically necessary dislocations (GND_s), two indents carried out in the same grain at different indentation depths would induce an equivalent stress state, the fact that a minimum indentation depth is necessary to activate twinning suggests that the volume of the material affected by the indentation plays a key role in this phenomenon. Moreover, if the nucleation process would be driven only by the stress sate of single point, independently of the surrounding material,

the high stress developed at very small indentations due to the effect of the GND_s would facilitate twinning. However, here the opposite effect is observed. Twin activation is a quite complex process ant may involve different states itself. For example, Yu et al. [30] suggested that the formation of a macroscopic twin is the result of several nanotwins merged together. On the other hand, Kim et al. [140] reported that, once a twin embryo is nucleated, a slow growth phase takes place prior the massive twin propagation process. In this research, only the formation of macroscopic twins, i.e., the "massive" twin activation phenomenon, is studied. Although the formation of nanotwins cannot be ruled out even at very small indentations, its effect in the accommodation of plastic strains is negligible. Therefore, the nucleation of twin embryos, which is thought to take place in the early stages of the twin activation process, is not analysed in this paper. For the sake of simplicity, it can be considered that win activation is a process that has to overcome an energy barrier E_{tw} and that can be thus expressed as:

$$V_{tw} * \sigma_{tw} \geqslant E_{tw} \tag{5.3}$$

which indicates that, in order for twin activation to occur, a volume V_{tw} must be subjected to a stress σ_{tw}. At very small indentation depths and certain crystallographic orientations (low δ), is is likely that the value of $V_{tw} * \sigma_{tw}$ is not larger than E_{tw}. A close analysis of the twin evolution in Grains 3 and 4 as a function of the indentation depth further confirms this hypothesis. Fig. 5.11d shows the simulated twins around the 4000 nm depth indent performed in Grain 4. In particular, simulations predict that the largest twin areas correspond to Twins 1 and 2 twins that should, therefore, be easiest to activate. Following the energetic criterion of Eq. 5.3, this result could imply that these two twins should be the ones that activate at smaller indentation depths. Indeed, Twins 1 and 2 are already visible in Grain 4 at an indentation depth of 2000 nm (Fig. 5.11b). Simulations also suggest that Twin Sim* should be the most difficult to activate, as it has the smallest area (Fig. 5.11d). In fact, Fig. 5.11c shows that this is particular twin is the only one that is not active at a depth of 4000 nm depth in the same grain. As the indentation depth increases, the activation criterion is fulfilled in more volumes and, therefore, more twins are activated. A very similar behaviour can be observed in Grain 3. According to Fig. 5.10, Twins 1 and 2 should be the ones that are activated at smaller indentation depths. This is confirmed experimentally by Figs. 5.9b (left) and 5.9c (left). On the other hand, Twins Sim* and Sim**, predicted in the simulations, should demand the highest indentation depth to be activated. Actually, theses twins are the only ones not observed in the 4000 nm depth indent (5.9d (left)).

Finally, it should be mentioned that a quantitative estimation of the criterion proposed in Eq. 5.3 was not possible. To do so, a complete characterisation of the three dimensional shape of the twins is needed. Moreover, the possible effects of strain gradients. i.e., GND_s, are difficult to interpret and make this analysis even more complex. Therefore, this objective will be studied in future works making use of other more suitable micromechanical techniques, like micropillar compression, where the applied stress is uniaxial, and therefore, free of strain gradient effects.

5.6 Conclusions

In this chapter, a combined approach including instrumented nanoindentation and CPFE modelling was used in order to study the effect of the crystallographic orientation of the indented plane and the indentation size on the activation of the different deformation modes of Mg, specially tensile twinning. The following conclusions can be drawn form the present study:

1. At large indentation depths, the deformation patterns induced on the free surface in the vicinity of the indents are driven by the activation and propagation of tensile twinning. While at low declination angles the preferential activation activation of TT_s at both sides of the indent leads to the formation of clear pile-up profiles, a characteristic sink-in deformation is found in highly prismatic grains, where twinning is favoured underneath the indentations. On the other hand, a mixture between these two behaviours is observed at intermediate orientations. These observations are supported by CPFE simulations, which are able not only to reproduce the location of the TT_s, but also their effect on the residual topography around the indents.

2. Tensile twinning is subjected to strong indentation size effects. In particular, the relative twinning activity is enhanced at large indentation depths and the ratio between the projected twinned area and the projected imprint area (Tw/Ap) increases dramatically as the indentation depth increases. Moreover, more TT_s are activated as the indentation size increases.

3. Tensile twinning is suppressed in grains with low declination angles at indentation depths smaller than a critical value that is a function of the orientation. This can be rationalised by considering that twin activation requires a concentration of high stresses in a certain activation volume. In fact, this hypothesis together with the output of CPFE simulations justifies the higher number of TT_s activated as the indentation depth increases.

4. Tensile twin activity has a strong influence on the P_{max} - δ curves, leading to a steep decrease in the hardness at large declination angles, an effect that is confirmed by CPFE simulations.

"Nothing in life is to be feared, it is only to be understood. Now is the time to understand more, so that we may fear less"

Marie Curie

6

Practical methodology to estimate the critical resolved shear stresses of Mg alloys by nanoindentation

6.1 Introduction

Based on the results obtained in the previous chapter, a practical methodology to measure the $CRSS_s$ of Mg and its alloys is developed here.

This methodology was aimed to be used in conventional Mg alloys, which introduced some peculiarities in the analysis. First, the grain size of wrought Mg alloys can be as small as 10 μm, which reduces the size of the indent that can be performed in an isolated grain avoiding grain boundary effects to 300 nm. Under these conditions, as shown in the previous chapter, tensile twinning is severely hindered, and therefore, this methodology is used only to study the slip activity. In addition, unlike in the previous chapter, where a sphero-conical indenter was used, here a conventional Berkovich tip was chosen for the analysis. This decision was made based on two main reasons: (i) this tip is much more common than the sphero-conical one among the scientific and industrial community, which will be a key factor

in the widespread application of this technique; and (ii), it is possible to easily calibrate the tip area function of a Berkovich probe, and therefore, the application of the Oliver and Pharr [115] method becomes straightforward. This allows to obtain "hardness - δ" (H - δ) curves instead of P_{max} - δ curves, which will facilitate the comparison of data between different researchers.

The proposed methodology, first validated in pure Mg, was then used to asses the effect of alloying elements of the MN11 alloy. This alloy was chosen for the analysis because, as commented in Section 1.1, rare-earth Mg alloys show a much more isotropic mechanical behaviour in comparison with pure Mg or other Mg alloys, which made them promising candidates for the development of novel Mg alloys with better performance.

6.2 Experimental procedure

The materials studied in this section are the annealed rolled sheet of pure Mg and the extruded bar of the MN11 Mg alloy described in Section 3.1. Microstructure characterisation was evaluated by EBSD using the Helios NanoLab^{TM} DualBeam^{TM} 600i microscope equipped with an Oxford-HKL EBSD detector described in Section 3.3.2. EBSD maps were performed at 15 kV using a step size ranging between 1 μm (MN11 alloy) and 10 μm (pure Mg). The limits of the areas mapped by EBSD were marked by Vickers microindentations in order to identify them in the nanoindentation tests. Regarding the sample preparation for nanoindentation and EBSD examination, *Route A* and *Route B* processes (Section 3.2) were applied to the MN11 alloy and the pure Mg respectively.

Based on the EBSD maps, individual grains with different δ were indented in both materials using the the Hysitron TI 950 Triboindenter® system described in Section 3.4.5 equipped with a Berkovich tip. Grain boundary effects were avoided by placing the indents in the middle of the grains and by using an indentation depth as small as 300 nm. Indentations were carried out in displacement control mode using a trapezoidal loading curve, with a loading and unloading time of 5 s, and a 2 s holding time at maximum depth. Hardness values were computed from the loading-unloading curves by applying the Oliver and Pharr method [115].

6.3 Numerical simulations

The CP model described in Section 4.2.1 (CP model 1) was integrated into the FE commercial software ABAQUS [129] using a UMAT. A three-dimensional FE model of the indentation process was generated. The model comprises a total of 10671 C3D10M elements, using a refined mesh in the contact area. Individual grains were modeled as large cubes so that the stresses at the borders could be neglected. The nodes at the bottom of the model were fully constrained. A fully rigid conical indenter was used in the simulations. By inspection of the area function of the Berkovich tip used in the experiments, the apex angle of the conical tip utilized in the simulations was set to 71.2°. This slightly larger than the theoretical apex angle (70.3°) of the conical tip that matches the area function of an ideal

Berkovich tip, but ensures the one-to-one equivalence between the real indenter used in the experiments and the conical tip used in the simulations. The indenter was only allowed to move in the z direction. Since friction is known to play a minor role in the load vs. displacement response during indentation [141], frictionless contact was assumed between the rigid indenter and the material surface. The following single-crystal elastic constants for Mg were used in all the simulations: C_{11} = 59.4GPa, C_{12} = 25.6 GPa, C_{13} = 21.4 GPa, C_{33} = 61.4 GPa and C_{44} = 16.4 GPa [49]. Due to the relatively low content of alloying elements, it was assumed that the elastic constants of the MN11 alloy were similar to those of pure Mg. Regarding the CP parameters, a total of 24 slip systems were considered, dived into four families (basal, prismatic, pyramidal $\langle a \rangle$ and First-order pyramidal $\langle c+a \rangle$), as summarized in Table 6.1. No twinning was considered because, as justified in Section 6.4.3, the twin activity in such small indentations is negligible. For the sake of simplicity, the self-hardening and latent-hardening parameters, ($q^{\alpha\beta}$ with $\alpha = \alpha$ and $\alpha \neq \beta$ respectively), were fixed to 1 for all the slip systems, so only three parameters, namely the initial yield stress, τ_0, the saturation yield stress, τ_s, and the initial hardening modulus, h_0, were allowed to vary. Moreover, a value of $1s^{-1}$ for the reference shear rate, $\dot{\gamma}_0$ was chosen in all the cases. For each set of parameters, the hardness evolution with the declination angle is determined from the calculated loading-unloading cruves in the same fashion as the experimental curves, i.e., applying the Oliver and Pharr method [115]. Finally, the CP parameters were optimized by fitting the simulated hardness-declination angle curves to the experimental ones.

Slip mode	Slip plane	Slip direction	Number of systems
Basal $\langle a \rangle$	$\{0002\}$	$\{11\bar{2}0\}$	3
Prismatic $\langle a \rangle$	$\{10\bar{1}0\}$	$\{11\bar{2}0\}$	3
Pyramidal $\langle a \rangle$	$\{10\bar{1}1\}$	$\{11\bar{2}0\}$	6
First-order Pyramidal $\langle c+a \rangle$	$\{10\bar{2}2\}$	$\langle 11\bar{2}3 \rangle$	12

Table 6.1: Slip systems included in the CP model.

6.4 Results and discussion

6.4.1 Indentation size effects in pure Mg

As mention in the Introduction of this Ph.D. thesis, one of the main limitation in the use of nanoindentation tests as a calibration method for CPFE models is the occurrence of the so-called ISE. It is well known that, in single-crystal metals, hardness increases as the indentation depth decreases [142–145]. The origin of this size effect is the increase in the plastic strain gradient that occurs for self-similar indenters with decreasing penetration depth [142]. This effect is particularly relevant at depths smaller than a few microns. This work is intended to develop a universal method that can be applied to conventional polycrystalline Mg alloys with typical grain sizes of $\sim$ 10 μm. As we aim at neglecting grain boundary effects, this results in the use of indentation depths $<$ 300 nm. However, at this indentation

depth range, the ISE may be significant. This effect is typically explained in terms of the GND_s [144]. The hardness, H, is considered to have two contributions: a size-independent contribution, H_{SSD}, which depends on the density of statistically stored dislocations (SSD_s), and a size-dependent contribution, H_{GND}, related to the density of GND_s. We have therefore evaluated the ISE in the current deformation conditions on pure Mg. Fig. 6.1 shows the variation of hardness with the indentation depth ranging between 100 and 3000 nm for grains with a low δ, where the effect of the activation of tensile twinning in the hardness is negligible (Section 5.4.5). This figure shows that the hardness reaches a plateau corresponding to the size-independent term, H_{SSD}, at depths $>$ 2500nm. At indentation depths of 300 nm, the hardness H_{300} shows a substantial size effect so that the size-dependent term H_{GND} accounts for the 67 % of the total hardness. Based on this result, a correction factor of 1.67 has been used in this work on the CPFE calculations to estimate the size-independent hardness H_{SDD}, i.e. $H_{300} = H_{SDD} * 1.67$. The use of a single corrector factor parameter relies on the assumption that ISE is independent of grain orientation. Even though some authors [146] have reported that the accumulation of GND_s might be a function of grain orientation, our current studies show a similar ISE, so the same correction factor was assumed to be valid for all orientations.

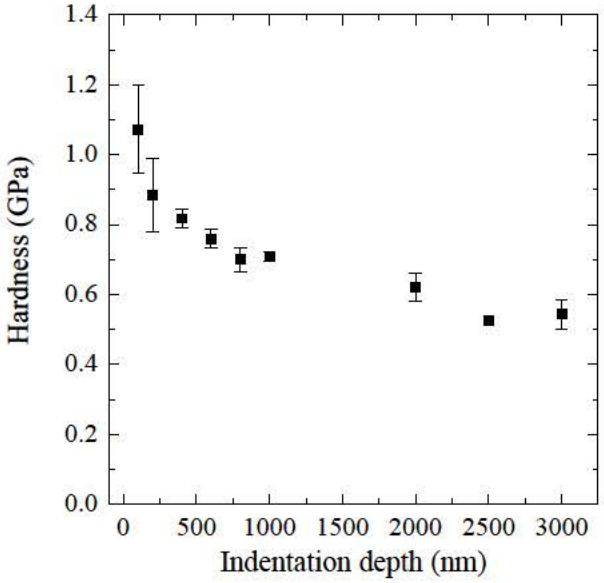

Fig. 6.1: Hardness vs. indentation depth curve corresponding to pure Mg.

6.4.2 Variation of the hardness with the grain orientation

Figs. 6.2a and 6.3a show the inverse pole figure EBSD maps for both pure Mg (along the normal direction, ND) and the MN11 alloy (along the extrusion direction, ED), respectively. Several indentations were performed at the centre of selected grains in both materials. Fig. 6.2b shows the load-displacement curves corresponding to two grains, namely Grain 1 and Grain 2 in Fig. 6.2a, in pure Mg. Grain 1, with a declination angle of 2°, is significantly stronger than Grain 2, which has a declination angle of 53°. Fig. 6.3b confirms that the

mechanical response of individual grains in the MN11 alloy is also strongly affected by the grain orientation. In particular, Grain 1, which has a small declination angle ($\delta = 7°$), is stronger than Grain 2, which displays a higher declination angle ($\delta = 64°$).

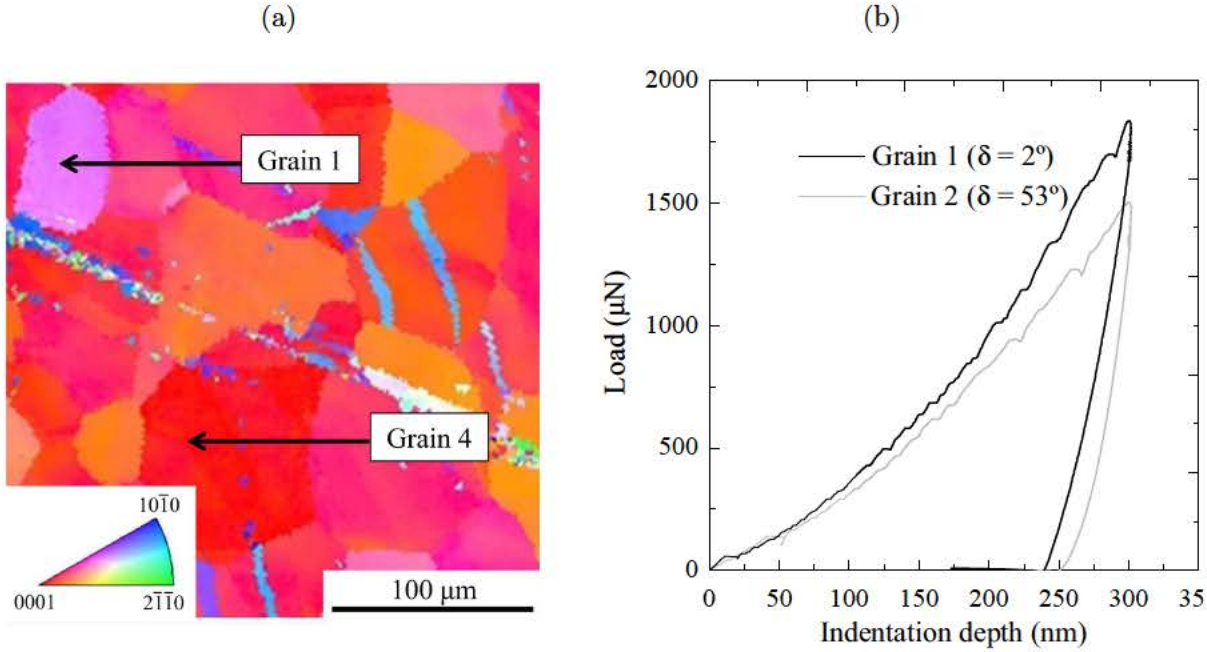

Fig. 6.2: (a) EBSD inverse pole figure map in the ND of pure Mg. (b) Effect of the declination angle on the load-displacement curve in pure Mg.

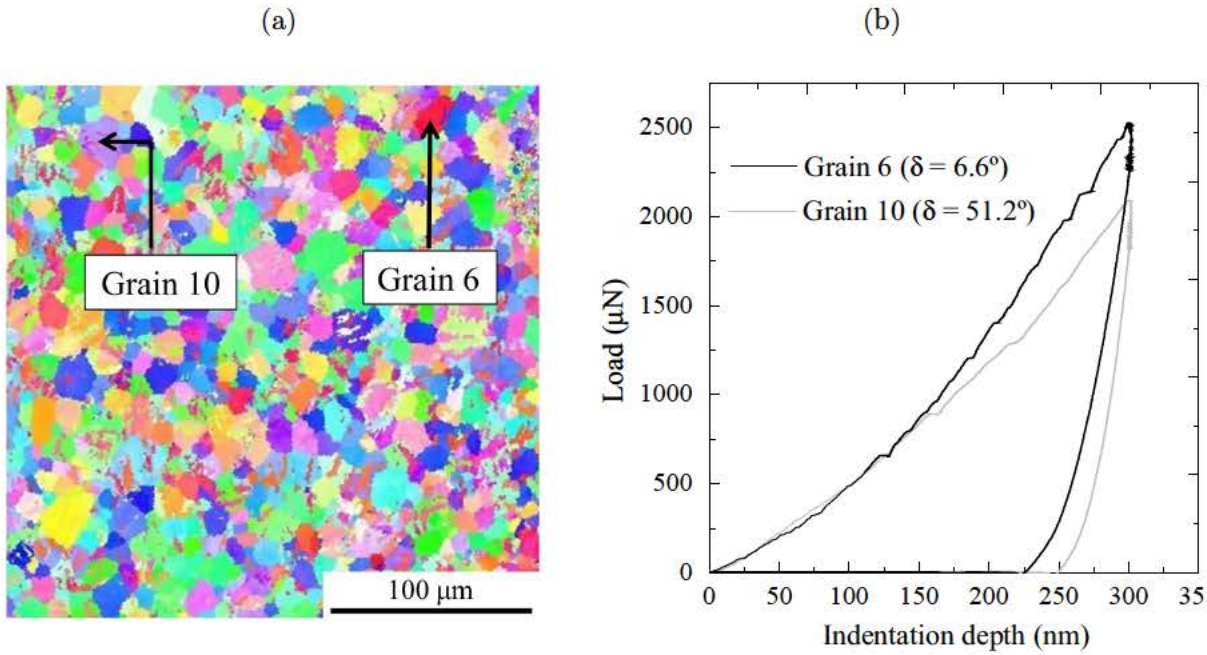

Fig. 6.3: (a) EBSD inverse pole figure map in the ED of the MN11 alloy. (b) Effect of the declination angle on the load-displacement curve in the MN11 alloy.

Fig. 6.4 plots the variation of the hardness with declination angle obtained for pure Mg and the MN11 alloy. While pure Mg exhibits a drop in the hardness at a declination angle ranging between 30° and 50°, the hardness drop takes place at a declination angle of $0-25°$ in the MN11 alloy. We ascribe this effect to the influence of grain orientation on the slip activity and the corresponding CRSS$_s$ values.

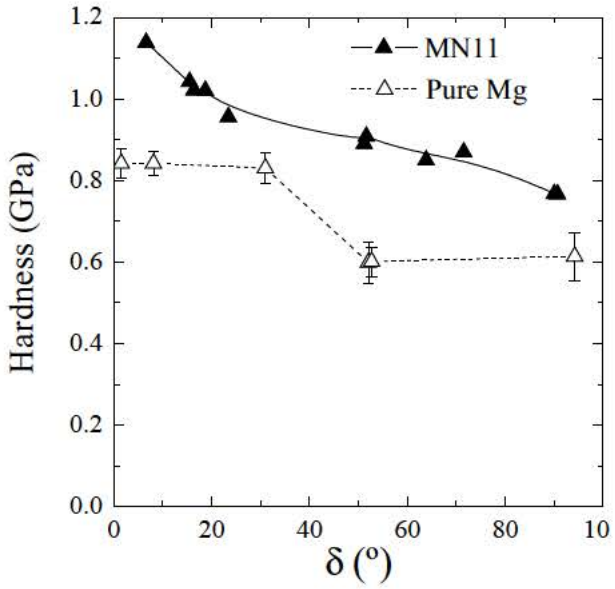

Fig. 6.4: H - δ curve corresponding to pure Mg and to the MN11 alloy.

6.4.3 Validation of the method for pure Mg

In order to assess the validity of the modelling approach used in this research, the experimental H - δ curve for pure Mg (Fig. 6.4) was reproduced using the simulation set-up described in Section 6.3. The parameters of the viscoplastic law (Eq. 4.4) were selected as those providing the best fit with the experimental curves. We set the reference strain rate, $\dot{\gamma}_0$, to 1 s^{-1} and the strain-rate sensitivity exponent, m_{sl}, to 0.3. The rest of the CP parameters which defines de model (τ_0, τ_s and h_0), which are specified in Table 6.2, were taken from the literature [49]. Fig. 6.5 shows that the agreement between the experimental and the simulated hardness variation with grain orientation is reasonable (Fig. 6.5), specially considering that the main CP parameters for pure Mg were taken from the literature, without performing any fitting procedure. This indicates that the reported behaviour is indeed a consequence of the different CRSS of each slip system in Mg and their different activity as a function of the grain orientation with respect to the indentation axis.

Slip system	τ_0 (MPa)	τ_s (MPa)	h_0 (MPa)
Basal $\langle a \rangle$	2 (0.5)	10 (-)	20
Prismatic $\langle a \rangle$	25	85	1500
Pyramidal $\langle a \rangle$	25	85	1500
Second-order Pyramidal $\langle c+a \rangle$	40	150	3000

Table 6.2: Set of inelastic parameters used in the validation of the model.

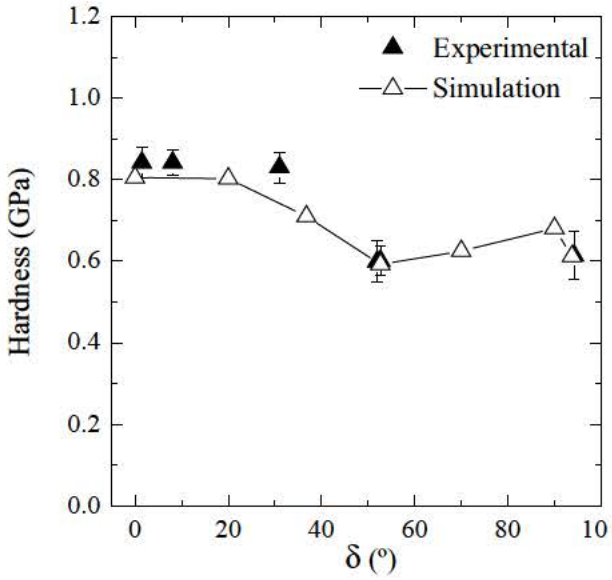

Fig. 6.5: Comparison between simulated and experimental H - δ curves for pure Mg.

Table 6.3 summarizes the cumulative activity of the different slip systems with the grain orientation obtained from CPFE simulations. The activation of basal slip was found to be almost independent of the declination angle δ. This is consistent with the fact that under the complex stress state that develops under the indent, basal slip is readily activated for all orientations due to its low CRSS. However, the harder pyramidal $\langle c+a \rangle$ and prismatic slip systems show opposite behaviours. While the activity of pyramidal $\langle c+a \rangle$ slip decreases with increasing δ, the activity of prismatic slip increases with it. This trend indicates that despite the complex stress state that develops under the indents, the activation of the hardest slip systems, namely pyramidal and prismatic, is mostly governed by their SF with respect to the stress component parallel to the indentation direction. The grain orientation with the highest SF for pyramidal $\langle c+a \rangle$ slip is at $\delta = 0°$. We thus associate the high hardness values obtained in grains with basal orientation, i.e., $\delta = 0°$, to the activation of pyramidal $\langle c+a \rangle$ slip. In particular, the ratio between between the activity of pyramidal $\langle c+a \rangle$ and prismatic slip shows a maximum value of 2.10 at $\delta = 0°$ and a minimum value of 0.20 at $\delta = 90°$ (prismatic orientation). Although pyramidal $\langle a \rangle$ was accounted for in the simulations, its activation was found to be negligible, in agreement with previous reports [12]. Finally it

is worth stressing that this exceptional agreement was reached without considering tensile twinning in the model. This is in complete agreement with our results included in Sections 5.4.2 and 5.4.4, where we showed that tensile twin activity under this testing conditions, i.e., small indentation depths, is negligible.

	Slip system activity (%)			
	Basal $\langle a \rangle$	Prismatic $\langle a \rangle$	Pyramidal $\langle a \rangle$	Pyramidal $\langle c+a \rangle$
Declination angle (°)				
0	65	11	1	23
20	65	16	1	17
37	62	24	2	12
53	63	24	1	11
70	62	25	1	12
90	52	36	2	10

Table 6.3: Slip system activity as a function of the declination angle during an indentation.

6.4.4 Parametric study

Motivated by the success of reproducing the hardness variation with the grain orientation in pure Mg, the CPFE model validated in the previous section was used to carry out a parametric study to assess the effect of the relative values of the different $CRSS_s$ on the H - δ curves. Eight different sets of CP parameters were considered, as summarized in Table 6.4. To minimize the number of variable parameters, a number of assumptions were made. First, the value of the initial hardening modulus of each slip system was set to that utilized in the validation study [49] (Table 6.5). Second, the ratio τ_{sat}/τ_0 for each slip system was set to the values shown in Table 6.5 [49]. Third, the CRSS ratio between pyramidal $\langle c+a \rangle$ and pyramidal $\langle a \rangle$ slip was set to 1.6 [49] (except Case 1, Table 6.4). Fourth, the strain-rate-sensitivity exponent, m_{sl}, was set to 0.1. The variation in hardness with grain orientation for each set of parameters is summarized in Fig. 6.6 as a function of two parameters, namely, the pyramidal ($\langle c+a \rangle$) to basal CRSS ratio, $\tau_0^{pyra.}/\tau_0^{basal}$, and the prismatic to basal CRSS ratio, $\tau_0^{pris.}/\tau_0^{basal}$. For each set, all hardness values were normalized with respect to the hardness in the basal orientation.

The following conclusions can be drawn from Fig. 6.6. First, the pyramidal to basal CRSS ratio has a significant influence on the slope of the left branch of the H - δ curve, which becomes increasingly more negative as the $\tau_0^{pyra.}/\tau_0^{basal}$ increases. This effect can be associated with the higher activation of pyramidal slip when the declination angle is small. On the other hand, the prismatic-to-basal CRSS ratio has a remarkable effect on the slope of the right branch of the curve, which increases with the increase of the $\tau_0^{pris.}/\tau_0^{basal}$ ratio. Curves such as those shown in Fig. 6.6 can provide a qualitative assessment of the impact of alloying elements on the CRSS ratios of basal, prismatic and pyramidal slip in novel Mg alloys. Quantitative determination would require an optimization procedures of the simulated hardness to determine the $CRSS_s$ that best fit the experimental results, as shown below for the MN11 alloy.

Set	$\tau_0 - \tau_s$ (MPa)			
	Basal $\langle a \rangle$	Prismatic $\langle a \rangle$	Pyramidal $\langle a \rangle$	Pyramidal $\langle c+a \rangle$
1	25 - 75	25 - 85	25 - 85	25 - 75
2	5 - 15	5 - 17	25 - 85	25 - 150
3	3 - 9	24 - 82	15 - 51	24 - 90
4	3 - 9	25 - 85	25 - 85	40 - 150
5	3 - 9	37.5 - 127.5	25 - 85	40 - 150
6	3 - 9	3 - 10]	37.5 - 127.5	60 - 225
7	3 - 9	37.5 - 127.5	37.5 - 127.5	60 - 225
8	3 - 9	60 - 205	37.5 - 127.5	60 - 225

Table 6.4: Sets of CP parameters taken into account in the parametric study.

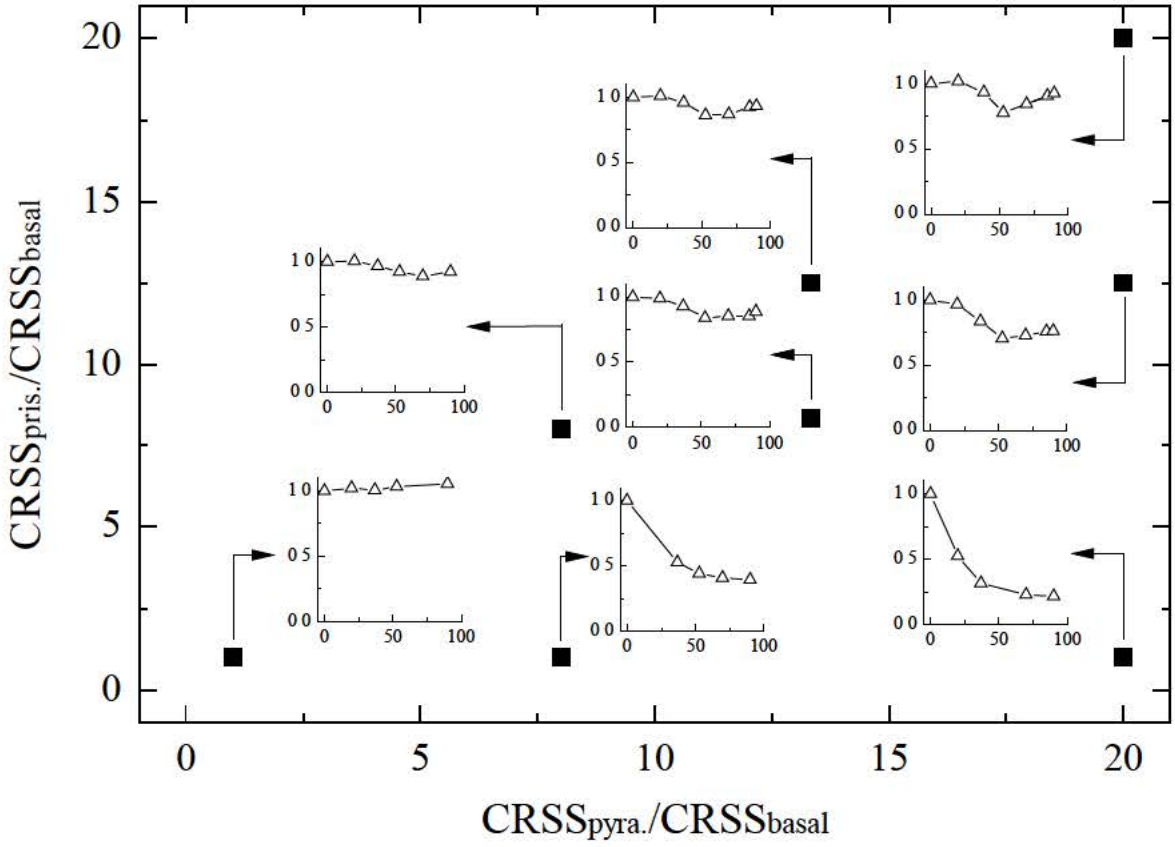

Fig. 6.6: Variation of the shape of the H - δ curve as a function of the ratios between the non-basal (prismatic and pyramidal $\langle c+a \rangle$) and the basal CRSS values.

Parameter	Slip systems			
	Basal $\langle a \rangle$	Prismatic $\langle a \rangle$	Pyramidal $\langle a \rangle$	Pyramidal $\langle c+a \rangle$
h_0 (MPa)	20	1500	1500	3000
τ_s/τ_0 (except set 1)	3	3.4	3.4	3.75

Table 6.5: Simplifications assumed during the parametric study.

6.4.5 Application of the method to an MN11 alloy

The H - δ curves obtained experimentally for pure Mg and for the MN11 alloys are shown in Fig. 6.4. The right branch of the curve for pure Mg displays a slightly positive slope, while the slope is negative for the MN11 alloy. According to the previous parametric study, this trend is indicative of a reduction in the prismatic-to-basal CRSS ratio in comparison to pure Mg (Fig. 6.5). This effect can be achieved by either increasing the basal CRSS, decreasing the prismatic CRSS, or a combination of both.

Fig. 6.7 reveals that increasing the basal CRSS 6.7a or decreasing the prismatic CRSS 6.7b independently leads to H - δ curves that differ widely from those measured experimentally. On the contrary, the experimental data are best matched by simultaneously increasing the basal CRSS, decreasing the prismatic CRSS and increasing the pyramidal $\langle c+a \rangle$ CRSS with respect to the values of pure Mg, as shown in Fig. 6.7c. The parameters that provide the best fit are summarized in Table 6.6.

The indentation results suggest that, while in pure Mg and conventional Mg alloys, such as AZ31, there is a large difference between the basal and prismatic $CRSS_s$, in the case of the MN11 alloy, basal and prismatic slip display similar $CRSS_s$. These results are consistent with previous reports that suggest softening of prismatic slip [147–149] and hardening of the basal slip [150] in Mg upon alloying with RE elements. These differences in the CRSS between pure Mg and the MN11 alloy have been attributed to the presence of Nd in solid solution and to Mg_3Nd precipitates [150].

Slip system	τ_0 (MPa)	τ_s (MPa)	h_0 (MPa)
Basal $\langle a \rangle$	35	105	20
Prismatic $\langle a \rangle$	20	80	1500
Pyramidal $\langle a \rangle$	60	300	1500
First-order Pyramidal $\langle c+a \rangle$	95	345	300

Table 6.6: Set of $CRSS_s$ values proposed for the MN11 alloy.

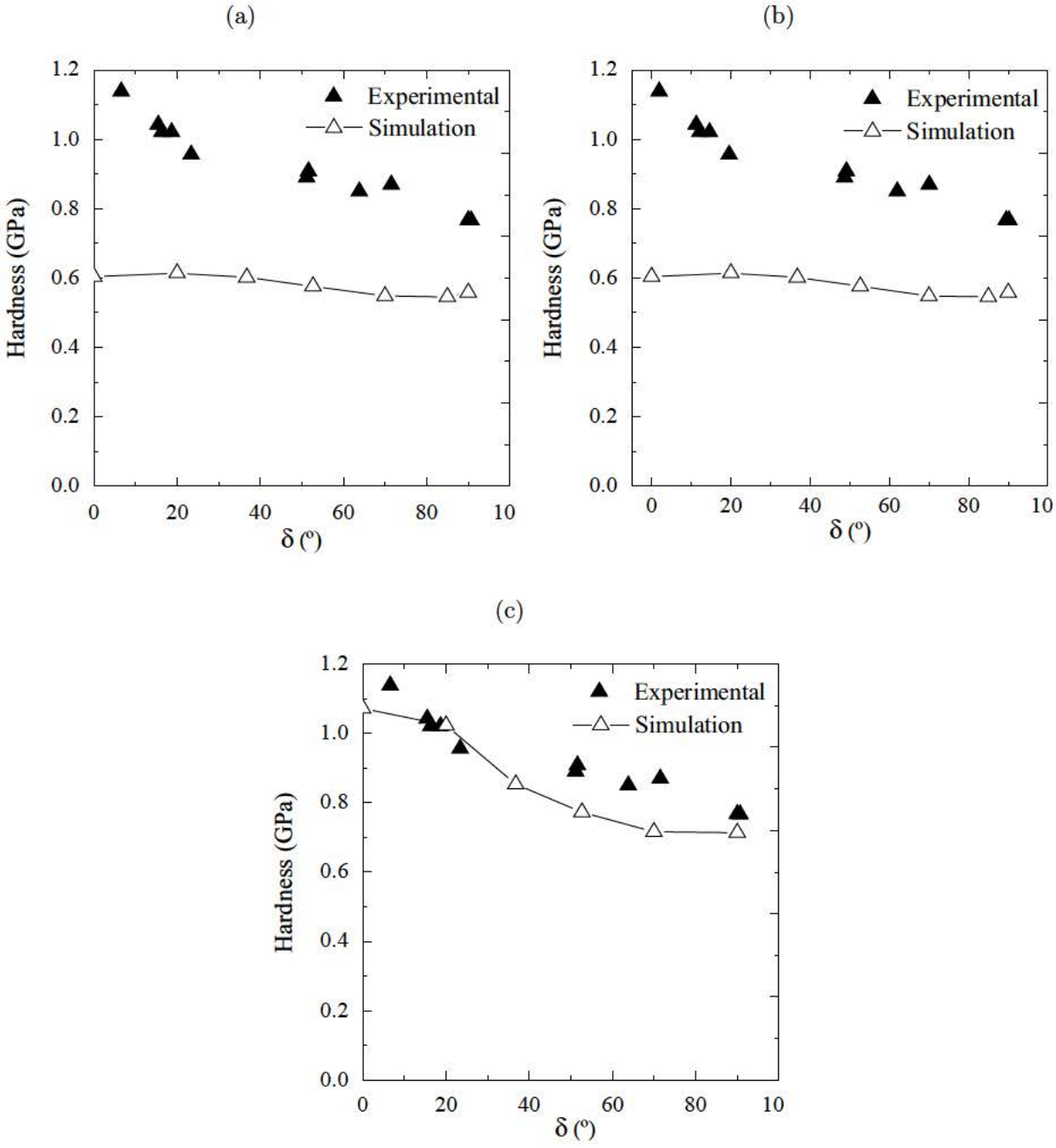

Fig. 6.7: Set of CRSS values tested in order to match the experimental and simulated H - δ of the MN11 alloy: (a) increase in the basal CRSS; (b) decrease in the prismatic CRSS; (c) combination of an increase in the basal CRSS and a decrease in the prismatic CRSS.

6.5 Conclusions

In the present chapter, a new methodology to estimate the CRSS$_s$ of industrial Mg alloys is presented. The main conclusions of this work can be summarised as follows:

1. A new methodology to estimate the CRSS$_s$ of the different slip systems in Mg alloys is proposed, which combines instrumented nanoindentation and CPFE simulations, based on the variation of hardness with the crystallographic orientation of the grains.

2. The method was validated in pure Mg. We obtain a very good match between the simulated and experimental variation of hardness with grain orientation when adopting a set of CP parameters measured recently by Zhang and Joshi in single crystals of pure Mg [49].

3. The CPFE model was used to simulate the variation of the hardness with grain orientation as a function of the CRSS ratios between the non-basal ans basal slip systems. The simulations show that the pyramidal-to-basal CRSS ratio is the most important parameter influencing the hardness of those grains oriented with the c-axis forming between 0° and 45° with the indentation axis. On the contrary, the prismatic-to-basal ratio influences mostly the hardness of those grains oriented with the c-axis forming between 45° and 90° with the indentation axis.

4. The proposed methodology was successfully used to estimate the CRSS$_s$ of the active slip systems in an extruded MN11 alloy. It was found that, with respect to pure Mg, the basal CRSS increases dramatically and that the prismatic CRSS decreases, to an extent that both become similar. These variations in the CRSS$_s$ are consistent with previous experimental observations of the effect of Nd solutes and Mg_3Nd plate precipitates on slip activity, and are in agreement with the low yield stress anisotropy showed by these rare-earth Mg alloys.

"Science knows no country, because knowledge belongs to humanity, and is the torch which illuminates the world"

Louis Pasteur

7

High temperature micromechanics of pure Mg studied by nanoindentation

7.1 Introduction

Here, the methodology developed in the last two chapters is extended to high temperature. In particular, special attention is paid to the variation with temperature between the activation of the different deformation modes under an indentation as a function of the crystallographic orientation of the indented planes.

7.2 Experimental procedure

The initial material was the rolled and annealed sheet of pure Mg further annealed at 500 °C described in Section 3.1 and used also in Chapter 5. A total of 8 different grains, whose Euler angles and declination angles are listed in Table 7.1, were investigated in this study. Up to three indentations were performed in each individual grain at 300 °C, 250 °C, 200 °C, 150 °C, 100 °C and RT. That specific sequence of decreasing temperatures was followed in order

to avoid undesirable recrystallization process in areas near the indents. Nanoindentations were conducted using the NanoTest^{TM} system from Micro Materials described in Section 3.4.5 fitted with a sphero-conical indenter with a tip radius of 1 μm and an apex angle of 90°. A maximum indentation depth of 4000 nm was applied in all the cases, choosing a loading and unloading time of 30 and 2 s, respectively, and a holding time of 3 s at maximum depth.

The microstructure around the indents was investigated by EBSD using the Helios NanoLab^{TM} DualBeam^{TM} 600i microscope equipped with an Oxford-HKL EBSD detector described in Section 3.3.2 operated at a voltage of 15 kV and at an emission current of 2.7 nA. In addition, the topography around the indents was characterized by AFM using the Park XE150 AFM microscope described in Section 3.3.3. Sample preparation for nanoindentation, EBSD and AFM characterisation was performed using the *Route B* procedure described in Section 3.2.

Grain	**Euler Angles (°)**			$\boldsymbol{\delta}$ (°)
	Phi 1	*PHI*	*Phi 2*	
1	114	7	41	7
2	142	15	43	15
3	32	151	56	29
4	79	42	52	42
5	22	58	50	58
6	12	72	46	72
7	54	98	20	82
8	64	92	2	88

Table 7.1: Euler angles and δ of the 8 grains studied in this section.

7.3 Numerical simulations

The CP model described in Section 4.2.3 was integrated into the FE commercial software ABAQUS by means of a UMAT [129]. The following elastic constant, which were considered to be temperature-independent, where used for pure Mg: C_{11} = 59.40 GPa, C_{12} = 25.61 GPa, C_{23} = 24.44 GPa, C_{33} = 61.60 GPa and C_{44} = 16.40 GPa [49]. On the other hand, the reference shear rate of slip, $\dot{\gamma}_0$, the hardening exponent for slip, a_{sl}, the slip-to-slip latent parameters, q_{sl-sl}, the minimum twinned volume fraction to "activate" a twin variant, f_{nucl}, the twinned volume fraction from which the CRSS for twinning is considered constant, f_{pro}, and the reference twinned volume transformation rate, $\dot{f}_0$, where fixed to $0.001s^{-1}$, 2, 0.2, 0.005, 0.5 and $7.752s^{-1}$ respectively. The parameters that complete the definition of the slip behaviour, i.e., the initial CRSS, τ_0, the saturation CRSS, τ_s, the initial hardening modulus, h_0, and the rate-sensitivity exponent for slip, m_{sl}, and the twin behaviour, i.e., the stress somehow related to the "nucleation" and "propagation" processes, τ_{nucl} and τ_{pro} respectively, and the rate-sensitive exponent for twinning, m_{tw}, were fitted for each slip and twin system at each testing temperature.

The indentation process was reproduced using a FE model which compromises a total of 7622 linear hexahedral (C3D8) elements. Individual grains were modelled as a pseudo-cylinder whose large dimensions guarantee the absence of significant stresses at the bottom and lateral borders, which were considered to be totally constrained. A fully-rigid spheroconical indenter with the same apex angle than in the experiments was used. While the experimental tip was 1 μm, this geometrical parameter was set to 2.5 μm in the simulations. In this way, coarser meshes could be used near the contact area between the sample and the indenter which resulted in an important reduction in the computational costs. In addition, the maximum indentation depth, which was set to 4 μm in the experiments, was properly modified in the simulations so the size of the experimental and simulated residual imprints were the same. A detailed analysis included in Appendix A shows that the possible changes in the stress state induced by these simplifications do not significantly affect both the residual deformation around the indents as as well as the maximum load reached during the indentation, which were the main parameters used in order to compare the experimental with the simulated results, for the range of indentation depths used in this study. A friction coefficient of 0.2 was used in all the simulations.

7.4 Results and discussion

7.4.1 Evolution of the microstructure and deformation patterns around the indents as a function of temperature

Fig. 7.1 shows the AFM topography maps and the EBSD inverse pole figure maps in the direction parallel to the indentation axis corresponding to representative indents carried out in Grains 1 (δ = 7°), 4 (δ = 42°) and 7 (δ = 82°) at temperatures ranging from RT to 300 °C. As it can be observed, the twinning activity as well as the deformation patterns that develop in areas near the indent are dramatically affected by both the crystallographic orientation of the indented plane and the testing temperature, which is in agreement with the results obtained previously in this Ph.D. thesis (Section 5.4.1). In particular, while the relative twinned area round the indent decreases as temperature increases for the 3 grains analysed in Fig. 7.1, noticeable differences are found between them. For example, significant twin activity is found up to 200 °C around the indent in Grain 1, where the development of twins is only clearly reduced at 250 and 300 °C. However, this transition seems to take place at lower temperatures in Grain 7, where the twin activity vanishes completely at 250 and 300 °C. The role of the crystallographic orientation on the reduction of twin activity with temperature will be studied in more detail in the following sections.

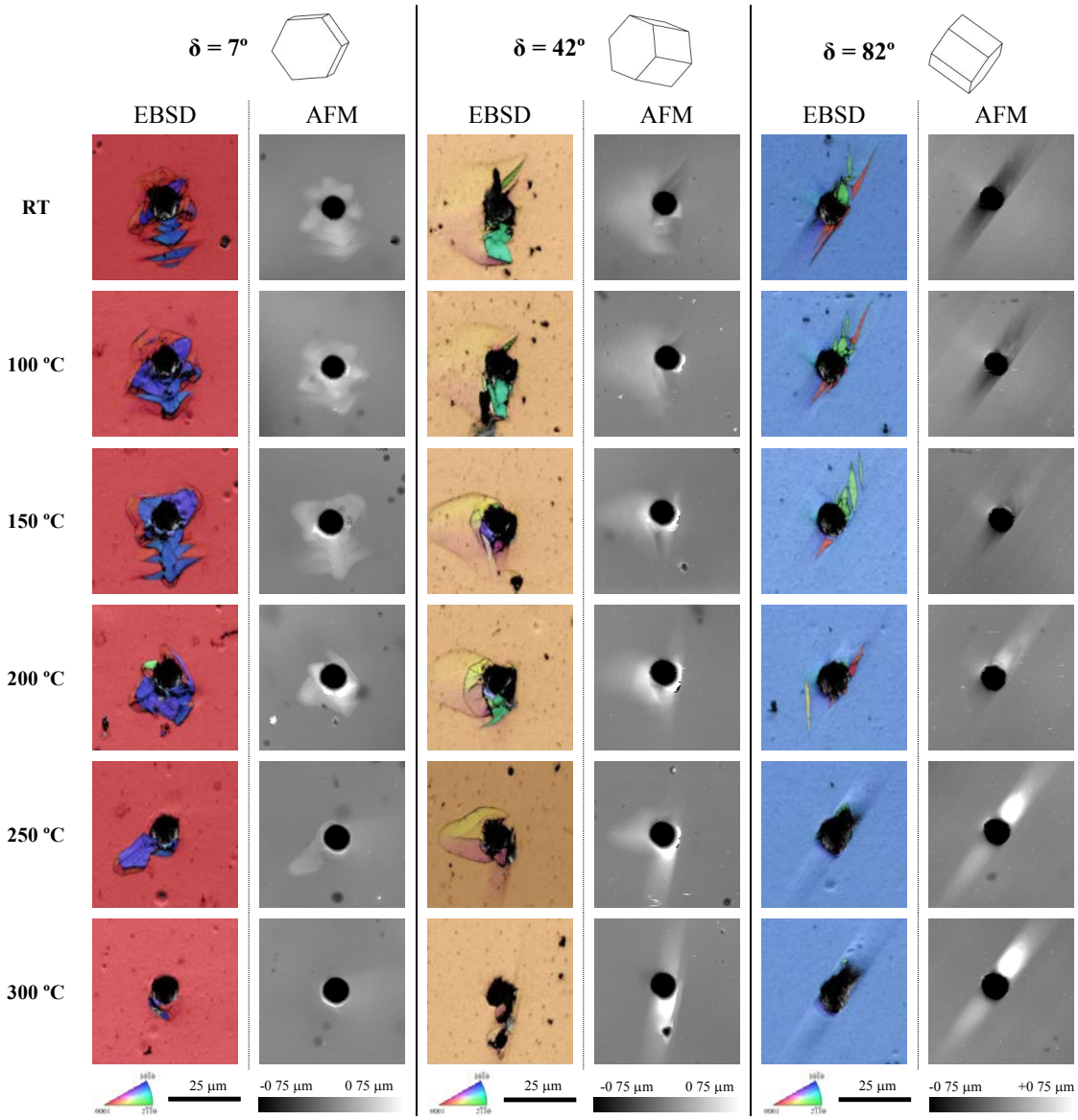

Fig. 7.1: AFM topography maps and EBSD inverse pole figure maps in the direction parallel to the indentation axis corresponding to representative indents performed in Grains 1, 4 and 7 at temperatures ranging from RT to 300 °C.

The evolution of the out-of-plane displacement profiles with temperature is also highly affected by the crystallographic orientation of the indented plane. Fig. 7.2 shows the projected areas of the pile-up (Fig. 7.2a) and sink-in (Fig. 7.2b) deformation patterns developed

around the indents in the 8 grains studied in this paper performed at different temperatures. Each of them has been properly positioned in the orientation space of Mg and has been in-plane rotated following the convection defined by Zambaldi and Raabe [57]. The corresponding pile-up and sink-in projected areas were obtained applying threshold heights of +0.10 μm and -0.07 μm, respectively. A combined analysis of Figs. 7.2a and 7.2b reveals that the evolution of the deformation patterns with temperature is driven by the δ of the indented plane. Grains 1 and 2, with low δ, are characterized by developing a concentric pile-up at RT which is a direct consequence of the activation and propagation of TT_s (Section 5.4.1). As temperature increases, this twin-induced concentric pile-up is reduced in both cases, although slight differences are found between them. Grain 1 seems to experience an increase in the twin-induced pile-up activity from RT to 150 °C. This issue will be further analysed in next sections. However, this pile-up activity is dramatically reduced from 200 °C, and almost vanishes at 300 °C. On the other hand, Grain 2 develops noticeable pile-ups even at high temperatures. Moreover, in this case, the concentric nature of the initial pile-up decreases as temperature increases, probably due to the activation of different deformation mechanisms than in Grain 1. Both grains do not exhibit any kind of sink-in at any temperature. A complete different behaviour is observed in grains with a high δ (Grains 6, 7 and 8). In this case, a two-fold sink-in pattern aligned with the basal planes is apparent at RT. This deformation pattern, which is induced by the development of TT_s (Section 5.4.1), gradually evolves into a two-fold pile-up pattern aligned with the basal planes as temperature increases. As pointed out in an complementary study carried out by the same authors of this Ph.D. thesis (Section B), this two-fold pile-up is justified by the combined activation of basal and prismatic slip. The transition temperature between these two behaviours is, for the three grains, between 150 °C and 200 °. On the other hand, the response of Grains 3 and 4 (intermediate δ) is a mixture between the two extreme instances described above. Due to the combined activation of tensile twinning and basal slip, a characteristic pile-up aligned with the ascending direction of the c-axis is induced at RT. At the same time, a slight twin-induced two-fold sink-in pattern aligned with the basal planes develops (Section 5.4.1). At temperatures higher than about 200 °C, this mixed displacement profiles evolves into a two-fold pile-up aligned with the basal planes, which is very similar to that found in grains with high δ at high.

Finally, Grain 5 is considered to have a medium-high δ, as its pile-up evolution is similar to the one observed in grains with at medium δ, but, at the same time, the evolution of their sink-in is quite similar to that displayed by grains with a high δ.

(a)

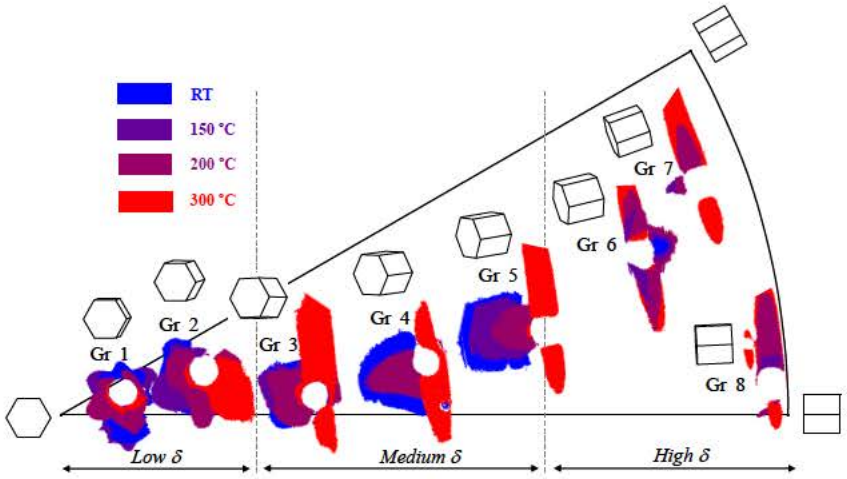

(b)

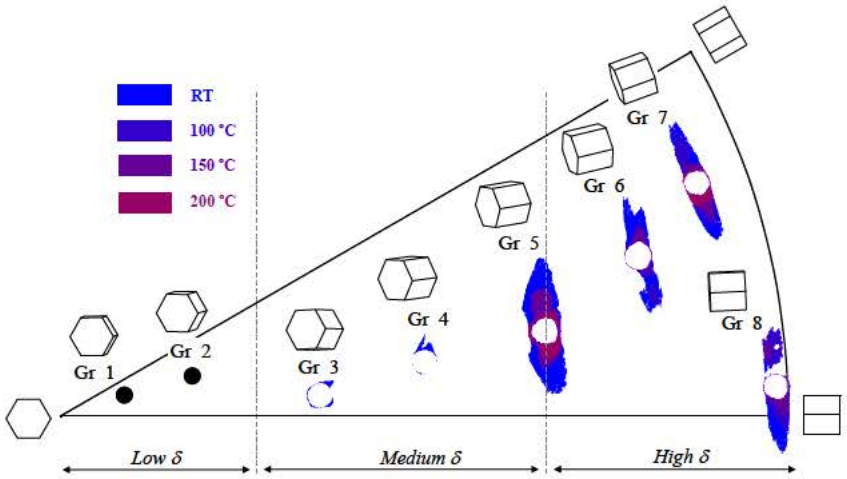

Fig. 7.2: Projected areas of the pile-up (a) and sink-in (b) deformation patterns developed around the indents performed in the 8 grains studied in this chapter at different temperatures.

7.4.2 Effect of temperature on the twin activity around the indents

In this section, a quantitative analysis of the activity of the different twin modes as a function of temperature and crystallographic orientation of the indented plane is carried out. As it was specified in the experimental description of this chapter, 3 indents were performed per grain and temperature. However, while all the indents corresponding to Grains 1 and 2 were subjected to advanced characterisation by EBSD and AFM, only one representative indent per grain and temperature was characterized for the rest of the grains. The minimum deviation angle approach [138] was utilized to analyse each twin. In particular, the following

tension and compression twin modes were considered: $\{01\bar{1}2\}$ $[0\bar{1}11]$ (tension), $\{01\bar{1}1\}$ $[0\bar{1}12]$ (compression 1) and $\{01\bar{1}3\}$ $[0\bar{3}32]$ (compression 2). Additionally, two possible double twinning modes were taken into account: compression 1 followed by tensile twinning (double twinning 1) and compression 2 followed by tensile twinning (double twinning 2). For the shake of simplicity, hereafter the term *compression twins* (CT_s) will denote all the modes that implied compression along the c-axis in any sate of the deformation (compression 1, compression 2, double twinning 1 and double twinning 2). Fig. 7.3 shows the number of tension and compression twins detected around representative indents performed in the 8 grains analysed in this study at different temperatures. For Grains 1 and 2, where 3 indents were performed and characterised per temperature, the average values are reported. As shown in Fig. 7.3, only the conventional tensile twin mode is activated at RT in all the analysed indents. However, CT_s are detected at temperatures from 100 °C up to 300 °C in indents carried out in grains whose declination angle is smaller than 43°. At higher declination angles, only TT_s are activated under any condition.

While it is clear from Fig. 7.1 that the global twinning activity decreases with temperature, it has been demonstrated that compression twinning develops exclusively when temperatures increases (Fig. 7.3), suggesting therefore an opposite trend. This is consistent with the more complex atomic shuffles involved in compression twinning, which therefore requires a higher degree of thermal activation [17, 151]. In order to shed further light into this issue, a quantitative analysis of the tensile twin activity is performed. Fig 7.4 shows the variation with temperature of the ratio between the projected twinned surface (Tw) and the projected imprint area (Ap) for the 8 grains analysed in this paper, including only TT_s in the analysis. With the exception of Grains 1 and 2, the relative tensile twin activity decreases gradually with temperature for all the grains analysed. It seems therefore that, although CT_s are activated at some range of temperatures, the global twin activity measured by 2D EBSD around the indent is dominated by tensile twinning, suggesting that TT_s are larger than CT_s. This observation, which is fully consistent with earlier studies on twinning in polycrystalline Mg alloys [151], will be further analysed in the next section.

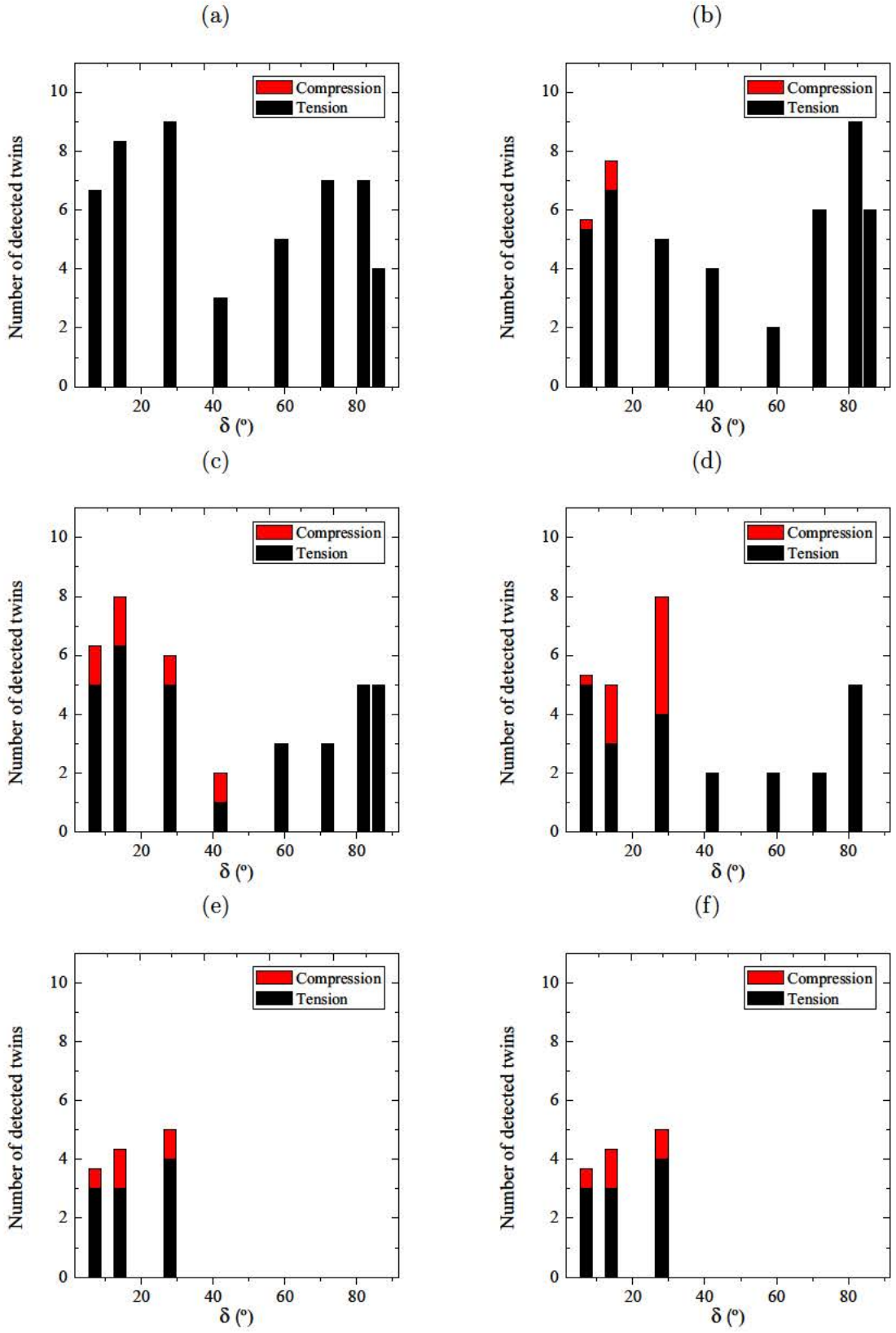

Fig. 7.3: Number of TT_s and CT_s detected around representative indents performed in the 8 grains analysed in this study at different temperatures: (a) RT; (b) 100 °C; (c) 150 °C; (d) 200 °C; (e) 250 °C; (f) 300 °C.

On the other hand, Grains 1 and 2 exhibit a rather surprising behaviour. Unlike the remaining orientations, where the maximum relative tensile twin activity occurs at RT, the activation of this deformation mode in these grains seems to be slightly more profuse at 100 and 150 °C than at RT. This result cannot be justified taking into account the established belief that both basal slip and tensile twinning are completely temperature-independent deformation mechanisms, while the non-basal slip systems as well as the different compression twinning modes show a clear decrease in their corresponding CRSS with increasing temperature [27]. In turn, the results shown in Fig. 7.4 may indicate that basal slip and/or tensile twinning could be affected somehow by temperature, although in a much less severe way than non-basal slip or compression twinning. Indeed, it is known that the formation of a TT requires a small degree of thermally activated atomic shuffling [17], which may result in an increase of tensile twin activity with respect to that of basal slip at temperatures smaller than 150 °C, at which the CRSS of non-basal slip systems is still rather high. On the other hand, Chapuis et al. [27] reported in their study of pure Mg single crystals a strange behaviour of basal slip at 150 °C, which seemed to be slightly harder at this temperature than at RT. Both aspects could justify the behaviour observed in this research. However, the temperature dependency of the non-basal slip systems is much more accused, and therefore, governs the evolution of the mechanical behaviour of pure Mg with temperature. For that reason, in this research, both basal slip and tensile twinning are considered not to be affected by temperature, and only the temperature dependency of the non-basal slip systems is further studied.

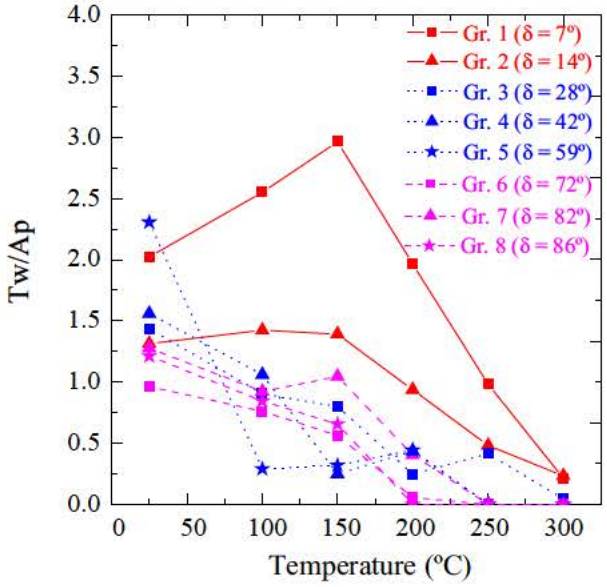

Fig. 7.4: Variation with temperature of the ratio between the projected twinned surface (Tw) and the projected imprint area (Ap) for the 8 grains analysed in this research including only TT_s in the analysis.

7.4.3 Effect of temperature and twin mode on the size, distribution and shape of the twins

It has been generally established that conventional TT_s display a plate-like morphology [12]. However, Fernández et al. [152] reported that the morphology of a TT_s is related to its SF. More specifically, they showed that, while primary TT_s variants, characterised by a high SF, are indeed endowed with the well-established plate-like morphology, secondary and tertiary TT_s variants, with a low SF and originated due to the presence of heterogeneous local stress fields, have in general irregular geometries. In order to study the possible effects of temperature on the shape of conventional TT_s, representative indents performed in Grain 1 at RT and 250 °C have been analysed (Fig. 7.5). As shown in Fig. 7.5a, TT_s formed at RT (marked with black arrows) displayed the typical plate-like morphology. However, as illustrated in Fig. 7.5b, the TT_s developed at 250 °C (marked with black arrows) have a much more rounded shape. Moreover, temperature seems to play also an important role in the number, location and distribution of TT_s. Fig. 7.5a shows several pairs of pseudo-parallel twins radially distributed around the indents performed at RT. This behaviour can be understood as follows. As the indentation depth increases, a larger fraction of the material around the indent should twin in order to accommodate the plastic deformation in the radial direction. While this could in principle be achieved by single twins growing steadily as the indentation depth increases, Fig. 7.5a shows that, instead, once a twin has attained a certain size, a new twin nucleates in order to further increase the twin volume fraction, without increasing the size of the initial twin. This behaviour reflects the lower energy required to form new twin boundaries than to overcome the backstresses associated to the initial twin [12]. At 250 °C (Fig. 7.5b), instead initial twins grow as the indentation depth increases, rendering the activation of new twins unnecessary. The reported differences in the twinning behaviour around the indent at RT and 250 °C reflect a temperature-induced alteration of the distribution of backstresses as well as of the matrix/twin interface energy.

The twinning mode also seems to play an important role on the size and location of the developed twin. While TT_s propagate easily, achieving large sizes, and extend to areas that are far away from the indenter contact area, CT_s are much smaller and are only located in areas very close to the indentation. Fig. 7.6 shows the EBSD inverse pole figure maps of representative indents perform in Grain 3 at RT and 200 °C, where the TT_s and CT_s are marked with black and white arrows, respectively. It can be clearly observed that CT_s are much smaller than TT_s. In addition, they are located in areas very close to the indenter contact area, i.e., they develop in volumes subjected to sever stress states. This is consistent with the fact that the core width of TT dislocations is much wider than that corresponding to CT dislocations, which implies a much more mobility of the former ones as the atomic shuffles involved in the propagation of a "wide" twin dislocation are much smaller than the ones corresponding to a "narrow" twin dislocation [37].

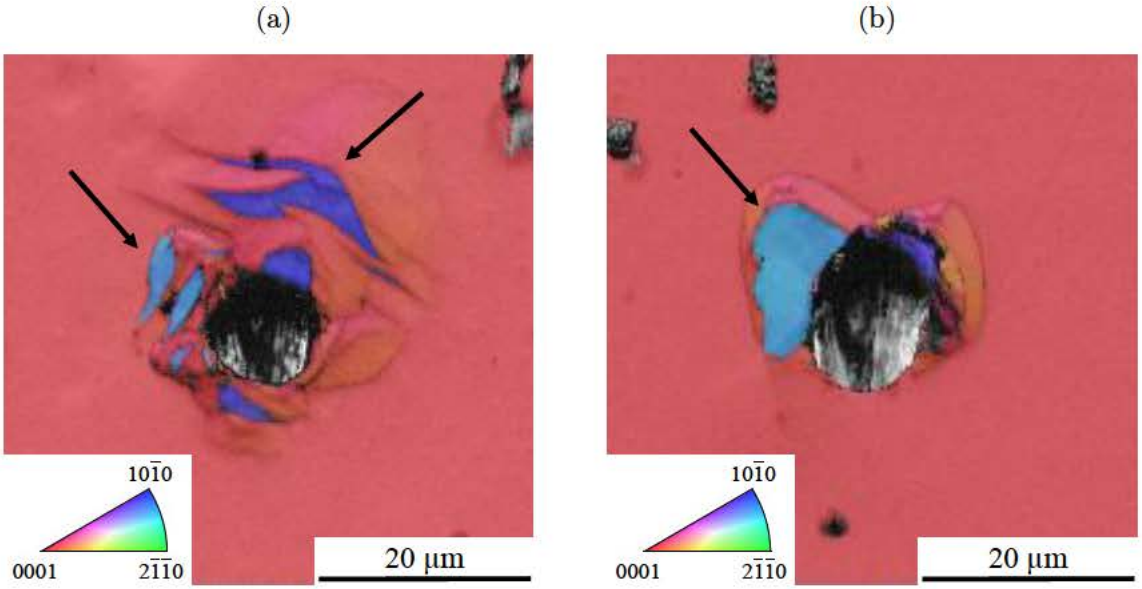

Fig. 7.5: EBSD inverse pole figure maps in the direction parallel to the indentation axis of representative indents performed in Grain 1 at RT (a) and 250 °C (b). TT_s are marked with black arrows.

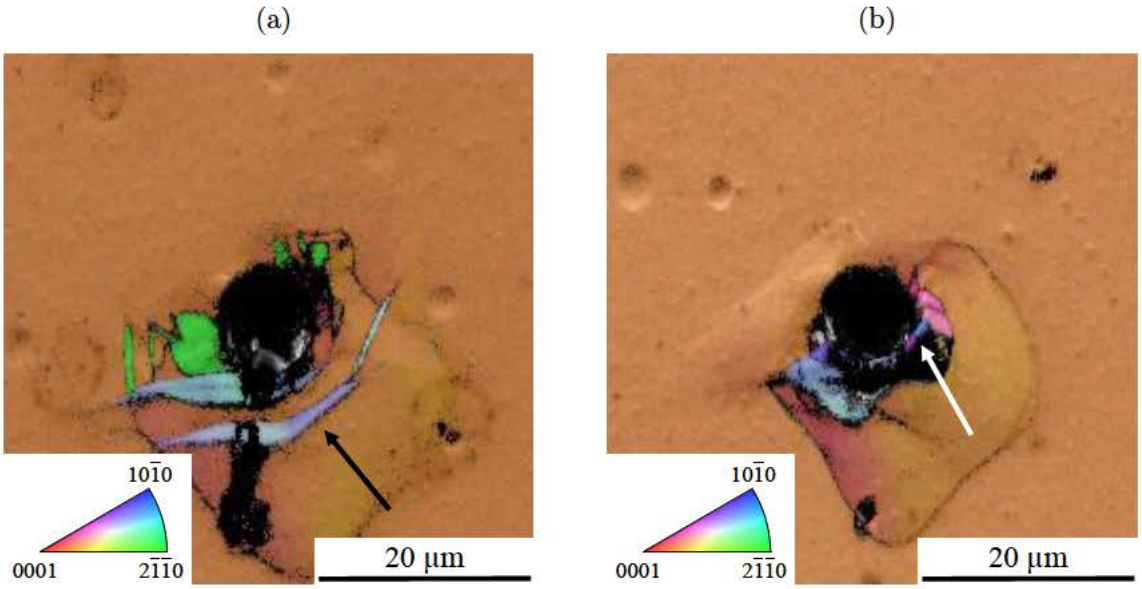

Fig. 7.6: EBSD inverse pole figure maps in the direction parallel to the indentation axis of representative indents performed in Grain 3 at RT (a) and 200 °C (b). TT_s and CT_s are marked with black and white arrows, respectively.

7.4.4 Effect of compression twinning on the load-displacement curves

Fig. 7.7 depicts the load-displacement curves corresponding to three different indents performed in Grain 3 at RT, 200 °C and 300 °C. It can be seen that, while the curves corresponding to RT and 300 °C are quite smooth, noticeable oscillations are present in the one

corresponding to 200 °C. This is not an isolated event and the curves corresponding to indentations performed in several grains exhibit similar features at intermediate temperatures. A careful analysis of the twin modes activated in each case has revealed that the presence of oscillations in the indentation curves is, to some extent, related to the activation of CT_s. Table 7.2 shows, indeed, that there is a very good correspondence between the occurrence of oscillations and the activation of CT_s. The presence of the former and absence of the latter, or the opposite case, are anomalies observed only in the 10 % of the cases. The first case only takes place at low temperatures. Under such conditions, the high CRSS of compression twinning can lead to the formation of CT_s so small that are not detectable by the EBSD system. On the other hand, the case in which TT_s were detected but their corresponding load-displacement curve did not show a clear oscillation only happens at very high temperatures. Under such conditions, the CRSS of compression twinning decreases significantly and therefore, the relaxation induced by the activation of this deformation mechanisms may become less severe in some cases.

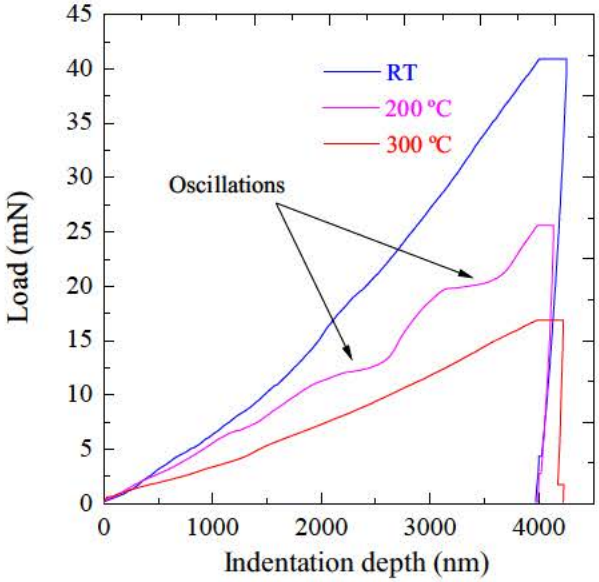

Fig. 7.7: Load-displacement curves corresponding to three different indents performed in Grain 3 at RT, 200 °C and 300 °C.

A detailed analysis of the crystallographic reorientation induced by compression twinning sheds light on the relation between the presence of an oscillation in the load-displacement curve and the activation of a compression twin. Let's imagine a Mg crystal subjected to pure compression along the c-axis. Under these conditions, only pyramidal slip and the different compression twin modes are favoured. In case the crystal undergoes compression twinning along the $\{01\bar{1}3\}$ plane, it will be reorientated as schematically shown by Fig. 7.8. While the SF of the most favoured basal slip and tensile twinning systems were both 0 in the initial configuration, they have changed to 0.341 and 0.338, respectively, in the twinned zone, and therefore, their activation is now favoured. As compression twinning is a much harder deformation mechanisms than basal slip or tensile twinning, the stress state of the crystal

		Testing temperature					
		RT	100 °C	150 °C	200 °C	250 °C	300 °C
Grain 1	*Oscillation*	NO	YES	YES	YES	YES	NO
$\boldsymbol{\delta = 7°}$	CT_s	NO	YES	YES	YES	YES	NO
Grain 2	*Oscillation*	NO	YES	YES	YES	YES	NO
$\boldsymbol{\delta = 15°}$	CT_s	NO	YES	YES	YES	YES	YES
Grain 3	*Oscillation*	NO	YES	YES	YES	NO	NO
$\boldsymbol{\delta = 29°}$	CT_s	NO	NO	YES	YES	YES	NO
Grain 4	*Oscillation*	NO	YES	YES	YES	NO	NO
$\boldsymbol{\delta = 42°}$	CT_s	NO	NO	YES	NO	NO	NO
Grain 5	*Oscillation*	NO	NO	NO	NO	NO	NO
$\boldsymbol{\delta = 58°}$	CT_s	NO	NO	NO	NO	NO	NO
Grain 6	*Oscillation*	NO	NO	NO	NO	NO	NO
$\boldsymbol{\delta = 72°}$	CT_s	NO	NO	NO	NO	NO	NO
Grain 7	*Oscillation*	NO	NO	NO	NO	NO	NO
$\boldsymbol{\delta = 82°}$	CT_s	NO	NO	NO	NO	NO	NO
Grain 8	*Oscillation*	NO	NO	NO	NO	NO	NO
$\boldsymbol{\delta = 88°}$	CT_s	NO	NO	NO	NO	NO	NO

Table 7.2: Presence of oscillations in the load-displacement curve and activation of CT_s in the different grains under investigation at temperatures ranging from RT to 300 °C.

after the compression twinning event will be quite severe and, due to the high SF of basal slip or tensile twinning, they will be abruptly activated inducing an important relaxation in the crystal that may be reflected in the oscillation events in the load-displacement curves observed in this research (Fig. 7.7 and Table 7.2). Very similar conclusions were obtained by Chapuis et al. [27] in their macroscopic single crystal experiments, where for some specific orientations, the activation of compression twinning followed by basal slip induced an important stress decrease in the stress-strain curves.

7.4.5 Simulations Results

Limitation of previous CP models

In this section, the limitation of previous CP models to capture the evolution of tensile twin activity with temperature is studied, placing special emphasis on the crystal law which governs such deformation mode. With that purpose, a simulation study in Grains 1 (δ = 7°), 3 (δ = 29°), 5 (δ = 58°) and 7 (δ = 82°), which were considered to cover the whole range of δ, was carried out using the model described in Section 4.2.2. This model will be called "Prev. CPM" hereafter. Two simulations were carried out for each grain, with the aim of modelling the mechanical behaviour or pure Mg at RT and 300 °C respectively. In all the simulations, m_{sl} and m_{tw} were fixed at 0.1. Table 7.3 depicts the τ_0, τ_s and h_0 of the different slip and twin systems corresponding to both temperatures. These parameters were

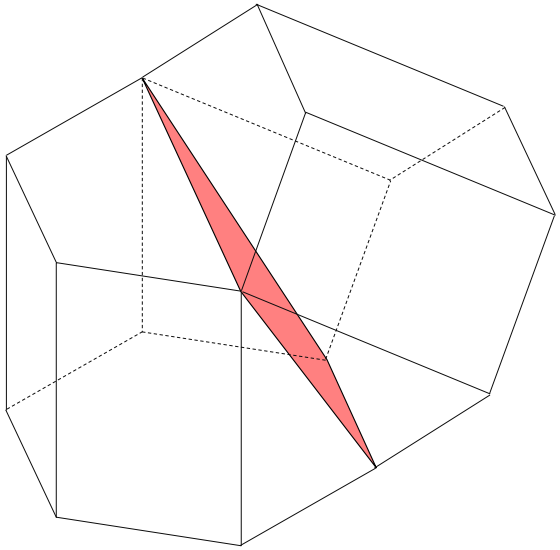

Fig. 7.8: Schematic illustrating the crystallographic reorientation induced by compression twinning along the $\{01\bar{1}3\}$ plane in an HCP crystal.

taken from the results obtained in the present Ph.D. theses in Chapter 5 (RT) and from an additional studied carried out by the same author of this Ph.D. thesis which is included in Appendix B (which would correspond to 300 °C). The CP parameters were configured in such a way that τ_0, τ_s and h_0 corresponding to basal slip and tensile twinning were the same at RT and 300 °C. It has to be mentioned that only basal, prismatic, second-order pyramidal $\langle c+a \rangle$ and tensile twinning were considered in the model. Compression twinning was not included in these calculations as, under these testing conditions (RT and 300 °C), the activation of this deformation mode was negligible (Section 7.4.4)

	RT			**300 °C**		
Slip/Twin system	τ_0	τ_s	h_0	τ_0	τ_s	h_0
Basal $\langle a \rangle$	2.5	7.5	50	2.5	7.5	50
Prismatic $\langle a \rangle$	25	85	1500	5	15	50
Pyramidal $\langle c+a \rangle$	40	150	3000	30	60	50
Tensile twinning	3.5	20	100	3.5	20	10

Table 7.3: Sets of CP parameters (MPa) corresponding to the preliminary simulation studied.

Fig. 7.9 shows the experimental and simulated residual deformation around the indents performed in Grains 1, 3, 5 and 7 at RT and 300 °C using the Prev. CPM. It can be noticed that earlier CP models, together with the specified set of $CRSS_s$, are able to fairly reproduce the experimental results at RT. In particular, the locations of the experimental pile-up/sink-in patterns in all the analysed orientations are qualitatively well captured in the simulations. This findings are in complete agreement with the results obtained in this Ph.D.

thesis in Chapter 5. However, at 300 °C, the dramatic change in the deformation patterns observed in the experiments is not captured in the corresponding simulations. Indeed, the simulated out-of-plane displacements at RT and 300 °C are quite similar. An analysis of the twin activity of these simulations revealed that this deformation mode is still quite active at 300 °C, which clearly contradicts the experimental results.

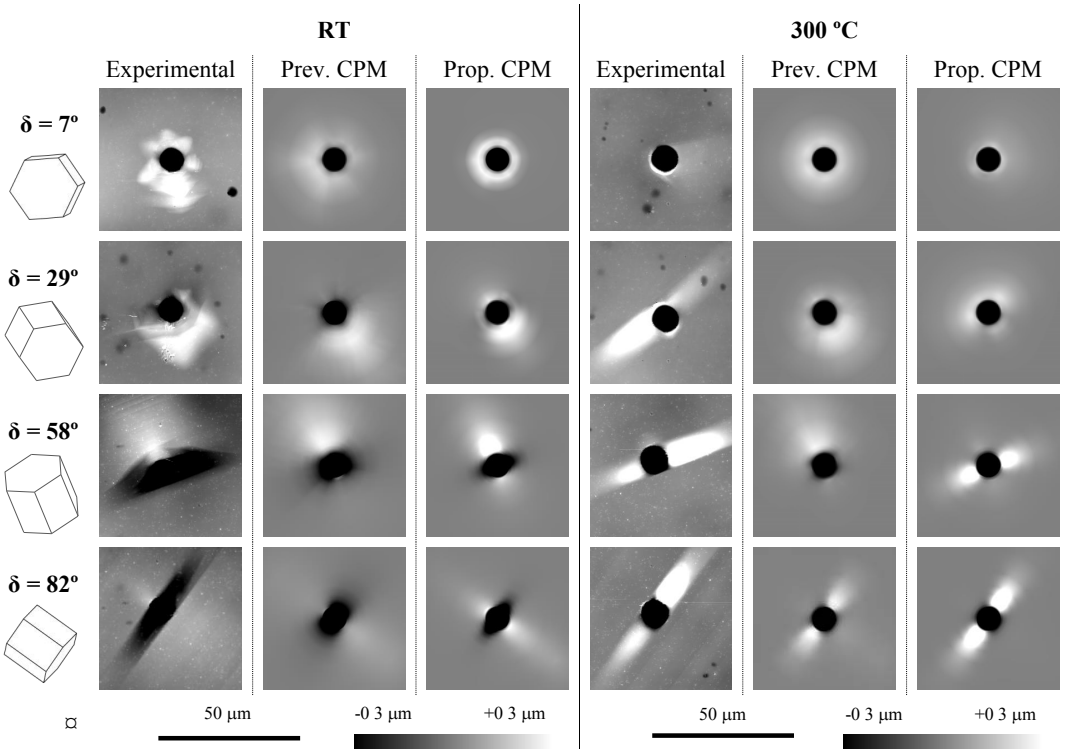

Fig. 7.9: Experimental and simulated residual deformation around the indents performed in Grains 1, 3 , 5 and 7 at RT and 300 °C. The simulations were carried out using the CP parameters specified in Table 7.3 together with the Prev. CPM and in Table 7.4 together with the Prop. CPM.

In the following sections, it will be shown how the enhanced model proposed in Section 4.2.3 (Prop. CPM), which includes the physically-based observation of a higher stress needed for twin nucleation than for twin propagation, is able to reproduce the micromechanics of pure Mg at a wide range of temperatures considering the actual temperature dependency of the different deformation modes.

Calibration of the CP model proposed in this research

In this section, the Prop. CPM described in Section 4.2.3 is used to reproduce the experimental behaviour of pure Mg showed previously under different testing conditions. In particular, a trial-and-error approach was performed in two steps. First, only the sets of $CRSS_s$ corresponding to RT and 300 °C were obtained. Then, based on these results, the $CRSS_s$ corresponding to the remaining testing conditions were calculated. Only basal, prismatic, second-order pyramidal $\langle c+a \rangle$ and tensile twinning were included in the model. Compression or double twinning were not considered. This issue did not have any important effect on the first step of the fitting procedure as these secondary twin modes were not activated at RT and 300 °C for the grains under study. Its effect on the second step of the fitting procedure will be discussed later. The main challenge involved in the first step of the fitting procedure was to obtained two sets of $CRSS_s$ corresponding to RT and 300 °C that were able to reproduce the global mechanical behaviour of pure Mg at these temperatures taking into account the real temperature dependency of the different deformation modes of pure Mg. To do so, the CP parameters of basal slip and tensile twinning were fixed for both sets, and only the ones corresponding to prismatic and second-order pyramidal $\langle c+a \rangle$ slip were allowed to vary. As in the previous section, this study was performed in Grains 1, 3, 5 and 7. In addition to the residual deformation around the indents, the P_{max} - δ curves were considered for this fitting procedure. After a significant number of trial and errors attempts, two final sets of $CRSS_s$ corresponding to RT and 300 °C were obtained (Table 7.4). The simulated topographies corresponding to these two sets of CP parameters are depicted in Fig. 7.9. It can bee clearly seen that the simulated residual topographies yielded by the enhanced CP model, together with the fitted set of CP parameters obtained for RT and 300 °C, reproduce fairly well the mechanical behaviour of pure Mg single crystals not only at RT, where basal slip and tensile twinning dominate, but also at 300 °C, where tensile twin activity has almost disappeared. This newly found correspondence between the experimental observations and simulations reveals that the consideration of the higher magnitude of twin nucleation stress with respect to twin propagation is essential. At low temperatures, the high $CRSS_s$ of the non-basal slip systems may induced a stress state that can promote tensile twinning. However, at high temperatures, these non-basal slip systems are soft enough so the induced stress state is not sufficiently severe to activate tensile twinning. To further check the validity of the obtained sets of $CRSS_s$, the experimental and simulated P_{max} - δ curves were compared. Fig. 7.10 reveals that there is also a good match between the experiments and simulations, and therefore, it can be concluded that the sets of CP parameters obtained for RT and 300 °C reproduce faithfully the mechanical behaviour of pure Mg single crystals at those temperatures.

	Slip/Twin system										
	Basal$\langle a \rangle$			*Prismatic*$\langle a \rangle$			*Pyramidal*$\langle c+a \rangle$			*TT*	
	τ_0	τ_{sat}	h_0	τ_0	τ_{sat}	h_0	τ_0	τ_{sat}	h_0	τ_{nucl}	τ_{pro}
RT	2.5	15	50	40	120	3000	50	150	3000	60	10
100 °C	2.5	15	50	31.25	97.5	2262.5	45	135	2375	60	10
150 °C	2.5	15	50	22.5	75	1525	40	120	1750	60	10
200 °C	2.5	15	50	13.75	52.5	787.5	35	105	1125	60	10
250 °C	2.5	15	50	6.09	32.81	142.19	30.63	97.88	578.13	60	10
300 °C	2.5	15	50	5	30	50	30	90	500	60	10

Table 7.4: Set of CP parameters (MPa) obtained in this research for pure Mg corresponding to RT, 100 °C, 150 °C, 200 °C, 250 °C, 300 °C.

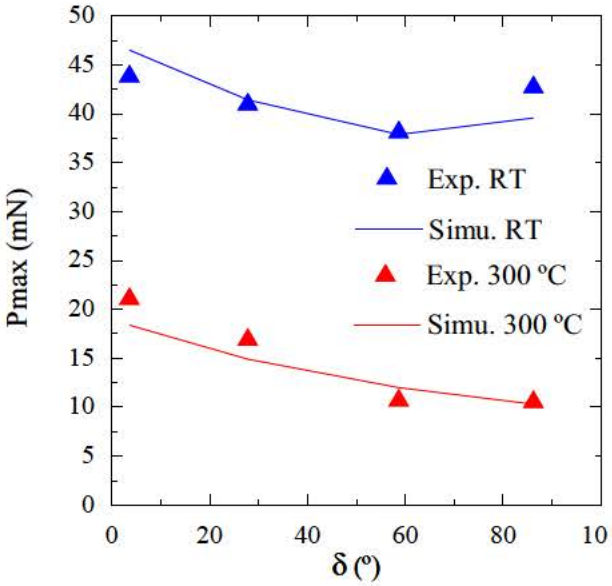

Fig. 7.10: Experimental and simulated P_{max} - δ curves corresponding to RT and 300 °C.

Using these results as lower and upper bounds, the CP parameters corresponding to 100 °C, 150 °C, 200 °C and 250 °C were obtained keeping the CP parameters of basal slip and tensile twinning constant, and only varying the ones corresponding to prismatic and second-order pyramidal $\langle c+a \rangle$ slip. In this second fitting procedure, only the residual topography around the indents were considered, excluding from the analysis the P_{max} - δ curves. This decision was based on the fact that compression and/or double twinning, deformation modes eventually activated during the indentations of grains under study at the specified testing conditions, were not considered in the CP model. As it has been shown in previous sections, CT_s are quite small in comparison with TT_s. Therefore, their effect on the residual topography is expected to be minimum. However, the stress relaxation related to the activation of these deformation modes leads to important oscillations on the load-displacement curves (Section 7.4.4), which may have an important effect on the corresponding P_{max} - δ curves. After a significant number of trial and errors attempts, the CP model was calibrated to reproduce also the mechanical behaviour of pure Mg at 100 °C, 150 °C, 200

°C, 250 °C. Fig 7.11 depicts the experimental and simulated topographies under such testing conditions, showing a fairly good agreement in the qualitative evolution with temperature of the deformation profiles around the indents.

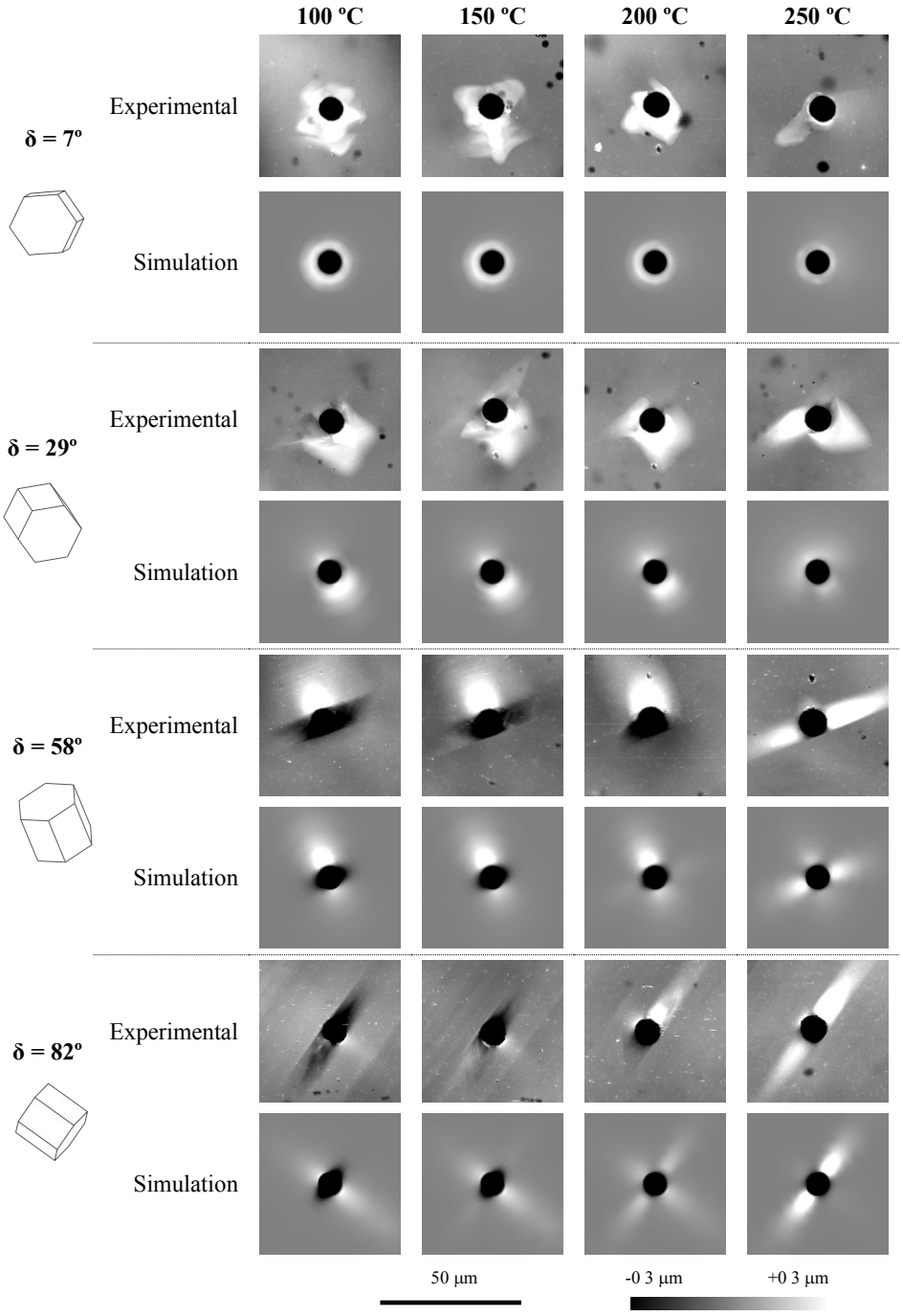

Fig. 7.11: Experimental and simulated residual deformation around the indents performed in Grains 1, 3, 5 and 7 at 100 °C, 150 °C, 200 °C and 250 °C. The simulations were preformed using the CP parameters listed in Table 4.

Table 7.4 includes a complete set of CP parameters that reproduce the mechanical behaviour of Mg at temperatures ranging from RT to 300 °C. Such evolution of the yield strength with temperature of the different slip and twinning systems is graphically described in Fig. 7.12. Regarding the slip systems (basal, prismatic and second-order pyramidal $\langle c+a \rangle$), only the initial CRSS is shown. However, for tensile twinning, the stress related to the nucleation, TT (Nucleation), and propagation, TT (Propagation) are included. For all the temperatures, the fitted values of the rate-sensitive exponent for slip (m_{sl}) and twinning (m_{tw}) are 0.1 and 0.03 respectively.

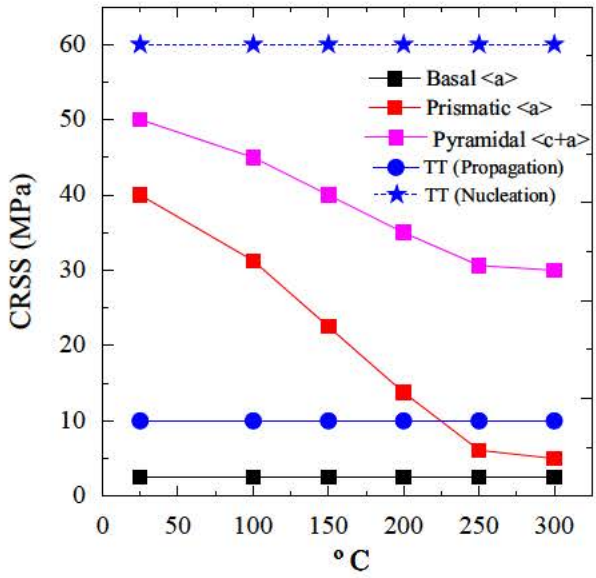

Fig. 7.12: Evolution with temperature of the yield strength of the different single crystal deformation modes obtained in this research. Regarding the slip (basal, prismatic and second-order pyramidal $\langle c+a \rangle$), only the initial CRSS is shown. However, for TT, the stress related to the nucleation (TT Nucleation) and propagation (TT Propagation) are included.

Finally, the evolution of the activities of the different slip and twinning systems with temperature was analysed. In order to calculate the relative activity, $rAct$, of each deformation mode i, the following equation is used:

$$rAct_i = \frac{tAct_i}{tAct} \tag{7.1}$$

where $rAct_i$ is the total activity of the deformation mode i and $rAct$ is the total activity of all the deformation modes. The total activity of the different slip systems (basal, prismatic and second-order pyramidal $\langle c+a \rangle$), $tAct_{Slp}$, is calculated as follows:

$$tAct_{Slp} = \sum_{Iter=0}^{FinalIter} \sum_{IP=0}^{TotalIO} \left(\left(\Delta\gamma_{Iter}^{IP} \right)_{Slp} * \left(1 - TTVF_{Iter}^{IP} * Vol_{Iter}^{IP} \right) \right) \tag{7.2}$$

where $Iter$ refers to each iteration number of the simulations, IP corresponds to each integration point number of the model, $\left(\Delta\gamma_{Iter}^{IP}\right)_{Slp}$ is the increment of the plastic shear, γ, of one particular IP in each $Iter$ of the slip system Slp, $TTVF_{Iter}^{IP}$ represents the total twin volume fraction of each IP in a specific $Iter$ and Vol_{Iter}^{IP} stands for the volume of the IP in each $Iter$. On the other hand, the total activity of tensile twinning, $tAct_{TT}$, is obtained using the following expression:

$$tAct_{TT} = \sum_{Iter=0}^{FinalIter} \sum_{IP=0}^{TotalIO} \left(\Delta TVF_{Iter}^{IP} * \gamma_{TT} * Vol_{Iter}^{IP}\right) \tag{7.3}$$

where ΔTVF_{Iter}^{IP} stands for the increment of the twin volume faction of each IP in a specific $Iter$ and γ_{TT} is the characteristic shear of tensile twinning, 0.129. Finally, $tAct$ can be calculated as the sum of the total activities of the slip systems, $tAct_{Slp}$, and tensile twinning, $tAct_{TT}$.

Fig. 7.13 shows the variation with temperature of the relative activity of the different slip and twinning systems for the 4 grains under study. First, it has to be mentioned that the low tensile twin activity observed at low temperatures can be justified as follows. On the one hand, in contrast with slip, tensile twinning has associated a fixed, and therefore, limited shear of 0.129 [17]. On the other hand, while the CP model developed in this research is able to reproduce the location of the twins at different temperatures, the size of such simulated twins is smaller than the one measured experimentally. This can be explained taking into account that the proposed CP model cannot capture the non-locality characteristic of tensile twinning. However, this issue does not alter significantly the global interpretation of our results. For the 4 grains analysed, basal slip is the most active deformation mode in the whole range of temperatures (RT - 300 °C). However, its activity decreases as temperature increases, effect that is more pronounced at medium and high declination angles. On the other hand, while prismatic activity is minor at RT, it dramatically increases with temperature. Such variation is more accused accused as the declination angle increases. Regarding the Second-order pyramidal $\langle c + a \rangle$ slip system, it is more active for any temperature in that grains with a smaller declination angle. In addition, all the grains show that the relative activity of this deformation mode is more or less constant from RT until 200 °C. At higher temperatures, its activity slightly decreases. Finally, tensile twin activity clearly decreases with temperature, becoming almost negligible at 300 °C.

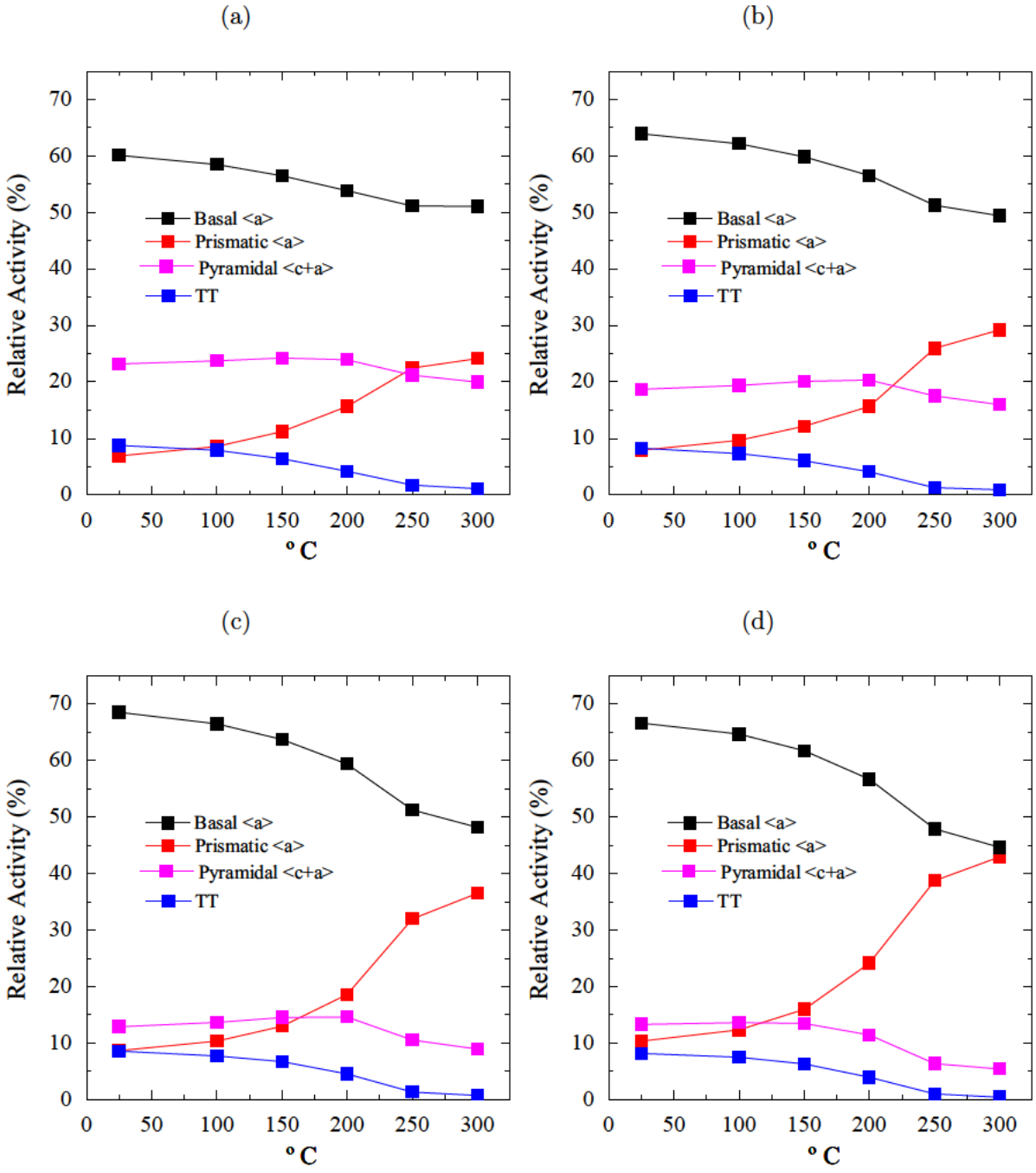

Fig. 7.13: Evolution of the relative activity of the different plastic deformation modes with temperature in the 4 grains analysed in the fitting procedure: (a) Grain 1; (b) Grain 3; (c) Grain 5; (d) Grain 7.

7.5 Conclusions

In the present chapter, the deformation mechanisms of pure Mg have been extensively studied combining experimental nanoindentation, EBSD, AFM and CPFE modelling at a wide range of temperatures. The following conclusions can be drawn:

- The analysis of the residual deformation and the microstructure around the indents confirms that the main deformation modes at RT are basal slip and tensile twinning. With increasing temperature, tensile twinning is progressively replaced by prismatic slip.
- Temperature has a strong influence on the shape, size, and distribution of TT_s. In particular, whilst TT_s develop the well-known lenticular shape at RT, they acquire a much more rounded shape at higher temperatures. Additionally, at RT, the strain is preferentially accommodated by the nucleation of successive TT_s, which grow up to a certain critical volume; however, at higher temperatures, the deformation is accommodated by the long-range propagation of individual twins.
- CT_s are observed at temperatures ranging from 100 °C to 300 °C in grains with low and medium declination angles, and their growth is more limited than that of TT_s. These observations are attributed to the complex shuffling events associated to this twinning mode
- A novel CP model that takes into account the specific features of the micromechanics of tensile twinning, i.e, the higher magnitude of nucleation stresses with respect to propagation stresses, has been successfully calibrated and implemented. This model is able to reproduce the mechanical behaviour of pure Mg single crystals at a wide range of temperatures considering the isolated temperature dependency of the different deformation modes.

"What we observe as material bodies and forces are nothing but shapes and variations in the structure of space"

Erwin Schrödinger

8

Conclusions and future work

8.1 Main conclusions

The following main conclusions can be drawn from this research:

- The competition between the main deformation mechanisms of pure Mg single crystals has been successfully analysed using nanoindentation from an experimental, analytical, and numerical point of view. In particular, it has been found experimentally that, the microtexture and deformation patterns developed near the indents, together with the hardness (or P_{max} reached during the indentation), highly depend on a combined action of the crystallographic orientation of the indented plane and testing temperature. The analytical and numerical models developed in this Ph.D. thesis show that, while the main active deformation modes at RT are basal slip and tensile twinning, as temperature increases, tensile twin activity decreases dramatically and, in turn, prismatic activity increases notably.
- A novel CP model which is able to successfully reproduce the competition between the different deformation modes of pure Mg at different temperatures has been developed. In contrast with previous CP models, the enhanced model proposed in this research

takes into account that twin activation is a process that demands a much more severe stress state than twin propagation. It is demonstrated that this aspect is essential in order to simulate the evolution of twin activity with temperature.

- The effect of twin mode and temperature on the shape of the developed twins has been deeply analysed. First, it is shown that, while the TT_s developed at RT depict the well-known lenticular configuration, they acquire a much more rounded shape at higher temperatures. In addition, while TT_s can readily grow and reach areas further away from the contact area between the indenter and the sample, CT_s developed at intermediate temperatures are very small and are located only in the areas near the indenter. In addition, it was shown that the activation of CT_s during an indentation process induces a relaxation of the system which gives rise to an important oscillation in the load-displacement curve.

- The effect of the indentation size on tensile twinning has been also deeply studied. It particular, it was found that the activation of this deformation mode decreases dramatically as the indentation depth decreases. For grains with a very low δ, tensile twin activity is completely suppressed below a critical indentation depth. These results confirm that twin activation is a process that requires the concentration of high stress in a certain volume.

- Finally, it is shown that nanoindentation, together with AFM, EBSD and CPFE simulation, can be used to estimate the $CRSS_s$ of novel Mg alloys in a quick and effective way at a wide range of temperatures. From a industrial point of view, a simplified approach to characterise the $CRSS_s$ of the basal and non-basal slip systems is proposed. The proposed approach, which has been designed to be as much practical as possible, is based on the variation of the hardness with the δ. This methodology was validated in pure Mg using a set of $CRSS_s$ taken from the literature. With the help of CPFE simulation, a set of practical graphs were developed that allows to easily identify the main active deformation modes based on the qualitative shape of the H - δ curves. This methodology was used to determine the effect of the alloying elements of the rare-earth Mg alloy MN11 on the different slip systems. It was found that, in comparison with pure Mg, the ratio between the $CRSS_s$ of the basal and non-basal slip systems is reduced dramatically, which explains why this kind of Mg alloys show a very low yield stress anisotropy.

8.2 Future work

The present Ph.D. thesis has constituted a significant step forward in studying the micromechanics of Mg alloys by instrumented nanoindentation, AFM, EBSD and CPFE simulation. The widespread application of the techniques developed in the framework of this investigation in the development of novel Mg alloys with enhanced mechanical properties seems a natural line of work. On the other hand, there are still several questions unresolved that need to be addressed. In particular, the following topics are proposed as future work:

- *Development of a novel non-local CP model to improve the prediction of the size and shape of the simulated TT_s.* The conventional CP models used in the first part of this Ph.D. were able to qualitatively reproduce the location of the TT_s and their corresponding effect on the residual deformation around the indent. However, they failed to reproduce the evolution of twin activity with temperature. This issue was solved in Chapter 7, where an enhanced CP model that takes into account the micromechanics of tensile twinning was developed. However, this CP model still has some limitations. In particular, the proposed model is not able to reproduce the actual size of the the TT_s, aspect that is clearly reflected in the different length of the experimental and simulated sink-ins. In order to address this problem, the development of a novel non-local CP model is necessary. This new model should assign a different twinning constitutive law to each IP depending on its state and on the one corresponding to the surroundings material points. If a specific material point, and the ones located in its vicinity, have not undergone twinning, a constitutive law that takes into account the severe stress state necessary to nucleate twinning should be applied. However, in the case that (i) a specific material point has already undergone twinning, or (ii) that material point has not twinned but at least one located in its surroundings has and they are properly aligned according to the active variant of the latter, a different constitutive law for twinning, which should be aimed at modelling twin propagation which demands a much less severe stress state than twin nucleation, should be applied. In this way, the size and shape of the simulated TT_s would reflect in a much more accurate way the experimental behaviour. The development of such advanced model may include other modelling techniques like phase field.

- *Application of inverse optimisation algorithms to the methodology developed in this Ph.D. thesis.* One of the main objectives of the present research has been to determine the CP parameters of pure Mg and several Mg alloys under different testing conditions. The proposed methodology is based on the comparison of the experimental and simulated H - δ and P_{max} - δ curves as well as the experimental and simulated topographies using a trial-and-error approach. This procedure could be improved by integrating an inverse optimization algorithm instead of the manual fitting procedure used so far. In addition, instead of the H - δ and P_{max} - δ curves, which only reflects the maximum load reached during the indentation, the whole load-displacement curves of the the simulated and experimental indents could be used as a fitting parameter, obtaining quantitative information about the elastic, viscoplastic and work hardening behaviours of the tested material. Regarding these objectives, first steps have already been taking in order to adapt the inverse optimization algorithm developed by Herrera-Solaz et al. [53] to the specific problem proposed in this research.

- *Study of new Mg alloys of industrial interest using the techniques developed in this research.* The micromechanic studies carried out in this Ph.D. have been focused on pure Mg. Only in Chapter 6 they were applied to a rare-earth Mg alloy, MN11, where the effect of the alloying additions on the $CRSS_s$ of the different slip systems was quantified at RT. As future work, it seems appropriate to apply the developed methodologies in this research, further enhanced by the improvements proposed in the last two points, to novel Mg alloys of special interest for the industry. In this sense, rare-earth Mg alloys constitutes ideal candidates as the intermetallic compounds formed in these alloys de-

crease significantly the difference between the $CRSS_s$ of the soft and hard slip systems, which is traduced in a much more isotropic and ductile mechanical behaviour of the material. Regarding this issue, close collaborators have already manufactured several Mg binaries alloys with Y and Gd additions respectively. In particular, the following binary systems have been produced: Mg-1%Y, Mg-3%Y, Mg-5%Y, Mg-1%Gd, Mg-3%Gd and Mg-5%Gd, some of which have already been tested. Once the experimental characterisation is finished, the effect of the alloying additions of each different system will be determined applying the described methodology. This study, which could be extended to high temperatures, will be performed by members of the department involved in the development of this research.

- *Study the effect of GB_s on twin transmission by nanoindentation and CPFE simulation.* All the studies carried out in this Ph.D. thesis and the previous tasks proposed as future work are targeted at studying the single crystal behaviour of Mg alloys, without considering the effect of GB_s. However, it is well known that GB_s have a tremendous effect on the global mechanical behaviour of polycrystalline Mg alloys [12, 29, 32, 153–159]. One vital aspect is the transmission of TT_s across GB_s, which is known to depend on the misorientation angle of the adjacent grains [152]. In particular, the smaller the misorientation angle, the easier the transmission of a TT across the GB_s becomes. However, the majority of the studies performed on this issue are carried out in post-mortem polycrystalline samples, aspect that imposes important limitations. For example, it is not possible to know the "direction" of the twin-transfer event, i.e., one does not know if the TT was originated in Grain A and then transmitted to Grain B or the other way around. In addition, it is well known that GB_s can act as nucleation sites for TT_s [160, 161]. In same cases, two TT_s are generated in the two adjacent grains. This process, which leads to the formation of the so-called *adjoining twin pairs* [158, 160], cannot be differentiate from a twin-transfer event from a post-mortem observation of a polycrystalline sample although the nature of both processes is completely different. Another disadvantage of the commented approached is that one cannot choose which GB will be subjected to a twin-transfer event, as the whole process is dominated by the complex field of local stresses develop across all the sample and therefore, cannot be controlled. Finally, although the misorientation angle is the main parameter that has been considered to dominate the twin transfer across GB_s, a GB is defined by a total of 5 parameters [162, 163], and therefore, the effect of some of them have not been studied. These limitations prevent (i) the complete experimental characterisation of the twin-transfer event across GB_s and (ii), the calibration of advanced CP models that take into account the effect of GB_s on twin transmission. In order to overcome these limitations, and as a part of future work, a new approach is proposed to study this phenomenon based on experimental nanoindentation, AFM, EBSD and CPFE simulation. In particular, the proposed method would rely on performing large indentations (in order to avoid possible ISE) in prismatic grains where the activation of TT_s is profuse and easily detectable due to the formation of a characteristic two-fold sink-in aligned with the basal planes (Chapter 5). If these indentations are placed close to a GB, the twin-transmission phenomenon could be studied by analysing the propagation of the sink-ins, and the associated twins, from the indented grain to the adjacent one. This methodology present important advantages in comparison with the

previous approach: (i) the "direction" of the twin-transfer event is known, (ii) the GB of study can be chosen beforehand and (iii), the study of pure twin-transfer events, and no other phenomena like the formation of "adjoining twin pairs", is guaranteed. The proposed study is quiet advanced and important part of the related tasks have already been performed. For example, Fig. 8.1 shows the EBSD inverse pole figure map in a direction parallel to the indentation axis of an sphero-conical indentation performed in a prismatic grain close to another grain, both grains with a very similar crystallographic orientation (misorientation angle = 8.6°). As it can be observed, the twins are easily transmitted across the GB. On the other hand, Fig 8.2 shows a similar indentation performed again in a prismatic grain but this time the adjacent grain has a quite different crystallograhic orientation (misorientation angle = 88.5°). As it can be observed, the TT_s are completely stopped by the GB. Pending tasks regarding this topic are focused on the analysis of the experimental data already obtained. Finally, this study will be completed by the development of and advanced CP model, which ideally will be a continuation of the one specified in the first task proposed above as future work, that models the twin transfer across GB_s taking into account its misorientation angle.

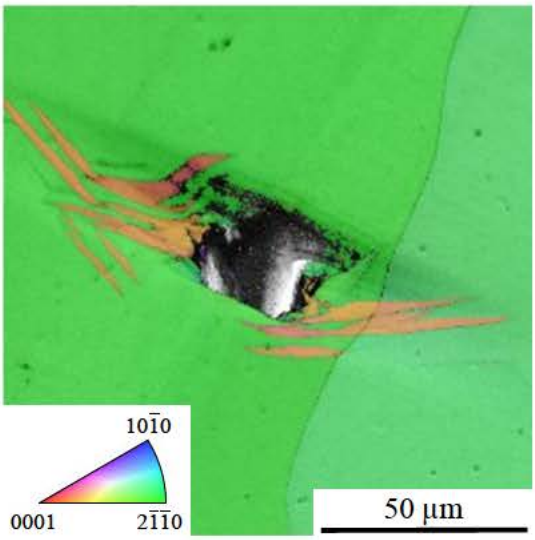

Fig. 8.1: EBSD inverse pole figure map in a direction parallel to the loading axis of an indentation performed in a prismatic grain close to another grain with a very similar orientation (misorientation angle = 8.6°).

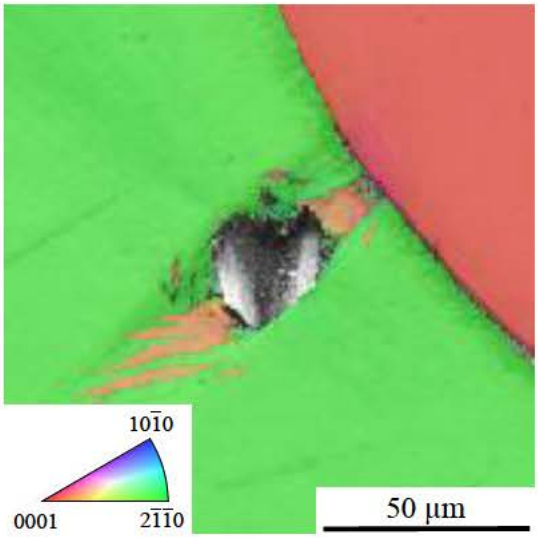

Fig. 8.2: EBSD inverse pole figure map in a direction parallel to the loading axis of an indentation performed in a prismatic grain close to another grain with a very different orientation (misorientation angle = 88.5°).

"Science, my lad, is made up of mistakes, but they are mistakes which it is useful to make, because they lead little by little to the truth"

Jules Verne

A

Effect of the of tip radius on the finite element simulation of an indentation

In this appendix, the effect of changing the tip radius of an sphero-conical indenter on the response of a simulated indentation process will be studied. This study is applied in Chapter 7, where the same geometrical modification was applied in the simulations procedures. In particular, an initial sphero-conical indenter with a tip radius of 1 μm and an apex angle of 90° is considered. Such initial indenter is modified so the tip radius is finally set to 2.5 μm. The main reason behind this simplification is that, in order to reproduce the simulations using the first configuration, very fine meshes were required in the FE model due to the very high deformation of the elements near the tip. This aspect means an important increase in the computational costs, and therefore, is especially important taking into account the large amount of simulations that were necessary in the trial-and-error fitting procedures carried out in Chapter 7. In addition, in order to obtain a residual imprint of the same size using the new tip radius than the one corresponding to the initial geometrical configuration, the final indentation depth has to be modified (Fig. A.1). If the initial tip radius (R_1) has associated an indentation depth of h_1, the modified indenter with a tip radius of R_2 ($R_2 > R_1$) has

associated an indentation depth of h_2 expressed as

$$h_2 = h_1 - h_{diff} \tag{A.1}$$

where h_{diff} is easily calculated using the following expression (Fig. A.1)

$$h_{diff} = (R_2 - R_1) * \left(\frac{1}{sin\alpha} - 1 \right) \tag{A.2}$$

Taking into account that for our specific case, $R_1 = 1\mu m$, $R_2 = 2.5\mu m$, $h_1 = 4\mu m$ and $\alpha = 45°$, Eq. A.2 yields a result of $h_{diff} = 0.621\mu m$, and therefore, $h_2 = 3.379\mu m$, which was the final indentation depth used in the simulations.

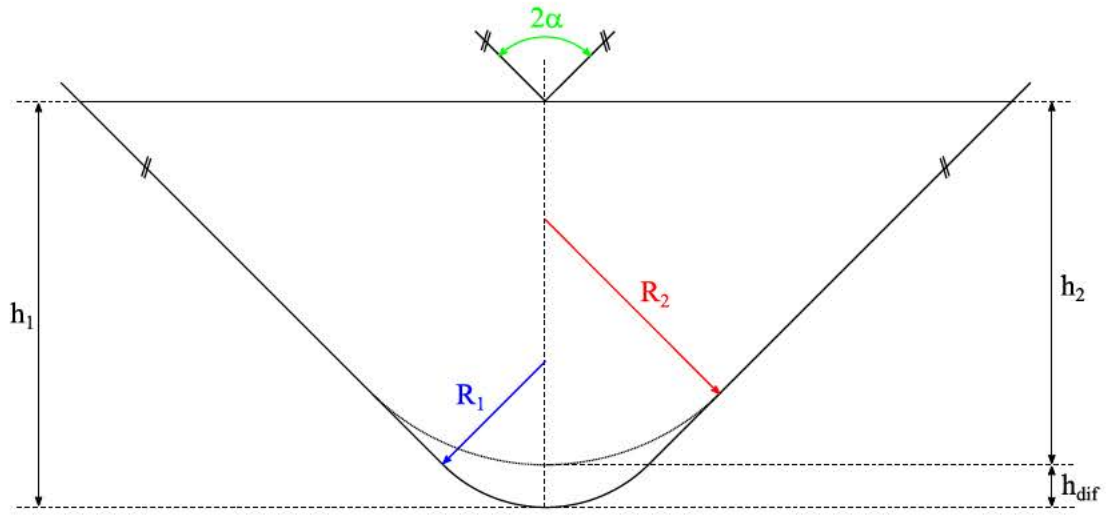

Fig. A.1: Schematic of the geometrical modification of the indenter tip.

In order to guarantee the validity of our results, a careful simulation analysis of the effect of the previous geometry modification on the residual deformation around the indent and on the maximum load reached during the indentation, which were the two main aspects used in order to compare the experimental and the simulated results, was performed. The CP model described in Section 4.2.3 was used for this purpose. In particular, this study was carried out in two crystallographic orientations, Grain 1 ($\delta = 7°$) and Grain 7 ($\delta = 82°$) of Chapter 7, and using in each case the two sets of $CRSS_s$ representative of the mechanical behaviour of Mg at RT and 300 °C (Table A.1). Two indents were simulated per grain and temperature: one of them with an indenter tip radius of 1 μm and applying an indentation depth of 4 μm (Full Model), an other one using an indenter tip of a radius of 2.5 μm and applying a final indentation depth of 3.379 μm (Red. Model). The final indentation depths were modified to 3.52 μm and 2.84 μm (using the same scheme than the ones shown in Fig. A.1) for the Full Model and Red. Model, respectively, in the case where Grain 1 was indented using the

$CRSS_s$ corresponding to 300 °C. In this particular case, the deformations induced in the Full Model (and applying an indentation depth of 4 μm) were so high that any of the tested meshes were able to give a proper convergence in the simulation. However, this particular instance is even more restrictive than the previous one as it is expected that the specified geometrical modification has a more severe effect as the final indentation depth decreases.

	Slip/Twin system										
	$Basal\langle a\rangle$			$Prismatic\langle a\rangle$			$Pyramidal\langle c+a\rangle$			TT	
	τ_0	τ_{sat}	h_0	τ_0	τ_{sat}	h_0	τ_0	τ_{sat}	h_0	τ_{nucl}	τ_{pro}
RT	2.5	15	50	40	120	3000	50	150	3000	60	10
300 °C	2.5	15	50	5	30	50	30	90	500	60	10

Table A.1: Set of CP parameters (MPa) corresponding to RT and 300 °C for pure Mg.

Fig. A.2 shows the residual deformation around the simulated indents performed in Grains 1 and 7, using the Full model and Red. Model, setting the CP parameters corresponding to RT. As it can be observed, negligible differences are found between the results issued by both models.

Very similar conclusions can be obtained using the CP parameters corresponding to 300 °C (Fig. A.3). In this case, only tiny differences are found in the residual topographies of Grain 1. However, they are still almost negligible and, as commented before, this case is more restrictive than the general one.

On the other hand, it is clear that the geometrical simplification previously described will affect the load-displacement curve, specially taking into account that the final indentation depth of both models is different. Fig. A.4 shows the loading segment of the load-displacement curves of the simulated indentations, each of them carried out using the Full Model and Red. Model, performed in the two grains analysed and setting the CP parameters to RT and 300 °C. As it can be observed, although the curves issued by both models are different, the maximum load registered is almost the same for both models for any testing condition.

It can be therefore concluded that the geometrical simplification introduced into the FE model has negligible effects on both the residual deformation around the indents as well as on the maximum load reached during the indentation, which were the main two parameters used in the fitting procedures, under any testing condition for the range of indentation depths used in this research.

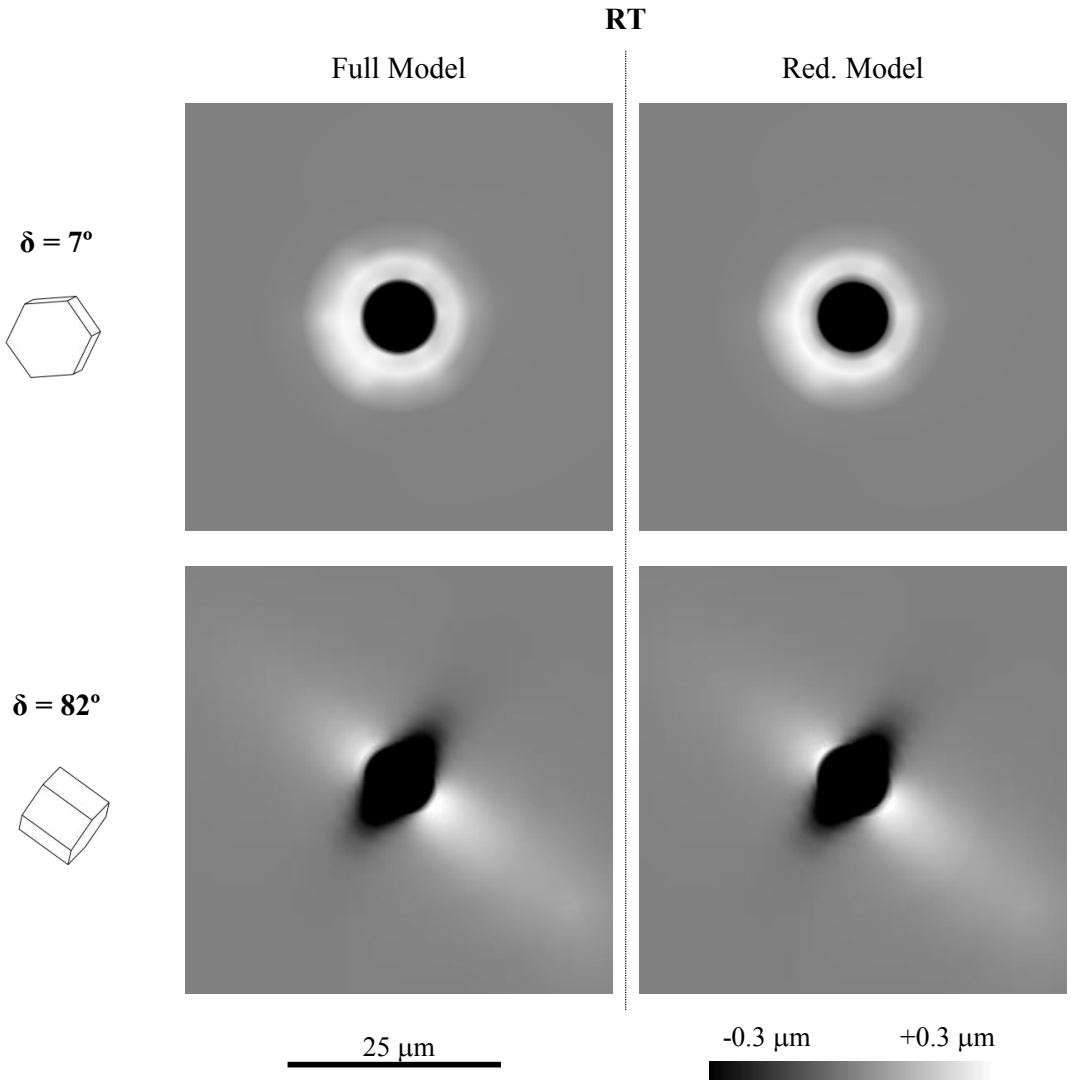

Fig. A.2: Residual deformation around the simulated indents preformed in Grains 1 and 7, using the Full Model and Red. Model, setting the CP parameter corresponding to RT.

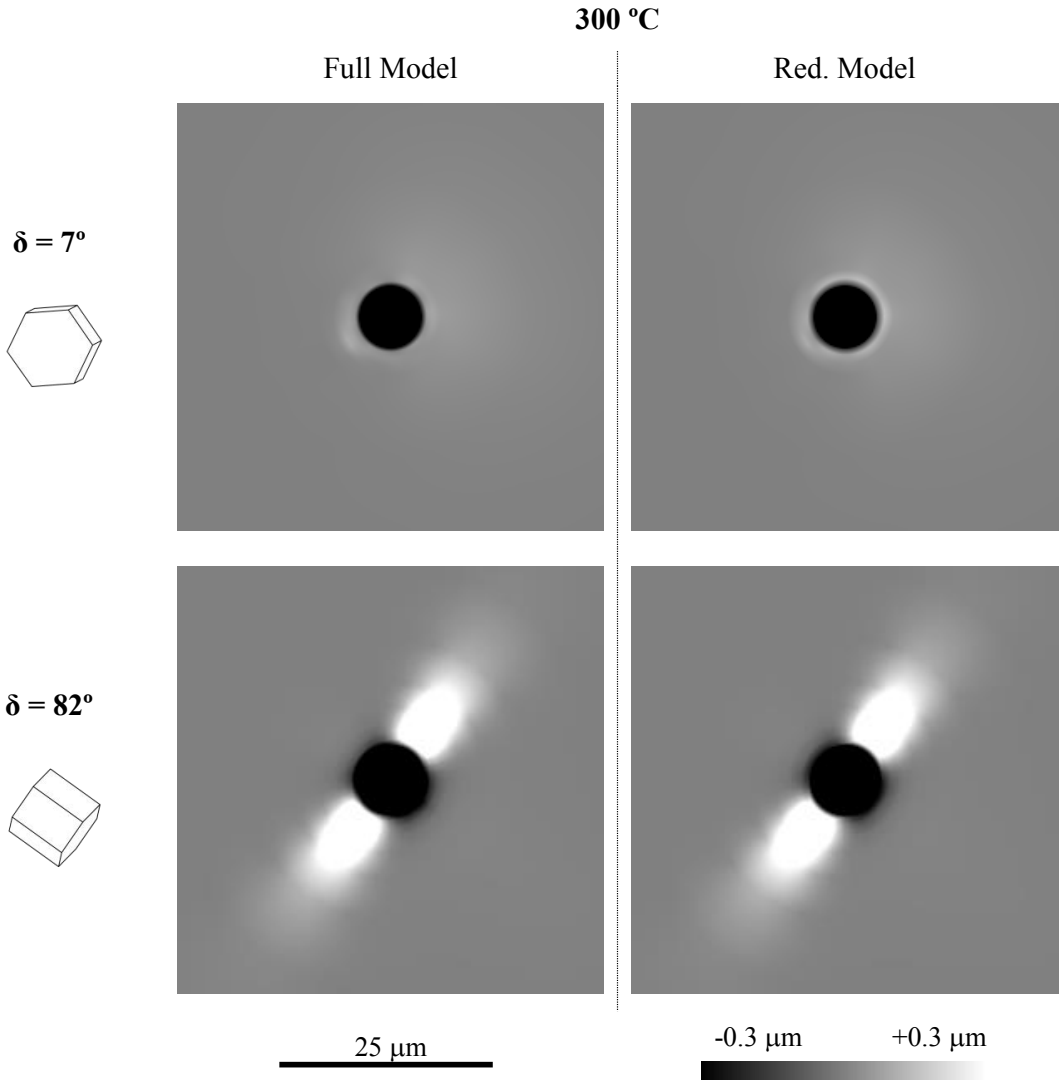

Fig. A.3: Residual deformation around the simulated indents preformed in Grains 1 and 7, using the Full Model and Red. Model, setting the CP parameter corresponding to 300 °C.

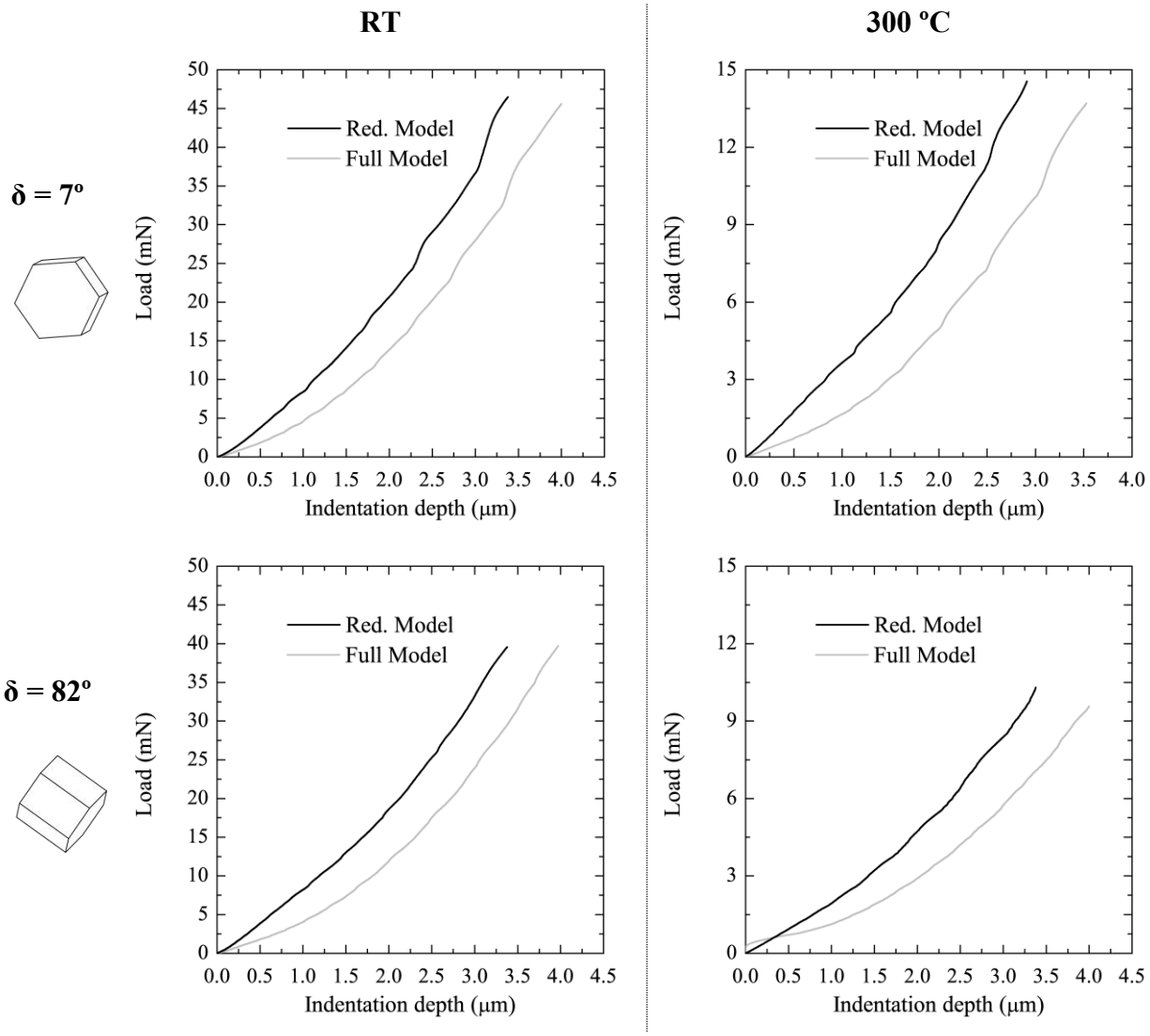

Fig. A.4: Loading segment of the load-displacement curves of the simulated indentations, each of them carried out using the Full Model and Red. Model, performed in the two grains analysed and setting the CP parameters corresponding to RT and 300 °C.

"The saddest aspect of life right now is that science gathers knowledge faster than society gathers wisdom"

Isaac Asimov

B

Slip activity in pure Mg at high temperature studied by nanoindentation

In this appendix, a study of the slip system activity of pure Mg at high temperature is performed combining nanoindentation, AFM, EBSD and CPFE simulation. This study is based on the experimental data shown in the present Ph.D. thesis in Chapter 7. In particular, the data from Grains 1 ($\delta = 7°$), 4 ($\delta = 42°$) and 7 ($\delta = 82°$) corresponding to 300 °C is used. The main objective of this study was to analyse the activity of the different slip systems under such conditions.

In order to perform this analysis, a CPFE simulation study was carried out based on a well-established CP model [57, 58]. This CP model is almost identical to the one described in Section 4.2.1, which differs only in the hardening laws. In particular, the evolution of the glide resistance, τ_c^α, of the CP model used in the current Appendix is govern by the following equation:

$$\dot{\tau}_c^\alpha = \sum_{\beta=1}^{N_{sl}} q^{\alpha\beta} h_0^\beta \left(1 - \frac{\tau^\beta}{\tau_{sat}^\beta}\right)^{a_{sl}} \left|\dot{\gamma}^\beta\right| \tag{B.1}$$

where $q^{\alpha\beta}$ is the interaction coefficient between the slip systems α and β, a_{sl} the hardening exponent, h_0^β the initial hardening modulus, τ^β the shear stress, τ_{sat}^β the saturation CRSS and $\dot{\gamma}^\beta$ the shear rate (the last 4 parameters correspond to the slip system β). In the present study, only the basal $\langle a \rangle$, prismatic $\langle a \rangle$ and second-order pyramidal $\langle c+a \rangle$ slip systems were considered (Table B.1). Tensile twinning was not included in the model formulation since negligible twinning activity was observed in the experiments at 300 °C. The elastic parameters, which where considered to be independent of temperature, were taken from Zhang and Joshi [49]. In particular, the following values were used: C_{11} = 59.40 GPa, C_{12} = 25.61 GPa, C_{13} = 24.44 GPa, C_{33} = 61.60 GPa and C_{44} = 16.40 GPa. For the sake of simplicity, the parameters h_0^β, a_{sl} and $q^{\alpha\beta}$, together with the reference shear strain rate, $\dot{\gamma_0}$ and rate-sensitive exponent m_{sl} (Eq. 4.4), were considered equal for all the simulations (Table B.1). While a full calibration of the model would have demanded a complete study of these parameters, this work is focused mainly on the quantification of the relative strength of the different slip modes at 300 °C.

Slip system	Slip plane	Slip plane	Number of systems	$\dot{\gamma}_0$ (s^{-1})	m	a_{sl}	$q^{\alpha\beta}$ $\alpha=\beta$	$q^{\alpha\beta}$ $\alpha=\beta$	h_0 (MPa)
Basal $\langle a \rangle$	$\{0002\}$	$\langle 11\bar{2}0 \rangle$	3						
Pris. $\langle a \rangle$	$\{1\bar{1}00\}$	$\langle 11\bar{2}0 \rangle$	3	0.001	10	2	1	0.2	50
Second-order Pyra. $\langle c+a \rangle$	$\{11\bar{2}2\}$	$\langle 11\bar{2}3 \rangle$	6						

Table B.1: Common material properties used in all the simulations procedures.

A three-dimensional FE indentation model was generated to reproduce the indentation process [164]. A total of 9160 hexahedral eight-node elements were used to discretize the sample. The indenter was modelled as a rigid conical body, keeping the same apex angle as in the experiments. The simulated tip radius was set to 2.5 μm although this parameter was 1 μm in the experiments in order to avoid excessive deformation of the elements in contact with the indenter tip. As specified in the Appendix A, this modification does not affect both the residual deformation around the indent and the maximum load reached during the indentations (which were the two main parameters used to compare the experimental and the simulation results). In addition, the final indentation depth was chosen in such a way that the experimental and simulated final imprint have the same size. Finally, the friction coefficient was set to 0.2 in all the simulations.

A manual fitting procedure was performed in order to obtain the non-fixed plastic parameters of the model: the initial CRSS, τ_0^α, the saturation CRSS, τ_{sat}^α and the initial hardening modulus, h_0, of each slip mode. Fig. B.2 shows the simulated topographies corresponding to four selected sets of $CRSS_s$ as a function of the grain orientation. It can be seen that the surface profiles around the indents are highly affected by both the crystallographic orientation of the indented plane as well as the choice of the CP parameters. In the first set of $CRSS_s$, basal slip is the softest deformation mechanisms. In the grain with $\delta = 7°$, the corresponding simulated profile is a well-defined concentric pile-up around the indent whereas in the other two orientations ($\delta = 42°$and $\delta = 82°$) the simulated profile is a twofold symmetric pileup

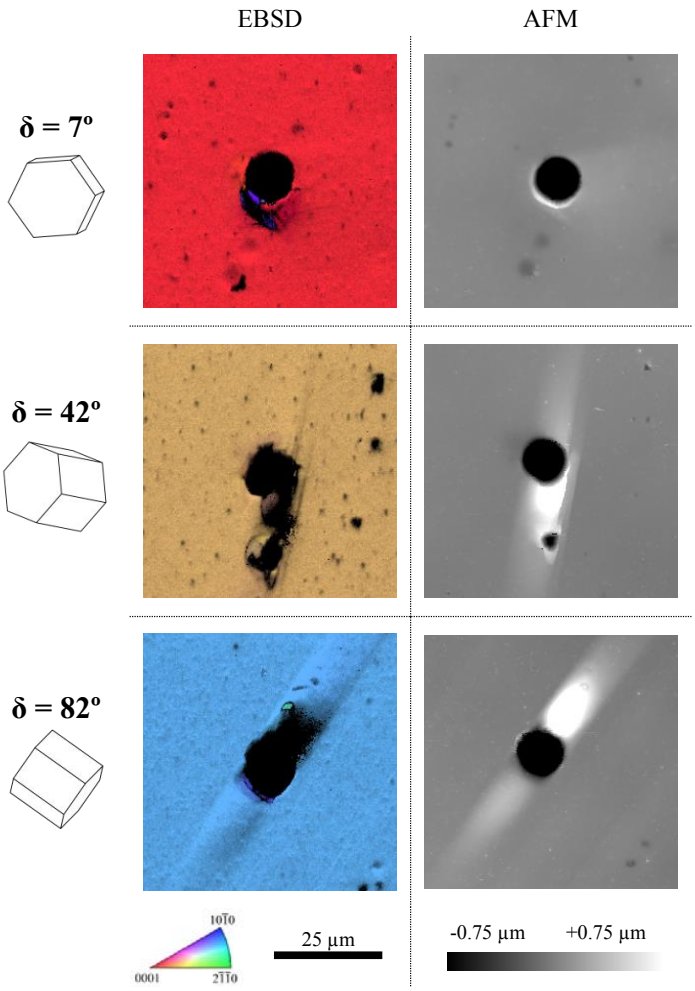

Fig. B.1: AFM topography maps and EBSD inverse pole figure maps in the direction parallel to the indentation axis corresponding to representative indents performed in the three grains under study.

aligned with the c-axis. In the second set of $CRSS_s$, second-order pyramidal $\langle c+a \rangle$ slip is the softest deformation mechanism. The deformation profiles around the indents are similar to those corresponding to the first set. However, in this case, the out-of-plane displacement profiles are significantly smoother. When the third set of $CRSS_s$, characterised by a very soft prismatic slip system, is used in the simulations, the grain with $\delta = 7°$ exhibits a diffuse concentric pile-up around the indent while in the two crystallographic orientations with higher declination angles ($\delta = 42°$ and $\delta = 82°$), a twofold symmetric pile-up pattern aligned with the basal planes develops. Based on these results, a trial-and-error approach was used to find an optimized set of $CRSS_s$ which gave a reasonably good match between the simulated and the experimental surface profiles around the indents. Fig. B.2 indicates the ratios of the initial CRSS and the saturation CRSS of non-basal slip systems with respect to the basal slip mode for the optimized set. It was found that a good match was obtained when the CRSS of

basal and prismatic slip were both significantly smaller than that of second-order pyramidal $\langle c+a \rangle$ systems. Using this optimized CRSS set, the sum of the basal and prismatic activity was found to represent, respectively, 85 %, 90 % and 99 % of the global activity at 300 °C in the three orientations studied ($\delta = 7°$, $\delta = 42°$ and $\delta = 82°$). Although it is known that the indentations performed in HCP metals where prismatic slip is the dominant deformation mechanisms lead to the same kind of twofold pile-up profiles as the observed in this work [58], only the combined activation of basal and prismatic slip can reproduce the elongated shape of the residual deformations that develop in Mg at 300 °C in the two grains with higher declination angles.

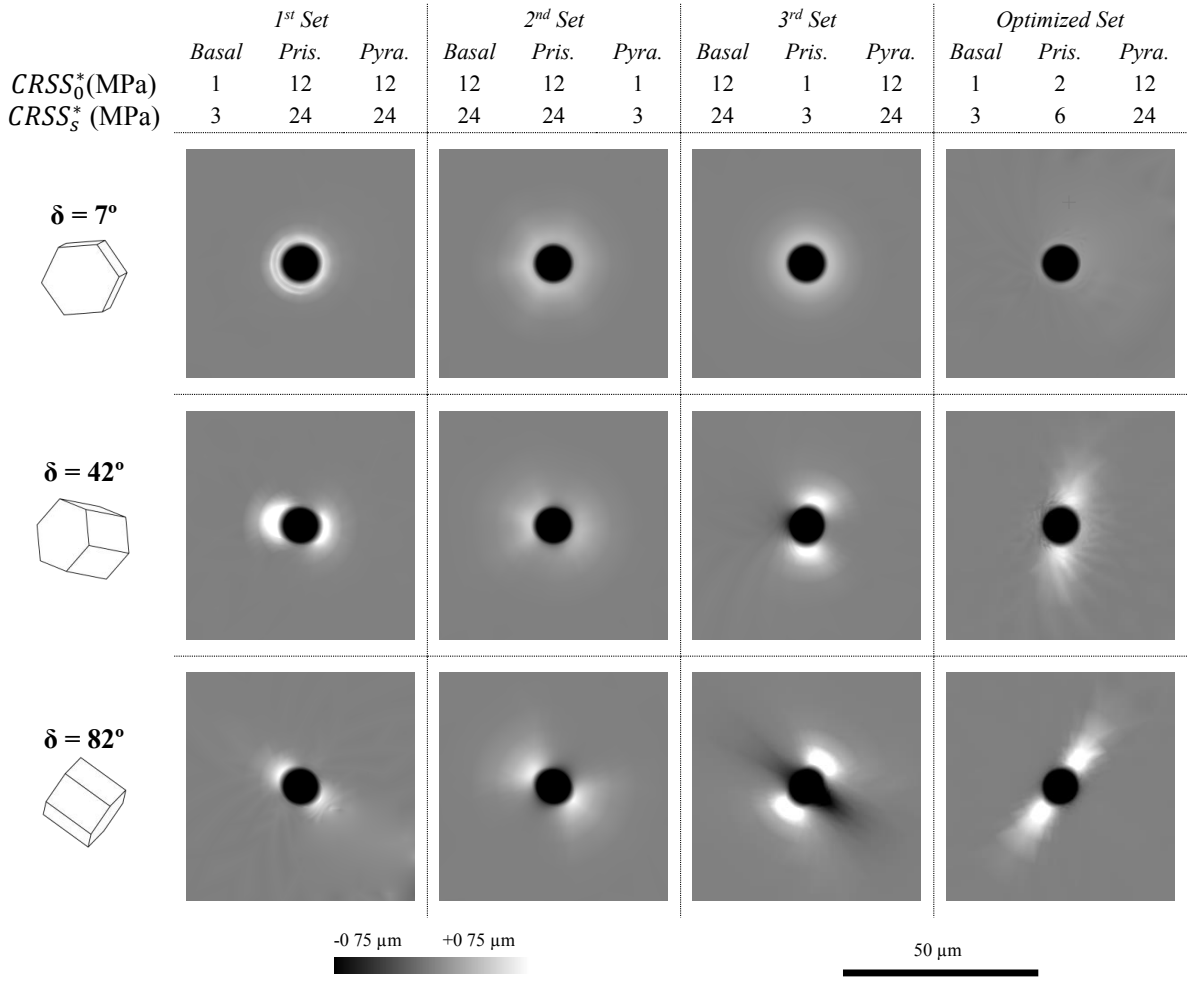

Fig. B.2: Simulated topographies corresponding to four selected sets of $CRSS_s$, each one tested in the 3 crystallographic orientations analysed. In each set, the corresponding $CRSS_s$ (detailed above the images) are normalized with respect to the initial CRSS of the softest deformation mode.

The variation of the P_{max} with the declination angle was also analysed. Fig. B.3 compares the outcome of the simulations for the four selected sets of CRSS ratios studied in Fig. B.2 with the experimental results. P_{max}, and not the hardness values, are compared as, due to the very large pile-ups observed experimentally at 300 °C, the application of the Oliver and Pharr method may lead to significant errors [165]. Since this study is focused on the relative comparison between the different slip systems, the maximum load was normalized with respect to that of the grain with the smallest declination angle ($\delta = 7°$). As with the residual topographies around the indents (Fig. B.2), the normalized P_{max} - δ curves are also strongly affected by the relative strength of the different slip systems. Fig. B.3 shows that only the normalized P_{max} - δ curve corresponding the optimized set of $CRSS_s$ provides a good match with the experimental data. The fact that both the pile-up patterns and the variation of the P_{max} with the declination angle are only reproduced by the one set of CRSS, provides additional validation of the optimized set.

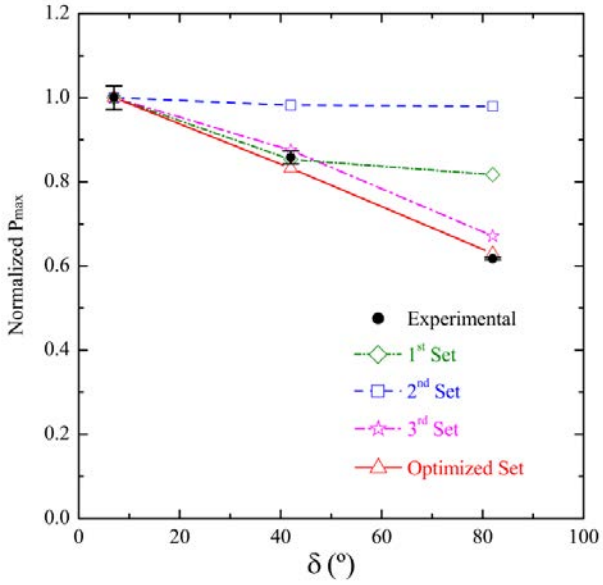

Fig. B.3: Comparison between the experimental and the simulated P_{max} - δ curves corresponding to the four selected sets of CRSS studied in Fig. B.2. In each case, the maximum load is normalized with respect to that of the grain with $\delta = 7°$.

Table B.2 compares the ratios between the initial CRSS of the non-basal and basal slip systems of pure Mg at RT and 300 °C, measured from single crystal and nanoindentation experiments combined with CPFE simulations by different authors. It should be mentioned that Table B.2 only includes data from studies in which both non-basal and basal values were measured, so that the actual ratios could be calculated. At RT, $CRSS_{pris.}/CRSS_{basal}$ ratios range from 12 to 50 and $CRSS_{pyra.}/CRSS_{basal}$ from 20 to 80 [49, 90, 136, 166]. Both ratios are drastically reduced at 300 °C to 6 and 12 [27], respectively. As it can be seen in Table B.2, the results obtained from the present study fit very well with the described trends [27, 49, 90, 136, 166], thus confirming that nanoindentation constitutes an efficient tool that allows studying the deformation mechanisms of Mg and its alloys at high temperature.

	RT	300 °C	
$CRSS_{pris.}/CRSS_{basal}$	$\sim$ 13-50 [49, 90, 136, 166]	6 [27]	2 [*]
$CRSS_{pyra.}/CRSS_{basal}$	$\sim$ 20-80 [49, 90, 136, 166]	12 [27]	12 [*]

Table B.2: Summary of the ratios between the initial glide resistance of the non-basal and basal slip systems of pure Mg at RT [49, 90, 136, 166] and 300 °C [27]-[*current work].

Bibliography

[1] U. Colin, *The elements: Magnesium*. Marshal Cavendish Corporation. New York, 2000.

[2] H. Watarai, "The trend of research and development for magnesium alloys," *Science & Technology Trends*, pp. 84 – 97, 2006.

[3] M. Easton, A. Beer, M. Barnett, C. Davies, and G. Dulop, "Magnesium alloy applications in automotive structures," *Journal of Materials*, vol. 60, no. 11, pp. 57–60, 2008.

[4] H. Watarai, "Trend of research and development for magnesium alloys," *Science & Technology trends*, vol. 7, no. 18, pp. 84 – 97, 2006.

[5] M. Gupta and N. M. L. Sharon, *Magnesium, Magnesium Alloys, and Magnesium Composites*. John Wiley & Sons, Inc., 2011.

[6] M. P. Staiger, A. M. Pietak, J. Huadmai, and G. Dias, "Magnesium and its alloys as orthopedic biomaterials: A review," *Biomaterials*, vol. 27, no. 9, pp. 1728 – 1734, 2006.

[7] I. S. Bert Verlinden, Julian Driver and R. D. Doherty, *Thermo-Mechanical Processing of Metallic Materials*. Elsevier, 2007.

[8] M. J. Zehetbauer and Y. T. Zhu, *Bulk Nanostructured Materials*. Wiley, 2013.

[9] H. D. Yuqing Weng and Y. Gan, *Advanced Steels*. Springer, 2011.

[10] H. B. Michael M. Avedesian, *Magnesium and Magnesium Aloys*. American Society for Metals. United States of America, 1999.

[11] "The influcence of alloying elements and heat treatment upon properties of elektron 21 (ev31a) alloy," *TMS Magnesium Technology*, pp. 303 – 308, 2005.

[12] C. J. Bettles and M. Barnett, *Advances in wrought magnesium alloys : fundamentals of processing, properties and applications / edited by Colleen Bettles and Matthew Barnett*. Woodhead Cambridge, England, 2012.

[13] D. R. Liu and P. G. Schultz, "Generating new molecular function: A lesson from nature," *Angewandte Chemie International Edition*, vol. 38, no. 1-2, pp. 36–54, 1999.

[14] J.-C. J.-C. Zhao, "The diffusion-multiple approach to designing alloys," *Annual Review of Materials Research*, vol. 35, no. 1, pp. 51–73, 2005.

[15] U. of Cambridge, "Slip geometry: the critical resolved shear stress." http://www.doitpoms.ac.uk/tlplib/slip/slip_geometry.php.

[16] G. I. Taylor, "Plastic strain in metals," *Journal of the Institute of Metals*, vol. 62, pp. 307 – 324, 1938.

[17] J. Christian and S. Mahajan, "Deformation twinning," *Progress in Materials Science*, vol. 39, no. 1–2, pp. 1 – 157, 1995.

[18] I. Ulacia, N. Dudamell, F. Gálvez, S. Yi, M. Pérez-Prado, and I. Hurtado, "Mechanical behavior and microstructural evolution of a mg {AZ31} sheet at dynamic strain rates," *Acta Materialia*, vol. 58, no. 8, pp. 2988 – 2998, 2010.

[19] S. R. Agnew and Özgür Duygulu, "Plastic anisotropy and the role of non-basal slip in magnesium alloy {AZ31B}," *International Journal of Plasticity*, vol. 21, no. 6, pp. 1161 – 1193, 2005. Plasticity of Multiphase Materials.

[20] A. Fernández, M. T. P. Prado, Y. Wei, and A. Jérusalem, "Continuum modeling of the response of a mg alloy {AZ31} rolled sheet during uniaxial deformation," *International Journal of Plasticity*, vol. 27, no. 11, pp. 1739 – 1757, 2011.

[21] A. Jain and S. Agnew, "Modeling the temperature dependent effect of twinning on the behavior of magnesium alloy {AZ31B} sheet," *Materials Science and Engineering: A*, vol. 462, no. 1–2, pp. 29 – 36, 2007. International Symposium on Physics of Materials, 2005.

[22] M. Knezevic, A. Levinson, R. Harris, R. K. Mishra, R. D. Doherty, and S. R. Kalidindi, "Deformation twinning in az31: Influence on strain hardening and texture evolution," *Acta Materialia*, vol. 58, no. 19, pp. 6230 – 6242, 2010.

[23] S. Sandöbes, S. Zaefferer, I. Schestakow, S. Yi, and R. Gonzalez-Martinez, "On the role of non-basal deformation mechanisms for the ductility of mg and mg-y alloys," *Acta Materialia*, vol. 59, no. 2, pp. 429 – 439, 2011.

[24] A. Galiyev, R. Kaibyshev, and G. Gottstein, "Correlation of plastic deformation and dynamic recrystallization in magnesium alloy {ZK60}," *Acta Materialia*, vol. 49, no. 7, pp. 1199 – 1207, 2001.

[25] M. Barnett, "Twinning and the ductility of magnesium alloys: Part i: "tension" twins," *Materials Science and Engineering: A*, vol. 464, no. 1–2, pp. 1 – 7, 2007.

[26] M. Barnett, "Twinning and the ductility of magnesium alloys: Part ii. "contraction" twins," *Materials Science and Engineering: A*, vol. 464, no. 1–2, pp. 8 – 16, 2007.

[27] A. Chapuis and J. H. Driver, "Temperature dependency of slip and twinning in plane strain compressed magnesium single crystals," *Acta Materialia*, vol. 59, no. 5, pp. 1986 – 1994, 2011.

[28] R. A. Lebensohn and C. N. Tomé, "A study of the stress state associated with twin nucleation and propagation in anisotropic materials," *Philosophical Magazine A*, vol. 67, no. 1, pp. 187–206, 1993.

[29] M. Meyers, O. Vöhringer, and V. Lubarda, "The onset of twinning in metals: a constitutive description," *Acta Materialia*, vol. 49, no. 19, pp. 4025 – 4039, 2001.

[30] Q. Yu, L. Qi, K. Chen, R. K. Mishra, J. Li, and A. M. Minor, "The nanostructured origin of deformation twinning," *Nano Letters*, vol. 12, no. 2, pp. 887–892, 2012. PMID: 22239446.

[31] Y. Wang, L.-Q. Chen, Z.-K. Liu, and S. Mathaudhu, "First-principles calculations of twin-boundary and stacking-fault energies in magnesium," *Scripta Materialia*, vol. 62, no. 9, pp. 646 – 649, 2010.

[32] M. Barnett, Z. Keshavarz, A. Beer, and D. Atwell, "Influence of grain size on the compressive deformation of wrought mg–3al–1zn," *Acta Materialia*, vol. 52, no. 17, pp. 5093 – 5103, 2004.

[33] Q. Yu, Z.-W. Shan, J. Li, X. Huang, L. Xiao, J. Sun, and E. Ma, "Strong crystal size effect on deformation twinning," *Nature*, vol. 463, no. 7279, pp. 335 – 338, 2010.

[34] K. E. Prasad, K. Rajesh, and U. Ramamurty, "Micropillar and macropillar compression responses of magnesium single crystals oriented for single slip or extension twinning," *Acta Materialia*, vol. 65, pp. 316 – 325, 2014.

[35] H. Conrad and W. Robertson, "Effect of temperature on the flow stress and strain-hardening coefficient of magnesium single crystals," *AIME Transactions*, vol. 209, pp. 503–513, 1957.

[36] H. Fan, Q. Wang, X. Tian, and J. A. El-Awady, "Temperature effects on the mobility of pyramidal ⟨c+a⟩ dislocations in magnesium," *Scripta Materialia*, vol. 127, pp. 68 – 71, 2017.

[37] A. Serra, R. Pond, and D. Bacon, "Computer simulation of the structure and mobility of twinning disclocations in h.c.p. metals," *Acta Metallurgica et Materialia*, vol. 39, no. 7, pp. 1469 – 1480, 1991.

[38] B. Wonsiewics and W. Backofen, "Plasticity of magnesium crystals," *Transactions of the Metallurgical Society of AIME*, vol. 239, pp. 1422 – 1431, 1967.

[39] B. Wonziewicz and W. Backofen, "Plasticity of magnesium crystals," *Transactions of the metallurgical society of AIME*, vol. 239, pp. 1422–1431, 1967.

[40] H. Yoshinaga and R. Horiuchi, "On the nonbasal slip in magnesium crystals," *Transactions of the Japan Institute of Metals*, vol. 5, pp. 14–21, 1964.

[41] H. Yoshinaga and R. Horiuchi, "Deformation mechanisms in magnesium single crystals compressed in the direction parallel to hexagonal axis," *Transactions of the Japan Institute of Metals*, vol. 4, pp. 1–8, 1963.

[42] T. Obara, H. Yoshinga, and S. Morozumi, "$\{11\bar{2}2\}\ \langle\bar{1}\bar{1}23\rangle$ slip system in magnesium," *Acta Metallurgica*, vol. 21, no. 7, pp. 845 – 853, 1973.

[43] P. Klimanek and A. Pötzsch, "Microstructure evolution under compressive plastic deformation of magnesium at different temperatures and strain rates," *Materials Science and Engineering: A*, vol. 324, no. 1–2, pp. 145 – 150, 2002.

[44] A. Ghaderi, F. Siska, and M. Barnett, "Influence of temperature and plastic relaxation on tensile twinning in a magnesium alloy," *Scripta Materialia*, vol. 69, no. 7, pp. 521 – 524, 2013.

[45] A. S. Khan, A. Pandey, T. Gnäupel-Herold, and R. K. Mishra, "Mechanical response and texture evolution of {AZ31} alloy at large strains for different strain rates and temperatures," *International Journal of Plasticity*, vol. 27, no. 5, pp. 688 – 706, 2011.

[46] J. Čapek, G. Farkas, J. Pilch, and K. Máthis, "Temperature dependence of twinning activity in random textured cast magnesium," *Materials Science and Engineering: A*, vol. 627, pp. 333 – 335, 2015.

[47] C. Cepeda-Jiménez, J. Molina-Aldareguia, and M. Pérez-Prado, "Origin of the twinning to slip transition with grain size refinement, with decreasing strain rate and with increasing temperature in magnesium," *Acta Materialia*, vol. 88, pp. 232 – 244, 2015.

[48] E. W. Kelley and W. F. Hosford, "Plane-strain compresion of magnesium and magnesium alloys crystals," *Transactions of the Metallurgical Society of AIME*, vol. 242, no. 1, pp. 5 – 13, 1968.

[49] J. Zhang and S. P. Joshi, "Phenomenological crystal plasticity modeling and detailed micromechanical investigations of pure magnesium," *Journal of the Mechanics and Physics of Solids*, vol. 60, no. 5, pp. 945 – 972, 2012.

[50] M. D. Uchic, D. M. Dimiduk, J. N. Florando, and W. D. Nix, "Sample dimensions influence strength and crystal plasticity," *Science*, vol. 305, no. 5686, pp. 986 – 989, 2004.

[51] W. D. Nix, J. R. Greer, G. Feng, and E. T. Lilleodden, "Deformation at the nanometer and micrometer length scales: Effects of strain gradients and dislocation starvation," *Thin Solid Films*, vol. 515, no. 6, pp. 3152 – 3157, 2007. TMS 2005 - Mechanical Behaviour of Thin Films and Small Structures.

[52] R. Soler, J. Molina-Aldareguia, J. Segurado, J. Llorca, R. Merino, and V. Orera, "Micropillar compression of lif single crystals: Effect of size, ion irradiation and misorientation," *International Journal of Plasticity*, vol. 36, no. 0, pp. 50 – 63, 2012.

[53] V. Herrera-Solaz, J. LLorca, E. Dogan, I. Karaman, and J. Segurado, "An inverse optimization strategy to determine single crystal mechanical behavior from polycrystal tests: Application to {AZ31} mg alloy," *International Journal of Plasticity*, vol. 57, pp. 1 – 15, 2014.

[54] Y. Liu, B. Wang, M. Yoshino, S. Roy, H. Lu, and R. Komanduri, "Combined numerical simulation and nanoindentation for determining mechanical properties of single crystal copper at mesoscale," *Journal of the Mechanics and Physics of Solids*, vol. 53, no. 12, pp. 2718 – 2741, 2005.

[55] Y. Wang, D. Raabe, C. Klüber, and F. Roters, "Orientation dependence of nanoindentation pile-up patterns and of nanoindentation microtextures in copper single crystals," *Acta Materialia*, vol. 52, no. 8, pp. 2229 – 2238, 2004.

[56] Y. Liu, S. Varghese, J. Ma, M. Yoshino, H. Lu, and R. Komanduri, "Orientation effects in nanoindentation of single crystal copper," *International Journal of Plasticity*, vol. 24, no. 11, pp. 1990 – 2015, 2008.

[57] C. Zambaldi and D. Raabe, "Plastic anisotropy of gamma-tial revealed by axisymmetric indentation," *Acta Materialia*, vol. 58, no. 9, pp. 3516 – 3530, 2010.

[58] C. Zambaldi, Y. Yang, T. R. Bieler, and D. Raabe, "Orientation informed nanoindentation of alpha-titanium: Indentation pileup in hexagonal metals deforming by prismatic slip," *Journal of Materials Research*, vol. 27, pp. 356–367, 2012.

[59] J.-H. Shin, S.-H. Kim, T. Ha, K. Oh, I.-S. Choi, and H. Han, "Nanoindentation study for deformation twinning of magnesium single crystal," *Scripta Materialia*, vol. 68, no. 7, pp. 483 – 486, 2013.

[60] C. Zambaldi, C. Zehnder, and D. Raabe, "Orientation dependent deformation by slip and twinning in magnesium during single crystal indentation," *Acta Materialia*, vol. 91, pp. 267 – 288, 2015.

[61] B. Selvarajou, J.-H. Shin, T. K. Ha, I. suk Choi, S. P. Joshi, and H. N. Han, "Orientation-dependent indentation response of magnesium single crystals: Modeling and experiments," *Acta Materialia*, vol. 81, pp. 358 – 376, 2014.

[62] H. M. Zbib, M. Rhee, and J. P. Hirth, "On plastic deformation and the dynamics of 3d dislocations," *International Journal of Mechanical Sciences*, vol. 40, no. 2–3, pp. 113 – 127, 1998.

[63] J. L. J. Segurado and I. Romero, "Computational issues in the simulation of twodimensional discrete dislocation mechanics," *Modelling and Simulation in Materials Science and Engineering*, vol. 15, no. 4, pp. 361 – 376, 2007.

[64] S. Groh, E. Marin, M. Horstemeyer, and H. Zbib, "Multiscale modeling of the plasticity in an aluminum single crystal," *International Journal of Plasticity*, vol. 25, no. 8, pp. 1456 – 1473, 2009.

[65] K. Danas, V. Deshpande, and N. Fleck, "Compliant interfaces: A mechanism for relaxation of dislocation pile-ups in a sheared single crystal," *International Journal of Plasticity*, vol. 26, no. 12, pp. 1792 – 1805, 2010.

[66] J. Wang, J. Hirth, and C. Tomé, "Twinning nucleation mechanisms in hexagonal-close-packed crystals," *Acta Materialia*, vol. 57, no. 18, pp. 5521 – 5530, 2009.

[67] L. Yue, H. Zhang, and D. Li, "A closer look at the local responses of twin and grain boundaries in cu to stress at the nanoscale with possible transition from the p–h to the inverse p–h relation," *Acta Materialia*, vol. 58, no. 7, pp. 2677 – 2684, 2010.

[68] D. Peirce, R. Asaro, and A. Needleman, "An analysis of nonuniform and localized deformation in ductile single crystals," *Acta Metallurgica*, vol. 30, no. 6, pp. 1087 – 1119, 1982.

[69] D. Peirce, R. Asaro, and A. Needleman, "Material rate dependence and localized deformation in crystalline solids," *Acta Metallurgica*, vol. 31, no. 12, pp. 1951 – 1976, 1983.

[70] R. Asaro and A. Needleman, "Overview no. 42 texture development and strain hardening in rate dependent polycrystals," *Acta Metallurgica*, vol. 33, no. 6, pp. 923 – 953, 1985.

[71] S. Kalidindi, C. Bronkhorst, and L. Anand, "Crystallographic texture evolution in bulk deformation processing of {FCC} metals," *Journal of the Mechanics and Physics of Solids*, vol. 40, no. 3, pp. 537 – 569, 1992.

[72] F. Roters, P. Eisenlohr, L. Hantcherli, D. Tjahjanto, T. Bieler, and D. Raabe, "Overview of constitutive laws, kinematics, homogenization and multiscale methods in crystal plasticity finite-element modeling: Theory, experiments, applications," *Acta Materialia*, vol. 58, no. 4, pp. 1152 – 1211, 2010.

[73] P. V. Houtte, A. K. Kanjarla, A. V. Bael, M. Seefeldt, and L. Delannay, "Multiscale modelling of the plastic anisotropy and deformation texture of polycrystalline materials," *European Journal of Mechanics - A/Solids*, vol. 25, no. 4, pp. 634 – 648, 2006. 6th {EUROMECH} Solid Mechanics ConferenceGeneral/Plenary Lectures.

[74] L. Anand and M. Kothari, "A computational procedure for rate-independent crystal plasticity," *Journal of the Mechanics and Physics of Solids*, vol. 44, no. 4, pp. 525 – 558, 1996.

[75] L. Anand, "Single-crystal elasto-viscoplasticity: application to texture evolution in polycrystalline metals at large strains," *Computer Methods in Applied Mechanics and Engineering*, vol. 193, no. 48–51, pp. 5359 – 5383, 2004. Advances in Computational Plasticity.

[76] Z. Zhao, S. Kuchnicki, R. Radovitzky, and A. Cuitiño, "Influence of in-grain mesh resolution on the prediction of deformation textures in fcc polycrystals by crystal plasticity {FEM}," *Acta Materialia*, vol. 55, no. 7, pp. 2361 – 2373, 2007.

[77] A. Jérusalem, M. Dao, S. Suresh, and R. Radovitzky, "Three-dimensional model of strength and ductility of polycrystalline copper containing nanoscale twins," *Acta Materialia*, vol. 56, no. 17, pp. 4647 – 4657, 2008.

[78] M. Lee, H. Lim, B. Adams, J. Hirth, and R. Wagoner, "A dislocation density-based single crystal constitutive equation," *International Journal of Plasticity*, vol. 26, no. 7, pp. 925 – 938, 2010.

[79] J. Rossiter, A. Brahme, M. Simha, K. Inal, and R. Mishra, "A new crystal plasticity scheme for explicit time integration codes to simulate deformation in 3d microstructures: Effects of strain path, strain rate and thermal softening on localized deformation in the aluminum alloy 5754 during simple shear," *International Journal of Plasticity*, vol. 26, no. 12, pp. 1702 – 1725, 2010.

[80] I. Watanabe, D. Setoyama, N. Iwata, and K. Nakanishi, "Characterization of yielding behavior of polycrystalline metals with single crystal plasticity based on representative characteristic length," *International Journal of Plasticity*, vol. 26, no. 4, pp. 570 – 585, 2010.

[81] S. Kuchnicki, R. Radovitzky, and A. Cuitiño, "An explicit formulation for multiscale modeling of bcc metals," *International Journal of Plasticity*, vol. 24, no. 12, pp. 2173 – 2191, 2008.

[82] J. Mayeur and D. McDowell, "A three-dimensional crystal plasticity model for duplex ti–6al–4v," *International Journal of Plasticity*, vol. 23, no. 9, pp. 1457 – 1485, 2007.

[83] J. Segurado and J. Llorca, "Simulation of the deformation of polycrystalline nanostructured ti by computational homogenization," *Computational Materials Science*, vol. 76, pp. 3 – 11, 2013.

[84] A. Alankar, P. Eisenlohr, and D. Raabe, "A dislocation density-based crystal plasticity constitutive model for prismatic slip in α-titanium," *Acta Materialia*, vol. 59, no. 18, pp. 7003 – 7009, 2011.

[85] P. Houtte, "Simulation of the rolling and shear texture of brass by the taylor theory adapted for mechanical twinning," *Acta Metallurgica*, vol. 26, no. 4, pp. 591 – 604, 1978.

[86] C. Tomé, R. Lebensohn, and U. Kocks, "A model for texture development dominated by deformation twinning: Application to zirconium alloys," *Acta Metallurgica et Materialia*, vol. 39, no. 11, pp. 2667 – 2680, 1991.

[87] S. R. Kalidindi, "Incorporation of deformation twinning in crystal plasticity models," *Journal of the Mechanics and Physics of Solids*, vol. 46, no. 2, pp. 267 – 290, 1998.

[88] T. Mayama, K. Aizawa, Y. Tadano, and M. Kuroda, "Influence of twinning deformation and lattice rotation on strength differential effect in polycrystalline pure magnesium with rolling texture," *Computational Materials Science*, vol. 47, no. 2, pp. 448 – 455, 2009.

[89] A. Staroselsky and L. Anand, "A constitutive model for hcp materials deforming by slip and twinning: application to magnesium alloy {AZ31B}," *International Journal of Plasticity*, vol. 19, no. 10, pp. 1843 – 1864, 2003.

[90] S. Graff, W. Brocks, and D. Steglich, "Yielding of magnesium: From single crystal to polycrystalline aggregates," *International Journal of Plasticity*, vol. 23, no. 12, pp. 1957 – 1978, 2007.

[91] S.-H. Choi, D. Kim, H. Lee, and E. Shin, "Simulation of texture evolution and macroscopic properties in mg alloys using the crystal plasticity finite element method," *Materials Science and Engineering: A*, vol. 527, no. 4–5, pp. 1151 – 1159, 2010.

[92] J. Lévesque, K. Inal, K. Neale, and R. Mishra, "Numerical modeling of formability of extruded magnesium alloy tubes," *International Journal of Plasticity*, vol. 26, no. 1, pp. 65 – 83, 2010.

[93] W. Tang, S. Zhang, Y. Peng, and D. Li, "Simulation of magnesium alloy {AZ31} sheet during cylindrical cup drawing with rate independent crystal plasticity finite element method," *Computational Materials Science*, vol. 46, no. 2, pp. 393 – 399, 2009.

[94] I. Minin and O. Minin, "Introduction," in *Diffractive Optics and Nanophotonics*, SpringerBriefs in Physics, pp. 1–5, Springer International Publishing, 2016.

[95] J. B. BINDELL, "2.2 - sem: Scanning electron microscopy," in *Encyclopedia of Materials Characterization* (C. R. Brundle, C. A. Evans, and S. Wilson, eds.), pp. 70 – 84, Boston: Butterworth-Heinemann, 1992.

[96] A. L. . T. Council, "Generation of x-rays in the electron microscope," 2012. Available at http://li155-94.members.linode.com/myscope/analysis/eds/xraygeneration/.

[97] C. C. C. for Welding + Joining, "Teaching microscopy: 1. scanning electron microscopy (sem/eds)." Available at http://www.ualberta.ca/ ccwj/teaching/microscopy/.

[98] P. University, "Scanning electron microscopy." https://www.purdue.edu/ehps/rem/rs/sem.htm.

[99] A. Bastos, S. Zaefferer, D. Raabe, and C. Schuh, "Characterization of the microstructure and texture of nanostructured electrodeposited nico using electron backscatter diffraction (ebsd)," *Acta Materialia*, vol. 54, no. 9, pp. 2451 – 2462, 2006.

[100] V. Randle, G. Rohrer, H. Miller, M. Coleman, and G. Owen, "Five-parameter grain boundary distribution of commercially grain boundary engineered nickel and copper," *Acta Materialia*, vol. 56, no. 10, pp. 2363 – 2373, 2008.

[101] M. G. Perez, E. A. Kenik, M. J. O. Keefe, F. S. Miller, and B. Johnson, "Identification of phases in zinc alloy powders using electron backscatter diffraction," *Materials Science and Engineering: A*, vol. 424, no. 1â€“2, pp. 239 – 250, 2006.

[102] A. J. Wilkinson, G. Meaden, and D. J. Dingley, "High-resolution elastic strain measurement from electron backscatter diffraction patterns: New levels of sensitivity," *Ultramicroscopy*, vol. 106, no. 4-5, pp. 307 – 313, 2006.

[103] O. Instrument, "Ebsd explained > basics of ebsd > pattern formation." Available at http://www.ebsd.com/ebsd-explained/basics-of-ebsd/pattern-formation.

[104] R. Schwarzer, "Ebsd and bkd: The multi-array image detector." Available at http://www.ebsd.info/detector.htm.

[105] FEI, "Helios nanolab™dualbeam™." https://www.fei.com/products/dualbeam/helios-nanolab/.

[106] O. Instruments, "Ebsd detector - nordlysnano." http://www.oxford-instruments.com/products/microanalysis/ebsd/ebsd-detectors-nordlys.

[107] W. de Souza and G. M. Rocha, "Atomic force microscopy: a tool to analyze the structural organization of pathogenic protozoa," *Trends in Parasitology*, vol. 27, no. 4, pp. 160 – 167, 2011.

[108] Bruker, "Spm training guide: Atomic force microscopy (afm)." Available at http://www.nanophys.kth.se/nanophys/facilities/nfl/afm/icon/bruker-help/Content/SPM

[109] Bruker, "Tappingmode: The most popular afm imaging mode, the backbone of specialized techniques." Available at https://www.bruker.com/products/surface-analysis/atomic-force-microscopy/modes/modes/imaging-modes/tapping-mode.html.

[110] J. Instruments, "Tutorials - atomic force microscopy (afm): Introduction to imaging modes." Available at http://usa.jpk.com/introduction-to-imaging-modes.433.us.html.

[111] P. Systems, "Park xe15 atomic force microscope." http://www.parkafm.com/index.php/products/research-afm/park-xe15/overview.

[112] A. QUANTUM, "Xe-150 large sample atomic force microscope from park systems." Available at http://www.azoquantum.com/equipment-details.aspx?EquipID=104.

[113] T. D., "The hardness and strength of metals," *Journal of the Institute of Metals*, vol. 79, 1951.

[114] J. K.L., "The correlation of indentation experiments," *Journal of the Mechanics and Physics of Solids*, vol. 18, pp. 115 – 256, 1970.

[115] W. Oliver and G. Pharr, "An improved technique for determining hardness and elastic modulus using load and displacement sensing indentation experiments," *Journal of Materials Research*, vol. 7, pp. 1564–1583, 1992.

[116] O. W. Pethica JB, Hutchings R, "Hardness measurement at penetration depths as small as 20 nm.," *Journal of Materials and Research*, vol. 48, pp. 593–606, 1983.

[117] I. N. Sneddon, "The relation between load and penetration in the axisymmetric boussinesq problem for a punch of arbitrary profile," *International Journal of Engineering Science*, vol. 3, no. 1, pp. 47 – 57, 1965.

[118] K. Technologies, "Keysight technologies – how to select the correct indenter tip: Support note," 2009. Available at http://literature.cdn.keysight.com/litweb/pdf/5990-4907EN.pdf?id=1791577.

[119] B. Mesa, "Micro star technologies: Spherical and rounded cone nano indenters." Available at http://www.microstartech.com/index/ConicalIndenters2.pdf.

[120] "A procedure to prevent pile up effects on the analysis of spherical indentation data in elastic–plastic materials," *Mechanics of Materials*, vol. 39, no. 11, pp. 987 – 997, 2007.

[121] M. Y. N'jock, D. Chicot, J. Ndjaka, J. Lesage, X. Decoopman, F. Roudet, and A. Mejias, "A criterion to identify sinking-in and piling-up in indentation of materials," *International Journal of Mechanical Sciences*, vol. 90, pp. 145 – 150, 2015.

[122] J. C. Trenkle, C. E. Packard, and C. A. Schuh, "Hot nanoindentation in inert environments," *Review of Scientific Instruments*, vol. 81, pp. 073901–073913, 2010.

[123] I. Hysitrion, "Ti 950 triboindenter®." https://www.hysitron.com/products-services/standalone-instruments/ti-950-triboindenter.

[124] M. Materials, "Nanotest®." http://www.micromaterials.co.uk/.

[125] Hysitron, "Electrostatic actuation: An overview of hysitron's patented transducer," 2013. Available at http://phi-gmbh.eu/wp-content/uploads/2013/10/Electrostatic-Actuation.pdf.

[126] S. Lotfian, *High Temperature Mechanical Behavior of Al/SiC Nanoscale Multilayers*. PhD thesis, Universidad Carlos III de Madrid, 2014.

[127] M. Materials, "Mechanical testing of polymeric materials on the nanoscale using the nanotest system," 2013. Available at http://www.azom.com/article.aspx?ArticleID=4746.

[128] Spectrum, "Nanotest vantage – nanoindenter for high-temperature applications," 2014. Available at http://lot-qd.com/news/product-application-news-spectrum/international-spectrum-e20/nanotest-vantage-nanoindenter-for-high-temperature-applications/?newsid=24.

[129] *ABAQUS/Standar v6.10 User's Manual*. ABAQUS Inc., Richmond, USA, 2009.

[130] J. Segurado and J. Llorca, "Simulation of the deformation of polycrystalline nanostructured ti by computational homogenization," *Computational Materials Science*, vol. 76, pp. 3 – 11, 2013.

[131] E. H. Lee, "Elastic-plastic deformation at finite strains," *Journal of Applied Mechanics*, vol. 36, pp. 1–6, 1969.

[132] J. W. Hutchinson, "Bounds and self-consistent estimates for creep of polycrystalline materials," *Proceedings of the Royal Society of London. A. Mathematical and Physical Sciences*, vol. 348, no. 1652, pp. 101–127, 1976.

[133] M. Kothari and L. Anand, "Elasto-viscoplastic constitutive equations for polycrystalline metals: Application to tantalum," *Journal of the Mechanics and Physics of Solids*, vol. 46, no. 1, pp. 51 – 83, 1998.

[134] L. Capolungo, I. Beyerlein, and C. Tomé, "Slip-assisted twin growth in hexagonal close-packed metals," *Scripta Materialia*, vol. 60, no. 1, pp. 32 – 35, 2009.

[135] E. A. de Souza Neto, D. Peric, and D. R. J. Owen, *Computational Methods for Plasticity: Theory and Applications*. Wiley, 2008.

[136] R. Sánchez-Martín, M. Pérez-Prado, J. Segurado, J. Bohlen, I. Gutiérrez-Urrutia, J. Llorca, and J. Molina-Aldareguia, "Measuring the critical resolved shear stresses in mg alloys by instrumented nanoindentation," *Acta Materialia*, vol. 71, pp. 283 – 292, 2014.

[137] N. Zaafarani, D. Raabe, R. Singh, F. Roters, and S. Zaefferer, "Three-dimensional investigation of the texture and microstructure below a nanoindent in a cu single crystal using 3d {EBSD} and crystal plasticity finite element simulations," *Acta Materialia*, vol. 54, no. 7, pp. 1863 – 1876, 2006.

[138] J. Jiang, A. Godfrey, W. Liu, and Q. Liu, "Identification and analysis of twinning variants during compression of a mg–al–zn alloy," *Scripta Materialia*, vol. 58, no. 2, pp. 122 – 125, 2008.

[139] G. Pharr, W. Oliver, and F. Brotzen, "On the generality of the relationship among contact stiffness, contact area, and elastic modulus during indentation," *Journal of Materials Research*, vol. 7, pp. 613–617, 2 1992.

[140] G. Kim, *Small Volume Investigation of Slip and* . PhD thesis, Université de Grenoble, 2011.

[141] A. Bhattacharya and W. Nix, "Finite element simulation of indentation experiments," *International Journal of Solids and Structures*, vol. 24, no. 9, pp. 881 – 891, 1988.

[142] G. M. Pharr, E. G. Herbert, and Y. Gao, "The indentation size effect: A critical examination of experimental observations and mechanistic interpretations," *Annual Review of Materials Research*, vol. 40, no. 1, pp. 271–292, 2010.

[143] J. W. Hutchinson, "Plasticity at the micron scale," *International Journal of Solids and Structures*, vol. 37, no. 1–2, pp. 225 – 238, 2000.

[144] W. D. Nix and H. Gao, "Indentation size effects in crystalline materials: A law for strain gradient plasticity," *Journal of the Mechanics and Physics of Solids*, vol. 46, no. 3, pp. 411 – 425, 1998.

[145] W. Poole, M. Ashby, and N. Fleck, "Micro-hardness of annealed and work-hardened copper polycrystals," *Scripta Materialia*, vol. 34, no. 4, pp. 559 – 564, 1996.

[146] F. P. E. D. T. B. Britton, H. Liang and A. J. Wilkinson, "The effect of crystal orientation on the indentation response of commercially pure titanium: experiments and simulations," *Proceedings ot the royal society A*, vol. 466, pp. 695 – 719, 2009.

[147] J. Robson, A. Twier, G. Lorimer, and P. Rogers, "Effect of extrusion conditions on microstructure, texture, and yield asymmetry in mg–6y–7gd–0.5 wt%zr alloy," *Materials Science and Engineering: A*, vol. 528, no. 24, pp. 7247 – 7256, 2011.

[148] T. Tsuru, Y. Udagawa, M. Yamaguchi, M. Itakura, H. Kaburaki, and Y. Kaji, "Solution softening in magnesium alloys: the effect of solid solutions on the dislocation core structure and nonbasal slip," *Journal of physics. Condensed matter*, vol. 25, no. 2, pp. 022202 – 022207, 2013.

[149] Y. Chino, M. Kado, and M. Mabuchi, "Compressive deformation behavior at room temperature - 773k in mg-0.2 mass%(0.035at.%)ce alloy," *Acta Materialia*, vol. 56, no. 3, pp. 387 – 394, 2008.

[150] P. Hidalgo-Manrique, S. Yi, J. Bohlen, D. Letzig, and M. Pérez-Prado, "Effect of nd additions on extrusion texture development and on slip activity in a mg-mn alloy," *Metallurgical and Materials Transactions A*, vol. 44, no. 10, pp. 4819–4829, 2013.

[151] N. Dudamell, I. Ulacia, F. Gálvez, S. Yi, J. Bohlen, D. Letzig, I. Hurtado, and M. Pérez-Prado, "Twinning and grain subdivision during dynamic deformation of a mg {AZ31} sheet alloy at room temperature," *Acta Materialia*, vol. 59, no. 18, pp. 6949 – 6962, 2011.

[152] A. Fernández, A. Jérusalem, I. Gutiérrez-Urrutia, and M. Pérez-Prado, "Three-dimensional investigation of grain boundary–twin interactions in a mg {AZ31} alloy by electron backscatter diffraction and continuum modeling," *Acta Materialia*, vol. 61, no. 20, pp. 7679 – 7692, 2013.

[153] M. Barnett, "A rationale for the strong dependence of mechanical twinning on grain size," *Scripta Materialia*, vol. 59, no. 7, pp. 696 – 698, 2008.

[154] B. Raeisinia and S. R. Agnew, "Using polycrystal plasticity modeling to determine the effects of grain size and solid solution additions on individual deformation mechanisms in cast mg alloys," *Scripta Materialia*, vol. 63, no. 7, pp. 731 – 736, 2010. Viewpoint set no. 47 Magnesium Alloy Science and Technology.

[155] H. Somekawa and T. Mukai, "Hall–petch relation for deformation twinning in solid solution magnesium alloys," *Materials Science and Engineering: A*, vol. 561, pp. 378 – 385, 2013.

[156] J. Bohlen, P. Dobroň, J. Swiostek, D. Letzig, F. Chmelík, P. Lukáč, and K. U. Kainer, "On the influence of the grain size and solute content on the {AE} response of magnesium alloys tested in tension and compression," *Materials Science and Engineering: A*, vol. 462, no. 1–2, pp. 302 – 306, 2007. International Symposium on Physics of Materials, 2005.

[157] C. H. Caceres, G. E. Mann, and J. R. Griffiths, "Grain size hardening in mg and mg-zn solid solutions," *Metallurgical and Materials Transactions A*, vol. 42, no. 7, pp. 1950–1959, 2011.

[158] I. Beyerlein, L. Capolungo, P. Marshall, R. McCabe, and C. Tomé, "Statistical analyses of deformation twinning in magnesium," *Philosophical Magazine*, vol. 90, no. 16, pp. 2161–2190, 2010.

[159] P. Dobroň, F. Chmelík, S. Yi, K. Parfenenko, D. Letzig, and J. Bohlen, "Grain size effects on deformation twinning in an extruded magnesium alloy tested in compression," *Scripta Materialia*, vol. 65, no. 5, pp. 424 – 427, 2011.

[160] I. Beyerlein, R. McCabe, and C. Tomé, "Effect of microstructure on the nucleation of deformation twins in polycrystalline high-purity magnesium: A multi-scale modeling study," *Journal of the Mechanics and Physics of Solids*, vol. 59, no. 5, pp. 988 – 1003, 2011.

[161] J. Wang, I. Beyerlein, and C. Tomé, "An atomic and probabilistic perspective on twin nucleation in mg," *Scripta Materialia*, vol. 63, no. 7, pp. 741 – 746, 2010. Viewpoint set no. 47 Magnesium Alloy Science and Technology.

[162] D. M. Saylor, B. S. E. Dasher, A. D. Rollett, and G. S. Rohrer, "Distribution of grain boundaries in aluminum as a function of five macroscopic parameters," *Acta Materialia*, vol. 52, no. 12, pp. 3649 – 3655, 2004.

[163] C.-S. Kim, Y. Hu, G. S. Rohrer, and V. Randle, "Five-parameter grain boundary distribution in grain boundary engineered brass," *Scripta Materialia*, vol. 52, no. 7, pp. 633 – 637, 2005.

[164] *A Matlab toolbox to analyze slip transfer through grain boundaries*, Zenodo, Sept. 2014. Final version DOI: http://dx.doi.org/10.1088/1757-899X/82/1/012090.

[165] J. Rodríguez and M. G. Maneiro, "A procedure to prevent pile up effects on the analysis of spherical indentation data in elastic–plastic materials," *Mechanics of Materials*, vol. 39, no. 11, pp. 987 – 997, 2007.

[166] R. Sánchez-Martín, M. Pérez-Prado, J. Segurado, and J. Molina-Aldareguia, "Effect of indentation size on the nucleation and propagation of tensile twinning in pure magnesium," *Acta Materialia*, vol. 93, pp. 114–128, 2015. cited By 7.

List of Figures

List of Tables

Personal contributions

Journal publications

- **R. Sánchez-Martín**, M.T. Pérez-Prado, J. Segurado, and J.M. Molina-Aldareguia, "Temperature dependency of slip and twinning in pure magnesium studied by nanoindentation," *To be submitted*.
- **R. Sánchez-Martín**, M.T. Pérez-Prado, J. Segurado, and J.M. Molina-Aldareguia, "Effect of indentation size on the nucleation and propagation of tensile twinning in pure magnesium," *Acta Materialia*, vol. 93, pp. 114 - 128, 2015.
- **R. Sánchez-Martín**, C. Zambaldi, M.T. Pérez-Prado, and J.M. Molina-Aldareguia, "High temperature deformation mechanisms in pure magnesium studied by nanoindentation," *Scripta Materialia*, vol. 104, pp. 9 - 12, 2015.
- **R. Sánchez-Martín**, M.T. Pérez-Prado, J. Segurado, J. Bohlen, I. Gutiérrez-Urrutia, J. Llorca, and J.M. Molina-Aldareguia, "Measuring the critical resolved shear stresses in Mg alloys by instrumented nanoindentation," *Acta Materialia*, vol. 71, pp. 283 - 292, 2014.

Conferences

- ECI 2015. 4-9 Oct, 2015. Albuferia, Portugal. J.M. Molina-Aldareguia, **R. Sánchez-Martín**, C. Cepeda-Jiménez, M.T. Pérez-Prado. Multiscale characterization of the micromechanics of pure Mg (Oral presentation).
- EUROMAT 2015. 20-24 Sept, 2015. Warsaw, Poland. **R. Sánchez-Martín**, C. Zambaldi, M.T. Pérez-Prado, J.M. Molina-Aldareguia. High temperature deformation mechanisms in Mg studied by nanoindentation (Oral presentation).

- ESMC 2015. 6-10 July, 2015. Madrid, Spain. **R. Sánchez-Martín (Speaker)**, M.T. Pérez-Prado, C. Zambaldi, J. Segurado, J.M. Molina-Aldareguia. High temperature nanoindentation of pure magnesium (Oral presentation).

- IWCMM24. 1-3 Oct, 2014. Madrid, Spain. **R. Sánchez-Martín**, M.T. Pérez-Prado, J. Segurado, J.M. Molina-Aldareguia (speaker). Effect of indentation size on the nucleation and propagation of tensile twinning in pure magnesium single crystals (Oral presentation).

- MSE 2014. 23-25 Sept, 2014. Darmstadt, Germany. C. Zambaldi, **R. Sánchez-Martín**, C. Zehnder, H.-O. Fabritius, M.T. Pérez-Prado, J.M. Molina-Aldareguia, D. Raabe. Slip and twinning in magnesium during indentation at room and elevated temperature (Poster).

- MSE 2014. 23-25 Sept, 2014. Darmstadt, Germany. **R. Sánchez-Martín**, M.T. Pérez-Prado, J. Segurado, J. Llorca, J.M. Molina-Aldareguia. Measuring the critical resolved shear stresses in Mg alloys by instrumented nanoindentation (Poster).

- 2014 TMS Annual Meeting & Exhibition. 16-20 Feb, 2014. San Diego, EEUU. Jon Molina-Aldareguia, **R. Sánchez-Martín**, M.T. Pérez-Prado, J.Segurado, J.Llorca. Measuring the critical resolved shear stresses in Mg alloys by instrumented nanoindentation (Poster).

- Euro LightMAT 2013. 3-5 Sept, 2013. Bremen, Germany. P. Hidalgo-Manrique, **R. Sánchez-Martín**, N.V. Dudamell, A. Chakkedath, Z. Chen, C.J. Boehlert, J. Segurado, S. Yi, J. Bohlen, D. Letzig, J.M. Molina-Aldareguía, M.T. Pérez-Prado (speaker). Microstructure, texture, and mechanical response of a magnesium-manganese alloy containing neodymium (Oral presentation).

- Magnesium Workshop Madrid 2013. 21-24 May, 2013. Madrid, Spain. **R. Sánchez-Martín (speaker)**, M.T. Pérez-Prado, J.Segurado, I. Gutierrez, J.Llorca, J.M. Molina-Aldareguia, Measuring the Critical Resolved Shear Stresses in Mg Alloys by Instrumented Nanoindentation (Oral presentation).